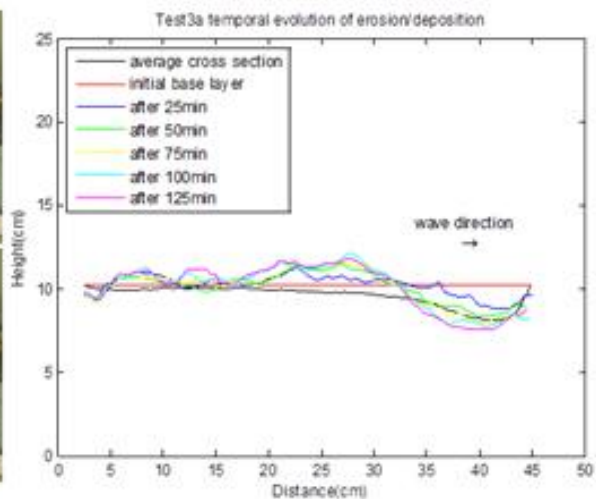
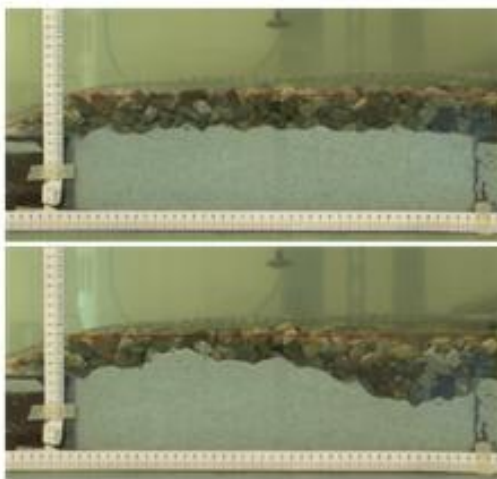


Scour below the toe of breakwaters

Investigation of scour formation through a geometrically open filter configuration located at the toe of a rubble mound breakwater lying upon sand



M_{Sc} thesis

Dimitrios Papadopoulos

Delft University of Technology
Faculty of Civil Engineering & Geosciences
Department of Hydraulic Engineering



Delta Marine Consultants
Department of Coastal Engineering
Royal BAM Group



Scour below the toe of breakwaters

Investigation of scour formation through a geometrically open filter configuration located at the toe of a rubble mound breakwater lying upon sand

A thesis submitted in partial fulfillment of the requirements
for the degree of

Master of Science in Hydraulic Engineering

at the

Delft University of Technology

Graduation Committee:

Prof.dr.ir. W.S.J. Uijtewaal
ir. H.J. Verhagen
ir. H. Verheij
ir. J.P. van den Bos
ir. J.S. Reedijk
dr.ir. M.O. Muttray

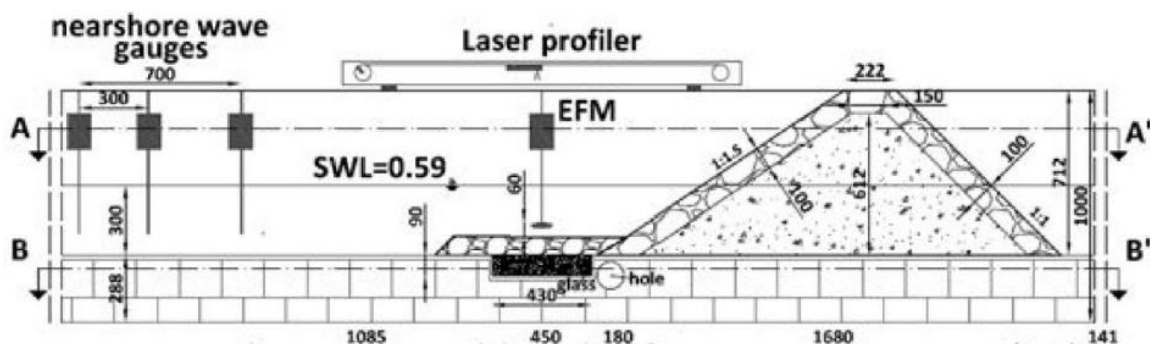
Delft University of Technology
Delft University of Technology
Delft University of Technology
Delft University of Technology
Delta Marine Consultants
Delta Marine Consultants

Summary

Scour formation at the toe of a rubble mound breakwater can lead to abrupt failure. Nowadays, counteraction of scour via geometrically closed filter rules, geotextiles or combinations is the common practice. Alternatively, in specific cases the use of geometrically open filters can save significant amount of time and decrease constructional costs. As a primary step towards this direction, the prediction of scour formation through a geometrically open filter can provide important information.

Nevertheless, at this moment the knowledge upon this issue is insufficient and limited. A variety of recommendations occurs in literature, separately for toe design and scour protection (with suggestions for additional bedding layers) and for the application of open filter criteria; however none of the studies treats these subjects combined. Therefore the objective of the present thesis is to get insight into scour formation and development through a breakwater toe lying upon sand and designed as a geometrically open filter. Thereby the research aims in drawing the link between scour characteristics with wave loading and filter configuration properties.

In order to accomplish the research objective 2D physical model tests were conducted in the 25m long, 1m deep and 0.6m wide wave flume of DMC, installed in the company's laboratory in Utrecht. The basic set-up of the physical model is illustrated in the figures below.



In total 23 tests were executed with irregular waves (Jonswap spectrum) and by varying wave loading and filter configuration properties. In particular, 5 different filter/base layer combinations were examined and 3 different wave conditions were used to investigate the

effects of relative grain diameter, relative filter thickness, grading of filter layer, base layer stability Number and storm duration.

Quantification of damage magnitude was accomplished via laser profile measurements of filter and base layer prior and after the execution of each test. Furthermore, wave particle velocity climate was determined via the use of an Electromagnetic Flow Meter (EMS) placed at the center of the toe. Finally, temporal evolution scour was captured through the right side glass and was examined by digitizing and analyzing snap-shots from predefined time steps.

Test results and observations have revealed the highly spatial character of scour formation. Nevertheless, tests with identical boundary conditions showed a surprising convergence in averaged maximum scour depth magnitude. In addition, in the majority of tests an S-curve erosion/deposition pattern was shaped while erosion started immediately at the downstream side of the box threatening breakwater stability.

Equilibrium maximum scour depth was reached for less than half the data set; thus erosion process was still in progress. Thereby two approaches were developed to investigate temporal evolution of scour. Firstly, for the total data set a linear function was fitted to relate final maximum scour depth with the square root of the number of peak waves under the form $S_{final} = \alpha_t * N_p^{0.5}$. Especially for tests that reaches equilibrium the following expression was derived while S_{final} and S_{max} are measured through the right side glass:

$$\frac{S_t}{S_{max}} = 1 - \exp\left(-2.668 \frac{N_t}{N_{max}}\right) \quad (6-1)$$

Dimensional analysis and literature review have revealed the most important parameters that have significant effect in scour formation. However, combination of the results from tests with different base materials would not be possible without the introduction of the base material stability Number (critical Shields' Number). The final outcome is expressed via eq. (6-7) while S_{aver} is the averaged maximum scour depth taken from the laser profile measurements:

$$\frac{S_{aver}}{H_s} = 0.0242 \left(\frac{N_p^{0.5} \left(\frac{D_{f50}}{D_{b50}}\right)^{0.5}}{\left(1000 \sinh\left(\frac{2\pi h_t}{L_{t,p}}\right)\right)^{1.35} (\Psi_{cb})^{1.6} \left(\frac{D_{f90}}{D_{f10}}\right)^{0.35}} \right) - 0.1131 \quad (6-7)$$

Eq. (6-7) is an empirical expression with limited physical background and range of validity. Additionally, eq. (6-7) overestimates maximum scour depth due to a serious model effect; the different buoyancy between filter and base layer that was causing initial damage and damage exaggeration.

On the other hand, the afore-mentioned expression is able to count for the deviation of relative grain diameter, relative water depth, storm duration, stability of the base layer (expressed in critical Shields' Number) and for the grading of the filter layer. Therefore, eq. (6-7) is capable of delineating the relative contribution of each parameter in scour depth formation.

For a more overall view of scour formation, further research will be needed in order to provide a more accurate quantification of the interrelation between the parameters that play a role in scour formation and development, and to implement the effect of missing parameters. Consequently, at the time being, the use of eq. (6-7) as a scour prediction tool in real life is not recommended.

Finally, in order to expand the knowledge upon this field the following strategy is recommended

- Tests with sand as base material and loose filter stones or tests with lightweight material as base material and glued filter stones
- Expansion of box length. A longer tracer model will be needed to mitigate the model effect due to transition induced scour
- Quantification of damping inside the filter to develop a process-based design tool with higher physical value.

Acknowledgements

The present report is an overview of the research project undertaken to obtain the degree of Master of Science at the Technical University of Delft. The subject of this Master Thesis is scour formation and development under the toe of rubble mound breakwaters.

The present study was commissioned, sponsored by Delta Marine Consultants (DMC/BAM Infraconsult b.v.) while the physical model tests were carried out in the laboratory facilities of DMC in Utrecht. In addition, part of the measuring equipment (Laser, EMS and supporting equipment) was granted disinterestedly from TU Delft's laboratory of Fluid Mechanics.

Accomplishing a project of such extent would not be possible without the aid of many people that I would like to thank. First of all, I would like to express my gratitude to DMC and especially to ir. J.S. Reedijk, for offering me the opportunity to work in such a sterling environment. In addition, I would like to thank all my colleagues from DMC and especially Michiel and Jay for their generous support in overcoming problems at the laboratory.

Furthermore, I would like to thank Sander de Vree for his invaluable help and technical advice. His contribution was decisive for the accomplishment of this project. At this point I would like to thank my friends Kostas and Apostolis for assisting me in building the physical model.

Finally, I would like to thank Prof.dr.ir. W.S.J. Uijttewaal, ir. H.J. Verhagen, ir. H. Verheij and ir. J.P. van den Bos, members of my graduation committee, for their interest and supervision. Their advice was substantial for the completion of the study. In addition, I would like to express my frank gratitude to dr.ir. M.O. Muttray for his invaluable advice.

Last but not least, I am very grateful to all "my" people for their psychological and sentimental support to run through this long journey.

Dimitrios Papadopoulos
Gouda, November 2012

Contents

SUMMARY	I
ACKNOWLEDGEMENTS	IV
CONTENTS	V
LIST OF FIGURES	VIII
LIST OF TABLES	XII
LIST OF SYMBOLS	XIII
1. INTRODUCTION	1
1.1. GENERAL INTRODUCTION.....	1
1.2. CONVENTIONAL RUBBLE MOUND BREAKWATER.....	2
1.2.1. <i>Breakwater compartments</i>	2
1.2.2. <i>Toe & granular filter criteria</i>	3
1.3. CLUB MYKONOS BREAKWATER; A REAL EXAMPLE.....	4
1.4. PROBLEM DEFINITION	6
1.5. RESEARCH OBJECTIVE	7
1.6. RESEARCH QUESTIONS & STUDY SCOPE.....	7
1.7. RESEARCH PLAN & STRUCTURE OF THE REPORT	8
2. SCOUR & GRANULAR FILTERS	10
2.1. SCOUR AROUND COASTAL STRUCTURES.....	10
2.1.1. <i>Scour around breakwaters</i>	10
2.1.2. <i>Scour around rubble mound breakwaters</i>	12
2.1.3. <i>Temporal evolution of scour depth</i>	15
2.2. GRANULAR FILTERS.....	15
2.2.1. <i>Geometrically closed filters</i>	16
2.2.2. <i>Hydraulically sand-tight (stable geometrically open) filters</i>	17
2.2.3. <i>Transport (unstable geometrically open) filters</i>	23
2.3. SUMMARY AND LINK TO THIS STUDY.....	23
3. MODEL & TEST SET-UP	25
3.1. PHYSICAL MODEL PROPERTIES.....	25
3.1.1. <i>Facility</i>	25
3.1.2. <i>Flume lay out</i>	25
3.1.3. <i>Rubble mound breakwater</i>	27
3.1.4. <i>Open filter configuration (toe & seabed material)</i>	29
3.2. TEST PROGRAM	31
3.3. MEASURING EQUIPMENT & MONITORING	34
3.4. TESTING PROCEDURE	37
4. TEST RESULTS	38
4.1. TEST SERIES 1.....	39
4.1.1. <i>Test1a</i>	39
4.1.2. <i>Test1b</i>	41
4.1.3. <i>Test1c</i>	42
4.1.4. <i>Test1d</i>	43

4.1.5.	<i>Test1e</i>	45
4.2.	TEST SERIES 2	47
4.2.1.	<i>Test2a</i>	47
4.2.2.	<i>Test2b</i>	48
4.2.3.	<i>Test2c</i>	50
4.2.4.	<i>Test2d</i>	51
4.2.5.	<i>Test2e</i>	53
4.2.6.	<i>Test2f</i>	55
4.3.	TEST SERIES 3	56
4.3.1.	<i>Test3a</i>	57
4.3.2.	<i>Test3b</i>	58
4.3.3.	<i>Test3c</i>	60
4.3.4.	<i>Test3d</i>	61
4.3.5.	<i>Test3e</i>	63
4.4.	TEST SERIES 4	64
4.4.1.	<i>Test4a</i>	65
4.4.2.	<i>Test4d</i>	66
4.4.3.	<i>Test4e</i>	68
4.5.	TEST SERIES 5	70
4.5.1.	<i>Test5a</i>	70
4.5.2.	<i>Test5b</i>	71
4.5.3.	<i>Test5c</i>	73
4.5.4.	<i>Test5d</i>	74
4.6.	SUMMARY	76
5.	QUALITATIVE ANALYSIS & OBSERVATIONS	77
5.1.	QUALITATIVE RELATIONS	77
5.1.1.	<i>Relative grain diameter D_{f50}/D_{b50}</i>	77
5.1.2.	<i>Relative thickness d_f/D_{f50}</i>	78
5.1.3.	<i>Filter grading</i>	78
5.1.4.	<i>Wave height H</i>	78
5.1.5.	<i>Wave period T</i>	79
5.1.6.	<i>Number of waves N</i>	79
5.2.	OBSERVATIONS.....	79
5.2.1.	<i>Stability of filter layer</i>	79
5.2.2.	<i>Hydraulically stable or unstable geometrically open filter?</i>	80
5.2.3.	<i>Transport mechanisms</i>	81
5.2.4.	<i>Erosion pattern & equilibrium state</i>	81
5.2.5.	<i>Video capturing from below (through flume's bottom)</i>	83
5.2.6.	<i>Filter profile measurements</i>	83
5.2.7.	<i>Weight of removed base material</i>	84
5.3.	TEST VALIDITY.....	84
5.3.1.	<i>Test repeatability</i>	85
5.3.2.	<i>Measurement errors</i>	87
5.3.3.	<i>Laboratory & model effects</i>	87
6.	QUANTITATIVE ANALYSIS	89
6.1.	CALCULATION OF TEST PARAMETERS	89
6.1.1.	<i>Wave loading properties</i>	89
6.1.2.	<i>Velocity measurements</i>	90

6.1.3.	<i>Calculation of important test parameters</i>	93
6.1.4.	<i>Damage specification</i>	94
6.1.5.	<i>Exclusion of Tests</i>	96
6.2.	TEMPORAL EVOLUTION OF SCOUR DEPTH.....	97
6.2.1.	<i>Analysis</i>	97
6.2.2.	<i>Discussion</i>	100
6.3.	RELATIONS AMONG DIMENSIONLESS PARAMETERS.....	101
6.3.1.	<i>Relative scour depth with relative grain diameter D_{f50}/D_{b50}</i>	102
6.3.2.	<i>Relative scour depth with critical Shield's Number Ψ_{cb}</i>	103
6.3.3.	<i>Relative scour depth with wave Reynolds' Number $Re_{w,p}$</i>	104
6.3.4.	<i>Relative scour depth with relative water depth $h/L_{t,p}$</i>	105
6.3.5.	<i>Relative scour depth with Dean Number $Dean_{b,p}$</i>	105
6.3.6.	<i>Relative scour depth with relative thickness d_f/D_{f50}</i>	106
6.3.7.	<i>Relative scour depth with Iribarren Number $\xi_{b,p}$</i>	107
6.3.8.	<i>Summary</i>	107
6.4.	SCOUR DEPTH=F(FILTER CONFIGURATION GEOMETRY, WAVE LOADING).....	108
6.4.1.	<i>$D_{b50}=360\mu\text{m}$</i>	108
6.4.2.	<i>$D_{b50}=210\mu\text{m}$</i>	110
6.4.3.	<i>General relation for $D_{b50}=360\mu\text{m}$ & $D_{b50}=210\mu\text{m}$</i>	111
6.4.4.	<i>Waves/Time</i>	113
6.4.5.	<i>Grading</i>	114
6.4.6.	<i>Summary & Discussion</i>	115
6.5.	COMPARISON WITH THE DATA SET OF SUMER <i>ET AL.</i> [2000].....	117
6.5.1.	<i>Example 1: Comparison with eq. (2-3) from Sumer et al. [2000]</i>	118
6.5.2.	<i>Example 2: Sumer et al. [2000] with protection</i>	120
6.5.3.	<i>Summary & discussion</i>	120
6.6.	RANGE OF APPLICABILITY & DESIGN SUGGESTIONS.....	121
6.7.	SUMMARY OF CHAPTER 6.....	122
7.	CONCLUSIONS & RECOMMENDATIONS	124
7.1.	CONCLUSIONS.....	124
7.1.1.	<i>Evaluation of the objective</i>	124
7.1.2.	<i>Conclusions from observations</i>	126
7.1.3.	<i>Relations between loading and erosion</i>	127
7.1.4.	<i>Lacking of knowledge after the analysis</i>	128
7.2.	RECOMMENDATIONS FOR FURTHER RESEARCH.....	129
	LIST OF REFERENCES	131
	APPENDIXES	133

List of figures

FIGURE 1-1 CONVENTIONAL RUBBLE MOUND BREAKWATER.....	2
FIGURE 1-2 LOCATION AND LAYOUT OF CLUB MYKONOS LANGEBAAN PLEASURE CRAFT HARBOR (BARTELS <i>ET AL.</i> [2003])	4
FIGURE 1-3 DESIGN CROSS-SECTION OF THE MAIN BREAKWATER CLUB MYKONOS LANGEBAAN (BARTELS <i>ET AL.</i> [2003])..	5
FIGURE 1-4 TIME EVOLUTION OF THE LEVEL OF THE TOP ARMOR LAYER (BARTELS <i>ET AL.</i> [2003]).....	5
FIGURE 1-5 BATHYMETRIC SURVEY (1997) AND GAP FORMATION BETWEEN TOP LAYER AND SPLASH WALL (BARTELS <i>ET AL.</i> [2003])	6
FIGURE 1-6 CLUB MYKONOS LANGEBAAN BREAKWATER AFTER THE REPAIR OF 1998 (BARTELS <i>ET AL.</i> [2003]).....	6
FIGURE 2-1 STREAMING PATTERN IN THE VERTICAL PLANE DUE TO STANDING WAVES. (SUMER <i>ET AL.</i> [2000])	11
FIGURE 2-2 EQUILIBRIUM SCOUR/DEPOSITION PATTERN IN FRONT OF A VERTICAL WALL BREAKWATER. 'COARSE' SAND BOTTOM & REGULAR WAVES. (SUMER <i>ET AL.</i> [2000])	12
FIGURE 2-3 SCOUR/DEPOSITION IN FRONT OF RUBBLE MOUND BREAKWATERS. REGULAR WAVES & 'COARSE' SAND. (SUMER <i>ET AL.</i> [2000])	13
FIGURE 2-4 RELATIVE SCOUR DEPTH S/H FOR VERTICAL WALL ($A=90^\circ$) AND RUBBLE MOUND BREAKWATER ($A=40^\circ$ & $A=30^\circ$). (SUMER <i>ET AL.</i> [2000])	13
FIGURE 2-5 NORMALIZED SCOUR DEPTH S/H AS A FUNCTION OF NUMBER OF LAYERS OF STONES N . (SUMER <i>ET AL.</i> [2000])	15
FIGURE 2-6 DISTRIBUTION OF MEAN AND CHARACTERISTIC LOAD (CUR 233 [2010])	18
FIGURE 2-7 PROBABILITY FUNCTIONS OF LOAD AND STRENGTH (GRASS [1970])	19
FIGURE 3-1 SIDE VIEW (UPPER) AND CROSS SECTION A-A' (DOWN) OF FLUME LAY OUT.....	26
FIGURE 3-2 SIDE VIEW/TOP VIEW (CROSS SECTION A-A & B-B') OF RUBBLE MOUND BREAKWATER AND TOE AREA.....	27
FIGURE 3-3 ARMOR LAYER SIEVE CURVE BASED ON INDIVIDUAL WEIGHING OF THE STONES.....	28
FIGURE 3-4 CORE MATERIAL SIEVE CURVE.	28
FIGURE 3-5 FILTER/PROTECTION MATERIAL SIEVE CURVES.	30
FIGURE 3-6 BASE MATERIAL SIEVE CURVES.	30
FIGURE 3-7 TEST SERIES PLOTTED IN TERMS OF RELATIVE GRAIN SIZE D_{F50}/D_{B50} AND RELATIVE FILTER THICKNESS D_f/D_{F50} .	34
FIGURE 3-8 LASER AND THE WOODEN FRAME FOR PROFILE MEASUREMENTS	35
FIGURE 3-9 EMS PROBE FOR PARTICLE VELOCITY MEASUREMENTS.....	36
FIGURE 4-1 TEST1A AFTER 0 MINUTES (LEFT) AND AFTER 125 MINUTES (RIGHT).	39
FIGURE 4-2 TEMPORAL EVOLUTION OF EROSION OF TEST1A	40
FIGURE 4-3 CONTOUR MAP OF EROSION OF TEST1A.....	40
FIGURE 4-4 TEST1B AFTER 0 MINUTES (LEFT) AND AFTER 100 MINUTES (RIGHT)	41
FIGURE 4-5 TEMPORAL EVOLUTION OF EROSION OF TEST1B	41
FIGURE 4-6 CONTOUR MAP OF EROSION OF TEST1B.....	42
FIGURE 4-7 TEST1C AFTER 0 MINUTES (LEFT) AND AFTER 125 MINUTES (RIGHT)	42
FIGURE 4-8 TEMPORAL EVOLUTION OF EROSION OF TEST1C	43
FIGURE 4-9 CONTOUR MAP OF EROSION OF TEST1C.....	43
FIGURE 4-10 TEST1D AFTER 0 MINUTES (LEFT) AND AFTER 125 MINUTES (RIGHT)	44
FIGURE 4-11 TEMPORAL EVOLUTION OF EROSION OF TEST1D	44
FIGURE 4-12 CONTOUR MAP OF EROSION OF TEST1D	45
FIGURE 4-13 TEST1E AFTER 0 MINUTES (LEFT) AND AFTER 125 MINUTES (RIGHT).....	45
FIGURE 4-14 TEMPORAL EVOLUTION OF EROSION OF TEST1E.....	46
FIGURE 4-15 CONTOUR MAP OF EROSION OF TEST1E.....	46
FIGURE 4-16 TEST PARAMETERS OF TEST SERIES 2	47
FIGURE 4-17 TEST2A AFTER 0 MINUTES (LEFT) AND AFTER 125 MINUTES (RIGHT)	47
FIGURE 4-18 TEMPORAL EVOLUTION OF EROSION OF TEST2A	48
FIGURE 4-19 CONTOUR MAP OF EROSION OF TEST2A.....	48
FIGURE 4-20 TEST2B AFTER 0 MINUTES (LEFT) AND AFTER 100 MINUTES (RIGHT)	49

FIGURE 4-21 TEMPORAL EVOLUTION OF EROSION OF TEST2B	49
FIGURE 4-22 CONTOUR MAP OF EROSION OF TEST2B.....	50
FIGURE 4-23 TEST2C AFTER 0 MINUTES (LEFT) AND AFTER 125 MINUTES (RIGHT)	50
FIGURE 4-24 TEMPORAL EVOLUTION OF EROSION OF TEST2C	51
FIGURE 4-25 CONTOUR MAP OF EROSION OF TEST2C.....	51
FIGURE 4-26 TEST2D AFTER 0 MINUTES (LEFT) AND AFTER 125 MINUTES (RIGHT)	52
FIGURE 4-27 TEMPORAL EVOLUTION OF EROSION OF TEST2D	52
FIGURE 4-28 CONTOUR MAP OF EROSION OF TEST2D	53
FIGURE 4-29 TEST2E AFTER 0 MINUTES (LEFT) AND AFTER 125 MINUTES (RIGHT).....	53
FIGURE 4-30 TEMPORAL EVOLUTION OF EROSION OF TEST2E.....	54
FIGURE 4-31 CONTOUR MAP OF EROSION OF TEST2E	54
FIGURE 4-32 TEST2F AFTER 0 MINUTES (LEFT) AND AFTER 218 MINUTES (RIGHT).....	55
FIGURE 4-33 TEMPORAL EVOLUTION OF EROSION OF TEST2F.....	56
FIGURE 4-34 CONTOUR MAP OF EROSION OF TEST2F	56
FIGURE 4-35 TEST3A AFTER 0 MINUTES (LEFT) AND AFTER 125 MINUTES (RIGHT)	57
FIGURE 4-36 TEMPORAL EVOLUTION OF EROSION OF TEST3A	58
FIGURE 4-37 CONTOUR MAP OF EROSION OF TEST3A.....	58
FIGURE 4-38 TEST3B AFTER 0 MINUTES (LEFT) AND AFTER 100 MINUTES (RIGHT)	59
FIGURE 4-39 TEMPORAL EVOLUTION OF EROSION OF TEST3B	59
FIGURE 4-40 CONTOUR MAP OF EROSION OF TEST3B.....	60
FIGURE 4-41 TEST3C AFTER 0 MINUTES (LEFT) AND AFTER 125 MINUTES (RIGHT)	60
FIGURE 4-42 TEMPORAL EVOLUTION OF EROSION OF TEST3C	61
FIGURE 4-43 CONTOUR MAP OF EROSION OF TEST3C.....	61
FIGURE 4-44 TEST3D AFTER 0 MINUTES (LEFT) AND AFTER 125 MINUTES (RIGHT)	62
FIGURE 4-45 TEMPORAL EVOLUTION OF EROSION OF TEST3D	62
FIGURE 4-46 CONTOUR MAP OF EROSION OF TEST3D	63
FIGURE 4-47 TEST3E AFTER 0 MINUTES (LEFT) AND AFTER 305 MINUTES (RIGHT).....	63
FIGURE 4-48 TEMPORAL EVOLUTION OF EROSION OF TEST3E.....	64
FIGURE 4-49 CONTOUR MAP OF EROSION OF TEST3E	64
FIGURE 4-50 TEST4A AFTER 0 MINUTES (LEFT) AND AFTER 100 MINUTES (RIGHT)	65
FIGURE 4-51 TEMPORAL EVOLUTION OF EROSION OF TEST4A	66
FIGURE 4-52 CONTOUR MAP OF EROSION OF TEST4A.....	66
FIGURE 4-53 TEST4D AFTER 0 MINUTES (LEFT) AND AFTER 125 MINUTES (RIGHT)	67
FIGURE 4-54 TEMPORAL EVOLUTION OF EROSION OF TEST4D	67
FIGURE 4-55 CONTOUR MAP OF EROSION OF TEST4D	68
FIGURE 4-56 TEST4E AFTER 0 MINUTES (LEFT) AND AFTER 125 MINUTES (RIGHT).....	68
FIGURE 4-57 TEMPORAL EVOLUTION OF EROSION OF TEST4E.....	69
FIGURE 4-58 CONTOUR MAP OF EROSION OF TEST4E	69
FIGURE 4-59 TEST5A AFTER 0 MINUTES (LEFT) AND AFTER 125 MINUTES (RIGHT)	70
FIGURE 4-60 TEMPORAL EVOLUTION OF EROSION OF TEST5A	71
FIGURE 4-61 CONTOUR MAP OF EROSION OF TEST5A.....	71
FIGURE 4-62 TEST5B AFTER 0 MINUTES (LEFT) AND AFTER 70 MINUTES (RIGHT)	72
FIGURE 4-63 TEMPORAL EVOLUTION OF EROSION OF TEST5B	72
FIGURE 4-64 CONTOUR MAP OF EROSION OF TEST5B.....	73
FIGURE 4-65 TEST5C AFTER 0 MINUTES (LEFT) AND AFTER 125 MINUTES (RIGHT)	73
FIGURE 4-66 TEMPORAL EVOLUTION OF EROSION OF TEST5C	74
FIGURE 4-67 CONTOUR MAP OF EROSION OF TEST5C.....	74
FIGURE 4-68 TEST5D AFTER 0 MINUTES (LEFT) AND AFTER 250 MINUTES (RIGHT)	75
FIGURE 4-69 TEMPORAL EVOLUTION OF EROSION OF TEST5D	75

FIGURE 4-70 CONTOUR MAP OF EROSION OF TEST5D	76
FIGURE 5-1 CLOUD OF SUSPENDED BASE MATERIAL (WINNOWING) AND BED LOAD TRANSPORT AT THE INTERFACE BETWEEN FILTER AND BASE LAYER.	81
FIGURE 5-2 SHEET FLOW TRANSPORT DURING SEVERE WAVE LOADING. FILTER MATERIAL WAS ABLE TO SETTLE MORE EASILY INTO THE UNDERLYING BASE LAYER.	81
FIGURE 5-3 SCOUR DEVELOPMENT OVER THE FLUME'S WIDTH. VIEW FROM BELOW THE FLUME. UPPER LEFT T=150MIN. UPPER RIGHT T=250MIN. DOWN T=305MIN	83
FIGURE 5-4 RAW FILTER PROFILE MEASUREMENTS OF TEST1A AT 10CM FROM THE RIGHT SIDE GLASS.....	84
FIGURE 5-5 COMPARISON OF MAXIMUM SCOUR DEPTH BETWEEN IDENTICAL TESTS	85
FIGURE 5-6 COMPARISON OF SCOUR HOLE LOCATION TEST1A-TEST1E.....	86
FIGURE 5-7 COMPARISON OF SCOUR HOLE LOCATION: TEST2A-TEST2E	86
FIGURE 5-8 COMPARISON OF SCOUR HOLE LOCATION: TEST4D-TEST4A	87
FIGURE 5-9 TEST4D; CLEAR WATER SCOUR AT THE UPSTREAM SIDE OF THE BOX	88
FIGURE 6-1 DETRENDED VELOCITY SIGNAL FOR TEST1A.....	91
FIGURE 6-2 VARIANCE DENSITY SPECTRUM FOR TEST1A.....	91
FIGURE 6-3 TEST1A BASE LAYER PROFILE MEASUREMENTS PRIOR AND AFTER THE TEST. CROSS SECTIONS 5CM (LEFT) AND 25CM (RIGHT) WITH RESPECT TO RIGHT SIDE GLASS.	94
FIGURE 6-4 AVERAGED REPRESENTATIVE CROSS SECTION FOR TEST1A FOR THE COMPUTATION OF S_{AVER}	95
FIGURE 6-5 TEMPORAL EVOLUTION OF MAXIMUM SCOUR DEPTH AS A FUNCTION OF N_p . MEASUREMENTS TAKEN THROUGH THE RIGHT SIDE GLASS. ALL TESTS WITH WC1.....	98
FIGURE 6-6 REPRESENTATIVE PLOT FOR TESTS 1A, 2A, 3A. MAXIMUM SCOUR DEPTH $S_{MAX}=F(N_p^{0.5})$. BEST FIT LINES AND CORRESPONDING A VALUES.	99
FIGURE 6-7 TEMPORAL EVOLUTION OF MAXIMUM SCOUR DEPTH FOR TESTS THAT REACHED EQUILIBRIUM MAXIMUM DEPTH. TESTS 1B, 1C, 1E, 2B, 2F, 3E & 5B	101
FIGURE 6-8 RELATIVE SCOUR DEPTH WITH RELATIVE GRAIN DIAMETER IN ALL WAVE CONDITIONS. UPPER PLOT WC1, LEFT PLOT WC2, RIGHT PLOT WC3.....	102
FIGURE 6-9 RELATIVE SCOUR DEPTH WITH RELATIVE GRAIN DIAMETER. TREND LINES FOR TESTS 1A, 1E ($D_{B50}=360MM$, $D_{F50}=1.43MM$), TESTS 2A, 2E ($D_{B50}=360MM$, $D_{F50}=1.33MM$), 3A ($D_{B50}=360MM$, $D_{F50}=0.96MM$) AND TESTS 4D, 4E ($D_{B50}=210MM$, $D_{F50}=0.68MM$), 5A ($D_{B50}=210MM$, $D_{F50}=0.96MM$).....	103
FIGURE 6-10 MODIFIED SHIELDS' DIAGRAM FOR WAVES USED FOR THE GRAPHICAL COMPUTATION OF CRITICAL SHIELDS' NUMBER Ψ_{cb} (FROM SCHIERECK [2004]).	103
FIGURE 6-11 RELATIVE SCOUR DEPTH CRITICAL SHIELDS' NUMBER FOR BASE LAYER.....	104
FIGURE 6-12 RELATIVE SCOUR DEPTH WITH WAVE REYNOLDS' NUMBER	105
FIGURE 6-13 RELATIVE SCOUR DEPTH WITH RELATIVE WATER DEPTH	105
FIGURE 6-14 RELATIVE SCOUR DEPTH WITH DEAN NUMBER.....	106
FIGURE 6-15 RELATIVE SCOUR DEPTH WITH RELATIVE GRAIN THICKNESS.....	106
FIGURE 6-16 RELATIVE SCOUR DEPTH WITH IRIBARREN NUMBER.....	107
FIGURE 6-17 BEST FIT LINE FOR TESTS 2A, 2B, 2C, 2E, 3A, 3B, 3C. $D_{B50}=360MM$, $D_f/D_{F50}=3.4$, NARROW GRADED FILTER LAYER AND ALL WCS.....	109
FIGURE 6-18 NEGLECTING WAVE REYNOLDS' NUMBER. BEST FIT LINE FOR TESTS 2A, 2B, 2C, 2E, 3A, 3B, 3C. $D_{B50}=360MM$, $D_f/D_{F50}=3.4$, NARROW GRADED FILTER LAYER AND ALL WCS	110
FIGURE 6-19 BEST FIT LINE FOR TESTS 4D, 4E, 5A, 5B, 5C. $D_{B50}=210MM$, $D_f/D_{F50}=3.4$, NARROW GRADED FILTER LAYER AND ALL WCS	111
FIGURE 6-20 BEST FIT LINE FOR $D_{B50}=360MM$ & $D_{B50}=360MM$. $D_f/D_{F50}=3.4$, NARROW GRADED FILTER LAYER AND ALL WCS. TESTS 2A, 2B, 2C, 2E, 3A, 3B, 3C, 4D, 4E, 5A, 5B, 5C.	112
FIGURE 6-21 NEGLECTING WAVE REYNOLDS' NUMBER. BEST FIT LINE FOR $D_{B50}=360MM$ & $D_{B50}=360MM$. $D_f/D_{F50}=3.4$, NARROW GRADED FILTER LAYER AND ALL WCS. TESTS 2A, 2B, 2C, 2E, 3A, 3B, 3C, 4D, 4E, 5A, 5B, 5C.....	112

FIGURE 6-22 INCORPORATING DURATION OF STORM EVENT. BEST FIT LINE FOR $D_{B50}=360\text{MM}$ & $D_{B50}=360\text{MM}$. $D_f/D_{F50}=3.4$, NARROW GRADED FILTER LAYER, ALL WCS, ALL DURATIONS. TESTS 2A, 2B, 2C, 2E, 2F, 3A, 3B, 3C, 4D, 4E, 5A, 5B, 5C, 5D. TEST3E.....	113
FIGURE 6-23 BEST FIT LINE FOR TESTS 1A, 1B, 1C, 1E, 2A, 2B, 2C, 2E, 2F, 3A, 3B, 3C, 4D, 4E, 5A, 5B, 5C, 5D WITHOUT GRADING CORRECTION. $D_{B50}=360\text{MM}$ & $D_{B50}=360\text{MM}$. $D_f/D_{F50}=3.4$, NARROW GRADED FILTER LAYER, ALL WCS, ALL DURATIONS	114
FIGURE 6-24 INCORPORATING GRADING VARIATION. BEST FIT LINE FOR $D_{B50}=360\text{MM}$ & $D_{B50}=360\text{MM}$, $D_f/D_{F50}=3.4$, NARROW GRADED FILTER LAYER, ALL WCS, ALL DURATIONS. TESTS 1A, 1B, 1C, 1E, 2A, 2B, 2C, 2E, 2F, 3A, 3B, 3C, 4D, 4E, 5A, 5B, 5C, 5D.....	115
FIGURE 6-25 RANGE OF VALIDITY FOR EQ. (6-7)	116
FIGURE 6-26 COMBINING THE TWO DATA SETS; PRESENT STUDY (BLUE CIRCLES) WITH SUMER <i>ET AL.</i> [2000] FOR NO PROTECTION & REGULAR WAVES (FILLED, MAGENTA DIAMONDS & GREEN SQUARES), NO PROTECTION & IRREGULAR WAVES (EMPTY, MAGENTA DIAMONDS) AND WITH PROTECTION (FILLED, RED SQUARES). IN ADDITION, EQ. (2-3) IS PLOTTED FOR $A=40^\circ$ (SOLID, MAGENTA), $A=30^\circ$ (SOLID, GREEN), $A=33.6^\circ$ (DISCONTINUOUS, CYAN) AND EQ. (6-9) (MODIFIED EQ. 2-3, DISCONTINUOUS, BLUE).....	118
FIGURE 6-27 COMPARISON BETWEEN EQ. (6-9) (MODIFIED EQ. (2-3) FROM SUMER <i>ET AL.</i> [2000]) AND EQ. (6-7)....	119

Appendixes

FIGURE C-1 HORIZONTAL DISTRIBUTION OF THE WAVE INDUCED PORE PRESSURE AMPLITUDES FROM BÜRGER <i>ET AL.</i> (1988)	C-7
FIGURE C-2 CORE PRESSURE DISTRIBUTION BY BURCHARTH <i>ET AL.</i> (1999)	C-8
FIGURE C-3 CORE PRESSURE DISTRIBUTION INSIDE THE BREAKWATER. ALL WAVE CONDITIONS.	C-9
FIGURE C-4 CORE PRESSURE DISTRIBUTION INSIDE THE BREAKWATER. ALL WAVE CONDITIONS.	C-10
FIGURE D-1 TEST2A: VARIANCE DENSITY SPECTRUM	D-1
FIGURE D-2 TEST2B: VARIANCE DENSITY SPECTRUM	D-1
FIGURE D-3 TEST2B: VARIANCE DENSITY SPECTRUM	D-2
FIGURE D-4 TEST2B: VARIANCE DENSITY SPECTRUM	D-2
FIGURE E-1 TEMPORAL EVOLUTION OF MAXIMUM SCOUR DEPTH. MEASUREMENTS TAKEN THROUGH THE RIGHT SIDE GLASS. TESTS WC1 AND REGULAR DURATION (3000 'PEAK' WAVES).....	E-1
FIGURE E-2 TEMPORAL EVOLUTION OF MAXIMUM SCOUR DEPTH. MEASUREMENTS TAKEN THROUGH THE RIGHT SIDE GLASS. ALL TESTS WC2.....	E-2
FIGURE E-3 TEMPORAL EVOLUTION OF MAXIMUM SCOUR DEPTH. MEASUREMENTS TAKEN THROUGH THE RIGHT SIDE GLASS. ALL TESTS WC3.....	E-2
FIGURE E-4 TEMPORAL EVOLUTION OF MAXIMUM SCOUR DEPTH FOR TESTS THAT REACHED EQUILIBRIUM MAXIMUM DEPTH. TESTS 1B, 1C, 1E, 2B, 2F, 3E & 5B	E-3

List of tables

TABLE 3–1 TEST INDEX	33
TABLE 4–1 GENERAL TEST PARAMETERS OF TEST SERIES 1	39
TABLE 4–2 TEST PARAMETERS OF TEST1A	39
TABLE 4–3 TEST PARAMETERS OF TEST1B	41
TABLE 4–4 TEST PARAMETERS OF TEST1C	42
TABLE 4–5 TEST PARAMETERS OF TEST1D	44
TABLE 4–6 TEST PARAMETERS OF TEST1E	45
TABLE 4–7 TEST PARAMETERS OF TEST2A	47
TABLE 4–8 TEST PARAMETERS OF TEST2B	48
TABLE 4–9 TEST PARAMETERS OF TEST2C	50
TABLE 4–10 TEST PARAMETERS OF TEST2D	52
TABLE 4–11 TEST PARAMETERS OF TEST2E	53
TABLE 4–12 TEST PARAMETERS OF TEST2F	55
TABLE 4–13 GENERAL TEST PARAMETERS OF TEST SERIES 3	57
TABLE 4–14 TEST PARAMETERS OF TEST3A	57
TABLE 4–15 TEST PARAMETERS OF TEST3B	58
TABLE 4–16 TEST PARAMETERS OF TEST3C	60
TABLE 4–17 TEST PARAMETERS OF TEST3D	62
TABLE 4–18 TEST PARAMETERS OF TEST3E	63
TABLE 4–19 GENERAL TEST PARAMETERS OF TEST SERIES 4	65
TABLE 4–20 TEST PARAMETERS OF TEST4A	65
TABLE 4–21 TEST PARAMETERS OF TEST4D	67
TABLE 4–22 TEST PARAMETERS OF TEST4E	68
TABLE 4–23 GENERAL TEST PARAMETERS OF TEST SERIES 5	70
TABLE 4–24 TEST PARAMETERS OF TEST5A	70
TABLE 4–25 TEST PARAMETERS OF TEST5B	71
TABLE 4–26 TEST PARAMETERS OF TEST5C	73
TABLE 4–27 TEST PARAMETERS OF TEST5D	75
TABLE 5–1 MAXIMUM COMPUTED TOE STONE DIAMETER FOR EACH TEST SERIES IN COMPARISON TO THE USED FILTER GRAIN DIAMETER.	80
TABLE 6–1 COMPREHENSIVE TABLE FOR THE PROPERTIES OF WAVE LOADING	90
TABLE 6–2 COMPARISON OF VELOCITY MEASUREMENTS WITH LINEAR WAVE THEORY COMPUTATIONS	92
TABLE 6–3 COMPREHENSIVE TABLE OF CALCULATED TEST PARAMETERS	93
TABLE 6–4 REPRESENTATIVE VALUES FOR DAMAGE SPECIFICATION	95
TABLE 6–5 a_r VALUES AND R-SQUARED VALUES FOR EVERY TEST	99
TABLE 0–1 UP-SCALING RESULTS FOR WAVE KINEMATICS, BREAKWATER CONFIGURATION AND FILTER LAYER PROPERTIES	B-1
TABLE 0–2 UP-SCALING OF RELATIVE GRAIN DIAMETER BASED ON DEAN NUMBER SIMILITUDE.	B-2
TABLE 0–3 UP-SCALING OF RELATIVE GRAIN DIAMETER BASED ON SHIELDS' NUMBER SIMILITUDE.	B-3

Appendixes

TABLE E-1 EQUILIBRIUM MAXIMUM SCOUR DEPTH S_{MAX} AND EQUILIBRIUM TIME EXPRESSED VIA N_{MAX} PER EACH TEST	E-2
TABLE F-1 ADDITIONAL TEST PARAMETERS PER TEST. FILTER LAYER GRADING PROPERTIES, TEST DURATION, REFLECTION COEFFICIENT AND WEIGHT OF THE REMOVED BASE MATERIAL	F-1
TABLE F-2 MAXIMUM SCOUR DEPTH S_{MAX} PER TEST AND PER CROSS SECTION. DISTANCE IS MEASURED FROM RIGHT SIDE GLASS.	F-1

List of symbols

Greek symbols

α	-	Seaside structural slope angle (from the horizontal)
α	-	Forchheimer coefficient (-)
α_d	-	coefficient (cm)
α_k	-	coefficient (cm)
α_t	-	turbulence coefficient (cm)
α_t	-	characteristic scale for temporal evolution of scour (cm)
α_v	-	coefficient (cm)
β	-	Forchheimer coefficient (-)
γ	-	transport parameter $\gamma=0.625$
γ	-	correction coefficient (-)
δ	-	correction coefficient (-)
Δ	-	submerged relative density (-)
λ	-	characteristic length scale (m)
ξ	-	Irribaren number (-)
ρ_s	-	mass density of granular material (kg/m^3)
ρ_{base}	-	mass density of base material (kg/m^3)
ρ_{filter}	-	mass density of filter material (kg/m^3)
ρ_w	-	mass density of water (kg/m^3)
ν	-	kinematic viscosity of water (m^2/s)
τ	-	shear stress (N/m^2)
τ_0	-	mean shear stress (N/m^2)
Ψ	-	Shields' Number (-)
Ψ_c	-	critical Shields' Number/stability number (-)

Roman symbols

h	-	water depth (m)
A_s	-	erosion area (m^2)
c_r	-	reflection coefficient (-)
d_f	-	toe/filter thickness (m)
d_s	-	erosion depth (m)
D^*	-	dimensionless grain diameter according to Van Rijn (-)
D_{n50}	-	base layer grain diameter (m)
D_{nx}	-	grain diameter, where x% of the mass has smaller diameter (m)
D_x	-	grain diameter, where x% of the grains has smaller diameter (m)
D_{rep}	-	characteristic grain diameter (m)
D_f	-	filter layer grain diameter (m)
D_b	-	base layer grain diameter (m)
Dean	-	Dean Number
Fr	-	Froude Number
g	-	gravitational acceleration (m/s^2)
H	-	wave height (m)
I	-	hydraulic gradient (-)
u^*	-	shear stress velocity (m/s)
u_f	-	porous flow/filter velocity (m/s)
L	-	wavelength (m) $L_0=gT^2/2\pi$, $L=L_0\tanh(kh)$
k_r	-	linear dimension of surface roughness granular material (m)

k_{rep}	-	relative permeability of breakwater structure (m/s)
n_{rep}	-	relative breakwater porosity (-)
n	-	scale factor (-)
N	-	number of waves (-)
N_o	-	test number (-)
N_m	-	number of waves with respect to mean period of the wave spectrum (-)
N_p	-	number of waves with respect to peak period of the wave spectrum (-)
N_{max}	-	number of waves that correspond to equilibrium maximum scour depth (-)
N_t	-	number of waves at a moment "t" in time (-)
P	-	notional permeability (-)
R^2	-	R-squared (-)
Re	-	Reynolds' Number (-)
Re_p	-	particle Reynolds' Number (-)
Re_w	-	wave Reynolds' Number (-)
R_u	-	run up (m)
R_d	-	run down (m)
s	-	relative density ρ_s/ρ_w (-)
S	-	Scour depth (m)
S_{aver}	-	averaged maximum scour depth (m)
S_{final}	-	maximum scour depth from the side glass at the end of the test (m)
$S_{max,aver}$	-	maximum averaged scour depth (m)
S_{dam}	-	damage number equivalent to van der Meer's notion of damage S (-)
S_{max}	-	equilibrium maximum scour depth from the side glass (m)
S_t	-	scour depth at a moment "t" in time (m)
T	-	wave period (s)
T_s	-	time scale in (s) or number of waves
T^*	-	dimensionless time scale
u	-	velocity in y (longitudinal) direction (m/s)
u_f	-	porous flow velocity (m/s)
$u_{l,m}$	-	velocity computed via Linear Wave theory and mean spectral period T_p (m/s)
$u_{l,s,p}$	-	velocity computed via Linear Wave theory and peak spectral period T_p (m/s)
u^*	-	shear velocity (m/s)
U_w	-	wave orbital velocity (m/s)
Xie	-	Xie Number (-)
V_{gr}	-	Grading of granular material (-)
W_{rem}	-	weight of the removed base material (kg)
w_s	-	settling velocity (m/s)

Abbreviations

<i>BIAS</i>	-	Mean difference between measured and calculated value
<i>eq.</i>	-	Equation
<i>D</i>	-	Depth
<i>EMS</i>	-	Electromagnetic flow meter
<i>FFT</i>	-	Fast Fourier Transformation
<i>L</i>	-	Length
<i>LWT</i>	-	Linear wave theory
<i>RMSE</i>	-	Root mean square error
<i>rms</i>	-	Root mean square
<i>VDS</i>	-	Variance Density Spectrum
<i>W</i>	-	Width

- WC - Wave condition
- WC_t - Wave condition at the toe of the breakwater

Frequently used indices

- b - refers to base layer
- b - refers to filter material
- c - critical
- m_0 - zero order moment of the spectrum
- p - refers to peak spectrum period
- s - refers to significant wave height
- s - refers to seabed material
- t - refers to the toe of the breakwater
- U - refers to velocity in x direction (longitudinal)
- V - refers to velocity in y direction (transversal to the flume)
- w - refers to water
- w - refers to waves
- 10 - refers to the mean of the upper 10%
- 2% - refers to a quantity exceeded by 2% of a population

1. Introduction

1.1. General introduction

Breakwaters are one of the most widely found, man-made interventions in the coastal environment. Their purpose is to protect the coastline against the eroding action of waves and currents, to efficiently control or deviate the sediment transport equilibrium of crucial areas and finally, to create safe conditions for vessel berthing and (un)loading.

However, the construction of a breakwater can prove to be a very complex and expensive enterprise which has to take place in the unfriendly marine environment. In fact, the latter affects not only the design characteristics of the structure but also the construction procedure resulting in an enormous increase of the total costs. Therefore, cost optimization in accordance with the acceptable level of safety, is of significant importance for the feasibility of the project and one of the priorities for further investigation.

Nowadays, the accent is paid into reducing the overall cost of a breakwater construction in combination with developing easier to realize constructional procedures. The developments in constructional equipment and the increase in capacities have reduced costs for bulk transport and positioning of the materials while labor intensive and accuracy demanding methods remain expensive (Ockeloen [2007]). Furthermore, and by considering the total lifetime costs, deformations to some degree can be accepted if the circumstances allow it and if the reduction in construction costs, compensate, the additional maintenance costs. Consequently, alternative designs and techniques have been developed such as berm breakwaters (dynamically stable structures with extra stones at the seaward slope that are redistributed by the waves) and the application of geometrically open, instead of closed, filter criteria.

The stability and the applicability of the latter is the subject of this study. Although the application of open filter criteria can take place in different parts of the structure, this study will focus on the toe area of a rubble mound breakwater that lays on a sandy seabed. Additionally, to investigate a common situation, the breakwater would be placed in intermediate waters. For this commonly met case in real life (since almost all breakwaters have a section subjected in intermediate conditions), the development of a reliable design tool will lead to simpler breakwater designs and facilitate the construction process resulting in substantial decrease of the overall cost.

During this study, physical model tests have been conducted in order to examine the behavior of the system; rubble mound breakwater (with an armor layer of physical rocks), toe (trapezoidal bund) and sandy seabed designed according the open filter rules. In particular, the system's performance will be investigated with respect to irregular waves, variation of wave characteristics (height, period, steepness), variation of filter (toe) characteristics (layer thickness, diameter, grading).

The objective of this thesis is to gain insight into the influence (qualitatively and quantitatively) of variations of hydraulic loading, toe dimensions, filter characteristics on

erosion patterns under a breakwater toe lying on sandy seabed and designed according to open filter criteria. To achieve the aforementioned the accent will be paid into the determination of the growth of the erosion pattern and the existence of an equilibrium state of the erosion process.

1.2. Conventional rubble mound breakwater

Different types of breakwaters occur and vary from rubble mound breakwaters, to vertical caissons and floating structures. Among them, the most widely used is the conventional rubble mound breakwater; a permeable or impermeable structure that consists of different layers of rubble mound material. This breakwater type is considered flexible (Verhagen *et al.* [2009]), since it can easily follow uneven settlements of foundation layers, and is characterized by a gradual failure mechanism. On the other hand, it is not the most suitable choice in case of relatively deep water due to the entailing large footprint.

1.2.1. Breakwater compartments

The main features of such a structure are indicated in figure 1-1;

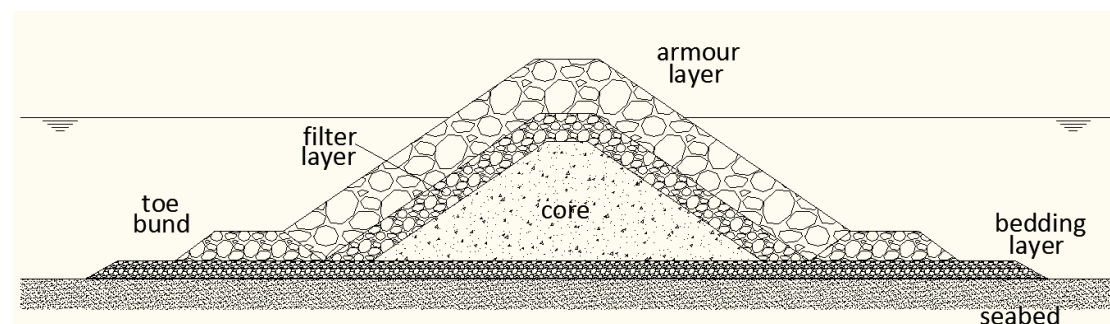


Figure 1-1 Conventional rubble mound breakwater

Core: Its main function is to form the basis for the upper layers and to reduce the transmitted energy. Most of the times consist of quarry run (stones 1 to 200kg) with relatively large gradation (large values of ratio $\frac{D_{85}}{D_{15}}$).

Filter layer (under-layer/secondary armor layer): They are used as an interface between core and armor layer in order to prevent the core material to be washed out through the pores of the armor layer. Actually, this describes the case of geometrically closed filter conditions. As a result multiple consequent filter layers may have to be constructed depending on the grading and the ratio of the diameters between the boundary layers (something that applies also below between the breakwater and the sea bed).

Armor layer: This layer is responsible for withstanding the forces imposed by the wave action during design conditions. Here, in case that natural stones are used, the gradation is lower. Apart from natural stones, when the design conditions are very demanding (high

design wave height) or when there is a lack of natural material concrete armor units (Xbloc) are used.

1.2.2. Toe & granular filter criteria

Depending on the type of the bed material the breakwater can be built directly on the sea bed or upon special filters/transitional layers made of quarried stones (bedding layer), geotextile or combinations. Consequently, the necessity for placement of additional filter layers, geotextiles or/and soil improvement in the interface between the breakwater and the sea bed is an aspect that leads in substantial increase on the total cost of the project. In fact, this is mainly the case when a breakwater has to be constructed on a sandy (fine or coarser) seabed.

One of the most sensitive and crucial parts of a breakwater is the structure's toe. The toe of a breakwater is mainly responsible for protecting the structure from sliding and is subject to waves directly and indirectly due to the resulting wave run up and run down that cause cycle flow conditions. Simultaneously, toe failure could result into many of the other failure mechanisms (CIRIA *et al.* [2007]) due to the implied deduced strength at the base of the slope. The higher the toe is placed the less armor is needed, although this results to larger stones because it is subjected to more intensive wave action.

Likewise, a breakwater toe placed directly on the sea bed will need several layers of filter material between the structure and the bed in order to prevent erosion of the sand that lies underneath. Therefore, the application of geometrically closed filter rules will lead to the design of a complex, multilayer filter, that is both expensive and most of the times difficult to construct in a marine environment which is dominated by waves and currents. Therewithal, the use of geotextiles to substitute the filter layers despite being a less expensive solution is also hard to apply and have a limited and ambiguous lifetime.

In some situations, as an alternative to the above solutions, it is possible to make use of geometrically open filter criteria for the design of the filter layer. Geometrically open filters can be divided into two categories depending on whether material from the base layer is allowed to pass through the pores of the upper layer; the 'hydraulic sand tight filters' or 'stable geometrically open filters' and the 'unstable geometrically open filters' or 'transport filters'.

In order to design a 'stable geometrically open filter' the hydraulic load applied on the base material has to be determined. By knowing that, it is possible to design a filter that is not allowing loss of base material during design conditions. Furthermore, and by allowing an acceptable loss of material, the number of layers of the filter will be far less than a corresponding 'geometrically sand tight filter'.

Instead of the above, an 'unstable geometrically open filter' can be used. The design of such filter demands a very precise estimation of the amount of material loss so that it can be taken into account during the design of the structure in order to avoid undesired consequences on the functioning of the breakwater. For that reason, extensive insight on

the initiation of movement of the base material (sandy bed) and the transportation of the filter layer (breakwater toe) has to be achieved.

1.3. Club Mykonos breakwater; a real example

The Club Mykonos Langebaan, the first privately owned pleasure craft harbor on the open coast of South Africa (Figure 1-2), was constructed in the late 80s with a total cost of 100 million US Dollars. It is situated to the east of Saldanha Bay (West Coast of South Africa) and in line with its entrance. In order to protect the 4ha harbor basin (capacity of 130 vessels with draft up to 3m), two breakwaters were constructed according to the layout of Figure 1-2.

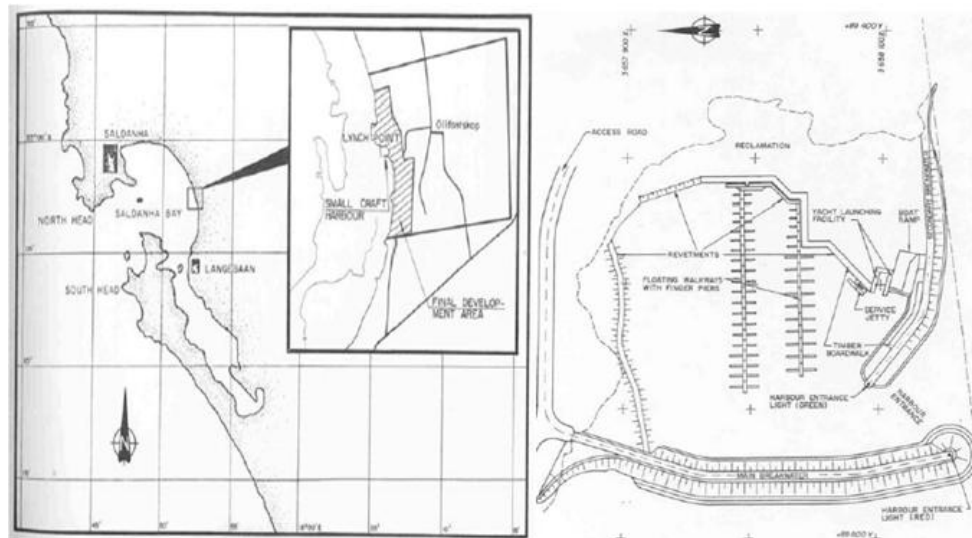


Figure 1-2 Location and layout of Club Mykonos Langebaan pleasure craft harbor (Bartels *et al.* [2003])

The interest is now paid on the main breakwater, which lays at the west side of the harbor. The design conditions (Bosman *et al.* [1990]) for the breakwater were:

- Water depth = 5.4m
- Significant wave height = 4.2m
- Wave period = 11-13s

Based on the aforementioned design conditions, a rubble mound breakwater was constructed, and protected by an armor layer of 9.6t (4m³) Accropodes® with a seaward slope of 4:3 (see Figure 1-3). In total, were used 45000m³ of rock, 1400 Accropodes® and 3000 m³ of concrete capping and wave-walls.

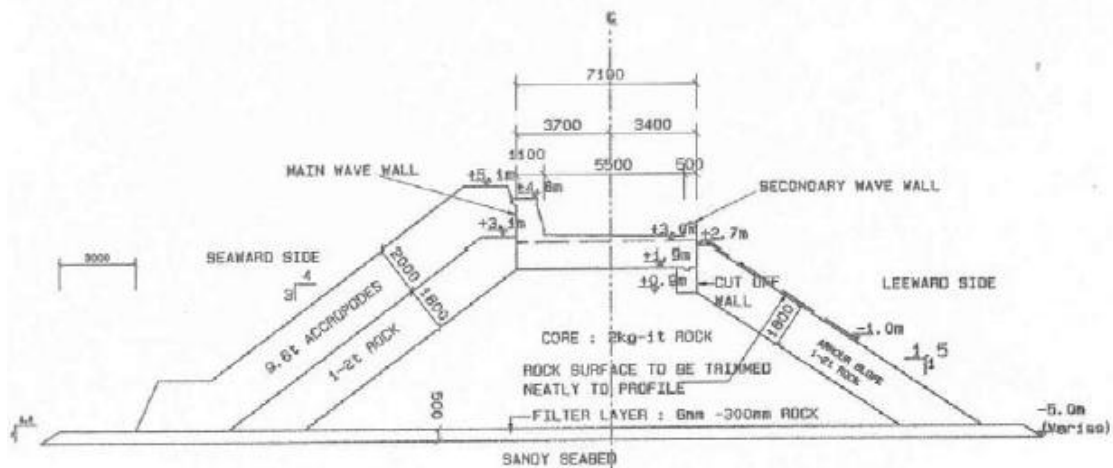


Figure 1-3 Design cross-section of the main breakwater Club Mykonos Langebaan (Bartels *et al.* [2003])

Despite that site's seabed consisted of fine sand with a D_{n50} equal to $140\mu\text{m}$, only a thin bedding layer (6-300mm stones) with a thickness of 0.5m was constructed, to act as a filter. In addition, a very narrow toe was formed, consisted of armor layer units placed on the bottom, while a 3m apron made of bedding layer material was used to cope with scour threat. However, with the breakwater lying upon this layer, open filter conditions were formed, especially in the interface between armor layer and filter. In fact, two years after the completion of the breakwater construction, were observed significant settlements of the armor layer.

Under the threat of an ultimate breakwater failure, a monitoring program (bathymetric, photographic, diver surveys) was installed in order to survey the evolution of the phenomenon. The results of the photographic survey between 1991 and 1997 are displayed in Figure 1-4. Here, the progress of the armor layer settlements is clearly visible.

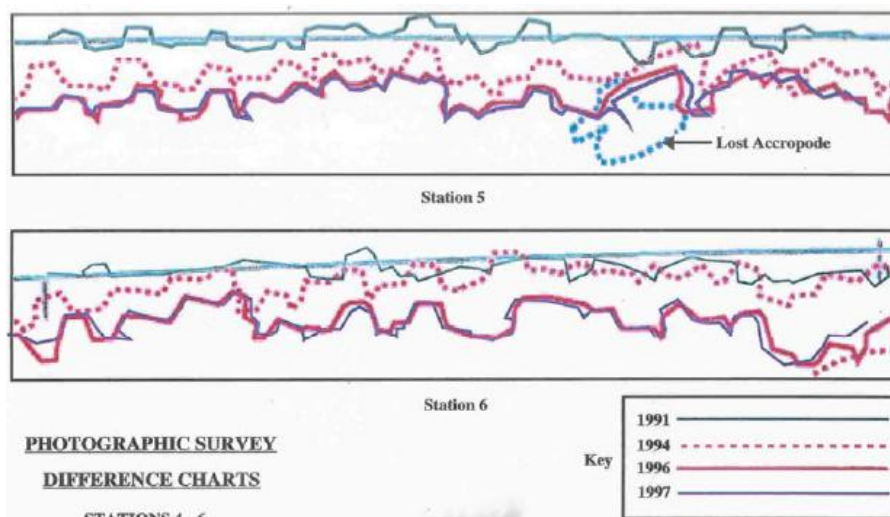


Figure 1-4 Time evolution of the level of the top armor layer (Bartels *et al.* [2003])

In addition, the bathymetric survey of 1997 showed the formation of a deep scour (-7.5m MSL) hole at the section C of the breakwater (Figure 1-5 left). Furthermore, the settlements had created an apparent gap between the splash wall and the top row of the armor layer (Figure 1-5 right).

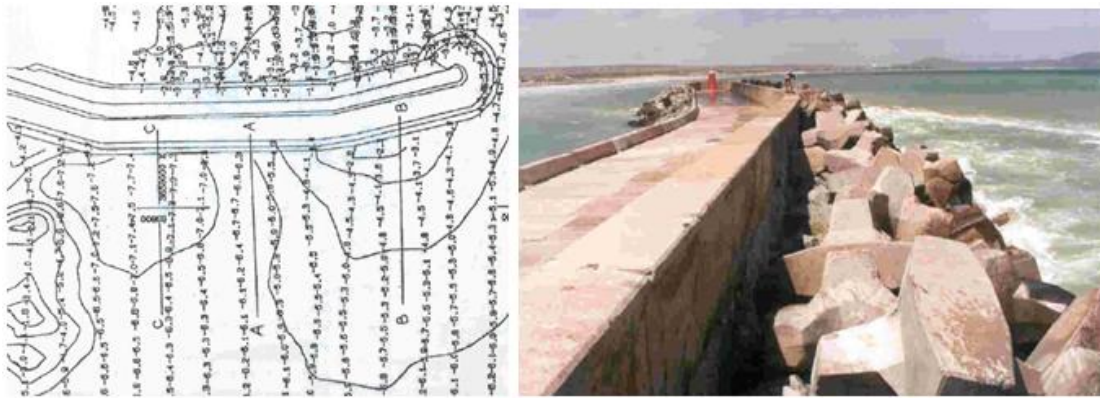


Figure 1-5 Bathymetric survey (1997) and gap formation between top layer and splash wall (Bartels *et al.* [2003])

Finally, in 1998 was taken the decision to repair the breakwater, by spoiling dredged material at the vulnerable cross sections of the breakwater and by constructing a wider rock toe to serve as anti-scour protection. As toe material, were used rocks of 2-4t (Figure 1-6) and therefore, closer filter rules were formed in order to reduce erosion and deal with settlements.

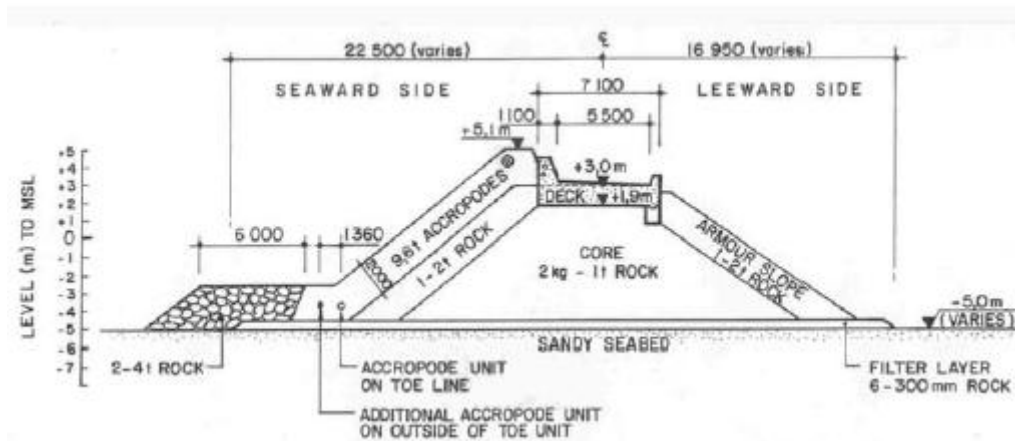


Figure 1-6 Club Mykonos Langebaan breakwater after the repair of 1998 (Bartels *et al.* [2003])

1.4. Problem definition

The construction of a breakwater upon a sandy seabed is a widely met case, where for the toe and the interface between the structure and the seabed, the application of 'geometrically closed filters' or geotextiles is the obvious solution. However, their replacement with 'geometrically open granular filter' structures that allow an acceptable and predictable loss of material could prove to be a more economical and easier to construct.

Nevertheless, at this moment the knowledge upon this issue is insufficient and limited. A variety of recommendations occurs in literature, separately for toe design & scour protection (with suggestions for additional bedding layers) and for the application of open

filter criteria; however none of the studies treats these subjects combined. Therefore the lack of knowledge can be summarized in the following question:

“What are the characteristics of scour formation and development through a breakwater toe lying upon sand and designed as a geometrically open filter? Does the system arrive at equilibrium and if so, which are the guidelines for an effective and trustworthy prediction?”

1.5. Research objective

The main objective of this study reads:

“To get insight into the link between scour formation and development with wave loading and filter configuration properties”.

In order to accomplish that, the following objectives have to be achieved first:

- To obtain quantitative expressions of the following governing parameters related with the design of the breakwater toe.
 - Hydraulic loading (wave height, wave period, water depth, storm duration)
 - Relative grain diameter of filter configuration (D_f/D_b)
 - Thickness of the toe (filter) (d_f)
 - Grading characteristics of the toe (filter)
- To get a clear image concerning the transportation (initiation of transport, transport rate of material) of the sandy material (coming from the seabed) through the toe of the breakwater under the non-stationary hydraulic conditions as they are formed in front of the structure.

1.6. Research questions & study scope

The main research questions that are arisen concerning the objectives and the validity of the present study are the following:

- a. Which is the dependency between erosion of seabed material and wave parameters?
- b. When does damage (erosion) start and how does it develop in time and loading?
- c. Does damage development arrive at an equilibrium state, and if so which parameters are decisive?
- d. How do filter configuration properties (grain size, filter thickness, grading) influence erosion pattern?
- e. Which are the scale effects due to physical model testing? How can they be quantified and mitigated?

The scope of the research is described by the following constraint:

- The subject of the study is the application of open granular filters in the toe of a breakwater in intermediate waters. In particular, it has to do with scour hole formation and development through a toe designed as a geometrically open filter.

1.7. Research plan & structure of the report

In order to accomplish the ultimate objective of this study, sequential steps will take place. The same sequence is harmoniously assembled in the structure of the report.

Chapter 2 discusses the corresponding theory for scour formation around rubble mound breakwaters and the application of filter criteria as a countermeasure. The important processes and the present design tools are presented and linked into the specific case of this study. The knowledge gaps are discussed and the corresponding governing parameters are defined. The toe bund will act as a filter layer, and therefore the thorough understanding of filter porous flow and load reduction is substantial.

Chapter 3 describes the test set up. Analytical information and selections reasoning is provided concerning the breakwater design, toe properties, granular filter criteria and scaling of the experiment's components. In addition, are presented illustrations of the scaled physical model along with the inventory of the conducted test cases.

Chapter 4 describes in detail the primary results and the observations from the conducted data set. Every test is treated separately with respect to the base layer profile before and after the conduction of a test and its temporal evolution.

Chapter 5 elaborates upon the important observations extracted from test execution by recognizing general trends of the properties of scour formation and development that are common between tests with mutual boundary conditions. Section 5.1 discusses the effect of each of the related boundary conditions on scour pattern and magnitude. Section 5.2 summarizes the important test observations. Finally, Section 5.3 elaborates upon the validity of the tests by discussing the repeatability of the tests and by indentifying laboratory effects and measurement errors.

Chapter 6 contains the analysis of the collected data set. After presenting the results for all the important parameters that are necessary to describe the test outcome, the chapter elaborates on the link between the scour formation and test boundary conditions (wave loading, filter configuration properties). Thereby, two major topics are treated; the temporal evolution of maximum scour depth and the determination of the relation between maximum scour depth with characteristic parameters that describe each experiment. Afterwards, Section 6.5 elaborates upon the comparison of the final relation found in Section 6.4. Finally, Chapter 6 ends by discussing the range of applicability of the proposed tool.

Chapter 7 contains the conclusions, the answers on the research questions and the recommendations for further research.

Appendix A provides the theoretical background on physical modeling scaling rules and on the Π -theorem. Additionally, it contains the analysis and description of the scaling procedure, the implying scale effects and their corresponding shortcomings. The analysis is based on Froude scaling and dimensional analysis of both the separate resulting processes and the ultimate resultant process. For the validation of the procedure comparisons take place with literature findings. The application of dimensional analysis done via Pi-theorem (Buckingham [1914]) will be applied here. By using the dimensionless parameters a two-fold goal has to be accomplished; physical scaling of the system and recognition of scale effects.

Appendix B attempts to draw the link between the investigated physical model and its fictitious prototype on the basis of two up-scaling techniques and Froude similarity. Appendix C elaborates upon the mitigation of scale effects of the porous flow inside the breakwater.

Appendices D & E present additional plots and graphs to provide insight on important aspects such as the variance density spectrum of the velocity field and the temporal evolution of scour pattern with respect to time and number of waves. Finally, Appendix F contains two tables with information with respect to additional test parameters that could not be presented in the main body of the report.

2. Scour & granular filters

Undoubtedly, in the vicinity of a seabed based structure (pile, vertical wall, rubble mound breakwater etc.) at an active marine environment, flow patterns are being disordered. The entailed changes mainly include the formation of eddies, vortices and the generation of turbulence. As a result, local sediment transport capacity increases leading to a sediment transport gradient; therefore scour formation.

Marine structures are very vulnerable to scour formation; failure due to scour is considered to be one of the major (if not the most important) failure mechanisms BRUUN [1985]. Therefore, extra care has to be paid in the protection measures. Especially for the case of rubble mound breakwaters, in order to cope with the danger of scour, a toe structure is constructed in the junction between breakwater and seabed. The toe can take the form of a bund or an apron and is designed on the basis of hydraulic loading and geometrically closed filter criteria.

In this Chapter is treated the phenomenon of scour formation around rubble mound breakwaters. Based on literature review, scour development is described with respect to the factors that affect its magnitude and temporal evolution. Special attention is paid in the empirical tool (Sumer *et al.* [2000]) for the prediction of maximum scour and the way that it can be linked with the present study.

Afterwards, is presented the design of granular filters as a measurement to prevent scour formation. Section starts by discussing the design rules for geometrical closed filters and continues with the design tools for the application of open granular filters and in particular hydraulically open filters.

The combination of these two has direct relation with the main scope of this study; how does scour develop through a geometrically open filter at the toe of a breakwater lying upon a sandy seabed.

2.1. Scour around coastal structures

Scour and the implicit danger that threatens the viability of coastal structures has been the topic of extended research over the years. Various researchers have investigated scour pattern and magnitude around vertical/composite breakwaters (de Best *et al.* [1971], Xie [1981, 1985], rubble mound breakwaters (Sumer *et al.* [2000]), vertical or inclined seawalls, piles and pipelines. For the present study the two former are of major importance.

2.1.1. Scour around breakwaters

For the case of vertical breakwaters or seawalls the key mechanism for scour formation is the mass transport current or wave induced streaming due to the presence of standing waves (Xie [1981], Sumer *et al.* [2000]).

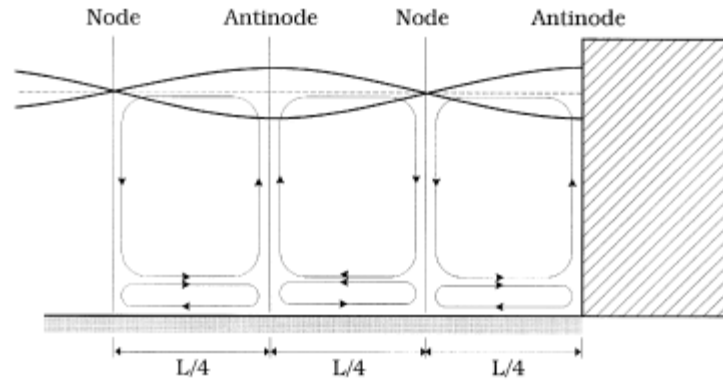


Figure 2-1 Streaming pattern in the vertical plane due to standing waves. (Sumer *et al.* [2000])

de Best *et al.* [1971] conducted physical model tests with three sand grain sizes ($D_{50}=130, 160 \text{ \& } 220\mu\text{m}$) to study the influence of standing waves on the seabed, in front of a vertical wall. An important observation was the difference in transport patterns between the case of fine ($D_{50}=130\mu\text{m}$) and coarse ($D_{50}=220\mu\text{m}$) seabed material. In particular, the former was transported under suspension from the nodes (maximum velocities) to the antinodes of the standing wave; therefore transport mainly took place in the upper cells of Figure 2-1. On the other hand, bed load mode of transport (bed shear) was dominating the transport of coarser material towards the node. As a result, bed was accreted at the node and eroded halfway between the node and antinode, while transport mainly occurred at the lower cells of Figure 2-1. Finally, it is important to mention that the intermediate grain size ($D_{50}=160\mu\text{m}$) was scoured significantly less.

In order to discern the difference between 'fine' and 'coarse' sand, Xie [1981] proposed a depiction based on two aspects; the sand grain size and the properties of wave loading in terms of wave height, wave period (thus wave length) and water depth. These aspects are incorporated into a dimensionless number which is given by the following formula where u_m is the wave orbital velocity, w the settling velocity and u_{cr} is the critical orbital velocity:

$$\frac{u_m - u_{cr}}{w} = X \quad (2-1)$$

The quantity X represents the boundary between 'fine' and 'coarse' regime and depending on the sand grain size can take several values. According to Xie [1981] 'fine' sand can be found for $X \geq 16.5$ while 'coarse' and mixed type sand occurs for $X < 16.5$. Equation (2-1) can also be expressed in terms of shear velocity u_* , with a corresponding limit for 'fine' sand $X \geq 1.12$.

For the computation of critical orbital velocity u_{cr} Xie [1981] compared different formulas proposed by Bagnold, Goddet, Komar & Miller and Swart. His observations showed that all formulas overestimate the magnitude of critical velocity. Nevertheless, Bagnold's formula appeared to be closer to test observations.

Based on the theory of Xie [1981], Sumer *et al.* [2000] conducted physical model tests to study scour at the trunk section of a rubble mound breakwater; however, as a reference case they also tested a vertical wall breakwater using regular waves. Figure 2-2 displays the

equilibrium scour/deposition pattern for the case of ‘coarse’ sand; it is also in agreement with the observations of de Best *et al.* [1971] and Xie [1981]¹. Finally, important to notice here is that scour at the junction between vertical wall and seabed has a zero value; thus it is not threatening the stability of the structure.

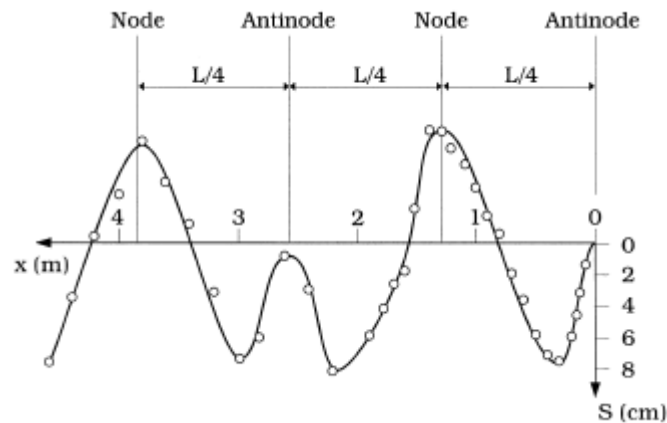


Figure 2-2 Equilibrium scour/deposition pattern in front of a vertical wall breakwater. ‘Coarse’ sand bottom & regular waves. (Sumer *et al.* [2000])

As a design tool, Xie [1981] proposed the following empirical formula that links maximum scour depth to wave height and relative water depth h/L (L is computed based on the mean spectral period, thus $L = f(T_m)$) for the case of ‘fine’ sand and live bed scour.

$$\frac{S}{H} = \frac{0.4}{\left(\sinh\left(\frac{2\pi h}{L}\right)\right)^{1.35}} \quad (2-2)$$

An equivalent expression for ‘coarse’ sand is found in Sumer *et al.* [2000] where 0.4 at the nominator is replaced with 0.3, meaning that for the same hydraulic loading scour depth is larger if seabed material is placed in the ‘fine’ regime.

2.1.2. Scour around rubble mound breakwaters

Similarly to the case of vertical walls, wave induced streaming is also responsible for the scour formation around rubble mound breakwaters. However, the sloping, porous surface of breakwater profile affects the amount of reflected wave energy leading to different scour patterns.

To get more insight on scour properties, Sumer *et al.* [2000] conducted physical model tests to investigate scour formation at the unprotected toe area, around the trunk of rubble mound breakwaters. In specific, they performed tests with regular and irregular non-breaking waves and with two breakwater slopes (1:1.2 & 1:1.75).

Figure 2-3 illustrates the observed scour/deposition pattern for the case of regular waves and ‘coarse’ sand. In contrast to the case of vertical walls, scour depth (thus streaming) at the junction of breakwater and seabed has a non zero value.

¹ In addition to that, Xie [1981] reported the existence of equilibrium state in about 6500~10000 waves.

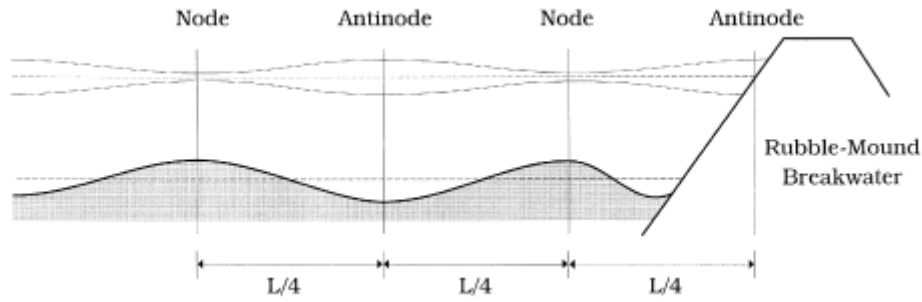


Figure 2-3 Scour/deposition in front of rubble mound breakwaters. Regular waves & 'coarse' sand. (Sumer *et al.* [2000])

However, the magnitude of maximum scour hole is less than the case of a vertical wall. The reason for that is the weaker streaming caused by the smaller reflection coefficient. In specific, for the same wave condition a smaller structural slope leads in smaller maximum scour depth. This is better illustrated in Figure 2-4 where the relative scour hole is plotted for three different cases; vertical wall (reference case $\alpha=90^\circ$) and rubble mound breakwater ($\alpha=40^\circ$ & $\alpha=30^\circ$).

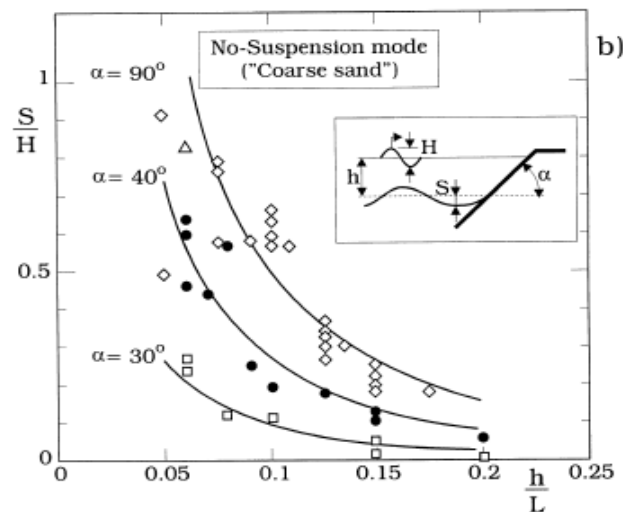


Figure 2-4 Relative scour depth S/H for vertical wall ($\alpha=90^\circ$) and rubble mound breakwater ($\alpha=40^\circ$ & $\alpha=30^\circ$). (Sumer *et al.* [2000])

Significant differences occur between regular and irregular² non-breaking waves. Specifically, for the same structure configuration, irregular waves cause smaller (with a factor of 2) maximum scour hole than regular waves. In addition, scour/deposition profiles emerge in narrower extent than the case of regular waves due to the 'weaker' standing waves (Schierck [2004]).

Based on dimensional analysis, Sumer *et al.* [2000] found that relative scour depth is a function of the following dimensionless products: $\frac{S}{H} = f\left(\frac{h}{L}, \alpha, \Psi, \frac{L}{D_{50}}, Re\right)$ where Ψ : Shields' Number, $Re = \alpha U_b / \nu$ wave Reynolds' Number, H is the wave height of regular waves or the root mean square wave height H_{rms} , h is the water depth and S the maximum scour depth.

² Based on H_{rms} and T_p taken from the spectrum.

With respect to that and correspondingly to Xie [1981] they presented eq. (2-3) which is formulated based on regular non-breaking waves and is valid for the ‘coarse’ sand regime:

$$\frac{S}{H} = \frac{f(a)}{\left(\sinh\left(\frac{2\pi h}{L}\right)\right)^{1.35}} \quad (2-3)$$

In the formula above, $f(a)$ represents the dependency on breakwater’s structural slope and is given by the following expression which is valid for structural slope $30^\circ \leq \alpha \leq 90^\circ$:

$$f(a) = 0.3 - 1.77e^{\left(-\frac{a}{15}\right)} \quad (2-4)$$

Despite that the proposed design tool approximates rather successfully the data set from Sumer *et al.* [2000], neglects the remaining three factors of the performed dimensional analysis. Sumer *et al.* [2000] limited their research in the case of live bed scour and ‘coarse’ sand. The first assumption diminishes the effect of Shields’ Number ψ on scour depth enhancement since $\psi > \psi_{cr}$, therefore ψ can be dropped out. The second assumption (‘coarse’ sand) drops out the Reynolds Number Re of the amplitude motion.

Furthermore, despite that they did not perform experiments with different base materials, based on the analysis from Xie [1981], they claimed that L/D_{50} has imperceptible effect on maximum scour depth; thus it can be neglected. For that reason, they used only one base material and they did not apply any correction factor to account for the use of a different base material.

However, in real life situations, sand is not always behaving as ‘coarse’ sand. Thereby, depending on the properties of hydraulic loading, seabed material under storm conditions can act either as rough wall (‘coarse’) or as smooth boundary (‘fine’). Especially the latter displays the eccentricity in which a larger Re value may lead to a smaller scour depth. Therefore, insight needs to be gained in the mixed case and in the case of ‘fine’ sand. The incorporation of the missing factors into a scour prediction tool could help to this direction.

Besides, Sumer *et al.* [2000] attempted to deploy toe protection design rules. To do so, they examined the width W_t and the thickness d_f of toe protection with respect to the normalized maximum scour depth S/H . By using a one layer apron and ratios between apron stones to base layer in the order of $D_{f50}/D_{b50}=235$, the necessary toe width should be equal to the width of the scour hole³ when no toe protection is applied.

For the determination of optimum toe thickness d_f , they carried out tests with ascending number of layers of stones N and a relative grain diameter of $D_{f50}/D_{b50}=150$. In Figure 2-5 as the number of layers N increases, the normalized scour depth S/H reaches a value where further increase of toe thickness is aimless. For values of $N=4-5$ optimum protection is achieved. The latter is in agreement also with the observations of Klar [2005]; where the relative turbulent intensity for non-uniform flows decreases exponentially with protection (filter) thickness until $4-5 \cdot D_{n50}$, where further increase of thickness does not enhance damping.

³ When $\alpha=40^\circ$ scour hole width equals $W_s=0.6(L/4)$. When $\alpha=30^\circ$ scour hole width equals $W_s=0.3(L/4)$.

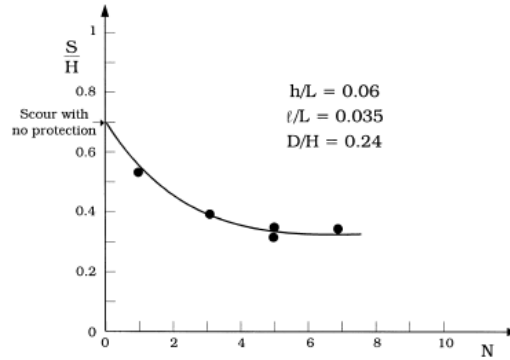


Figure 2-5 Normalized scour depth S/H as a function of number of layers of stones N . (Sumer *et al.* [2000])

To sum up, as it was mentioned further above, Equation (2-3) predicts the maximum scour depth for the unprotected seabed, at the toe of a rubble mound breakwater, based on the structural slope α and the relative water depth h/L . The equation was formulated based on a single base material (sand), under regular non-breaking waves and in the ‘coarse’ sand regime. By introducing the effect of relative grain diameter (toe protection and base layer) the maximum scour hole can be predicted with respect to the dimensions of base and the protective granular material. Consequently, the coupling of the proposed prediction tool of eq. (2-3) with the relative grain diameter could form the basis for a wider applicable design tool that overcomes the distinction between ‘coarse’ and ‘fine’ sand.

2.1.3. Temporal evolution of scour depth

Apart from the magnitude, also the temporal evolution of scour formation is of great importance. Similarly to the normalized scour depth, the dimensionless⁴ time scale T^* of scour pattern is given by eq. (2-5) Sumer *et al.* [2000]:

$$T^* = \frac{[g(s-1)D_{50}^3]^{1/2}}{H^2} T_s \quad (2-5)$$

T_s correspond to the time scale for which significant amount of scour takes place. For deeper waters (h/L) equilibrium scour depth is reached slower than shallower water because also normalized scour depth S/H decreases for bigger values of h/L . However, due to the subjectivity in determining T_s , the determination of T^* is also ambiguous.

2.2. Granular filters

In practice, the most common solution to counteract scour formation is to apply a granular filter. However, based on their function granular filters can be distinguished into three categories:

- Geometrically closed filters
- Hydraulically sand-tight (stable geometrically open) filters

⁴ Based on dimensional analysis dimensionless time scale is given by $T^* = f\left(\frac{h}{L}, \alpha, \Psi, \frac{L}{D_{50}}, Re\right)$.

- Transport (unstable geometrically open) filters

Furthermore, based on their gradation granular filters are distinguished (CIRIA et al. [2007]) for rock:

- Narrow gradation $\frac{D_{85}}{D_{15}} < 1.5$
- Wide gradation $1.5 < \frac{D_{85}}{D_{15}} < 2.5$
- Very wide gradation $\frac{D_{85}}{D_{15}} > 2.5$

On the other hand, for the distinction based on gradation CUR [2010] proposes the following criteria for gravel:

- Standard gradation $\frac{D_{85}}{D_{15}} < 2.5$
- Wide gradation $\frac{D_{85}}{D_{15}} > 2.5$

2.2.1. Geometrically closed filters

The concept behind the design of geometrically closed filters is to come up with configurations that assure base layer stability by protecting it through layer(s) of sufficiently fine filter material. Thereby, interface stability is succeeded since erosion is mechanically prevented.

Besides, sand tightness can hinder the flow of drainage or seepage water through the pores of the filter. This can lead to undesired under-pressure formation, uplifting and probably serious damage to filter configuration. In order to avoid that, filter should be permeable enough to allow sufficient water flow.

Apart from preventing base layer erosion, filter should be designed such way that is internally stable, and no filter material is washed out. Prevention of internal erosion protects filter layer from failure mechanisms such as piping and heave. On the other hand, this requirement is in contradiction with the necessity of an adequately permeable filter.

Finally, the aforementioned pursuits will only be accomplished if filter layer has in all extent a sufficient thickness, prescribed by specific practical requirements. In particular the traditional filter rules for the design of geometrically closed filter configurations can be found below⁵.

Retention rule

The worst scenario for the stability of a filter-base configuration takes place when the finer aggregates of base material are able to pass through the voids formed between the coarser aggregates of the filter layer. However, interface stability is threatened when even the coarser part of the base layer can erode. To prevent this possibility, Terzaghi and Peck (eq. 2-

⁵ It should be mentioned that the described geometrically filter rules will be applied in the design of the breakwater armor layer with regard to core material properties (For more information see Chapter 3).

6) and U.S. Army Corps of Engineers⁶ (eq. 2-7 & 2-8) (CUR 233 [2010]) derived the following empirical rules:

$$D_{f15}/D_{b85} < 4 \quad (2-6)$$

$$D_{f15}/D_{b85} < 5 \quad (2-7)$$

$$D_{f50}/D_{b50} < 25 \quad (2-8)$$

Permeability rule

The aim of this rule is to prevent clogging of filter material's voids due to accumulation of base material's fines. In case of a decreased filter permeability, under-pressures will rise that may lead to uplifting of filter layer and finally, to the destruction of filter configuration. For uniform filter and base materials Terzaghi and Peck (CUR 233 [2010]) gave the following rule:

$$D_{f15}/D_{b15} > 4 \quad (2-9)$$

Internal stability rule

In case of an internally unstable filter, finer filter particles can be washed out and cause filter failure due to piping or heave. The time scale of the latter is more rapid than failure due to internal erosion. Kennedy and Lau (CUR 233 [2010]) derived the following rules:

$$D_{10}/D_5 < 4, D_{20}/D_{10} < 4, D_{30}/D_{15} < 4, D_{40}/D_{20} < 4 \quad (2-10)$$

Required filter thickness

In order to perform effectively, a filter has to be constructed with a thickness at least 2~3 times the grain diameter of the larger base material particles. Especially, in case of underwater placement it should be 2~3 times the diameter of the larger particles of filter layer and at least 0.3m thick.

2.2.2. Hydraulically sand-tight (stable geometrically open) filters

The concept behind the design of stable geometrically open filters is that no transport through the pores of the filter is allowed because the corresponding hydraulic load is lower than a threshold value that leads to incipient motion and thus erosion.

For the design a variety of formulas exist depending on the occurring flow conditions (permanent or not, uniform or not). However, all of them apply a similar design approach, by relating filter thickness (expressed as relative thickness to a representative diameter) to a ratio of characteristic diameters of filter and base layer. Besides, in order to cope with the different flow conditions and the implied magnitude of turbulence design formulas include dustbin parameters.

Permanent flow conditions (from CUR 233 [2010])

Until now, extensive research has been conducted in the field of geometrically open filters with regard to permanent uniform and non-uniform flow conditions. For these cases, reference is made to CUR 161 [1993] and the work of Breteler, Bakker *et al.*, and Wörman [1989]. Furthermore, based on the work of Klar, Verheij, Hoffmans *et al.* in CUR 233 [2010]

⁶ Experiments were carried out with the use of narrowly graded sand and grain size distributions with $D_{90}/D_{10} < 5$.

new design formulas including an alternative expression of the design criterion of Wörman, are derived for the case of non-uniform flow conditions. The derivation procedure was based on three steps and is briefly explained below.

1. Application of Grass hypothesis

In general, sediment transport takes place when load exceeds a critical value (threshold of motion). For the present study, load is expressed by shear stress in the interface between filter and base layer while strength is represented by particle stability. However, in order to determine whether or not particle transport takes place characteristic values of load and strength have to be derived (Figure 2-6). This is done because apart from the mean (time and/or space averaged) values, load and strength also include fluctuating terms while the shape of their distribution is difficult to be specified. In fact, for the case of load the instantaneous relative turbulence intensity should be added, while for the case of strength the gradation of material has to be taken into account.

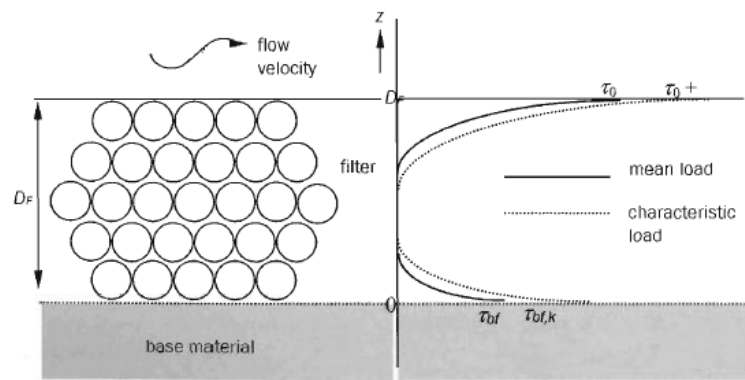


Figure 2-6 Distribution of mean and characteristic load (CUR 233 [2010])

By applying the Grass hypothesis (Grass [1970]) for the upper layer of the filter a characteristic bed shear stress (load) $\tau_{0,k}$ and a critical characteristic bed shear stress (strength) $\tau_{G,k}$ were derived with respect to Figure 2-7:

$$\tau_{0,k} = \tau_0 + \gamma \sigma_0 \quad (2-11)$$

$$\tau_{G,k} = \tau_G - \gamma \sigma_G \quad (2-12)$$

In which:

γ : coefficient determined by an allowable transport of bed material (-) (Grass [1970])

τ_0 : mean bed shear stress (N/m^2)

τ_G : critical mean bed shear stress (N/m^2) with $\tau_G \gg \tau_c$

$\sigma_0 = V_0 \tau_0$: standard deviation of instantaneous bed shear stress (N/m^2)

V_0 : variation coefficient representing bed turbulence

$\sigma_G = \tau_G V_G$: standard deviation of critical instantaneous bed shear stress (N/m^2)

V_G : $V_G = 1 - D_{f15}/D_{f50}$ variation coefficient representing the non-uniformity of materials and variation of strength

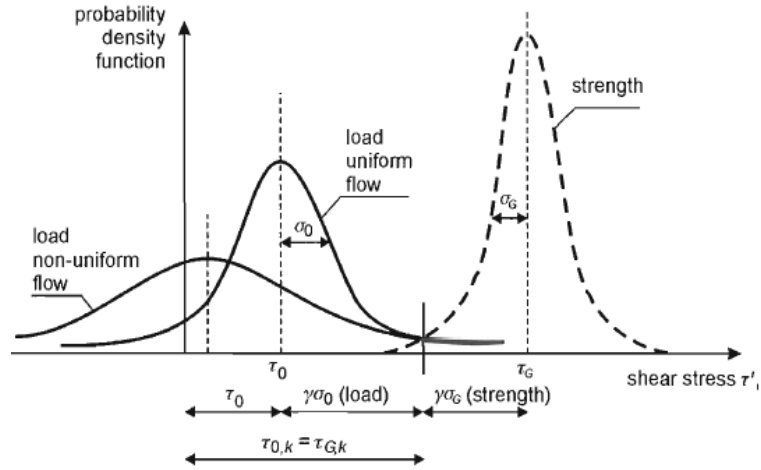


Figure 2-7 Probability functions of load and strength (Grass [1970])

Likewise, the hypothesis of Grass is applied for the interface between filter's base layer and under-layer (bottom of Figure 2-6). Additionally, the notion of relative load $\eta = \tau_{bf,k} / \tau_{0,k}$ is introduced to make use of eq.(2-11 & 2-12) and end up to:

$$\tau_{bf,k} = \eta(\tau_0 + \gamma\sigma_0) \quad (2-13)$$

$$\tau_{G,bf,k} = \tau_{Gb} - \gamma\sigma_{Gb} \quad (2-14)$$

Analogously to Shields, shear stress and thus characteristic strength of filter and base layer (eq. 2-12 & 2-14) can be expressed by:

$$\tau_{G,f,k} = \Psi_{Gf} \Delta_f \rho_w g D_{f50} (1 - \gamma V_{Gf}) \quad (2-15)$$

$$\tau_{G,bf,k} = \Psi_{Gb} \Delta_b \rho_w g D_{b50} (1 - \gamma V_{Gb}) \quad (2-16)$$

Critical situation occurs when $\tau_{0,k} = \tau_{G,k}$ and $\tau_{bf,k} = \tau_{G,bf,k}$. Thereby, the relative strength η_c can be defined as the ratio of the mean strength of the base layer $\tau_{c,bf}$ at the transition of the filter-base layer and the mean strength at the top of the filter layer $\tau_{c,f}$.

$$\eta_c = \frac{\tau_{c,bf}}{\tau_{c,f}} \quad (2-17)$$

Similarly, the relative strength η_c can also be used to express the relation between characteristic strength of base material $\tau_{c,bf,k}$ and filter material $\tau_{c,f,k}$ according to eq.(2-18).

$$\eta_c = \frac{\tau_{c,bf,k}}{\tau_{c,f,k}} = \frac{\Psi_{Gb} \Delta_b D_{b50} (1 - \gamma V_{Gb})}{\Psi_{Gf} \Delta_f D_{f50} (1 - \gamma V_{Gf})} \quad (2-18)$$

Consequently, the derivation of the design formula is based on the hypothesis that movement of base layer (stability of interface between filter and under-layer) will not take place as long as filter's upper layer stability is maintained. Therefore, incipient motion for the upper layer and the base layer will take place simultaneously and for the same boundary condition (load).

Finally, for the critical situation eq.(2-18) can be transformed to the equation that was derived by Verheij et al. [2000].

$$\frac{D_{f50}}{D_{b50}} = \frac{1}{\eta_c} \frac{\Delta_b (1 - \gamma V_{Gb})}{\Delta_f (1 - \gamma V_{Gf})} \frac{\Psi_{Gb}}{\Psi_{Gf}} \quad (2-19)$$

2. Damping of turbulence into the filter

Based on the work of Klar [2005] for uniform flow conditions, local turbulence energy decreases with depth, according to the following exponential expression:

$$k_f(z) = k_{ref} e^{\frac{z}{\zeta(z)}} \quad (2-20)$$

In which:

$k_{ref} = \alpha_{ref} u_*'^2$: turbulence energy at a reference level (m^2/s^2)

α_{ref} : coefficient to account for reference level in local turbulence energy computation (-)

$r_{f,bf}$: local relative turbulence intensity⁷ (-)

z : vertical coordinate, $z=0$ at bed

$\zeta(z) = \alpha_\chi D_{f15}$: length scale

α_χ : coefficient to account for length scale in local turbulence energy computation (-)

Afterwards, the application of the hypothesis of Boussinesq for shear stress in the interface between filter and base layer, and an expression for the local eddy viscosity⁸ are used to derive an expression (eq.(2-21)) for damping of turbulence in the filter. Eq. (2-21) is written in terms of relative load η , of the interface between filter and base layer and the top of the filter layer:

$$\eta = \frac{\tau_{bf}}{\tau_0} = \frac{1}{2r_{f,bf}^2} \alpha_\kappa \alpha_{ref} e^{\left(\frac{-d_f}{\alpha_\chi D_{f15}}\right)} \quad (2-21)$$

3. Required filter thickness

By substituting eq.(2-21) with eq.(2-19) and rearranging the parameters, the design equation is formed. Eq.(2-22) relates the relative layer thickness $\frac{d_f}{D_{f15}}$ with material properties and loading conditions. More specifically, for the case of non-uniform conditions the new formula writes:

$$\frac{d_f}{D_{f15}} = \alpha_\chi \ln \left(\frac{\alpha_{ref}}{2r_{f,bf}^2} \alpha_\kappa \frac{\Delta_f D_{f50} \Psi_{cf} (1-\gamma V_{gf})}{\Delta_b D_{b50} \Psi_{cb} (1-\gamma V_{gb})} \right) \quad (2-22)$$

In which:

α_κ : coefficient to account for the magnitude of relative turbulence intensity r_0 . Range of values from 0.05 for uniform flow to 0.5 for non-uniform flow conditions (-)

Δ_f, Δ_b : $(\rho_s - \rho_w) / \rho_w$ relative density (-)

In case that $r_{f,bf}=1$, $\alpha_\chi=2$ and $\alpha_{ref}=2$ then eq.(2-17) can be written as:

$$\frac{d_f}{D_{f15}} = 2 \ln \left(\alpha_\kappa \frac{\Delta_f D_{f50} \Psi_{cf} (1-\gamma V_{gf})}{\Delta_b D_{b50} \Psi_{cb} (1-\gamma V_{gb})} \right) \quad (2-23)$$

Additional design formulas

⁷ for range of values of mean relative turbulence intensity r_0 address to Hoffmans [1993]

⁸ Detailed explanation in CUR 233 [2010]

Except from eq.(2-22 & 2-23), two additional formulas can be used for the design of stable geometrical open filters under permanent flow conditions. These are the modified Wörman formula and a modified expression of eq.(2.23) derived by Hoffmans (de Sande [2012]). These design rules are treated below.

Hoffmans (de Sande [2012])

Similarly to eq.(2-22 & 2-23), Hoffmans (de Sande [2012]) derived a new design tool. The main difference is the different approach used to include the damping of turbulence in the filter. This deviation resulted in the extraction of the dustbin parameter α_k from the logarithm (now used as α_d). In particular, instead from eq.(2-20), damping of local turbulence kinetic energy is given by:

$$k_f(z) = k_{f,s} + (k_b - k_{f,s})e^{\frac{z}{L_d}} \quad (2-24)$$

In which:

$L_d = \alpha_d D_{f15}$: damping length, equivalent to $\zeta(z)$ from eq.(2-20) (m)

Based on Bejuizen and Köhler (1998)⁹ damping length is given by:

$$L_d = \sqrt{\frac{T_p c_v}{\pi}} \quad (2-25)$$

In which:

T_p : peak period from wave spectrum (s)

c_v : consolidation coefficient 10^{-3} (m²/s)

As a result the new design formula writes:

$$\frac{d_f}{D_{f15}} = \alpha_d \ln \left(\frac{\Delta_f D_{f50} \psi_{cf} (1 - \gamma V_{gf})}{\Delta_b D_{b50} \psi_{cb} (1 - \gamma V_{gb})} \right) \quad (2-26)$$

Especially for the relative thickness parameter de Sande [2012] suggests D_{f50} instead of D_{f15} .

Modified Wörman formula

Finally, the modified Wörman formula¹⁰ (CUR 233 [2010]) for a single layer bed protection under non-uniform flow conditions writes:

$$\frac{d_f}{D_{f15}} = \alpha_v \chi_l^{-1} \frac{D_{f50}}{D_{b50}} \quad (2-27)$$

In which:

α_v : coefficient to account for the magnitude of turbulence, similar to α_k of eq.(2-21)

(-)

χ_l : factor for turbulence damping. Linked to α_v with $1.2 \leq \chi_l \leq 4.7$ (-)

⁹ They have examined stability of revetment structures under loading by wind and ship induced waves.

¹⁰ The original, general Wörman equation writes $\frac{d_f}{D_{f15}} = \alpha \frac{\Delta_f}{\Delta_b} \frac{n_f}{1 - n_f} \frac{D_{f85}}{D_{b85}}$ and was derived for single layer bed protections around bridge piers and under non-uniform flow conditions.

The main difference between the modified Wörman formula and the other design equations is that instead of eq.(2-21) the former formula assumes linear damping of turbulence inside the filter, in agreement with the following equation:

$$\eta = \frac{\tau_{bf}}{\tau_0} = \alpha_v (\chi_l^{-1} \frac{D_f^{1.5}}{d_f}) \quad (2-28)$$

Wave conditions

The derived equations, namely eq. (2-26) and (2-27) use dustbin parameters to account for the turbulence intensity related to the loading conditions. This is an advantage because, despite that they are derived for permanent (uniform and non-uniform) flow conditions can also be applied for the case of wave loading. This can be done by appropriately adjusting the dustbin factors to comply with wave induced turbulence. However, separately for every design case a reliable range of values for these factors has to be specified because none of the derived equations has been tested for waves.

Wave loading and structure interactions are the aspects that are responsible for scour formation at the toe of a rubble mound breakwater. Consequently, eq. (2-26) derived by Hoffmans (de Sande [2012]) and adjusted to wave climate could be used as the design formula in order to establish the test set-up of the present study. However, special care has to be taken for two reasons:

- Derived equation has been tested for relative grain diameter of filter and base material with a ratio $\Delta_f/\Delta_b=1\sim 1.2$.
- Based in this formula, optimum design is succeeded when filter layer and base material start to move simultaneously.

The present study displays a major particularity; the breakwater lies upon sand. The choice for the simulation of sand in physical model tests would be decisive for the usefulness of this equation. In particular, if a lighter material is applied as seabed material then relative grain diameter ratio will be doubled and it would be hard to accomplish simultaneous movement of filter and base material.

An organized attempt to investigate the application of open granular filters on breakwaters with sand core took place by Uelman [2006] and Ockeloen [2007]. The former, used relative thickness $\frac{d_f}{D_{f50}}$ ranging from 2-12 and relative filter to base layer grain ratio $110 < \frac{D_{f50}}{D_{b50}} < 275$. The conducted physical model tests showed both sheet flow transport and suspended sediment transport, while the latter was enhanced when proceeding to larger filter stone sizes and thinner filter layers. In general, an S-shaped profile was formed under the armor layer of the breakwater while for larger relative thicknesses, erosion showed a decreasing tendency.

Ockeloen [2007] performed a step further to relate dimensionless erosion area with relative thickness. Based on his physical model tests and the work of Uelman [2006] he developed the following best fit formula:

$$\frac{A_e}{H_{rms}L_f} = 0.21(s_{rms} \frac{N}{d_f/D_{f50}})^{0.2} - 0.4 \quad (2-29)$$

In which:

A_e : erosion area (m²)

L_f : fictitious wave length equivalent to deep water wave length L_0 (m)

s_{rms} : root mean square value of gradient parallel to slope (-)

N : number of waves (-)

Nevertheless, the aforementioned formula suffers from two shortcomings; the absence of base material and the difficulty behind the determination of hydraulic gradient in the interface between filter and base layer (CUR 233 [2010]).

2.2.3. Transport (unstable geometrically open) filters

Transport filters are established under the framework of a predictable and acceptable loss of under-layer material. Afterwards, by applying maintenance techniques the base layer can be restored to the initial state. However, this is not always possible rendering transport filters to be less appealing. In fact, especially for the present study that focuses on the toe area, inspection of damage and maintenance are both costly and rarely operational.

2.3. Summary and link to this study

Unprotected seabed in front of a coastal structure is subject to scour formation. The properties of the latter depend and thus vary with respect to the amount of reflection due to the presence of the structure (vertical walls, rubble mounds etc.), the type of loading (wave properties etc.), the relative water depth h/L , and the seabed characteristics. In order to obtain a holistic prediction of scour patterns the aforementioned factors need to be combined effectively.

Especially for the case of a rubble mound breakwater, the empirical formula proposed by Sumer *et al.* [2000] gives an accurate prediction of the normalized scour depth S/H of the unprotected seabed, at the toe of a rubble mound breakwater. In particular, it is valid for 'coarse' sand and live bed scour under non-breaking waves; consequently the effect of base material grain diameter is neglected. In addition, no information is available about the damping of normalized scour depth when protection is applied.

Further upon, the seabed around a coastal structure during the structure's lifetime is subject to a variety of loading conditions. Based on them the seabed can display different behaviors from pure 'fine' sand to a mixed type and until pure 'coarse' sand behavior. According to Xie [1981] for the same loading conditions 'fine' sand behavior leads to deeper scour holes. However, it has to be investigated whether different diameters of seabed material display the same behavior.

Undoubtedly, the safest approach to counteract scour formation is the application of the geometrically closed granular filter criteria. Nevertheless, their entailed constructional and

financial drawbacks render geometrically open filter criteria to be more appealing. Therefore, the recent years research into this direction has already been proceeding systematically.

The most important outcomes of this effort are the design equations (2-19) derived by Verheij et al. [2000] and (2-26) by Hoffmans (de Sande [2012]). They were developed for the case of uniform and non-uniform flow conditions although it is believed that they can also be used for the design under wave loading with proper modification of the included dustbin parameters. The main difference between these two is the way that they take into account damping of turbulent energy inside the filter layer; for the former it is accomplished logarithmically, while for the latter linear damping is assumed. Apart from that they both count for the homogeneity of the filter and base layer and they assume simultaneous movement of filter and base material by incorporating the ratios of relative density Δ_f/Δ_b and critical Shields' Number Ψ_{cf}/Ψ_{cb} .

For the present study, decisive for the applicability of the aforementioned design equations is the selection of scaling strategy. The prerequisite of simultaneous movement of filter and base layer is translated into the use of sand in both real life and physical model. However, this contradicts with the subject of the present study where the breakwater is lying upon sand. Thereby, if in the present study will be used a lightweight material to simulate the behavior of sand, the ratios of relative density Δ_f/Δ_b and critical Shields' Number Ψ_{cf}/Ψ_{cb} will be disordered, the assumption of simultaneous movement will not be valid anymore and therefore the application of either eq. (2-19) or eq. (2-26) will be ambiguous.

3. Model & test set-up

Undoubtedly, innumerable combinations of parameters exist that can test the behavior and performance of the filter in the toe of the breakwater. This chapter describes the choices made with respect to the properties and dimensions of the physical model and the characteristics of applied testing conditions.

In Paragraphs 1.5&1.6 the research direction is described in detail, Chapter 2 has provided insight on the related parameters and processes that play role in scour formation along with the guidelines for filter design at the toe of a rubble mound breakwater. Consequently, this chapter elaborates upon the choices made in order to build a physical model that will be used to investigate scour formation and development through a geometrically open filter placed at the toe of a rubble mound breakwater placed upon sand.

3.1. Physical model properties

3.1.1. Facility

2D physical model tests were conducted in the 25m long, 1m deep and 0.6m wide wave flume of DMC, installed in the company's laboratory in Utrecht. Flume's side walls and basis are made of transparent material offering the possibility to inspect the tests by various positions.

The flume is equipped with wave paddle that can generate regular and irregular waves and can provide automatic reflection compensation. The paddle extends until 2.5m from the start and creates long waves as water particles are ascending from the bottom to water surface. Therefore, space is needed for the wave to obtain the regular orbital behavior.

The flume is capable to host a great range of foreshores via the eyes (circular holes) that exist on the side glass walls, at a distance of 3cm from the bottom. The foreshore is fayed at the side glass and the eye is glued with silicone to avoid leakage.

3.1.2. Flume lay out

Starting from left to right, the flume layout can be divided into five parts:

1. The first part contains the wave generator that extends to a length of 2.5m and an equally long buffer area where neither a foreshore nor a measurement device should be located.
2. The second part contains the deep water wave gauges and the inclined part of the wooden foreshore. The first deep water wave gauge is placed immediately after the end of the buffer area. The inclined foreshore starts half a meter (0.5m) after the third deep water wave gauge. It has a length of 7.5m, a slope of 1:26 and ascends until a level of 0.288m.
3. The horizontal part of the foreshore along with the nearshore wave gauges are include in the third part. The first nearshore wave gauge is located 3m after the

start of the horizontal foreshore. The third part ends with the third nearshore wave gauge.

4. The most important part is the fourth; it has a length of 4.78m and it contains the toe area with the combination of filter/base layer and the breakwater. In front of the breakwater the foreshore's continuity is disturbed and a wooden box is formed in order to host the base layer. Detailed information on the properties of the rubble mound breakwater, toe and seabed box are given in the proceeding paragraphs.
5. The fifth part contains the area behind the structure and after the end of the platform. Just before the rear flume wall a sponge is placed to absorb the amount of reflected energy. This area has no particular interest for this research.

Figure 3-1 illustrates the most important aspects of flume's lay out. The upper part of the image is the side view through the flume's side glass. The down part of the image is a top view cross section (A-A') of the flume. Dimensions are in millimeters. Y-axis is parallel to the longitudinal direction (length of the flume) and x-axis parallel to the transversal direction (width of the flume).

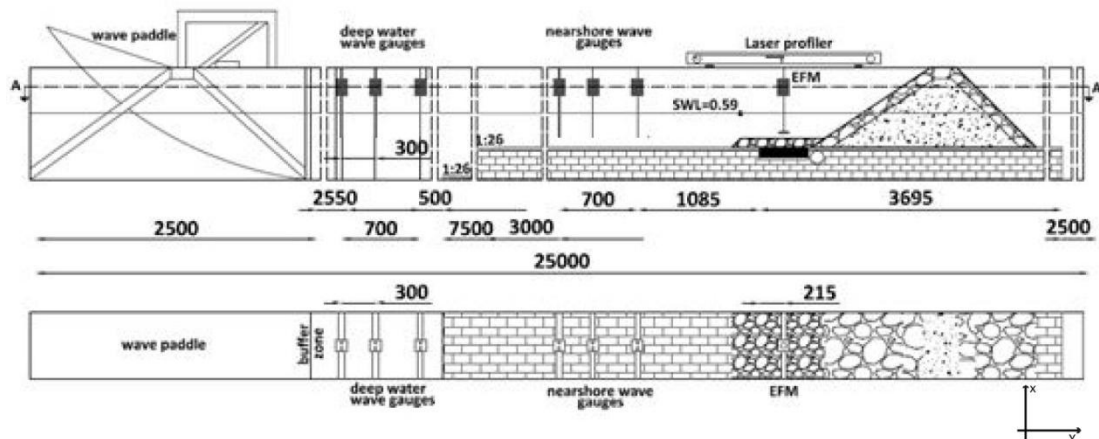


Figure 3-1 Side view (upper) and cross section A-A' (down) of flume layout.

Box for base material

Base material is hosted in a box just below the toe of the breakwater. The box's bottom and the shoreward side are made of wood. However, three out of four sides of the box are transparent; the side walls of the flume and the side just below the breakwater. This provides the opportunity to inspect the scour evolution from the sides and from below. The net dimensions of the box are: length=0.43m, width=0.60m and depth=0.09m.

Foreshore & foreshore slope

The slope of the foreshore is selected to be as mild as possible (Verhagen *et al.* [2006], Sayao [2007]) so that it is not causing abrupt wave height change and wave breaking before the breakwater. In addition, after it reaches 0.288m then it becomes horizontal. This compartment was selected as long as possible so that waves have time to adjust in the new water depth and the measured wave height at the gauges is as representative as possible. A limitation of the above is the total length of the wave flume and the necessary foreshore height in order to inspect the box during the test.

Finally, at the side walls of the foreshore in the area just below the base of the breakwater and next to the box a hole is formed in order to send light in the area below the flume. Thereby, video capturing can take place through the glass bottom of the flume.

3.1.3. Rubble mound breakwater

The structure itself is not the main target of this study. Therefore it had to be kept as simple as possible in order to decrease the involving uncertainties. For that reason, is used a breakwater configuration with a reported notional permeability value of $P=0.5^{11}$ that consists of an armor layer and core material. Figure 3-2 provides the lay-out of the breakwater structure. The armor layer acts also as a granular, closed filter that prevents wash out of the core material. In particular, the most important structure properties described below:

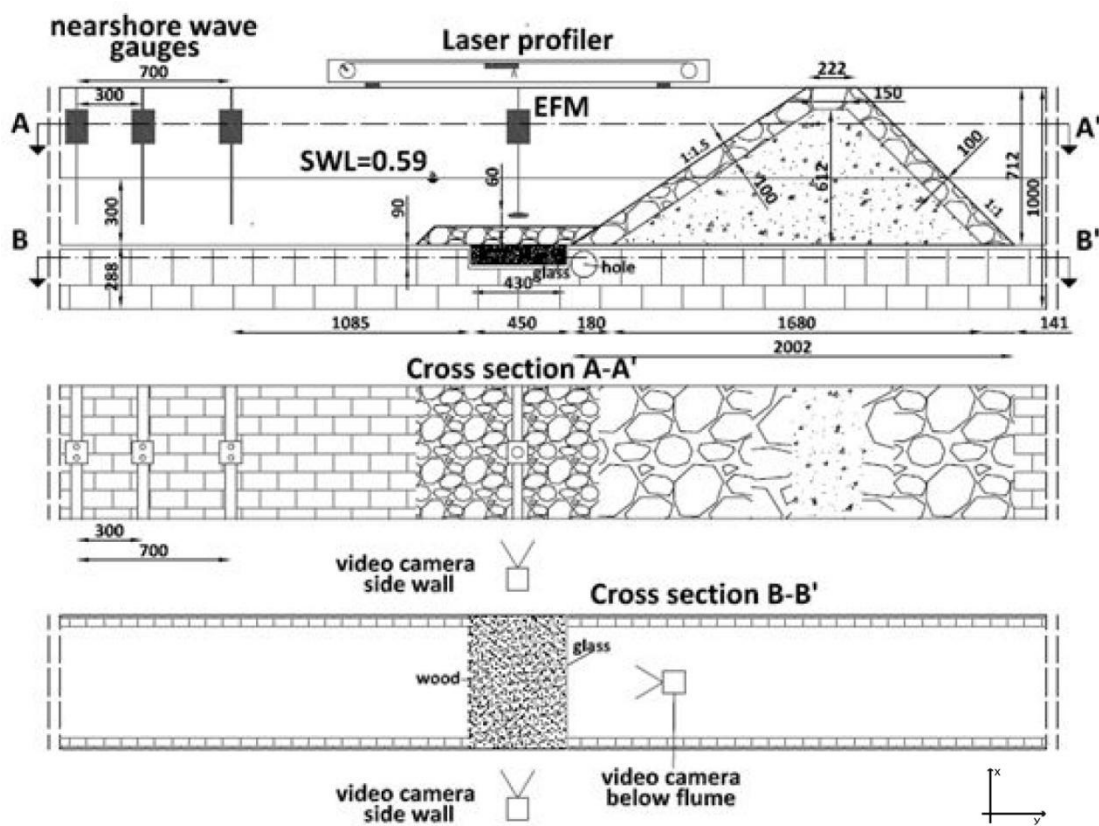


Figure 3-2 Side view/top view (cross section A-A & B-B') of rubble mound breakwater and toe area.

Armor layer

The used armor layer had the following properties: $D_{n50}=0.041m$, $D_{85}=0.045m$, $D_{15}=0.037m$. It is narrow graded with $D_{85}/D_{15}=1.22$ with a density $\rho=2650kg/m^3$. Properties were computed based on individual weighing of the stones. The armor layer thickness was $10cm$ ($2.5 \cdot D_{n50}$). Figure 3-3 illustrates the corresponding sieve curve.

¹¹ Meer, van der [1988].

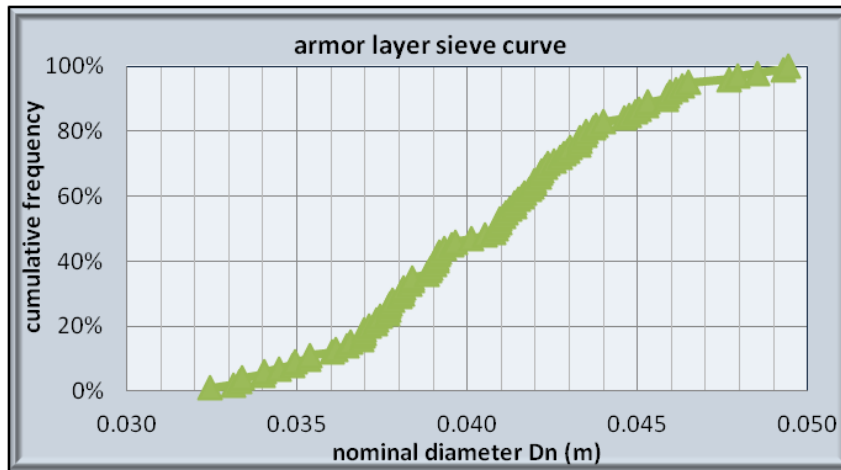


Figure 3-3 Armor layer sieve curve based on individual weighing of the stones.

Finally, in order to preserve similar testing conditions between, and during the tests, damage of seaward¹² armor layer is prevented by applying a wire mesh. The wire mesh prevents stone from moving due to the wave action so that the amount of reflection is exactly the same.

Core material

After the specification of the armor layer sieve curve, the core material sieve curve can be designed by applying the geometrically closed filter rules. Thereupon, the scaling method of Burcharth *et al.* (1999) is applied (see concept at Paragraph A-4, see application at 0) in order to preserve a characteristic value of hydraulic gradient inside the breakwater configuration and mitigate the viscous induced scale effects.

Conclusively, the used core material had the following properties: $D_{n50}=0.015\text{m}$, $D_{85}=0.020\text{m}$, $D_{15}=0.012\text{m}$. It has a standard grading with $D_{85}/D_{15}=1.67$ and a density of $\rho=2650\text{kg/m}^3$. Figure 3-4 illustrates the corresponding sieve curve.

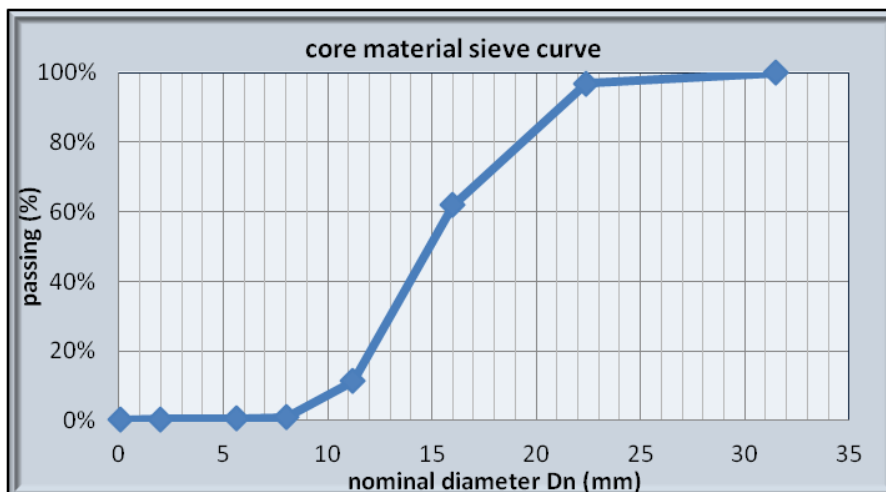


Figure 3-4 Core material sieve curve.

Overtopping

¹² At the rear side and crest stones are not glued together. However the same stone size is used for simplicity.

No overtopping is allowed so that no measures have to be taken for the protection of the rear slope. The crest height measured from the bottom of the flume is 1m and addresses to wave height higher than the design wave height.

Structure slope

Seaward structure slope is selected to be 1:1.5; is considered to be realistic in real life since it is used in practice. In addition it is between the range of validity of eq. (2-3). Indeed it is in between the two breakwater slopes tested by Sumer *et al.* [2000]. On the other hand, for the rear side a steeper slope 1:1 is selected, since no overtopping is allowed and also space and material requirements can be decreased.

3.1.4. Open filter configuration (toe & seabed material)

The scope of the study is to dampen scour formation in the toe of a breakwater which lies upon a sandy seabed by designing open granular filter configurations; therefore in this study toe material is considered as the filter material or protective layer and seabed material is the base material that is placed right beneath the model's toe. Furthermore, the term 'filter configuration' addresses to the combination of the filter/protective material with the corresponding base material. Indeed, 4 filters and 2 base materials are used in order to test 5 filter configurations.

Toe/filter material

Firstly, application of the Van der Meer equation (Meer, van der [1998]) for toe stability gave the following range of required toe stone dimensions [0.014 0.022]. This gave a first clue about the range of filter dimensions. Apart from that, filter dimensions should also be in agreement with the dimensionless grain diameter D_{f50}/D_{b50} , so that it would be possible to test different filter configurations. Based on the aforementioned criteria and the stone availability the following filters were selected:

- Filter 1 (wide graded): Class 8-22.4mm, $D_{f50}=14.3\text{mm}$, $D_{f85}=20\text{mm}$, $D_{f15}=9.5\text{mm}$, $D_{f85}/D_{f15}=2.11$ $\rho_f=2640\text{kg/m}^3$
- Filter 2 (narrow graded): Class 11.2-16mm, $D_{f50}=13.3\text{mm}$, $D_{f85}=15.5\text{mm}$, $D_{f15}=10.3\text{mm}$, $D_{f85}/D_{f15}=1.48$ $\rho_f=2650\text{kg/m}^3$
- Filter 3 (narrow graded): Class 8-11.2mm, $D_{f50}=9.6\text{mm}$, $D_{f85}=11\text{mm}$, $D_{f15}=8.4\text{mm}$, $D_{f85}/D_{f15}=1.31$ $\rho_f=2620\text{kg/m}^3$
- Filter 4 (narrow graded): Class 5.6-8mm, $D_{f50}=6.8\text{mm}$, $D_{f85}=7.5\text{mm}$, $D_{f15}=6\text{mm}$, $D_{f85}/D_{f15}=1.25$ $\rho_f=2715\text{kg/m}^3$

Filter thickness had to stay intact during the test. By gluing all the stones together erosion magnitude would be enhanced since a gap would form in between the stiff filter layer and the eroded base layer. Therefore, the filter layer had to be able to follow the erosion pattern of the base layer. To cope with that, a wire mesh was applied at a small distance for the filter surface. The mesh was allowing filter stones to move but could prevent major filter damage. Thereby, filter stone movement could be identified while major deviations of filter thickness were avoided. Figure 3-5 contains the sieve curves of the applied filter materials.

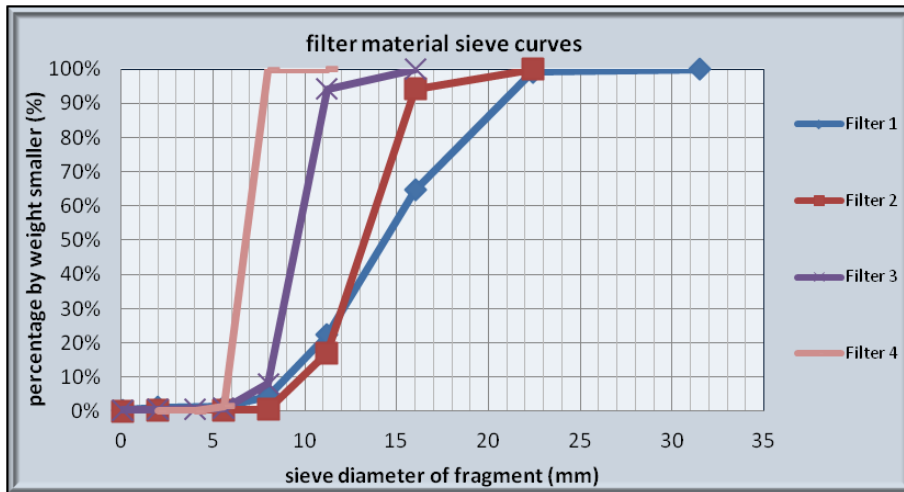


Figure 3-5 Filter/protection material sieve curves.

Base material

Argumentation behind the selection of base material is provided in Appendix A and especially in Sections A-2 & A-4. In brief, a fundamental prerequisite of the present study is that in the up-scaled situation, the breakwater will be lying upon sand. By using sand in the model this cannot be accomplished; therefore sand behavior will be modeled via the use of a lightweight material.

Finally, the grading of the base material is selected such that it couples with the available filter materials to form a desired set of relative grain diameter ratios D_{f50}/D_{b50} . Consequently, based on all the above two gradings of the same material were chosen.

- MC-5 (60/100) 150-250 μ m, $D_{b50}=210\mu$ m, $\rho_b=1500\text{kg/m}^3$
- MC-4 (40/60) 250-420 μ m, $D_{b50}=360\mu$ m, $\rho_b=1500\text{kg/m}^3$

Selected material is made of plastic and is used as an abrasive material. It is strong and does not react with water. The sieve curves of the selected base material are provided by Figure 3-6.

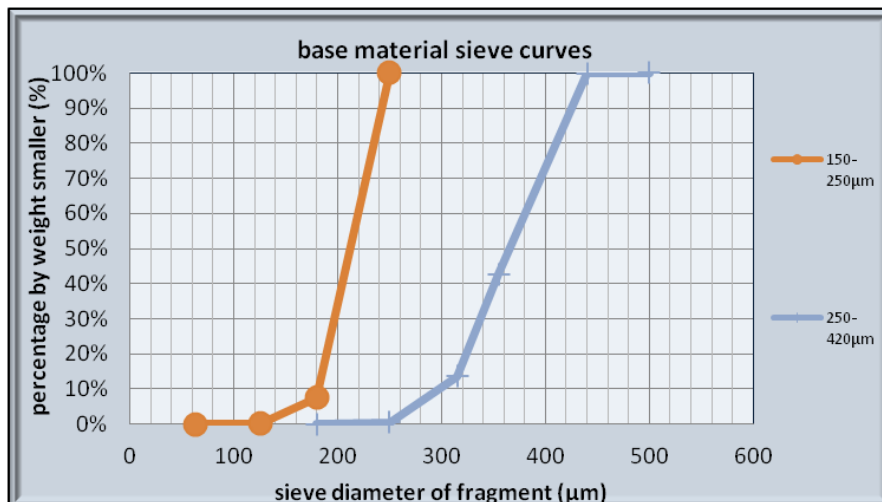


Figure 3-6 Base material sieve curves.

3.2. Test program

Relative importance between relative grain diameter D_{f50}/D_{b50} and relative thickness d_f/D_{f50} is critical for the design of geometrically open filters. However, insight has to be gained in the erosion properties with respect to the loading conditions for every combination of $d_f/D_{f50}=f(D_{f50}/D_{b50})$. The designed test programs focuses on this direction; to relate filter configurations with wave loading and the corresponding erosion properties.

Irregular waves

The choice was made for an irregular wave field produced during a storm event. For that reason a Jonswap spectrum is used which represents a young sea state. In addition, the open filter will be examined with respect to different wave steepness and thus an irregular wave field is more appropriate. Jonswap spectrum is described by the following spectrum energy density function:

$$E(f) = \alpha g^2 (2\pi)^{-4} f^{-5} e^{\left[-\frac{5}{4}\left(\frac{f}{f_m}\right)^{-4}\right]} \gamma_0 e^{\left[-0.5\left(\frac{f-f_m}{\sigma f_m}\right)\right]} \quad (4-1)$$

E: spectral energy density (m^2/Hz)

α : scaling parameter (Pierson-Moskowitz spectrum) (-)

f: frequency (Hz)

f_m : peak frequency (Hz)

γ_0, σ : peak enhancement factors (-)

Wave loading

Three wave conditions were used and were selected based on overlapping. Firstly, wave condition 1 (WC1) was selected by defining a deep water significant wave height and a peak period. Then, for wave condition 2 (WC2), the significant wave height was kept the same, but was accompanied by a shorter peak period. Finally, for wave condition 3 (WC3) a smaller significant wave height was selected and accompanied with the peak period selected for wave condition 1. In particular:

- WC1: $H_{m0}=12cm, T_p=2.5s$
- WC2: $H_{m0}=12cm, T_p=2s$
- WC3: $H_{m0}=9cm, T_p=2.5s$

From Sumer *et al.* [2000] it was found that for the same breakwater slope, longer waves cause deeper scour formation. Therefore, filter configurations were tested with relatively long waves that are located in the wind wave regime that is closer to swell waves.

Number of waves N/Test duration

Assuming a 9 hours storm and a mean wave period of 11.8s, leads to a total of 2800waves. When a period of 14.8s is assumed then 2200 waves are enough. Consequently, a total $N=3600$ waves are adequate to represent a 9hours storm and provide time space for the base layer to reach an equilibrium state. Furthermore, the use of lightweight material accelerates the time scale of the processes, thus equilibrium state will be reached sooner than reality. Therefore, 3600 waves are considered sufficient and on the safe side.

Grading variation

Filters 2-4 are narrow graded, and sometimes even narrower than the grading of materials applied in hydraulic engineering works. In order to investigate the effects of a wider grading filter 1 is selected to have a relative grain diameter D_{f50}/D_{b50} close to filter 2, but with a wider grading.

Filter thickness d_f /relative thickness d_f/D_{f50}

Normally, a thicker filter leads to less erosion; thus for the same relative grain diameter D_{f50}/D_{b50} less amount of erosion is expected for a larger relative thickness d_f/D_{f50} . Klar [2005] stated that mitigation of turbulent energy takes place until a thickness 4 to 5 times the nominal diameter of the filter material. Additionally, Van Os (1998)¹³, found that porous flow velocity inside the filter decreases only until a depth of 1.5 times the nominal diameter of the filter layer.

Apart from turbulent energy and velocity also the pathway that a base layer particle has to cover through the filter increases with a thicker filter. On the contrary, thicker filter thus thicker toe bund means that filter stones are exposed in higher particle velocities; therefore for the same filter grain diameter filter becomes less stable.

For the present study one relative filter thickness was used $d_f/D_{f50}=3.4$ (3.5 for Test series 1) to simplify the analysis. Additionally, in order to investigate the effect of relative thickness increase, Test series 1, 2 & 3 were investigated with two filter thicknesses; in particular:

- Test1a: Repeated by Test1d with thicker filter
- Test2a: Repeated by Test2d with thicker filter
- Test3a: Repeated by Test3d with thicker filter

Water level

One water level is used $h_0=0.589\text{m}$. At the toe of the structure the water depth is equal to $h=0.30\text{m}$. Tidal variations are not examined.

Test schedule/Test sequence

In total five test series were carried out which address to equal amount of filter configurations. In particular:

- Test series 1: Test1a, Test1b, Test1c, Test1d, Test1e
- Test series 2: Test2a, Test2b, Test2c, Test2d, Test2e, Test2f
- Test series 3: Test3a, Test3b, Test3c, Test3d, Test3e
- Test series 4: Test4a, Test4d, Test4e
- Test series 5: Test5a, Test5b, Test5c, Test5d

Every test series corresponds to a unique combination filter/base material grain size (filter configuration). Firstly, the coarser base material 250-420 μm is tested, followed by the finer 150-250 μm . Test sequence was designed with a decreasing relative grain diameter D_{f50}/D_{b50} for test series 1-3 and increasing relative grain diameter D_{f50}/D_{b50} for test series 4-5.

¹³ From de Sande [2012]

Firstly, every filter configuration is tested on the three wave conditions (WC1, WC2, WC3) and then, a thicker filter is increasing the relative thickness ratio d_f/D_{f50} . Test series 4 & 5 are exceptions. For test series 4, Test 4a is carried out by applying WC1; the rest of the tests are repetition tests because the amount of damage found in Test 4a was imperceptible. For test series 5 a thicker filter was not tested.

Table 3–1 summarizes the aforementioned and Figure 3-7 plots test series with respect to relative grain diameter D_{f50}/D_{b50} (x-axis) and relative thickness d_f/D_{f50} (y-axis):

Test Series	N_0 (-)	D_{f50} (m)	D_{b50} m	D_{f50}/D_{b50} -	d_f/D_{f50} -	d_f -	h_t (m)	H_{m0} (m)	T_p (s)	waves (-)
1	Test1a	0.0143	0.00036	39.83	3.50	0.050	0.30	0.120	2.5	3600
	Test1b	0.0143	0.00036	39.83	3.50	0.050	0.30	0.120	2.0	3600
	Test1c	0.0143	0.00036	39.83	3.50	0.050	0.30	0.090	2.5	3600
	Test1d	0.0143	0.00036	39.83	5.00	0.072	0.30	0.120	2.5	3600
	Test1e	0.0143	0.00036	39.83	3.50	0.050	0.30	0.120	2.5	3600
2	Test2a	0.0133	0.00036	36.81	3.40	0.045	0.30	0.120	2.5	3600
	Test2b	0.0133	0.00036	36.81	3.40	0.045	0.30	0.120	2.0	3600
	Test2c	0.0133	0.00036	36.81	3.40	0.045	0.30	0.090	2.5	3600
	Test2d	0.0133	0.00036	36.81	4.50	0.060	0.30	0.120	2.5	3600
	Test2e	0.0133	0.00036	36.81	3.40	0.045	0.30	0.120	2.5	3600
	Test2f	0.0133	0.00036	36.81	3.40	0.045	0.30	0.120	2.5	7500
3	Test3a	0.0096	0.00036	26.67	3.40	0.033	0.30	0.120	2.5	3600
	Test3b	0.0096	0.00036	26.67	3.40	0.033	0.30	0.120	2.0	3600
	Test3c	0.0096	0.00036	26.67	3.40	0.033	0.30	0.090	2.5	3600
	Test3d	0.0096	0.00036	26.67	4.30	0.041	0.30	0.120	2.5	3600
	Test3e	0.0096	0.00036	26.67	3.40	0.033	0.30	0.120	2.5	9000
4	Test4a	0.0068	0.00021	32.33	3.40	0.023	0.30	0.120	2.5	3600
	Test4d	0.0068	0.00021	32.33	3.40	0.023	0.30	0.120	2.5	3600
	Test4e	0.0068	0.00021	32.33	3.40	0.023	0.30	0.120	2.5	3600
5	Test5a	0.0096	0.00021	45.71	3.40	0.033	0.30	0.120	2.5	3600
	Test5b	0.0096	0.00021	45.71	3.40	0.033	0.30	0.120	2.0	3600
	Test5c	0.0096	0.00021	45.71	3.40	0.033	0.30	0.090	2.5	3600
	Test5d	0.0096	0.00021	45.71	3.40	0.033	0.30	0.120	2.5	7500

Table 3–1 Test index

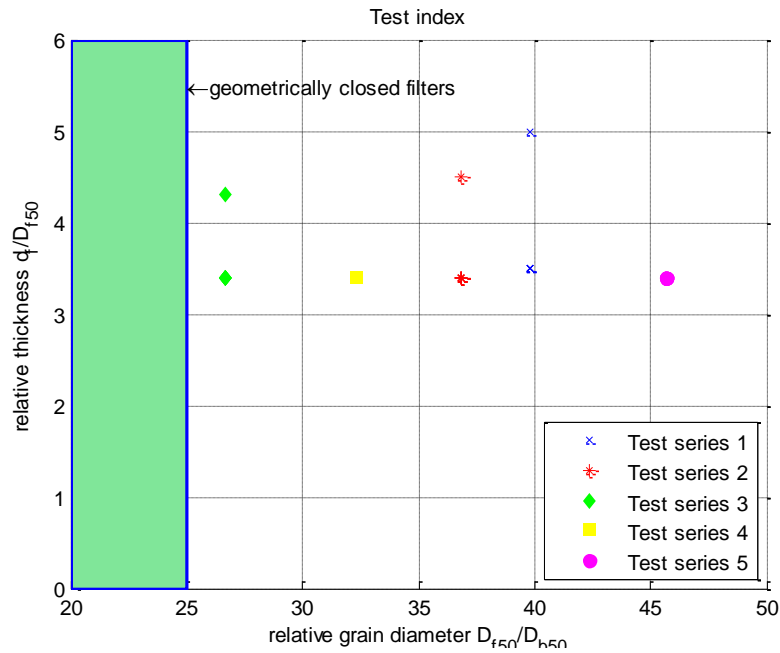


Figure 3-7 Test series plotted in terms of relative grain size D_{f50}/D_{h50} and relative filter thickness d_f/D_{f50} .

Repeatability

Test repeatability is also examined in order to identify the influence of structural inconsistencies or other type of asymmetries. For that reason repetition tests are carried out. In specific the following repetition tests were executed:

- Test1e: Repetition of Test1a
- Test2e: Repetition of Test2a
- Test4d & Test4e: Repetitions of Test4a

Pilot tests

Pilot tests were conducted to accurately determine (tuning) wave loading prior to the execution of real tests. In addition, pilot tests were conducted to investigate filter layer stability under the selected wave loading. Finally, it was attempted to quantify maximum scour depth for the case of no filter protection; however, pilot tests were unsuccessful.

3.3. Measuring equipment & Monitoring

The selection of the measuring equipment is very important for the proper reproduction of the test results; however, it is limited by their availability. For the present study, damage is related to the erosion of the base layer. Apart from that, the temporal evolution of the erosion process is also important; therefore, test execution needs to be monitored. Finally, a precise description of wave loading is a prerequisite in order to associate damage with the filter configuration properties.

Sentiently during every test, the following measurements were conducted along with the monitoring procedure:

- Base layer profile measurements (laser)
- Filter layer profile measurements (laser)
- Water particle velocity measurements at 6cm above filter surface (EMS)
- Water surface elevation offshore and nearshore (wave gauges)
- Side wall video recording during the test (video camera)
- Video recording from below the flume (video camera)
- Inspection photo shots
- Weighing of removed base material after sieving the filter layer (electronic scale)

Wave gauges

Two rows of three wave gauges are placed inside the flume. The offshore row measures the produced wave climate right after the wave paddle and the nearshore row specifies the actual wave climate that attacks the filter configuration and the breakwater. The latter is also capturing the partially reflected waves.

At every row, the second gauge is placed at 0.3m from the first. The distance between the first and the third gauge is 0.7m.

Laser profiler

A laser device is used to profile filter and base layer prior and after the test. The device is measuring with a desired frequency and the outcome is a continuous signal. Furthermore, it is blind for the first 25cm and after that it has a range of 75cm; thus it can measure until a distance of 1m.

Measurements are taken in longitudinal cross sections. The laser device (Figure 3-8) was mounted in a wooden frame. It was able to move in the longitudinal direction by moving manually a pulley. In the transverse direction the whole frame was being displaced every 5cm. The first cross section measurement is taken 5cm of the right side wall and the last 5cm from the left side wall. In between 9 additional cross sections are measured; thus a measurement step of 5cm is used. In total, 11 longitudinal cross sections are profiled.

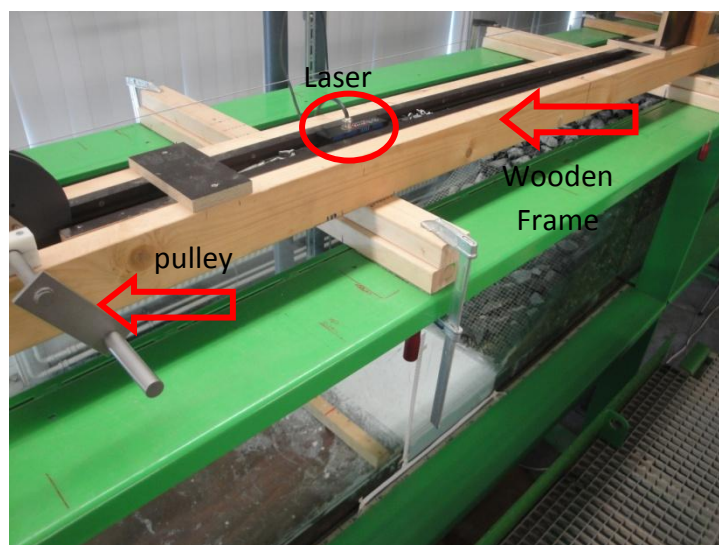


Figure 3-8 Laser and the wooden frame for profile measurements

Electromagnetic flow meter (EMS)

Water particle velocity measurements were conducted via an Electromagnetic Flow Meter (EMS) (Figure 3-9). Velocity measurements are taken based on the induction law of Faraday. Before each test the device was calibrated in order to neutralize the effect of external electromagnetic fields located in the vicinity of the probe.

The device was mounted at 30cm from the flume walls and at the center of the box hosting the base layer. The probe was placed at a distance of 6cm from the filter's surface. Not much disturbance is expected due to the presence of the probe. Finally, measuring frequency was set to be 100Hz.

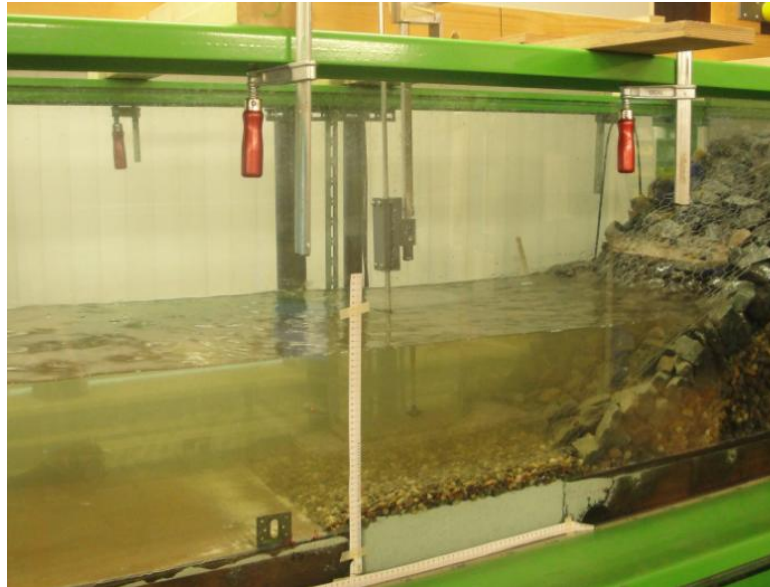


Figure 3-9 EMS probe for particle velocity measurements

Video camera

Two video cameras were used (see Figure 3-2). One was placed next to the right side wall in order to capture through the glass the longitudinal temporal evolution of scour. Additionally, flume's bottom and the shoreward side of the box containing the base material were also made of glass. Thereby, the second camera was placed below the flume pointing towards the glass to capture the temporal evolution of scour in the transverse direction of the flume.

Photo camera

A digital photo camera was used in order to specify filter/base layer damage and damage asymmetry in the transverse direction of the flume. Constructional inconsistencies can cause damage asymmetries like for example the difference of erosion pattern between the two side walls.

Electronic scale

An electronic scale was used to weigh the eroded filter material that was stuck in the voids and the grains of the filter layer as the latter was removed. In between the removed material was dehydrated in an oven for 10hours and at a temperature of 130C°.

3.4. Testing procedure

Absolute reproduction of testing procedure during every test is of significance for the validity of physical model research. Every test was carried out by sequential execution of 11 steps which are described below. The described testing procedure was followed precisely during the conduction of every test.

1. Manual filling of box with base material. Profiling of box to capture base material's initial state.
2. Manual application of filter layer. Profiling of filter to capture initial state of filter layer. Application of wire mesh that prevents filter material erosion.
3. Filling of flume with water until the desired water level.
4. Calibration of wave gauges. Calibration of EMS.
5. Start of test. Switch on video cameras.
6. End of test. Switch off wave generator. Switch off cameras and EMS.
7. Visual inspection of box. Photo shooting of filter layer and filter configuration from side walls.
8. Profiling of filter layer.
9. Removal of filter layer. Visual inspection of base layer. Photo shooting of base layer from side walls.
10. Profiling of base layer.
11. Sieving of removed filter layer. Weighing of removed base material.

Total test duration

Tests were carried out during the period from 1st of July until 15th August 2012.

4. Test results

Chapter 4 is an inventory of results and observations per each of the conducted tests. The total data set is categorized in five test series, with respect to geometrical and material properties of the tested filter configurations. Mainly, are examined three issues; erosion/deposition pattern, its temporal evolution (snapshots through the side glass) and finally, scour pattern over the entire box with special interest into the maximum scour depth.

Table 3–1 presented the input parameters of the study's test program. Tests that belong to each of the test series, have mutual parameters such as the filter grain diameter D_{f50} , base material grain diameter D_{b50} and their corresponding densities ρ_f , ρ_b . Especially for Test series 4 & 5, also filter thickness d_f and relative filter thickness d_f/D_{f50} is mutual along the tests, since the effect of filter thickness deviation was not investigated.

Results are treated separately for each test. Presentation starts with the comparison of the initial and the final state of the filter configuration by apposing the corresponding side glass snapshots. Afterwards, is investigated the temporal evolution and the shaping of base layer erosion.

In Paragraph 3.3 it was mentioned that every test was captured with video cameras; therefore snapshots are extracted from video analysis and digitized to compare the temporal trend of erosion pattern. In general, snapshots are taken every 25 minutes for tests with input $T_p=2.5s$ and every 20min for tests with input $T_p=2.5s$; however for some special cases analysis of the video was not possible. To simplify comparisons and to investigate whether damage at the side glass is representative for the whole flume, the profiled 11 cross-sections (see also Section 3.3) are averaged over the flume's width and the result is plotted along with the curves that represent the temporal evolution of erosion/deposition process through the side glass.

Finally, a contour map is plotted which illustrates the base layer profile after the removal of the filter stones and is used in order to specify the spatial particularities of scour formation. Contour maps are created based on the interpolation of base layer profile measurements at the 11 cross sections (explained in Section 3.3).

The vertical axis of the map coincides with the longitudinal axis of the flume (y-coordinate); thus the horizontal axis coincides with the transversal axis of the flume (x-coordinate). The breakwater is situated at the upper part of the map. In addition, the first 4cm from the offshore side of the box and the last 2cm from the side in front of the breakwater were excluded from the analysis to mitigate model effects caused by the transitional area; therefore they are not illustrated into the map.

For most of the tests input targets were accomplished; however, for the remaining cases it was not possible. Fortunately, for some of them the deviation was common for all tests (i.e. target T_p was 2.5sec but in tests was found to be 2.485s) simplifying the comparison process. On the other hand, these deviations are important because they can provide explanations in

questions that would be raised during the analysis; thus they need to be incorporated into the analysis.

4.1. Test series 1

Test series 1 consists of 5 tests; Test1a, Test1b, Test1c, Test1d & Test1e. In test series 1, the coarser filter layer (Filter 1, $D_{f50}=1.43\text{cm}$) was combined with the coarser base material ($D_{b50}=360\mu\text{m}$) to form the filter configuration. The pursuit behind the execution of Test series 1 was to investigate the effect of using a filter layer with wider gradation. Thereby a wider grading namely $D_{f85}/D_{f15}=2.11$ was applied to the filter which according CUR *et al.* [2007] belongs to wide graded filters. Table 4–1 summarizes the common test parameters between tests of Test series 1.

Test Series	D_{f50} cm	D_{b50} μm	D_{f50}/D_{b50} -	ρ_{filter} kg/m^3	ρ_{base} kg/m^3	D_{f85}/D_{f15} -
1	1.43	360	39.83	2640	1500	2.11

Table 4–1 General test parameters of Test series 1

4.1.1. Test1a

Test parameters of Test1a are presented in Table 4–2. The target input significant wave height was successfully reached in contrast to the design peak period.

Test	N_m -	D_{f50} cm	D_{b50} μm	D_{f50}/D_{b50} -	d_f/D_{f50} -	d_f m	D_{f85}/D_{f15} -	Target WC	T_p s	H_s m
Test1a	3686	1.43	360	39.83	3.50	0.050	2.11	WC1	2.485	0.120

Table 4–2 Test parameters of Test1a

Side glass snapshot comparison at $t=0\text{min}$ and $t=125\text{min}$ revealed an S-curve erosion pattern of the base layer. Filter layer was able to follow the erosion/deposition formation of base layer; thus settled in the scour hole and uplifted at the offshore side of the box (Figure 4-1).



Figure 4-1 Test1a after 0 minutes (left) and after 125 minutes (right).

Based on the temporal evolution of erosion/deposition pattern, the scour hole formation seems to expand in size. After an abrupt increase of erosion depth, it seems to slow down, in contrast to the length of the hole which expands from the middle of the box towards the side in front of the breakwater. On the contrary, the deposition part arrived in equilibrium after 50min of testing. No further increase of bar height or length was observed later in the test.

In terms of maximum scour depth, the average cross section (black line) and the final profile (magenta line, after 125min) are not in agreement. Their shape is similar; however the damage observed through the glass is not representative. Scour depth at the side of the box in front of the breakwater is nearly zero; thus it is not threatening the stability of the breakwater. However, the lateral expansion of scour hole should not be omitted.

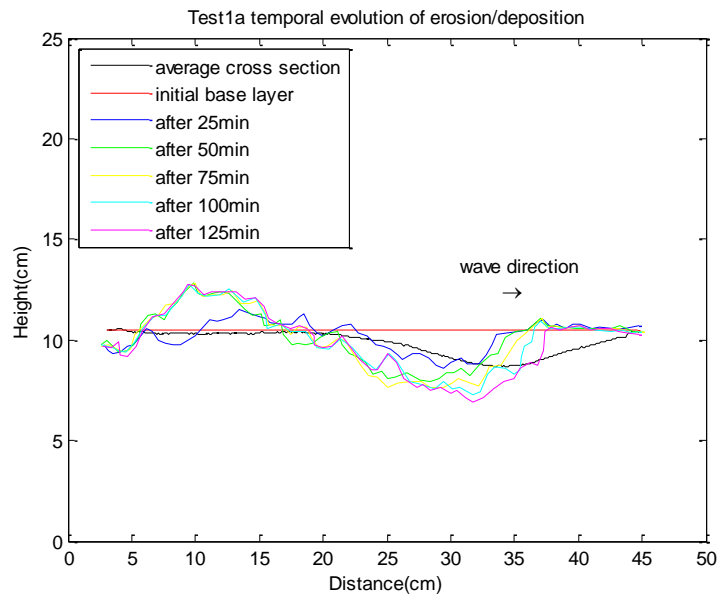


Figure 4-2 Temporal evolution of erosion of Test1a

Scour formation extends almost over the full width of the flume. In the longitudinal direction it seems to be symmetrical with two maximum depths near each of the flume's side glasses. Maximum depth is smaller than 2.5cm.

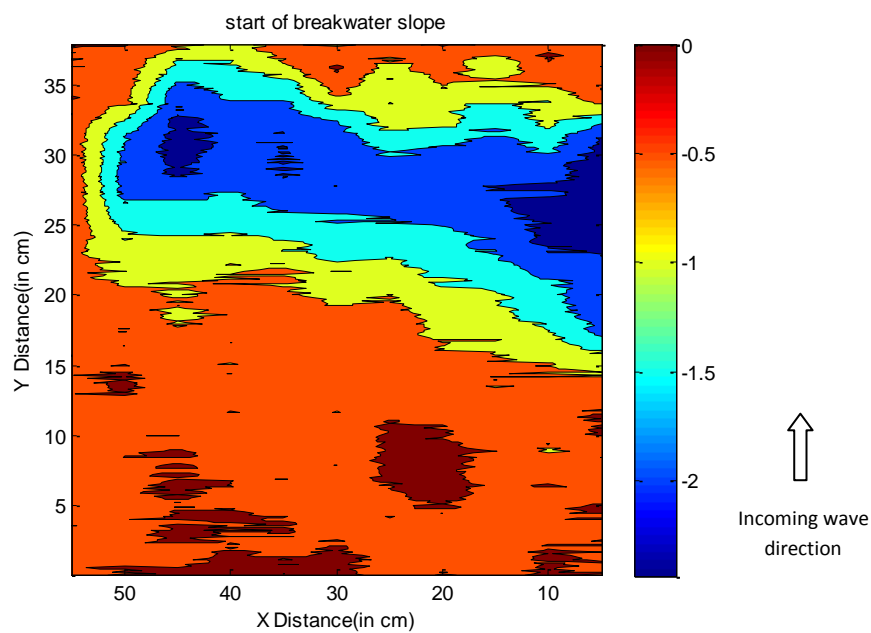


Figure 4-3 Contour map of erosion of Test1a

4.1.2. Test1b

Total test duration of Test1b was 100min. Likewise to Test1a, target significant wave height was accomplished and target peak period showed a slight deviation. Table 4–3 displays the corresponding test parameters.

Test	N_m	D_{f50} cm	D_{b50} μm	D_{f50}/D_{b50}	d_f/D_{f50}	d_f m	D_{f85}/D_{f15}	Target WC	T_p s	H_s m
Test1b	3699	1.43	360	39.83	3.50	0.050	2.11	WC2	2.032	0.120

Table 4–3 Test parameters of Test1b

Erosion/deposition profile was S-shaped but with less discrete characteristics. The most distinctive characteristic is the symmetry between the erosion and deposition area (Figure 4-4).

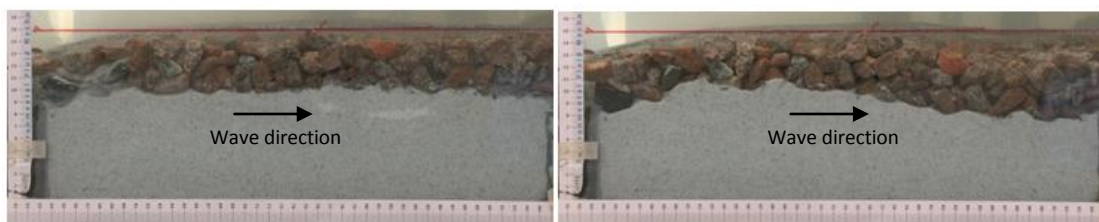


Figure 4-4 Test1b after 0 minutes (left) and after 100 minutes (right)

However, the temporal evolution of erosion/deposition pattern through the side glass has shown that the base layer has reached equilibrium after 80min (Figure 4-5). In addition, final profile (magenta line) and average cross section (black line) are well in agreement. Scour depth next to the breakwater is significant; thus it is a threat to its stability.

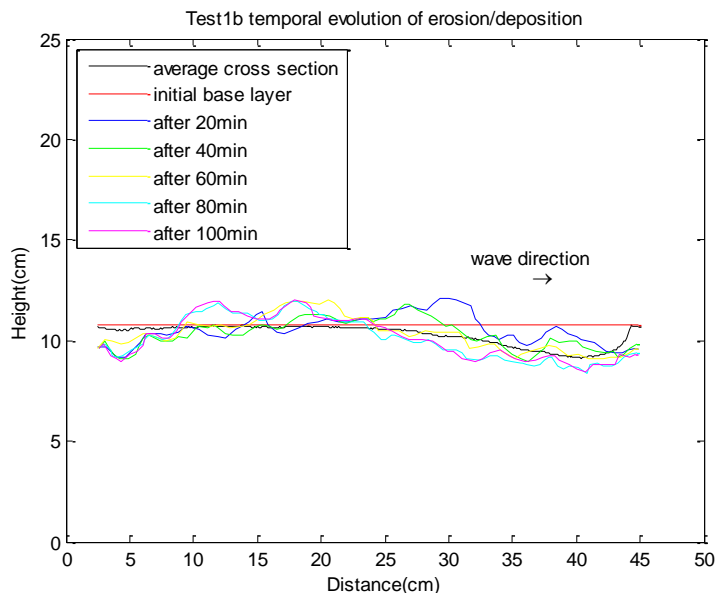


Figure 4-5 Temporal evolution of erosion of Test1b

From Figure 4-6 it can be seen that there is spatial deviation of scour depth. Highest amounts of scour are gathered near the flume's glasses while in the middle scour depth is halved. In addition, scour is not symmetrical with respect to any axis.

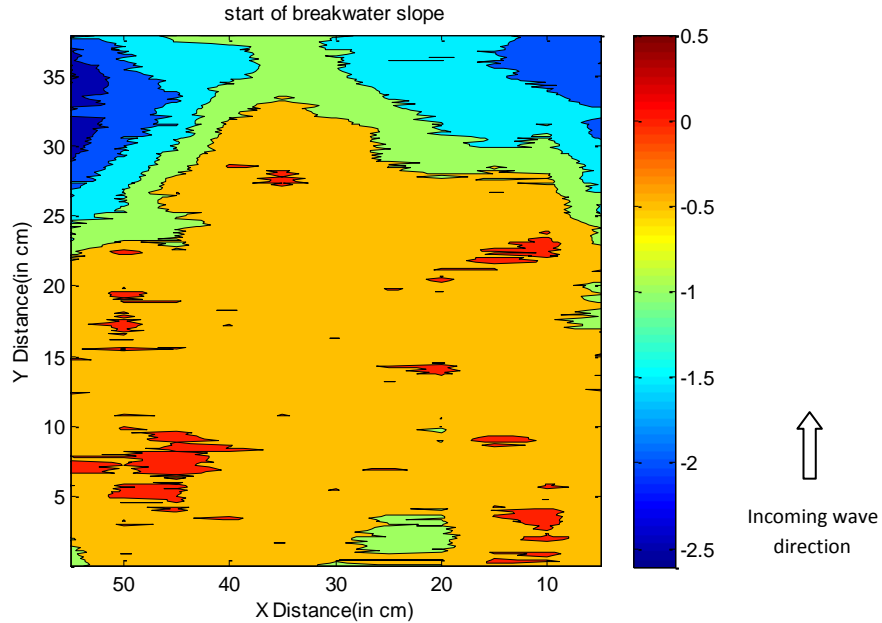


Figure 4-6 Contour map of erosion of Test1b

4.1.3. Test1c

Table 4–4 summarizes the input parameters of Test1c. This test was found to have the highest value of reflection coefficient between the tests of Test series 1. Nevertheless, the measured root mean square velocity was smaller than Test1a & Test1b. The weight of removed base material is on the same order as the previously mentioned tests.

Test	N_m	D_{f50} cm	D_{b50} μm	D_{f50}/D_{b50}	d_f/D_{f50}	d_f m	D_{f85}/D_{f15}	Target WC	T_p s	H_s m
Test1c	3676	1.43	360	39.83	3.50	0.050	2.11	WC3	2.485	0.101

Table 4–4 Test parameters of Test1c

Erosion/deposition pattern as seen from the right side glass is not very clear. A scour hole is formed at the middle of the box and towards the offshore side of the box. However, the depth of the hole is less than 1.5cm (Figure 4-7).



Figure 4-7 Test1c after 0 minutes (left) and after 125 minutes (right)

Figure 4-8 displays the evolution of scour formation. No deposition pattern is observed. In addition, the erosion pattern has reached equilibrium state at around 75min. Changes with respect to time still occur, however they do not affect the dimensions of scour hole.

Despite its small magnitude, scour depth next to the breakwater slope is not zero; thus it can cause structure instability. Final profile (magenta line) and average cross section (black line) agree well in terms of maximum scour depth; however their shape is completely different.

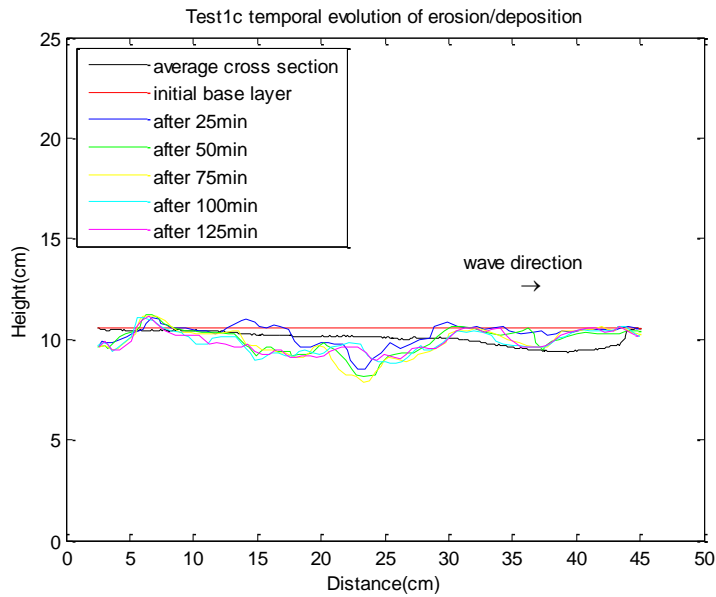


Figure 4-8 Temporal evolution of erosion of Test1c

On the other hand, Figure 4-9 illustrates a substantial asymmetry on scour formation between the two sides of the flume. Thereby, two scour holes are formed next to the left side glass and right in front of the breakwater toe. Indeed, the scour depth exceeds 2cm.

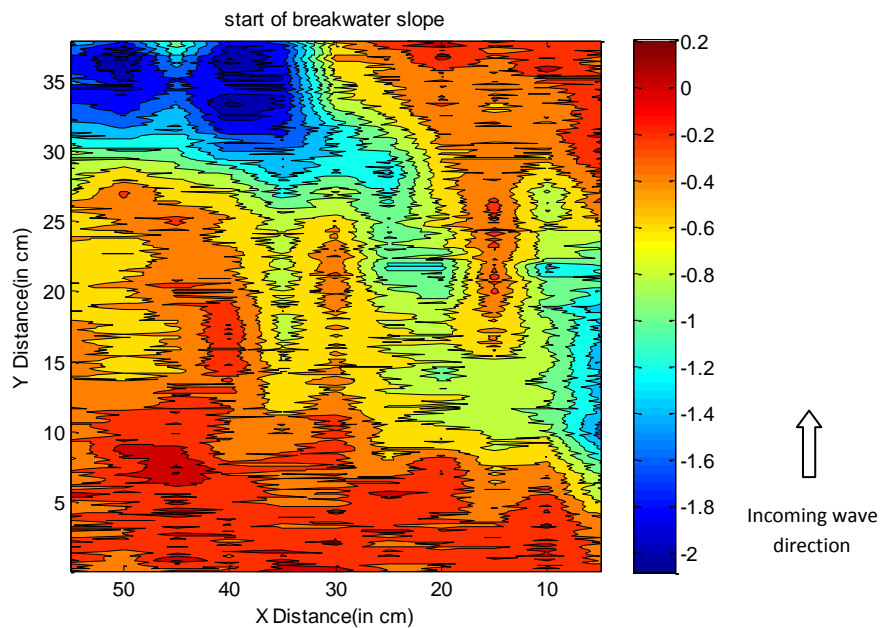


Figure 4-9 Contour map of erosion of Test1c

4.1.4. Test1d

In Test1d a thicker filter was used ($d_f/D_{f50}=5$ instead of 3.50) and loaded with the same deep water wave conditions as Test1a. However, apart from the target peak period also the target significant wave height was not reached. The measured significant wave height in front of the toe of the breakwater was 0.115cm (Table 4–5).

Test	N_m	D_{f50} cm	D_{b50} μm	D_{f50}/D_{b50}	d_f/D_{f50}	d_f m	D_{f85}/D_{f15}	Target WC	T_p s	H_s m
Test1d	3738	1.43	360	39.83	5.00	0.072	2.11	WC1	2.485	0.115

Table 4-5 Test parameters of Test1d

In Figure 4-10 the S-curve of the erosion/deposition profile is clearly visible. The deposition is smaller and lower in magnitude than the erosion. Filter layer follows the erosion/deposition pattern and suffers a significant settlement just in front of the breakwater.

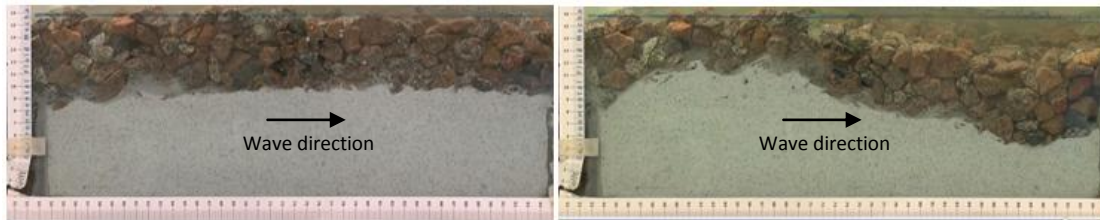


Figure 4-10 Test1d after 0 minutes (left) and after 125 minutes (right)

The formed scour hole increases abruptly at the first minutes of the test but slows down after 50min and it reaches equilibrium after 100min. The same holds for the deposition area (Figure 4-11).

Erosion patterns from the final profile (magenta line) and from the average cross section (black line) are well in-agreement; however observation of damage through the side glass overestimates the actual damage. Additionally, scour hole is formed right in front of the breakwater and thus it is a major danger to its stability.

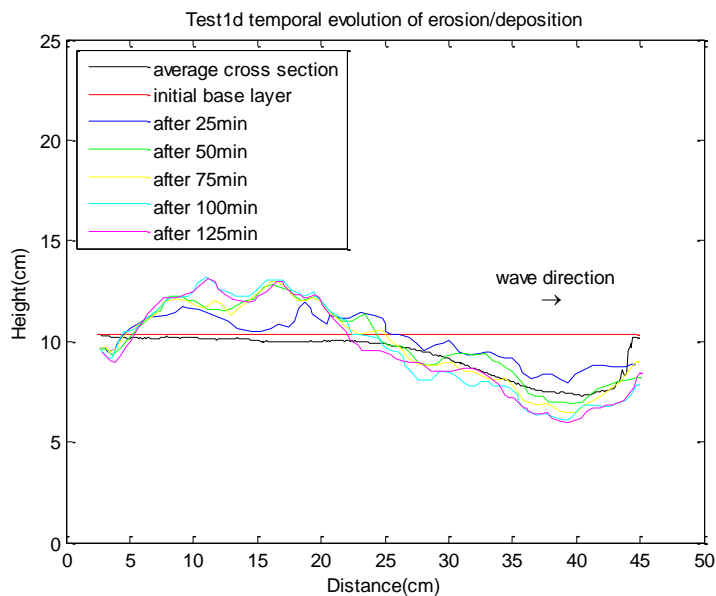


Figure 4-11 Temporal evolution of erosion of Test1d

In general the scour formation is uniform across the width of the flume. Maximum depth is larger at the right side glass (3.5cm); however the difference in magnitude is small (0.5cm) (Figure 4-12).

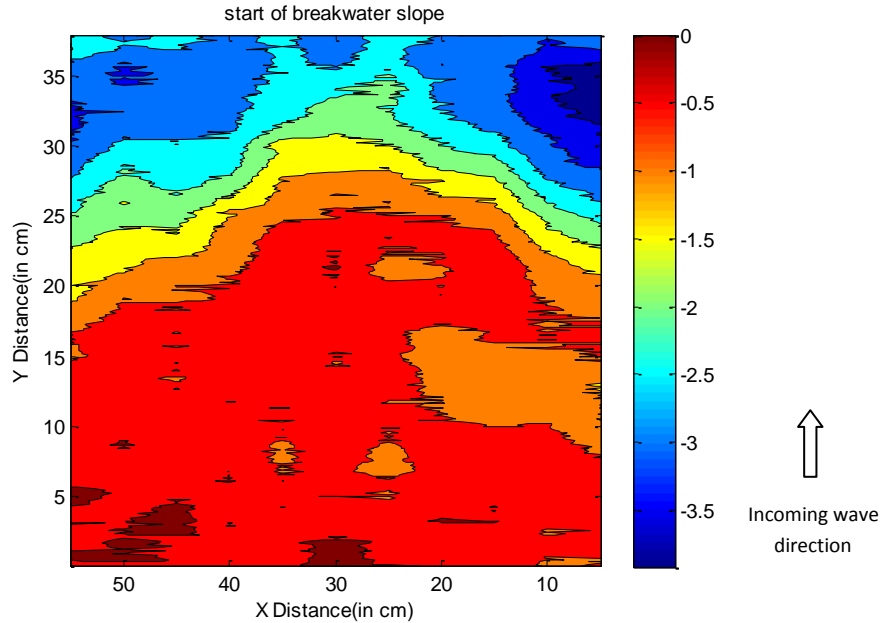


Figure 4-12 Contour map of erosion of Test1d

4.1.5. Test1e

Test1e is a repetition test of Test1a. Test conditions have been repeated successfully and only imperceptible deviations occur. The main difference is the larger weight of removed base material which was found 0.85kg (Test1a $W_{rep}=0.686\text{kg}$). Indeed, after the test a great amount of material was found lying on the foreshore. Table 4–6 summarizes the test parameters of Test1e.

Test	N_m	D_{f50} cm	D_{b50} μm	D_{f50}/D_{b50}	d_f/D_{f50}	d_f m	D_{f85}/D_{f15}	Target WC	T_p s	H_s m
Test1e	3908	1.43	360	39.83	3.50	0.050	2.11	WC1	2.485	0.119

Table 4–6 Test parameters of Test1e

An S-curve pattern also appeared in the right side glass. The erosion area starts immediately at the breakwater side of the box while a small bar arises at the middle of the box. Nevertheless, it is limited since a smaller and narrower scour hole is formed right after it at the offshore side of the box.

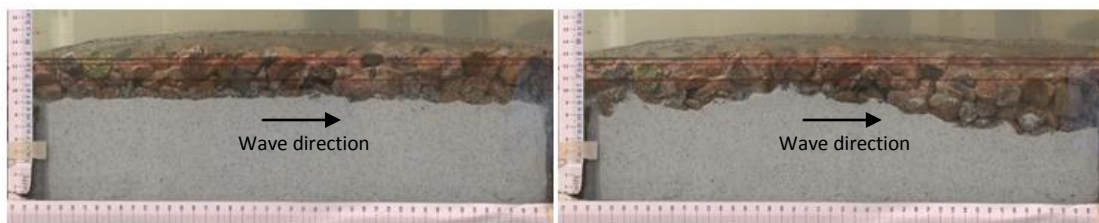


Figure 4-13 Test1e after 0 minutes (left) and after 125 minutes (right)

Erosion rate starts slowly and accelerates after the first 25min. Finally it arrives in equilibrium after 100min. The maximum scour depth near the glass is around 3cm.

Damage observed through the side glass is exaggerated with respect to the rest of the flume. However, erosion patterns from the final profile (magenta line) and from the average

cross section (black line) are well in-agreement. Additionally, scour hole is formed right in front of the breakwater and thus it is a major danger to its stability.

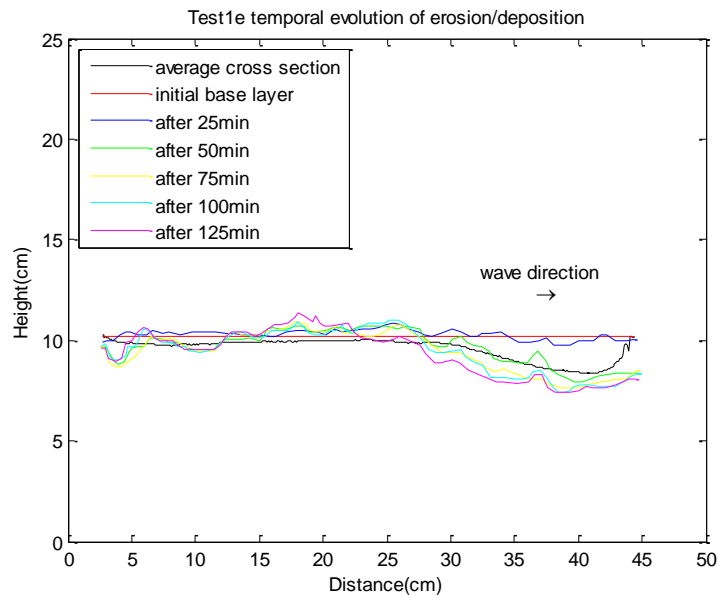


Figure 4-14 Temporal evolution of erosion of Test1e

However, the erosion pattern over the flume's width is highly asymmetrical. Scour formation is uniform at the right half of the flume with a depth in the order of 3cm and then increases to a maximum of 3.5cm in the middle. Finally, the left half of the flume remained intact with a maximum scour depth that is less than 0.7cm (Figure 4-15).

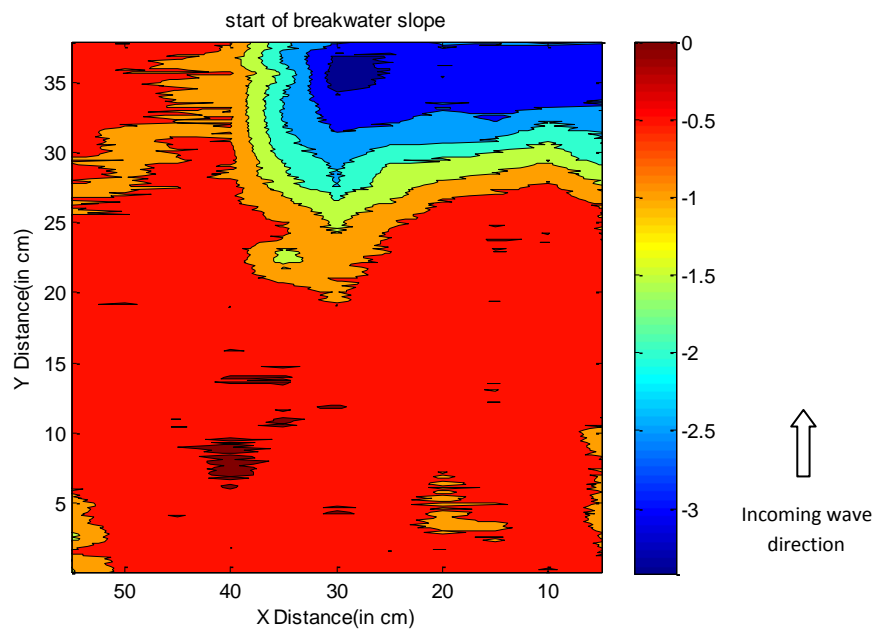


Figure 4-15 Contour map of erosion of Test1e

4.2. Test series 2

Test series 2 consists of six tests; namely Test2a, Test2b, Test2c, Test2d, Test2e & Test2f. For this group of tests, a filter grain diameter was used that is close to the corresponding diameter of Test series 1 but with a narrower grading. Consequently, a new dimensionless grain diameter is formed which is different than the existing of Test series 1 but is close so that it allows comparisons with respect to filter gradation. Furthermore, thickness variation was also tested by applying larger relative thickness in Test2d. Finally, Test2f is a long duration test conducted to investigate the effect of loading duration.

Figure 4-16 presents the test parameters of Test series 2.

Test Series	D_{f50} cm	D_{b50} μm	D_{f50}/D_{b50} -	ρ_{filter} kg/m^3	ρ_{base} kg/m^3	D_{f85}/D_{f15} -
2	1.33	360	36.81	2650	1500	1.48

Figure 4-16 Test parameters of Test series 2

4.2.1. Test2a

In Test2a the succeeded significant wave height was lower than the target. Target peak period is also lower; however it is equal to the corresponding tests of Test series 1. Additionally, apart from filter sieving, removed material was also picked up from the foreshore.

Test	N_m -	D_{f50} cm	D_{b50} μm	D_{f50}/D_{b50} -	d_f/D_{f50} -	d_f m	D_{f85}/D_{f15} -	Target WC	T_p s	H_s m
Test2a	3751	1.33	360	36.81	3.40	0.045	1.48	WC1	2.485	0.117

Table 4-7 Test parameters of Test2a

The shaped S-curve is characterized by a wide and thin depositional area and a deep and wide scour hole. Indeed, the latter is formed just in front of the breakwater and therefore threatens its stability (Figure 4-17).

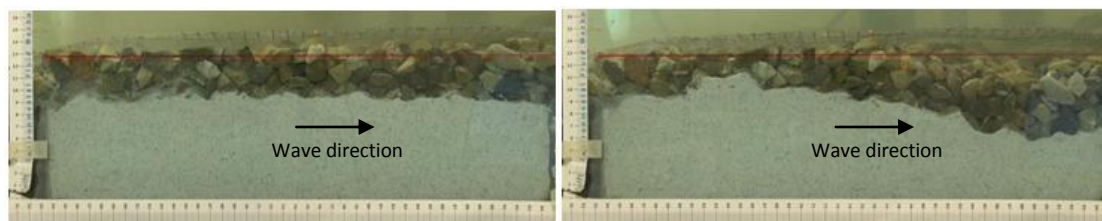


Figure 4-17 Test2a after 0 minutes (left) and after 125 minutes (right)

On the other hand, both the parts of the S-curve have arrived into equilibrium after around 75-100min. The maximum scour depth near the right side glass approximates 3.2cm.

Erosion patterns from the final profile (magenta line) and from the average cross section (black line) are well in-agreement in both shape and magnitude. Additionally, scour hole is formed right in front of the breakwater and thus it is a major danger to its stability.

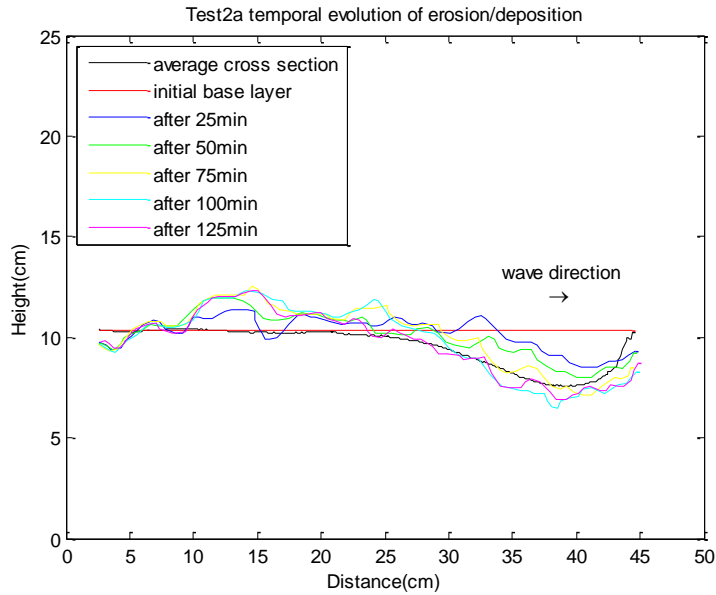


Figure 4-18 Temporal evolution of erosion of Test2a

Additionally, scour formation covers the full width of the flume. Despite that is not uniform in magnitude, it can be characterized as symmetrical over the width. At the left side glass maximum depth reaches 3.5cm while at the middle it is limited.

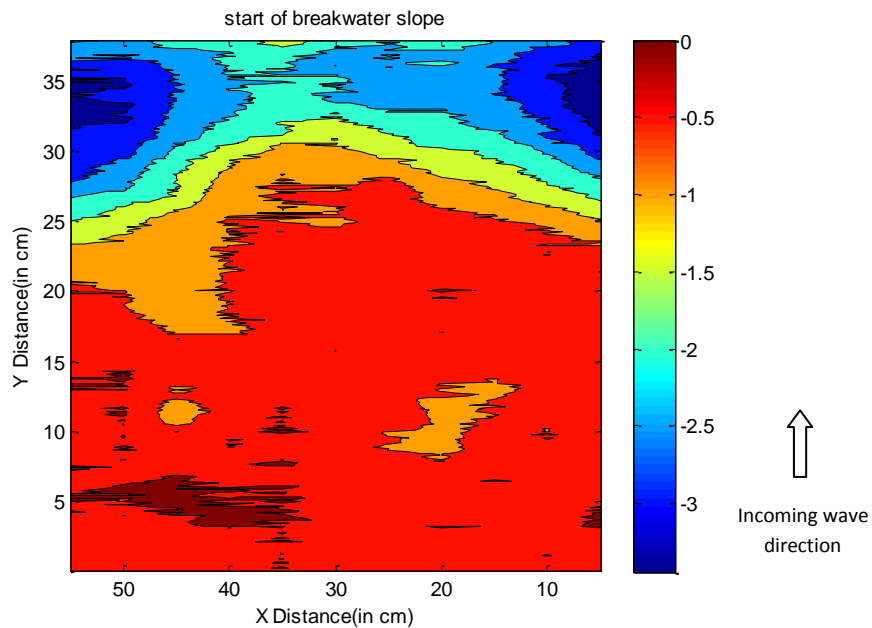


Figure 4-19 Contour map of erosion of Test2a

4.2.2. Test2b

Table 4–8 summarizes the test parameters of Test2b. For this test, shorter waves are attacking the structure with $H_s=0.119\text{m}$ and $T_p=2.032\text{s}$. The total test duration is 100min.

Test	N_m	D_{f50} cm	D_{b50} μm	D_{f50}/D_{b50}	d_f/D_{f50}	d_f m	D_{f85}/D_{f15}	Target WC	T_p s	H_s m
Test2b	3636	1.33	360	36.81	3.40	0.045	1.48	WC2	2.032	0.119

Table 4–8 Test parameters of Test2b

After the execution of the test an S-curve erosion/deposition pattern was formed at the right side glass. Pattern characteristics were rather weak with limited depth/height and narrow width. Concerning the breakwater stability, base layer was eroded at the side of the box next to the breakwater (Figure 4-20).

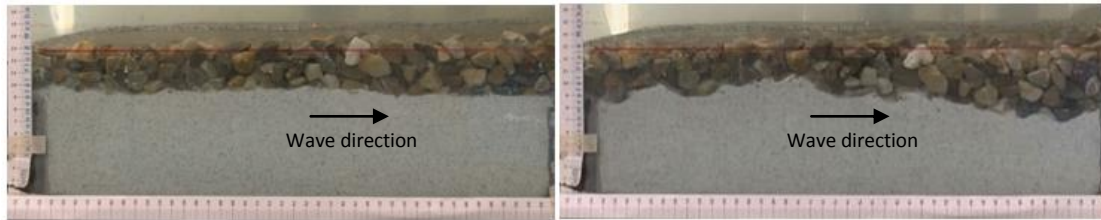


Figure 4-20 Test2b after 0 minutes (left) and after 100 minutes (right)

Figure 4-21 presents the temporal evolution of erosion/deposition pattern for Test1b. It can be seen that after the first 20min the bar has reached equilibrium. The corresponding time interval for erosion pattern was 80min. The erosion area still changes shape, however maximum erosion depth stays unchanged and less than 2cm.

In addition, final profile (magenta line) and average cross section (black line) agree well in shape but not in magnitude. The averaged maximum scour depth is half the maximum scour depth observed through the side glass. Finally, scour depth next to the breakwater is significant; thus it is a threat to its stability.

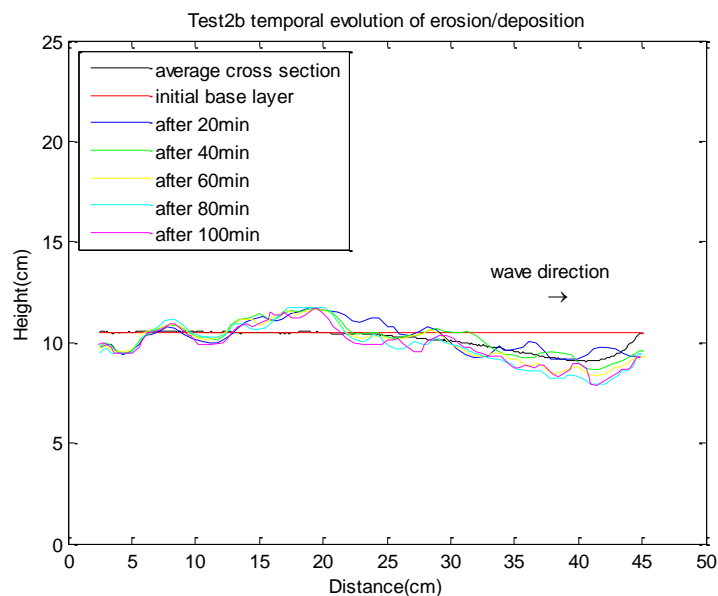


Figure 4-21 Temporal evolution of erosion of Test2b

The same pattern was also observed on the left side glass. On the contrary, at the center of the flume the maximum scour depth was 30-50% less than the sides. Figure 4-22 verifies the aforementioned.

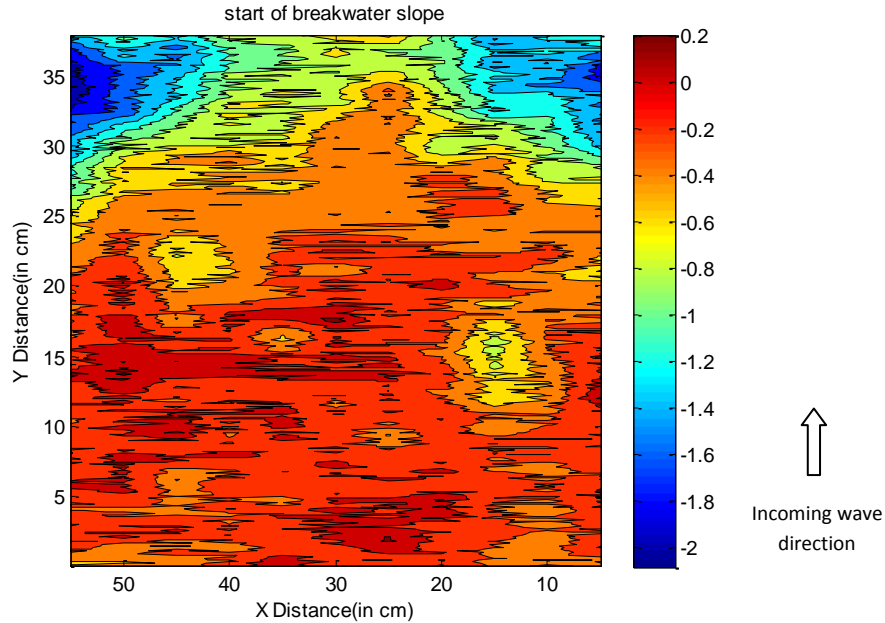


Figure 4-22 Contour map of erosion of Test2b

4.2.3. Test2c

Likewise to Test1c, Test2c displayed the highest reflection coefficient. However, the weight of the removed base material and the measured root mean square velocity was lower than the rest of the tests of Test series 2. Besides, significant amount of base material was found on the foreshore. Table 4–9 summarizes the test parameters of Test2c.

Test	N_m -	D_{f50} cm	D_{b50} μm	D_{f50}/D_{b50} -	d_f/D_{f50} -	d_f m	D_{f85}/D_{f15} -	Target WC	T_p s	H_s m
Test2c	3675	1.33	360	36.81	3.40	0.045	1.48	WC3	2.485	0.097

Table 4–9 Test parameters of Test2c

Despite the lower velocity magnitude a wide and deep scour hole was formed right in front of the breakwater. With respect to Figure 4-23 no bar was formed at the right side glass.

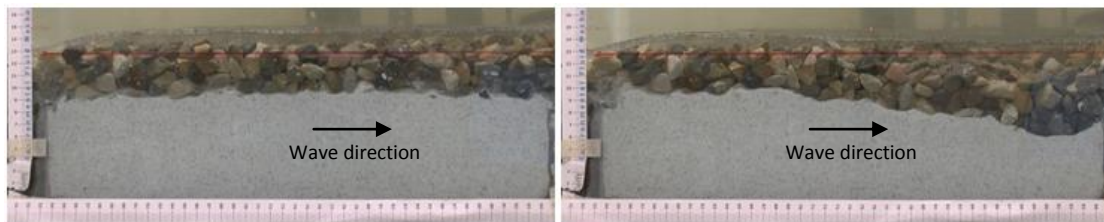


Figure 4-23 Test2c after 0 minutes (left) and after 125 minutes (right)

The erosion rate proceeded steadily and rapidly until the first 75minutes. Afterwards, erosion process was slowed down but seems not to have reached equilibrium until the end of the test. In between the 100th and the 125th minute, maximum scour depth had increased less than the other time intervals, but significantly to assume that erosion process was still active.

Shape of erosion patterns from the final profile (magenta line) and from the average cross section (black line) is well in-agreement. The averaged maximum scour depth is smaller than

the maximum scour depth observed through the side glass; nevertheless the difference is trivial. In addition, scour depth in front of the breakwater is not zero; thus it is threatening breakwater stability.

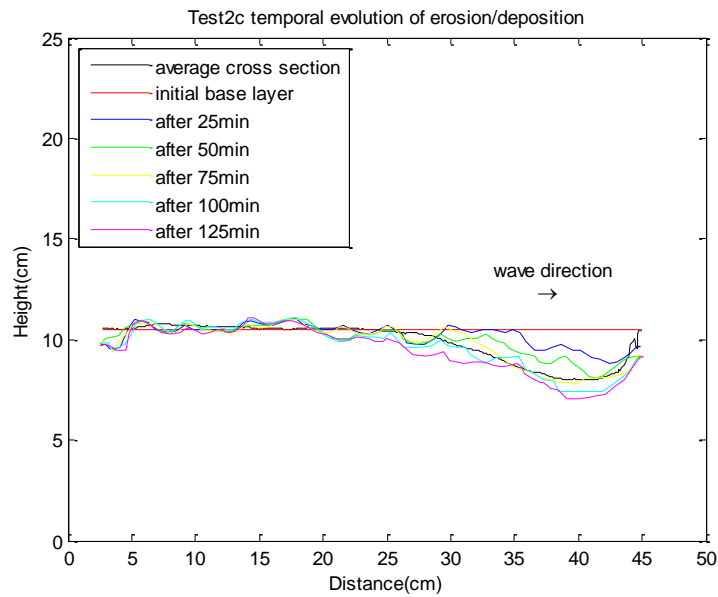


Figure 4-24 Temporal evolution of erosion of Test2c

Furthermore, erosion was uniformly distributed over the entire width of the flume. Maximum scour depth was measured 2.9cm next to the right side glass. Finally, the length of the scour hole was approximately 7cm.

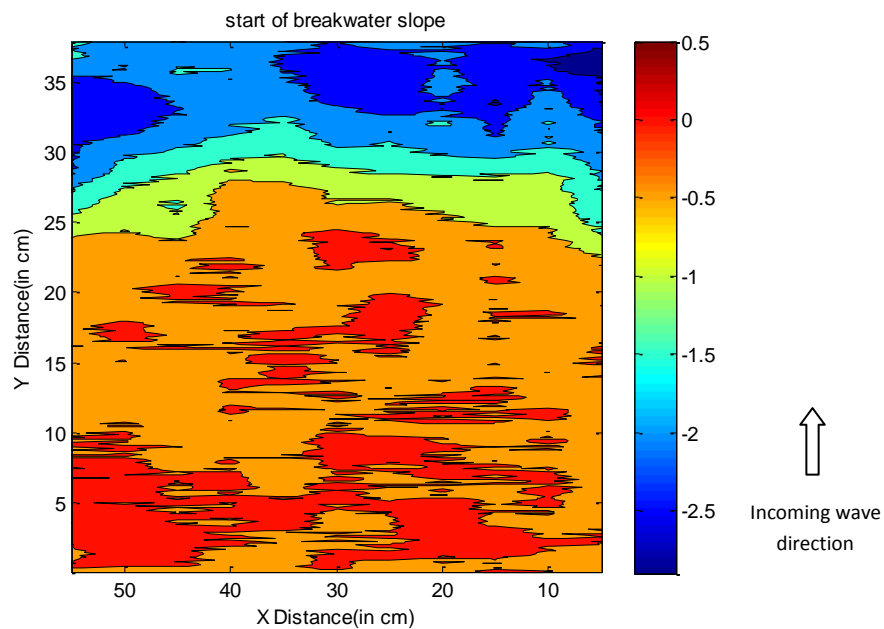


Figure 4-25 Contour map of erosion of Test2c

4.2.4. Test2d

Test2d was similar to Test2a but with a larger relative thickness $d_f=4.25$ (instead of $d_f=3.15$). The peak period was also similar, however the accomplished significant wave height was

found to be slightly smaller ($H_s=115\text{cm}$). On the contrary, the measured velocity and the removed base material were larger than Test2a (Table 4–10).

Test	N_m	D_{f50} cm	D_{b50} μm	D_{f50}/D_{b50}	d_f/D_{f50}	d_f m	D_{f85}/D_{f15}	Target WC	T_p s	H_s m
Test2d	3737	1.33	360	36.81	4.50	0.060	1.48	WC1	2.485	0.115

Table 4–10 Test parameters of Test2d

In Figure 4-26, the formation of an S-curve erosion/deposition pattern is clearly visible at the right side glass. The material that is eroded at the breakwater side of the box is transported towards the offshore side of the box. The deposition area is large in magnitude but still smaller than the erosion area.



Figure 4-26 Test2d after 0 minutes (left) and after 125 minutes (right)

Based on Figure 4-27, bar (deposition area) had already arrived in equilibrium after 50min of testing. For the erosion part, the case is not very clear. On the one hand, the maximum scour depth was reached after 100min and after that no further increase was observed. On the other hand, the scour hole expands towards the offshore side of the box.

Erosion patterns from the final profile (magenta line) and from the average cross section (black line) are identical, in both shape and magnitude. Furthermore, scour depth in front of the breakwater is not zero; thus it is threatening breakwater stability.

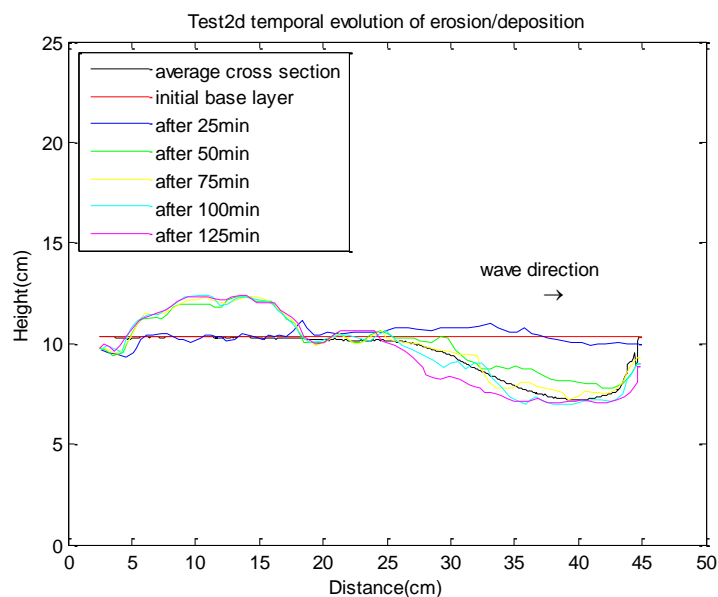


Figure 4-27 Temporal evolution of erosion of Test2d

Maximum scour depth has reached 3.89 at 10cm from the right glass, 2.49 at the middle of the flume and 2.92 at 10cm from the left glass. In general, the scour hole extended in the entire flume width until a distance of approximately 10cm from the breakwater.

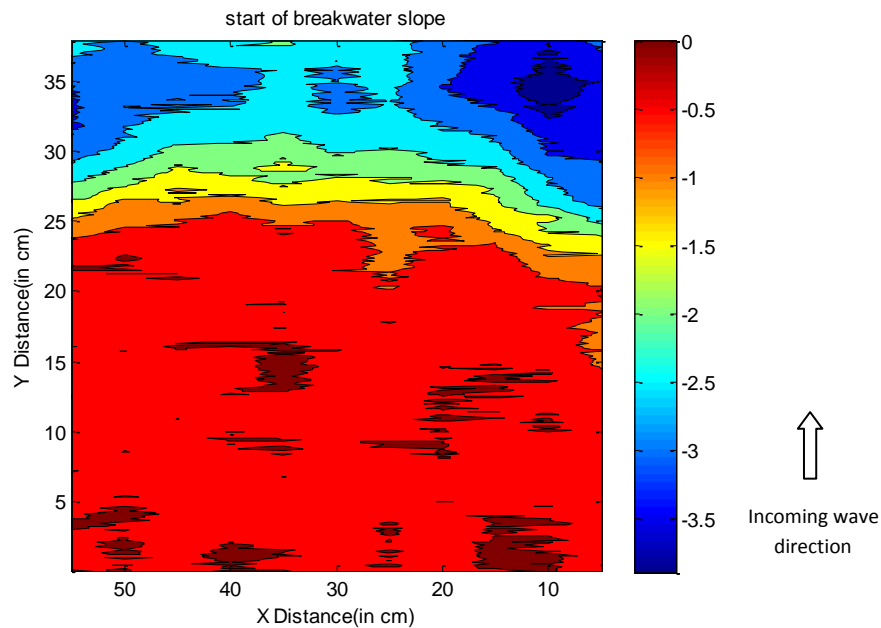


Figure 4-28 Contour map of erosion of Test2d

4.2.5. Test2e

Test parameters of Test2a were successfully reproduced in Test2e. In general, there is significant convergence between the test parameters of the two tests, apart from a slight divergence in the measured velocities. In addition, a great amount of material was picked up from the foreshore.

Test	N_m	D_{f50} cm	D_{b50} μm	D_{f50}/D_{b50}	d_f/D_{f50}	d_f m	D_{f85}/D_{f15}	Target WC	T_p s	H_s m
Test2e	3748	1.33	360	36.81	3.40	0.045	1.48	WC1	2.485	0.116

Table 4-11 Test parameters of Test2e

Analogous to Test2a, the erosion/deposition profile of Test2e was S-shaped but with flatter depositional part and slightly shallower erosion part.

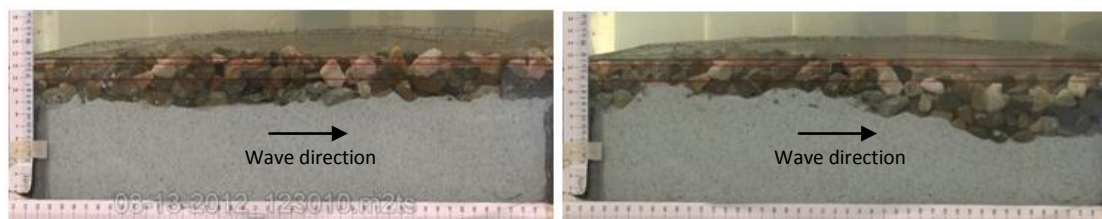


Figure 4-29 Test2e after 0 minutes (left) and after 125 minutes (right)

Monitoring of scour/deposition temporal evolution was interrupted and a gap occurs between the first 16min of testing until the 100th minute. Despite the lack of date, it can be seen that the maximum bar height has been reached although scour formation continues to

evolve. Nevertheless, the measure maximum scour depth was 1.5mm smaller than the corresponding maximum scour depth extracted from Test2d.

Erosion patterns from the final profile (magenta line) and from the average cross section (black line) are well in agreement in both shape and magnitude. Furthermore, scour hole is formed right in front of the breakwater; thus it is a threat to breakwater stability.

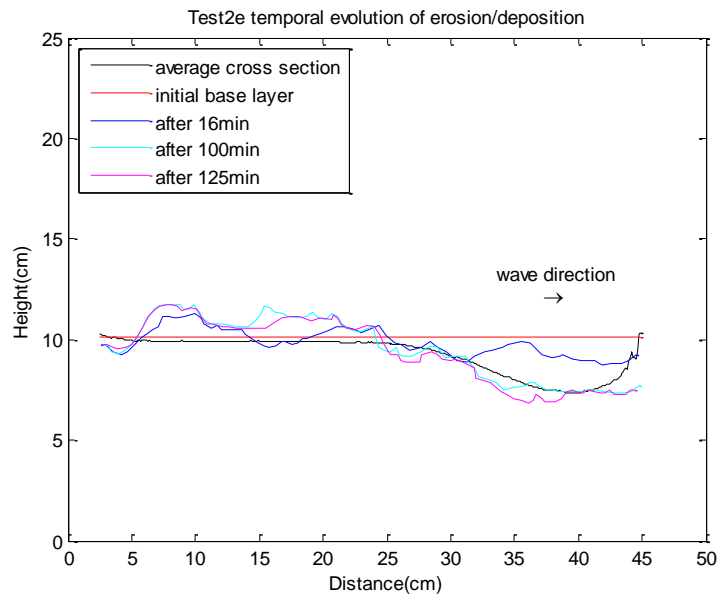


Figure 4-30 Temporal evolution of erosion of Test2e

In particular, the maximum scour depth at the right glass was found 3.32 (at 5cm from the glass), 2.63 at the middle of the flume and 2.96 at 10cm from the left glass. Furthermore, the general erosion pattern in front of the breakwater displayed equivalent characteristics to the case of Test2a.

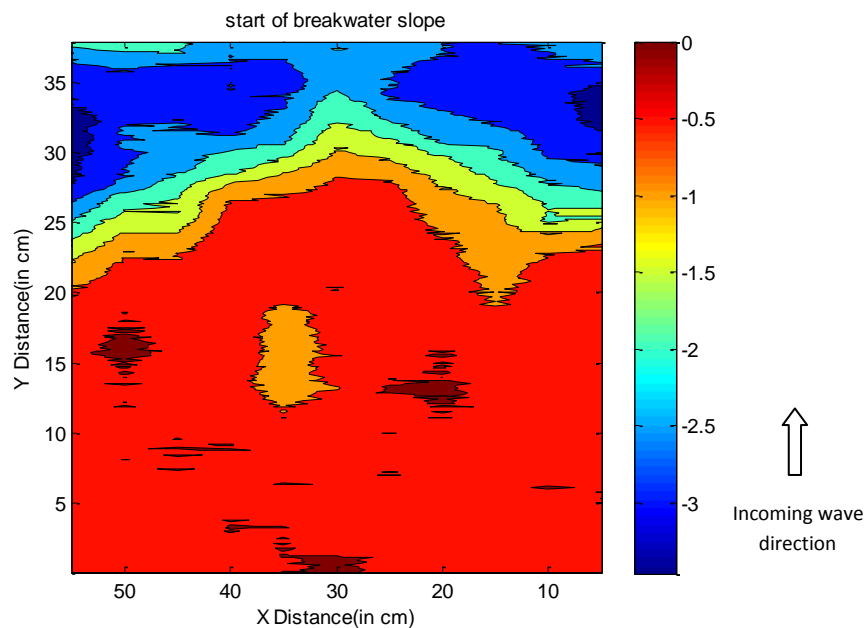


Figure 4-31 Contour map of erosion of Test2e

4.2.6. Test2f

Test2f was carried out in order to get insight on the long term development of erosion/deposition pattern. 7500 waves had attacked the structure and the total test duration was nearly 220min. A substantial amount of base material was picked up from the foreshore; the total weight of the removed material was $W_{rem}=2.194\text{kg}$. Besides, the remaining test parameters were similar to Test2a & Test2e. Table 4–12 provides the test parameters of Test2f.

Test	N_m	D_{f50}	D_{b50}	D_{f50}/D_{b50}	d_f/D_{f50}	d_f	D_{f85}/D_{f15}	Target WC	T_p	H_s
	-	cm	μm	-	-	m	-		s	m
Test2f	7502	1.33	360	36.81	3.40	0.045	1.48	WC1	2.485	0.118

Table 4–12 Test parameters of Test2f

The inspection of erosion/deposition pattern showed a reinforced erosion part and a flat bar. The S-curve pattern was maintained however, the erosion part prevailed clearly.

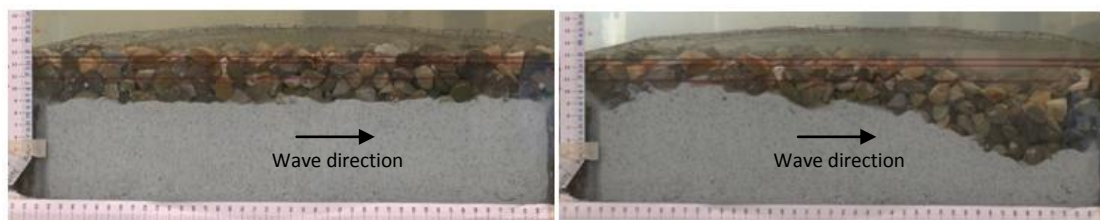


Figure 4-32 Test2f after 0 minutes (left) and after 218 minutes (right)

From Figure 4-33 it can be concluded that the maximum scour depth increased with slower pace after the 150th minute of the test. Temporarily, It seemed to have reached a maximum depth ($t=150\text{min}$) but 25min after it increased again. Scour hole has reached its maximum length after 175min of testing. The deposition area had arrived into equilibrium prior than 150min of testing.

The averaged maximum scour depth is smaller than the maximum scour depth observed through the side glass; nevertheless the difference is of minor importance. The shape of erosion patterns from the final profile (magenta line) and from the average cross section (black line) is well in-agreement. In addition, scour depth in front of the breakwater is not zero; thus it is threatening breakwater stability.

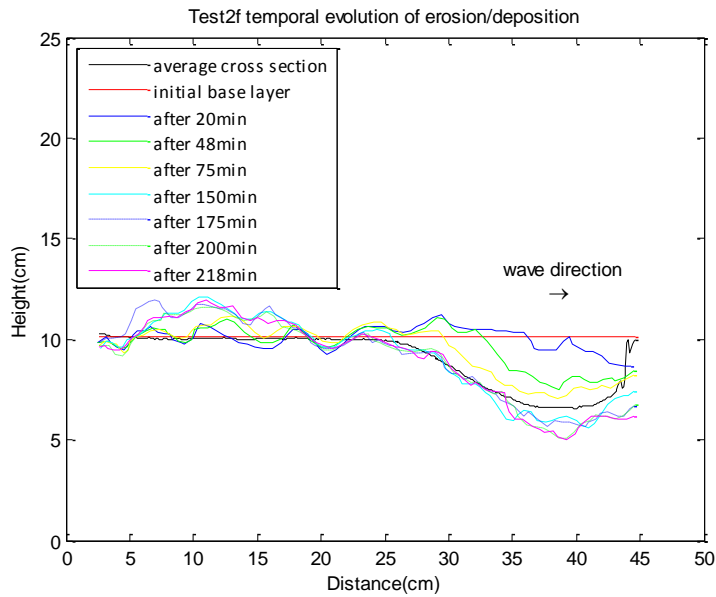


Figure 4-33 Temporal evolution of erosion of Test2f

The maximum scour depth was found 4.41cm at a distance of 5cm from the right side glass. In general, scour formation was uniform covering the entire width of the flume but with a decreasing magnitude from right to left (Figure 4-34).

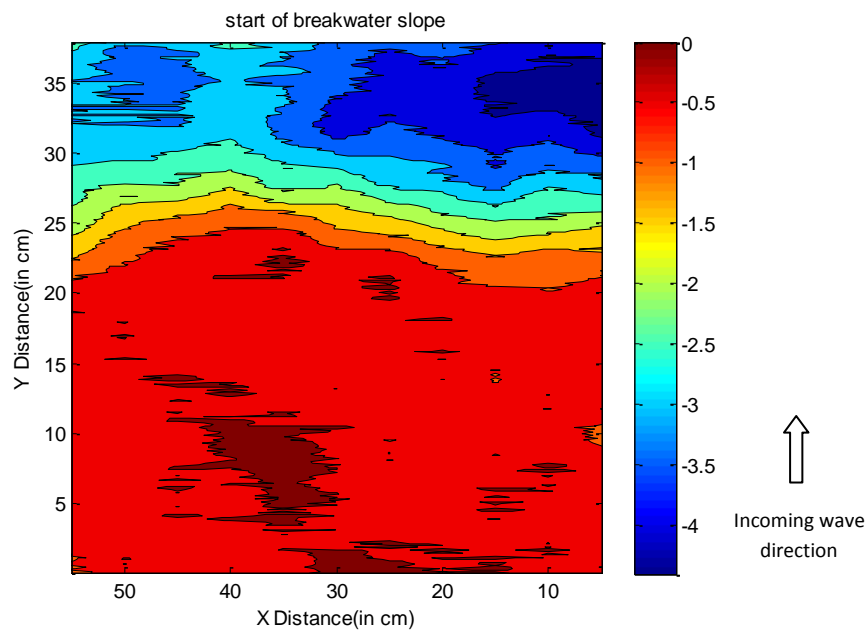


Figure 4-34 Contour map of erosion of Test2f

4.3. Test series 3

Test series 3 consists of 5 tests; Test3a, Test3b, Test3c, Test3d & Test3e. In these five tests, the filter configuration was formed by Filter 3, $D_{f50}=0.96\text{cm}$ (as a filter layer, common with Test series 1, 2) $D_{b50}=360\mu\text{m}$ (as base layer, common with Test series 5). The tested relative

grain diameter ($D_{f50}/D_{b50}=26.67$) of Test series 3 is the lowest tested and the closest to the geometrically closed filters. In addition, the density of the filter stones is also the lowest ($\rho_{\text{filter}}=2620\text{kg/m}^3$). Finally the filter is narrow graded.

Table 4–13 summarizes the test parameters of Test series 3.

Test Series	D_{f50} cm	D_{b50} μm	D_{f50}/D_{b50} -	ρ_{filter} kg/m^3	ρ_{base} kg/m^3	D_{f85}/D_{f15} -
3	0.96	360	26.67	2620	1500	1.31

Table 4–13 General test parameters of Test series 3

4.3.1. Test3a

Table 4–14 provides the test parameters of Test3a. Despite that the target input significant wave height was not reached ($H_s=0.114\text{m}$) the weight of removed material was larger than Test1a & Test2a. Finally, although the reflection coefficient was slightly increased the measured velocity was slightly smaller than expected.

Test	N_m -	D_{f50} cm	D_{b50} μm	D_{f50}/D_{b50} -	d_f/D_{f50} -	d_f m	D_{f85}/D_{f15} -	Target WC	T_p s	H_s m
Test3a	3665	0.96	360	26.67	3.40	0.033	1.31	WC1	2.485	0.114

Table 4–14 Test parameters of Test3a

After the test an S-curve was shaped at the right side glass. The erosion part of the curve was narrow while the deposition part was flat but larger in extend (Figure 4-35).

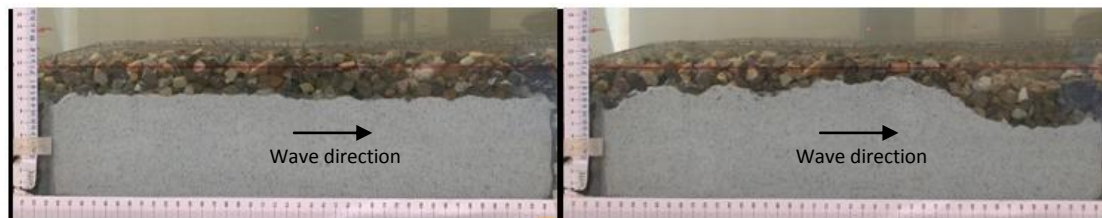


Figure 4-35 Test3a after 0 minutes (left) and after 125 minutes (right)

The deposition part arrived in equilibrium really quickly, in contrast to the scour hole which was still evolving until the end of the test. The pace of erosion development was quicker for the initial stages of the test and slower when the end of the test was approaching.

Shape of erosion pattern from the final profile (magenta line) and from the average cross section (black line) is well in-agreement. However, the averaged maximum scour depth is smaller than the maximum scour depth observed through the side glass; nevertheless the difference is not significant. In addition, scour depth in front of the breakwater is not zero; thus it is threatening breakwater stability.

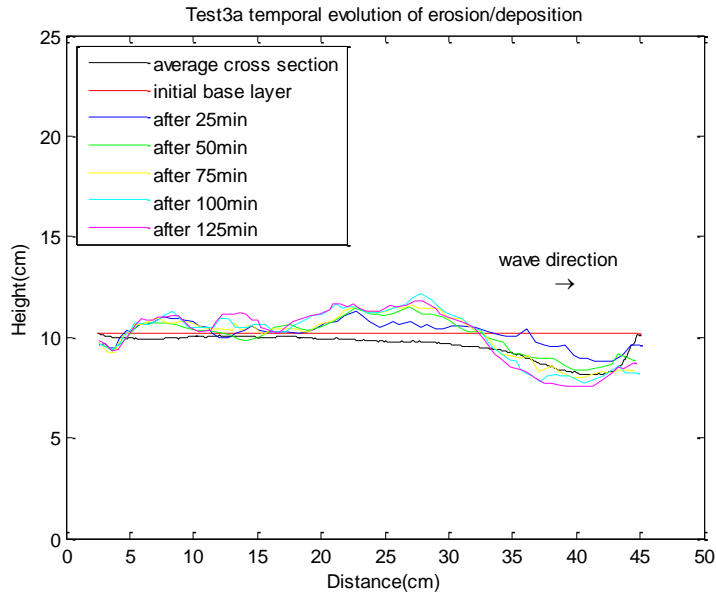


Figure 4-36 Temporal evolution of erosion of Test3a

Nevertheless, the scour pattern was asymmetrical with respect to the flume width. At the left side glass the maximum scour depth was found less than 2cm while in the middle it was not exceeding 1.6cm.

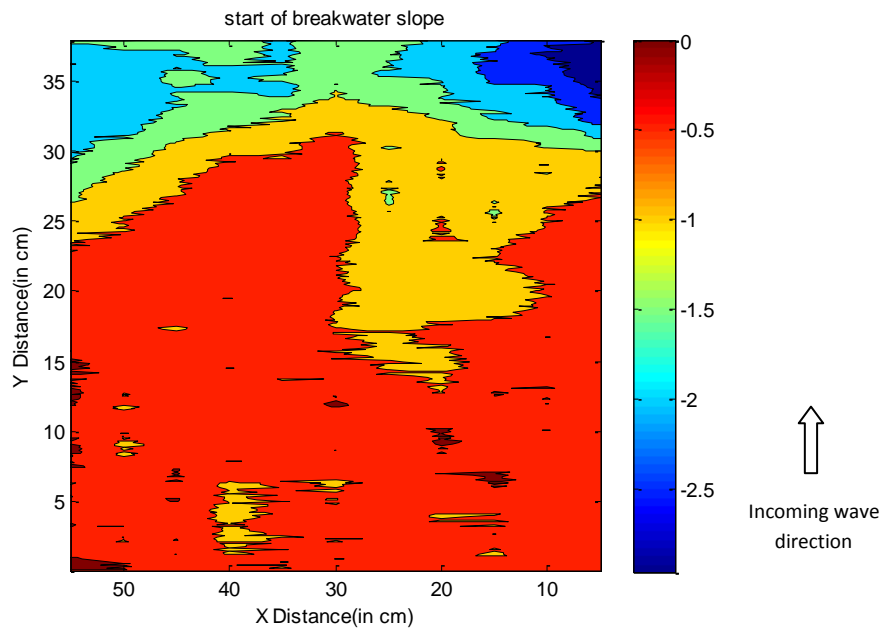


Figure 4-37 Contour map of erosion of Test3a

4.3.2. Test3b

Table 4–15 summarizes the test parameters of Test3b. Despite that, the significant wave height was higher than Test3a the weight of the removed material was far less.

Test	N_m	D_{f50} cm	D_{b50} μm	D_{f50}/D_{b50}	d_f/D_{f50}	d_f m	D_{f85}/D_{f15}	Target WC	T_p s	H_s m
Test3b	3579	0.96	360	26.67	3.40	0.033	1.31	WC2	2.032	0.120

Table 4–15 Test parameters of Test3b

The inspection of the filter configuration through the right side glass did not reveal any clear erosion/deposition trend (Figure 4-38).

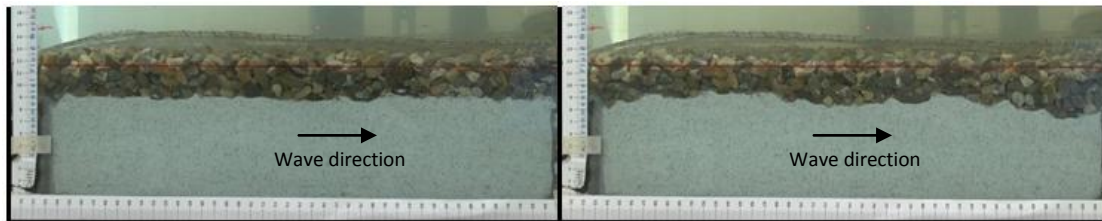


Figure 4-38 Test3b after 0 minutes (left) and after 100 minutes (right)

Figure 4-39 verifies the aforementioned. Profile seems to be in equilibrium. In addition, the scour formation at the right of Figure 4-39 resembles more to clear water scour.

In addition, final profile (magenta line) and average cross section (black line) agree well in shape and magnitude. Despite that the maximum scour depth is rather small and seems to approach into equilibrium state, it is located in front of the breakwater threatening its stability.

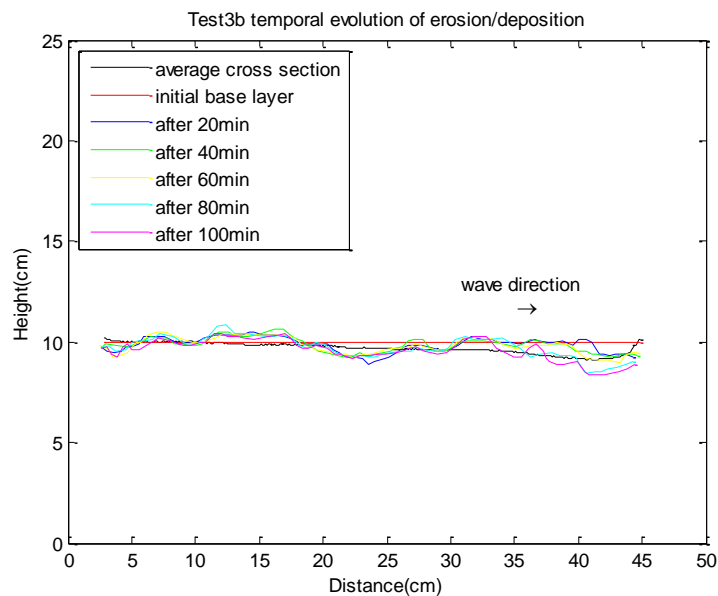


Figure 4-39 Temporal evolution of erosion of Test3b

The maximum scour depth was located nearly at the center of the flume. The maximum depth exceeded 1.2cm. However, base layer at the left part of the flume remained intact (Figure 4-40).

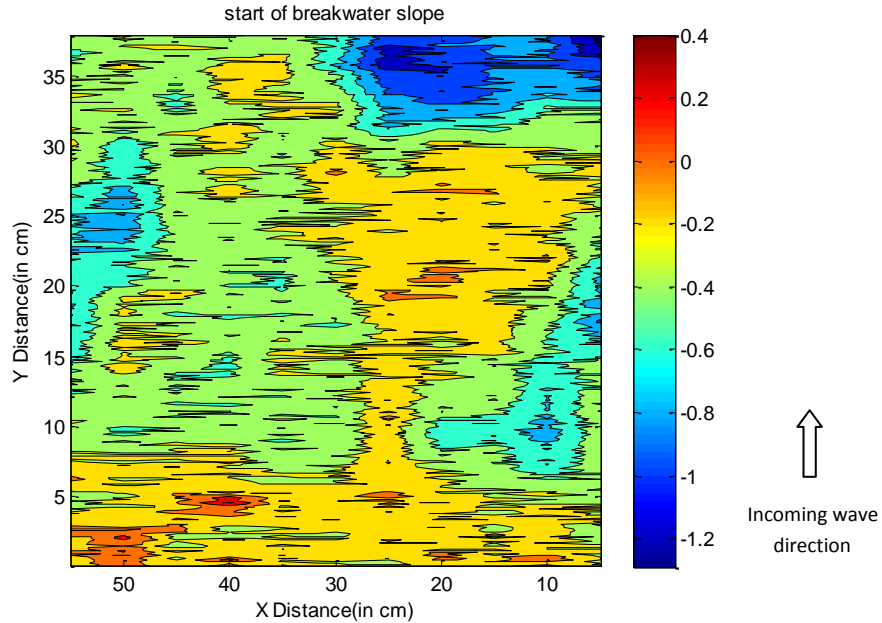


Figure 4-40 Contour map of erosion of Test3b

4.3.3. Test3c

Table 4–16 displays the test parameters of Test3c.

Test	N_m	D_{f50} cm	D_{b50} μm	D_{f50}/D_{b50}	d_f/D_{f50}	d_f m	D_{f85}/D_{f15}	Target WC	T_p s	H_s m
Test3c	3671	0.96	360	26.67	3.40	0.033	1.31	WC3	2.485	0.098

Table 4–16 Test parameters of Test3c

At Test3c, the scour hole was formed in the middle of the flume. The S-curve profile was not able to fully develop and showed a limited deposition part near the offshore side of the box (Figure 4-41).

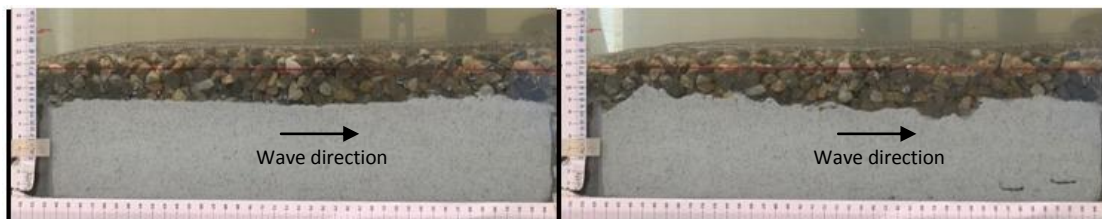


Figure 4-41 Test3c after 0 minutes (left) and after 125 minutes (right)

Figure 4-42 illustrates the temporal evolution of erosion/deposition pattern through the right side glass. The deposition area arrived in equilibrium after 50min. Erosion area continues to evolve, however the rate of change is slow and also maximum depth seems to have reached its maximum value. Therefore, it is considered not to threaten the breakwater stability.

Scour depth next to the breakwater is zero; thus structure is safe. Final profile (magenta line) and average cross section (black line) agree well in terms of maximum scour depth; however their shape is completely different.

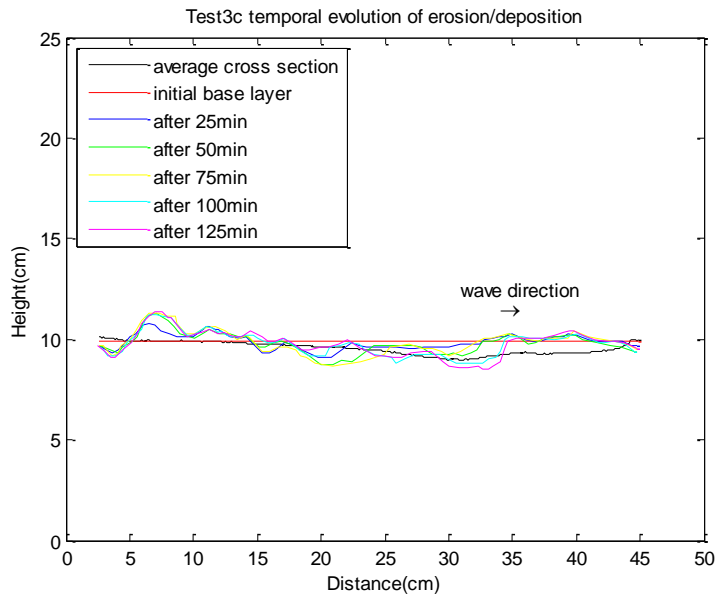


Figure 4-42 Temporal evolution of erosion of Test3c

From Figure 4-43 it was found that two major scour holes were formed. They were situated in the middle of the box and at some distance from the breakwater. Their maximum depth does not exceed 1.3cm.

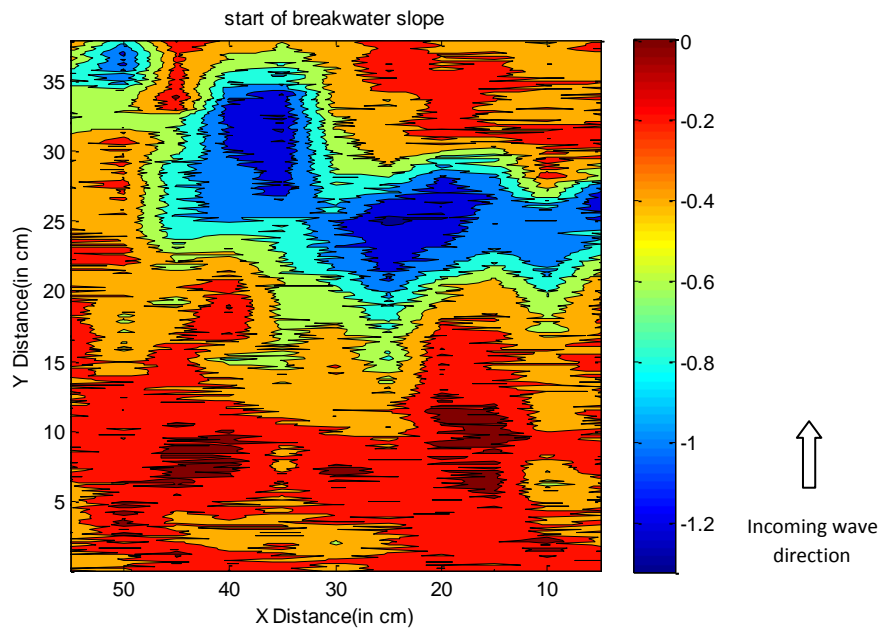


Figure 4-43 Contour map of erosion of Test3c

4.3.4. Test3d

In Test3d the test conditions of Test3a were repeated but with a thicker filter ($d_f/D_{f50}=3.6$). Significant wave height was smaller in contrast to the measured velocity and removed base material which found to be similar to Test3a.

Test	N_m	D_{f50} cm	D_{b50} μm	D_{f50}/D_{b50}	d_f/D_{f50}	d_f m	D_{f85}/D_{f15}	Target WC	T_p s	H_s m
Test3d	3514	0.96	360	26.67	4.30	0.041	1.31	WC1	2.485	0.109

Table 4–17 Test parameters of Test3d

Figure 4-44 displays the S-shaped erosion/deposition profile after the end of Test3d. Likewise to Test3a, the deposition bar was flat and thin while the scour hole was narrow.



Figure 4-44 Test3d after 0 minutes (left) and after 125 minutes (right)

The former arrived into equilibrium after the first 25min. The corresponding time for the latter was 100min.

Erosion patterns from the final profile (magenta line) and from the average cross section (black line) are identical, in both shape and magnitude. Furthermore, scour depth in front of the breakwater is not zero; thus it is threatening breakwater stability.

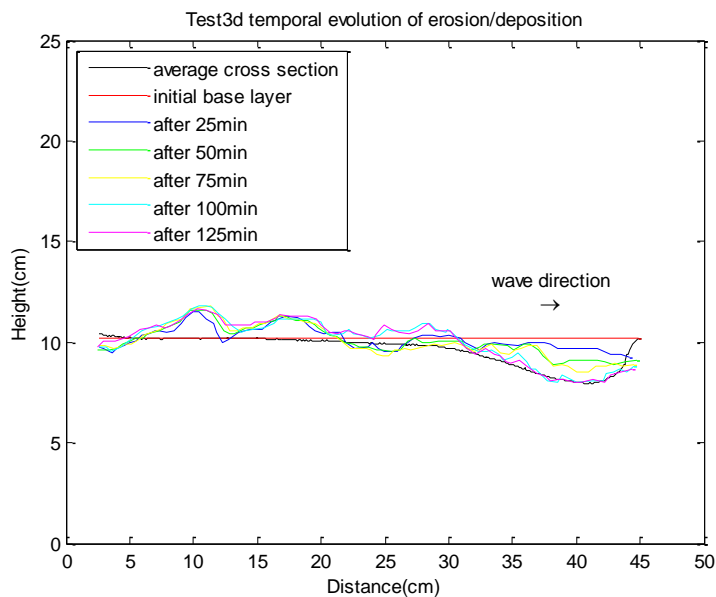


Figure 4-45 Temporal evolution of erosion of Test3d

Scour formation showed a very clear trend with respect to the flume width. Scour depth was almost uniform in the entire width, with a maximum value of 2.57cm.

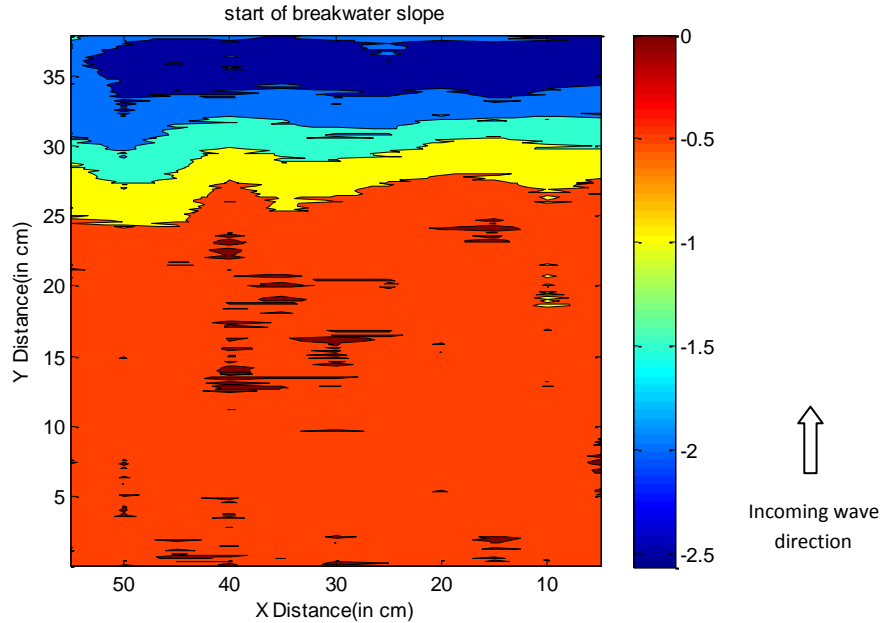


Figure 4-46 Contour map of erosion of Test3d

4.3.5. Test3e

Test3e is the longest test of Test series 3. A total of 9000 waves (305min) were used to attack the structure. Input parameters were similar to Test3a (also same relative thickness) however, the amount of removed material was smaller than expected. Table 4–18 summarizes the parameters of Test3e.

Test	N_m	D_{f50}	D_{b50}	D_{f50}/D_{b50}	d_f/D_{f50}	d_f	D_{f85}/D_{f15}	Target WC	T_p	H_s
	-	cm	μm	-	-	m	-		s	m
Test3e	9000	0.96	360	26.67	3.40	0.033	1.31	WC1	2.485	0.113

Table 4–18 Test parameters of Test3e

The comparison of the side glass snapshots of Test3e displays the existence of deposition bar with weak characteristics. On the contrary a distinct scour hole was formed at the middle of the box and expanded laterally at both sides.

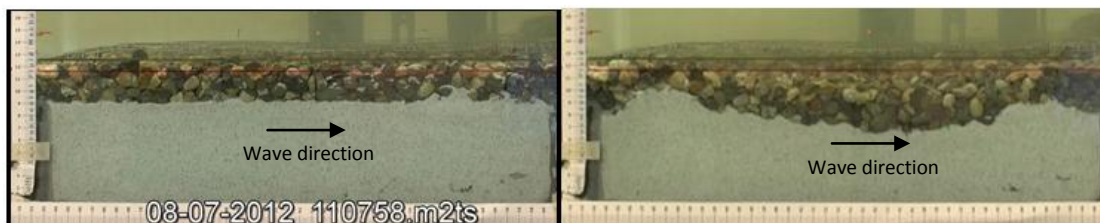


Figure 4-47 Test3e after 0 minutes (left) and after 305 minutes (right)

For the scour hole the equilibrium was not reached until 290min after the start of the test. Nevertheless, after $t=200-250\text{min}$ maximum scour depth seems not to evolve further.

In addition, final profile (magenta line) and average cross section (black line) agree well in shape but not in magnitude. The averaged maximum scour depth is less than half the maximum scour depth observed through the side glass. Finally, scour depth next to the breakwater is zero; thus structure is considered to be safe.

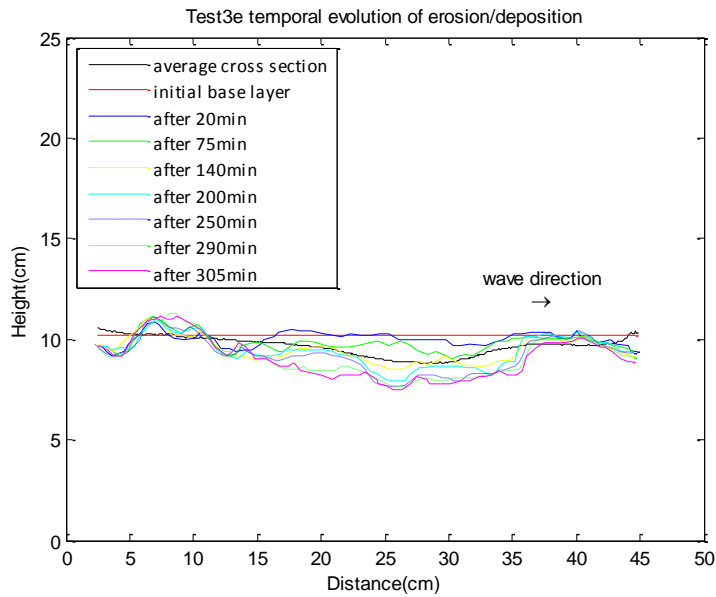


Figure 4-48 Temporal evolution of erosion of Test3e

Figure 4-49 illustrates the erosion distribution over the entire flume width. The largest part of the base material remained intact with erosion which was less than 1cm. While this occurred at the middle area, the cross sections near the sides were significantly eroded. Holes were formed at the middle of the box with maximum depths at around 2.5cm.

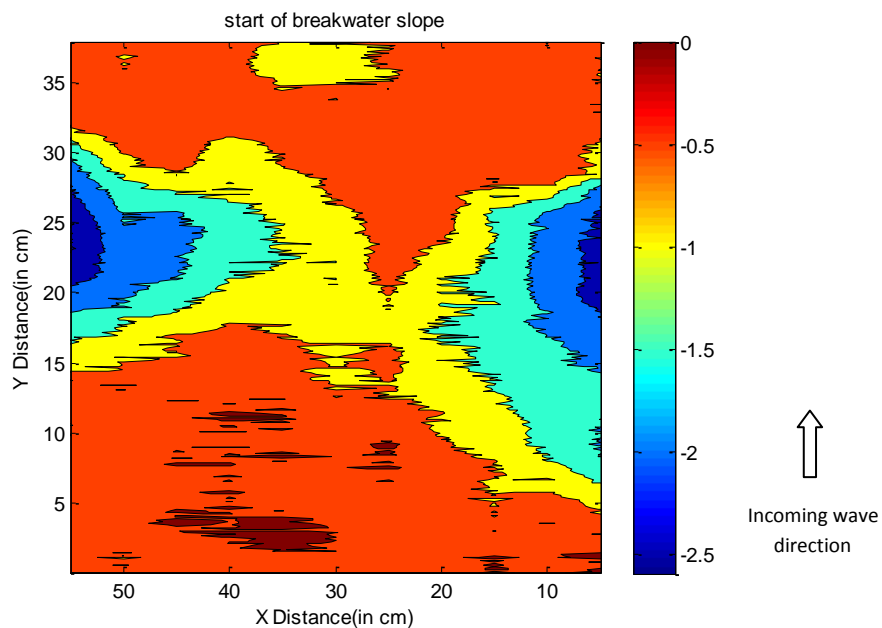


Figure 4-49 Contour map of erosion of Test3e

4.4. Test series 4

Until now (Test series 1, 2 & 3), the grain diameter of base material was $D_{b50}=360\mu\text{m}$. In Test series 4 a base material with $D_{b50}=210\mu\text{m}$ is used. In total, 3 tests are executed; firstly Test4a is executed and then Test4d, Test4e are Test4a's repetitions. The reason for that is the

available time for testing and that erosion in Test4a was found to be imperceptible; therefore repetitions were executed to get insight into the erosion pattern. In addition, filter layer consists of the finest filter material, Filter 4 ($D_{f50}=0.68\text{mm}$). The filter layer is narrow graded. The effects of duration and relative thickness increase are not treated here.

Table 4–19 presents the test parameters of Test series 4.

Test Series	D_{f50} cm	D_{b50} μm	D_{f50}/D_{b50} -	d_f/D_{f50} -	d_f m	ρ_{filter} kg/m^3	ρ_{base} kg/m^3	D_{f85}/D_{f15} -
4	0.68	210	32.33	3.40	0.023	2715	1500	1.25

Table 4–19 General test parameters of Test series 4

4.4.1. Test4a

Table 4–20 presents the test parameters of Test4a. In comparison with executed tests with similar parameters (Test1a, Test2a, Test3a etc.), no significant differences occur.

Test	N_m -	D_{f50} cm	D_{b50} μm	D_{f50}/D_{b50} -	d_f/D_{f50} -	d_f m	D_{f85}/D_{f15} -	Target WC	T_p s	H_s m
Test4a	3566	0.68	210	32.33	3.40	0.023	1.25	WC1	2.485	0.118

Table 4–20 Test parameters of Test4a

In Figure 4-50, a scour hole was formed at the right side glass. Apart from that, no significant changes occur in the transitional area between filter and base layer.

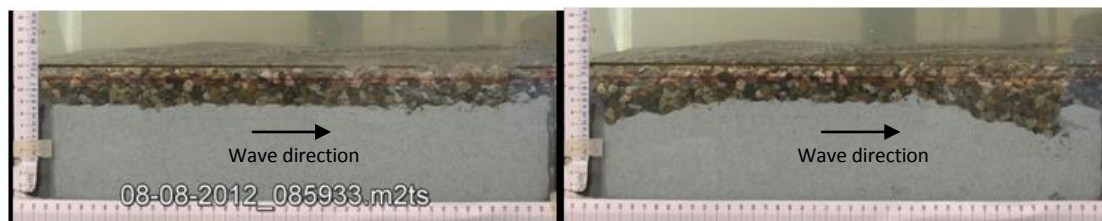


Figure 4-50 Test4a after 0 minutes (left) and after 100 minutes (right)

Based on Figure 4-51, the aforementioned scour hole did not reach the equilibrium depth. Part of the eroded base material is transported further upstream; however the depositional profile did not show discrete characteristics.

Final profile (magenta line) and average cross section (black line) are inconsistent to each other, both in shape and magnitude. According to the former, erosion is imperceptible; thus filter configuration prevents scour formation. Scour hole formed through the side glass is probably caused by model effects (gap between filter and glass).

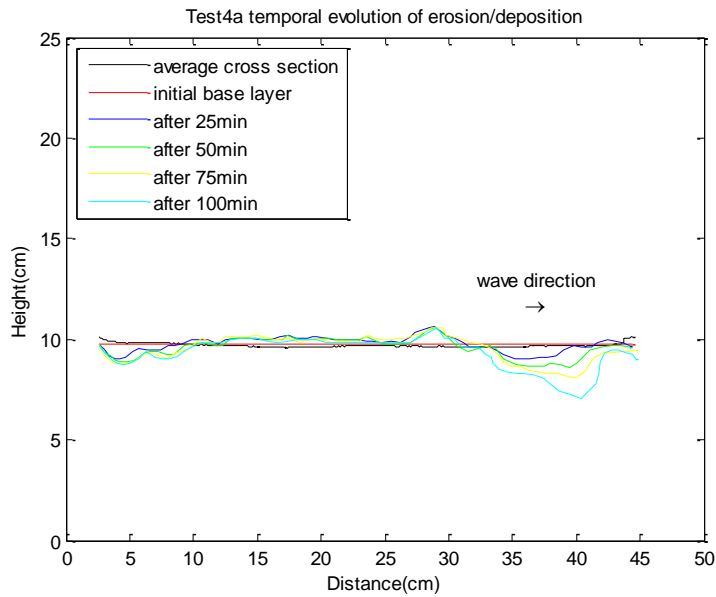


Figure 4-51 Temporal evolution of erosion of Test4a

After the removal of the filter layer, base material in the box was found intact. Scour depth had reached a maximum of 0.45cm at specific but dispersed locations. In these locations, blocks of filter layer stones had settled into the weakened base layer due to the wave action.

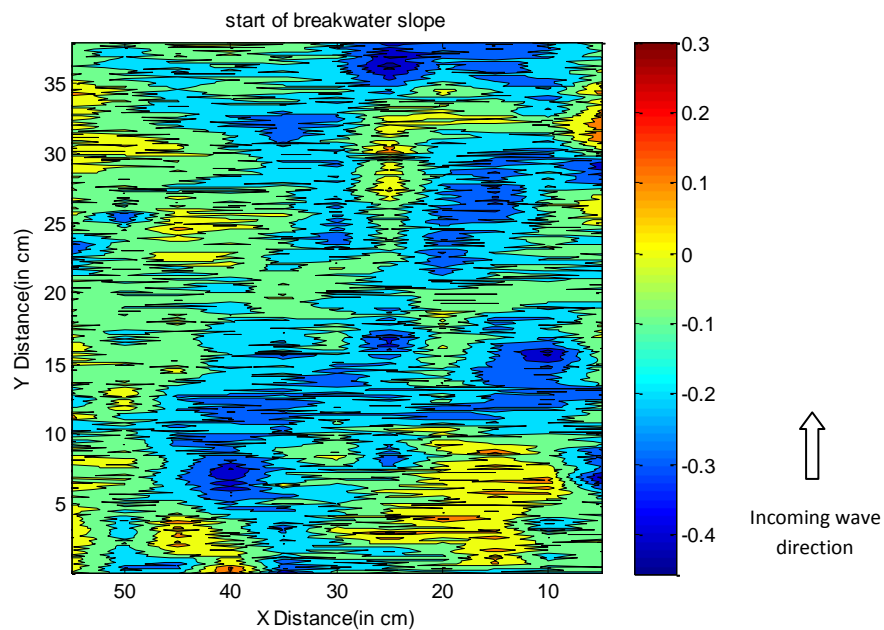


Figure 4-52 Contour map of erosion of Test4a

4.4.2. Test4d

The absence of significant scour formation in Test4a led to the execution of Test4d, which is a repetition of Test4a. Test parameters were repeated successfully simplifying the comparison.

Test	N_m	D_{f50} cm	D_{b50} μm	D_{f50}/D_{b50}	d_f/D_{f50}	d_f m	D_{f85}/D_{f15}	Target WC	T_p s	H_s m
Test4d	3479	0.68	210	32.33	3.40	0.023	1.25	WC1	2.485	0.118

Table 4–21 Test parameters of Test4d

In Figure 4-53 two bars were formed with base material that is transported offshore. At the right picture of Figure 4-53 (t=125min) clear water scour was formed in the upstream side of the box.

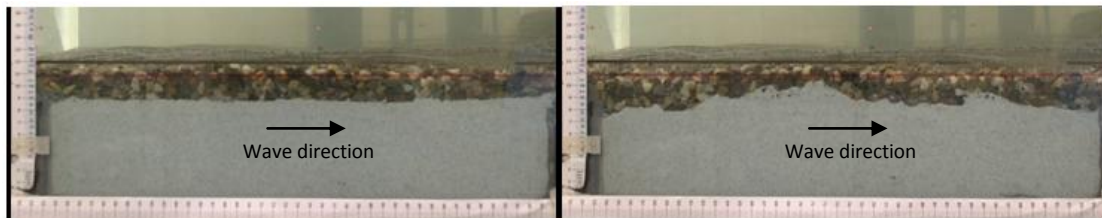


Figure 4-53 Test4d after 0 minutes (left) and after 125 minutes (right)

From Figure 4-54 maximum scour depth and bar height seem to increase; however no significant increase is expected.

Final profile (magenta line) and average cross section (black line) agree well in magnitude but not in shape. In general, scour depth is small; however, it is considered a threat to breakwater stability since based on observations through the side glass it is located in front of it.

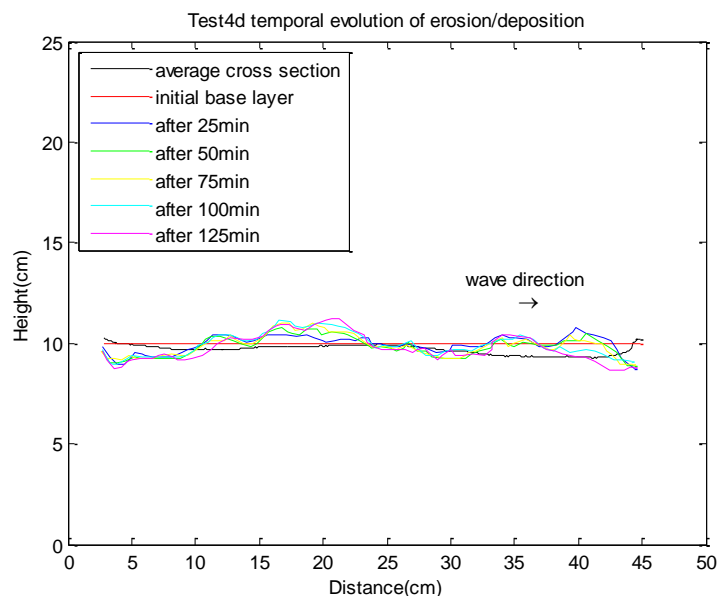


Figure 4-54 Temporal evolution of erosion of Test4d

In general, the amount of erosion after the test was found to be imperceptible except from a highly spatial scour hole. Based on Figure 4-55 a scour hole is formed in the breakwater side (downstream) of the box nearly at the center of the flume. Maximum scour depth was found to be 1.6cm.

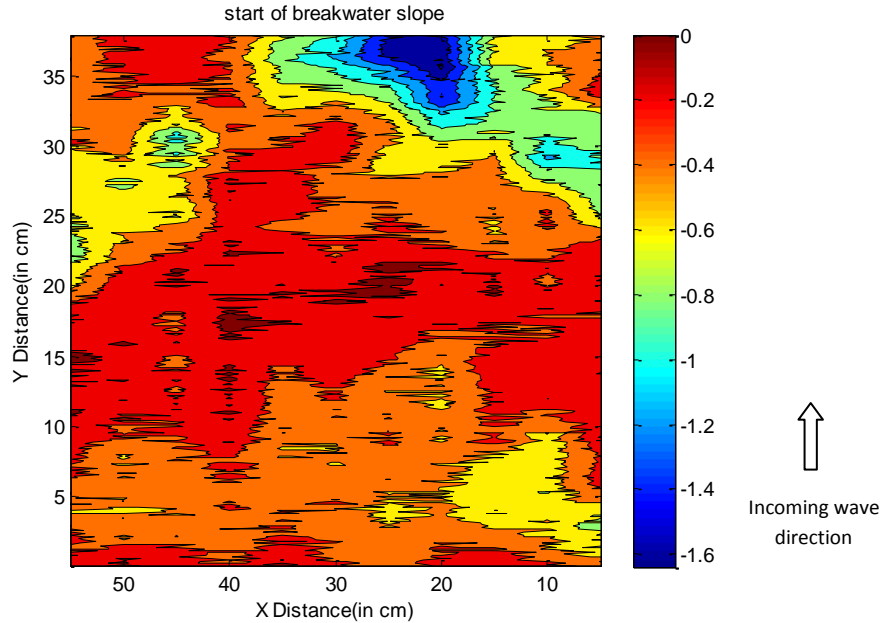


Figure 4-55 Contour map of erosion of Test4d

4.4.3. Test4e

Additionally, Test4e was a repetition of Test4a & Test4d. Slightly longer than the other two tests, Test4e verified the results taken from Test4d. Table 4–22 summarizes the test parameters of Test4e.

Test	N_m -	D_{f50} cm	D_{b50} μm	D_{f50}/D_{b50} -	d_f/D_{f50} -	d_f m	D_{f85}/D_{f15} -	Target WC	T_p s	H_s m
Test4e	3729	0.68	210	32.33	3.40	0.023	1.25	WC1	2.485	0.117

Table 4–22 Test parameters of Test4e

In Figure 4-56 clear water scour is formed at the upstream and downstream side of the box. In the middle a shallow scour hole is surrounded by two bars. However, scour depth and bar height are negligible.

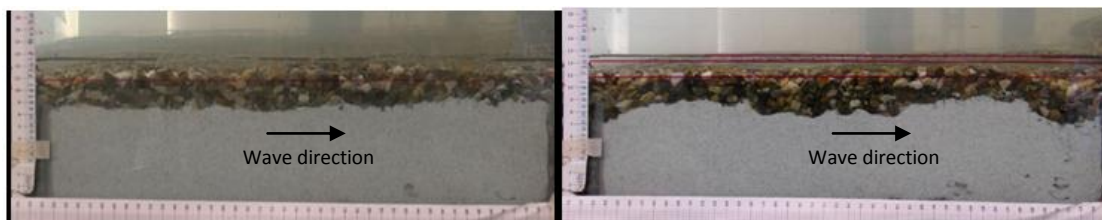


Figure 4-56 Test4e after 0 minutes (left) and after 125 minutes (right)

In Figure 4-57 the scour hole in the middle of the box expands laterally at the upstream side. The related scour depth also develops; however this tendency is considered rather weak.

Final profile (magenta line) and average cross section (black line) are well in-agreement in terms of magnitude but completely inconsistent in terms of shape. According to the former, maximum erosion is observed in front of the breakwater; thus scour is threatening breakwater stability. Based on the latter, maximum scour is formed towards the center of the box. Because observations through the side glass are subject to more severe model

effects it is considered that filter protects structure stability; however it does not fully prevent scour formation.

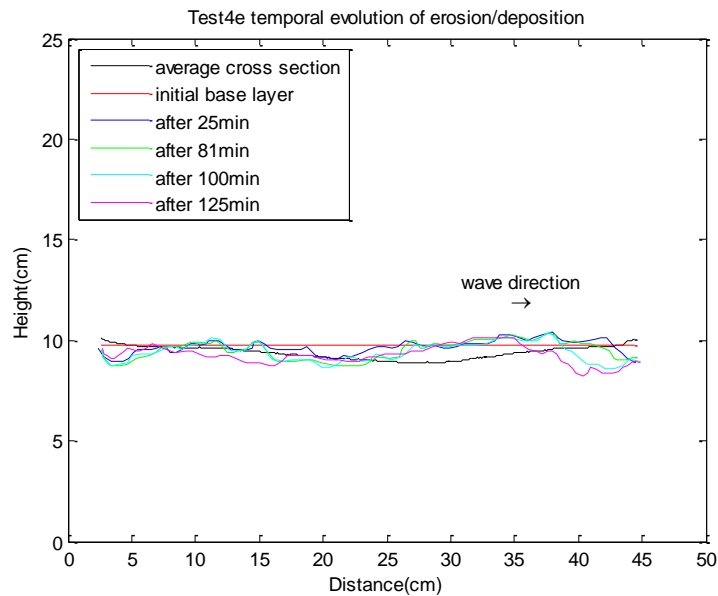


Figure 4-57 Temporal evolution of erosion of Test4e

Apart from the glass three scour holes were formed in the middle of the flume and in the middle of the right and left half of the flume. The measured maximum scour depth slightly exceeds 1.3cm and is in the order of the scour depth measured in Test4d.

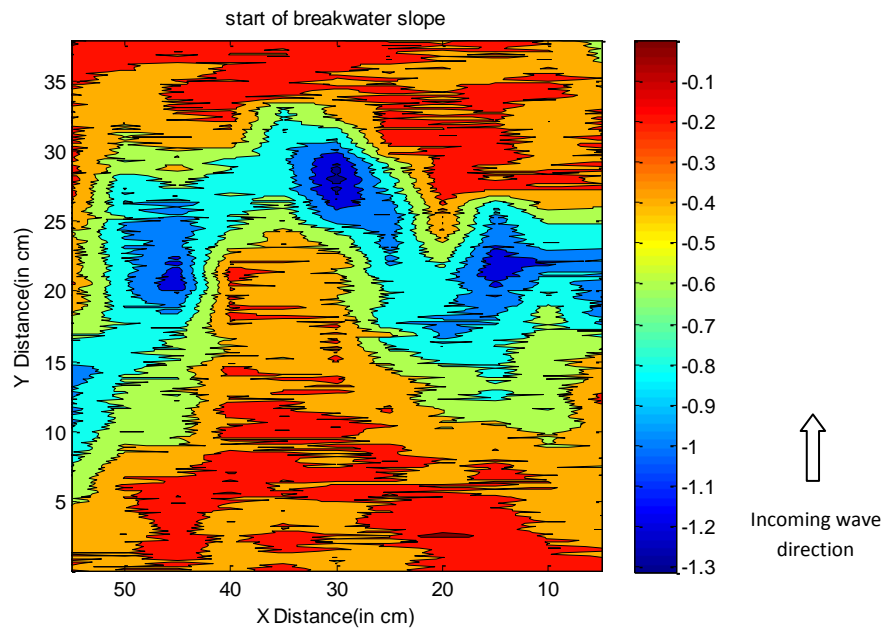


Figure 4-58 Contour map of erosion of Test4e

4.5. Test series 5

Similarly to Test series 4, Test series 5 uses the same base layer ($D_{b50}=210\mu\text{m}$). Base layer is combined with a coarser filter (Filter 3, $D_{f50}=0.68\text{mm}$, common with Test series 3) leading to the highest tested relative grain diameter $D_{f50}/D_{b50}=45.71$. In total, 4 tests were executed; namely Test5a, Test5b, Test5c & Test5d. The latter is carried out to investigate the effect of loading duration. No test was executed to investigate the effect of relative thickness increase.

Table 4–19 summarizes the test parameters of Test series 5.

Test Series	D_{f50} cm	D_{b50} μm	D_{f50}/D_{b50} -	d_f/D_{f50} -	d_f m	ρ_{filter} kg/m^3	ρ_{base} kg/m^3	D_{f85}/D_{f15} -
5	0.96	210	45.71	3.40	0.033	2620	1500	1.31

Table 4–23 General test parameters of Test series 5

4.5.1. Test5a

Table 4–24 provides the test parameters of Test5a.

Test	N_m -	D_{f50} cm	D_{b50} μm	D_{f50}/D_{b50} -	d_f/D_{f50} -	d_f m	D_{f85}/D_{f15} -	Target WC	T_p s	H_s m
Test5a	3908	0.96	210	45.71	3.40	0.033	1.31	WC1	2.485	0.119

Table 4–24 Test parameters of Test5a

After the execution of the test, at the right side glass a scour hole has appeared at the downstream side of the box.

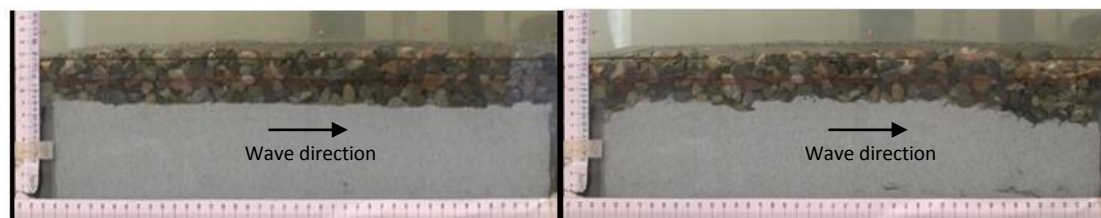


Figure 4-59 Test5a after 0 minutes (left) and after 125 minutes (right)

After 125min the scour depth was still increasing. The depth was increasing slowly until 100min after the start of the test. Then erosion procedure seems to be accelerated.

Final profile (magenta line) and average cross section (black line) agree well in magnitude but not in shape. Likewise to Test4e, according to the former, maximum erosion is observed in front of the breakwater; thus scour is threatening breakwater stability. Based on the latter, maximum scour is formed towards the center of the box. Because observations through the side glass are subject to more severe model effects it is considered that filter prevents structure instability; however it does not fully prevent scour formation.

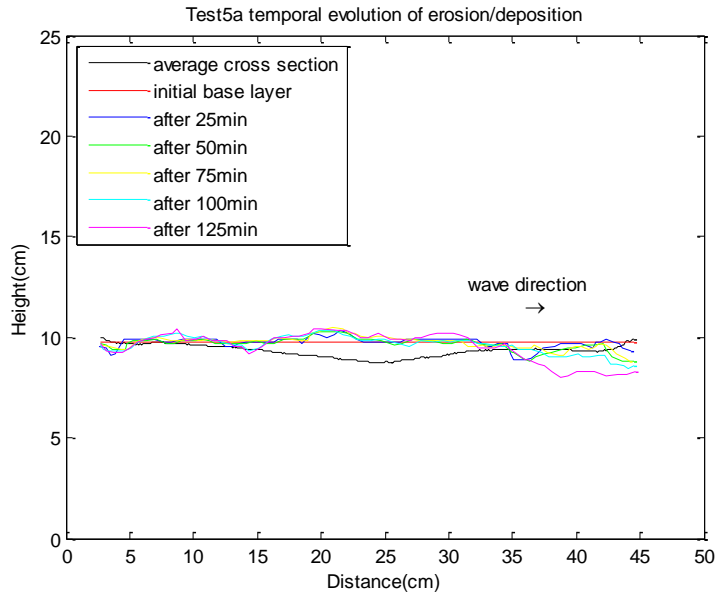


Figure 4-60 Temporal evolution of erosion of Test5a

In total, three scour holes were finally formed. In the middle of the right half of the flume and in the middle of the left half maximum scour depth approximated 1.8cm. The scour hole in the flume's middle had a depth less than 1.4cm. Finally, the maximum depth was observed in the scour hole that was formed next to the right side glass (2.09cm).

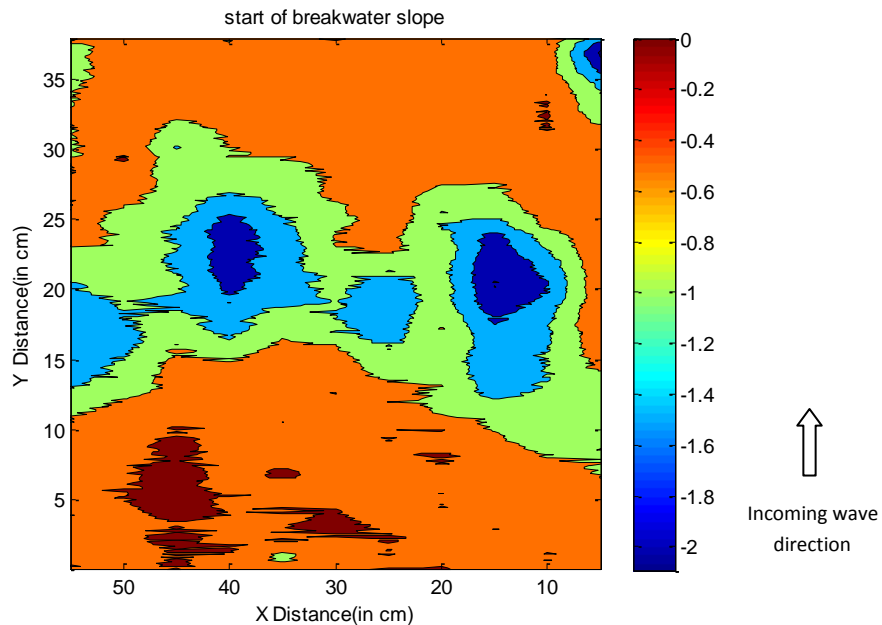


Figure 4-61 Contour map of erosion of Test5a

4.5.2. Test5b

Table 4–25 provides the test parameters of Test5b.

Test	N_m	D_{f50} cm	D_{b50} μm	D_{f50}/D_{b50}	d_f/D_{f50}	d_f m	D_{f85}/D_{f15}	Target WC	T_p s	H_s m
Test5b	3572	0.96	210	45.71	3.40	0.033	1.31	WC2	2.032	0.121

Table 4–25 Test parameters of Test5b

For this test, video capturing was interrupted; thus for the side glass comparison the snapshot at $t=70\text{min}$ was used. Based on Figure 4-62, erosion is observed immediately at the downstream side of the box and is succeeded by a flat bar. Afterwards, another scour hole is formed with depth proportional to the downstream scour hole.



Figure 4-62 Test5b after 0 minutes (left) and after 70 minutes (right)

Furthermore, the downstream scour hole had reached equilibrium scour depth at 25min after the start of the test and then it was expanding only laterally towards the offshore side of the box. The upstream scour hole is slightly shallower but is expanding both laterally further downstream and in vertical direction.

Erosion patterns from the final profile (magenta line) and from the average cross section (black line) are similar, in both shape and magnitude. The only difference is that according to the former, maximum scour depth is located in front of the breakwater while for the latter is not. This makes a difference whether breakwater stability is threatened or not.

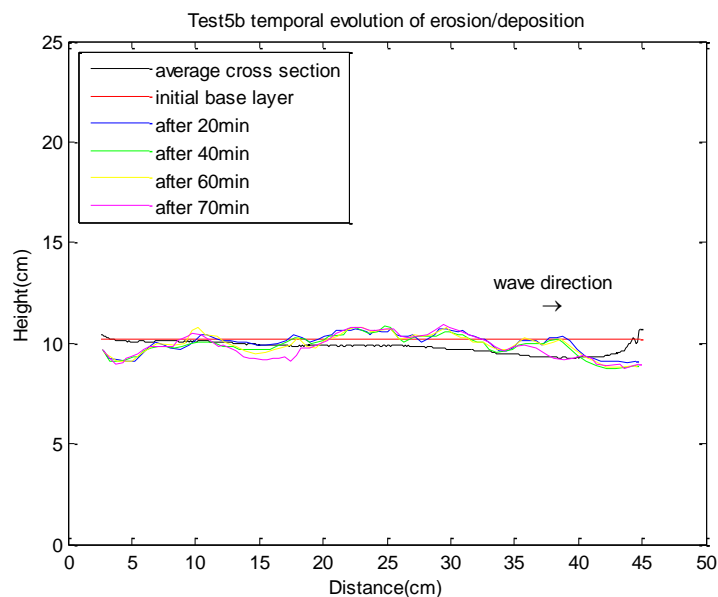


Figure 4-63 Temporal evolution of erosion of Test5b

Nevertheless, apart from the right side glass and the cross sections near it, the rest of the box did not display any serious erosion. Only at the left side of the box erosion approximated 1cm. In general, the maximum scour depth was found to be 2.31cm.

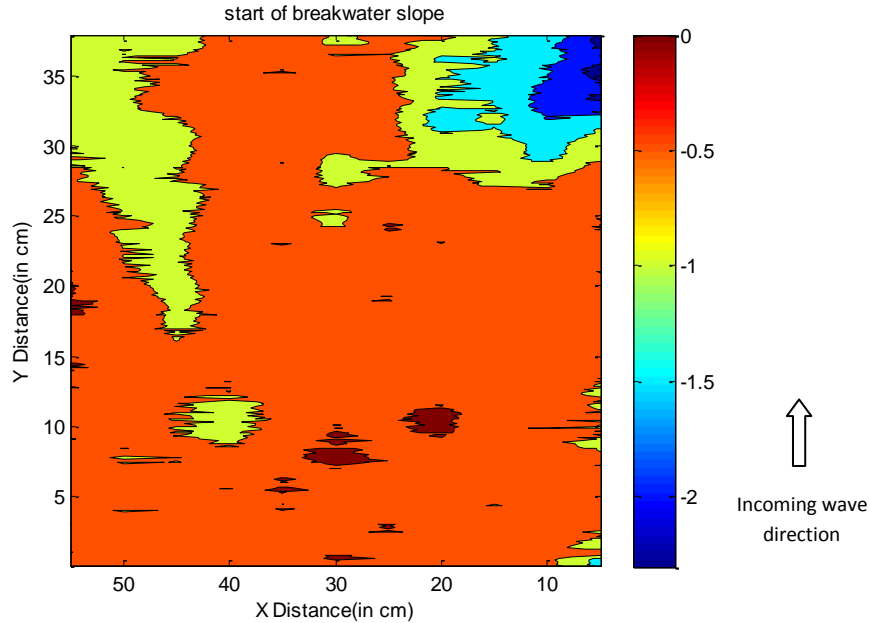


Figure 4-64 Contour map of erosion of Test5b

4.5.3. Test5c

Table 4–26 summarizes the test parameters of Test5c.

Test	N_m	D_{f50} cm	D_{b50} μm	D_{f50}/D_{b50}	d_f/D_{f50}	d_f m	D_{f85}/D_{f15}	Target WC	T_p s	H_s m
Test5c	3863	0.96	210	45.71	3.40	0.033	1.31	WC3	2.485	0.102

Table 4–26 Test parameters of Test5c

The inspection of erosion/deposition pattern revealed the formation of two erosion areas; a flatter and wider at the upstream middle of the box and a narrower but deeper at the downstream side in front of the breakwater. The two scour holes are separated by flat bar that vanishes with the time (Figure 4-65 & Figure 4-66).

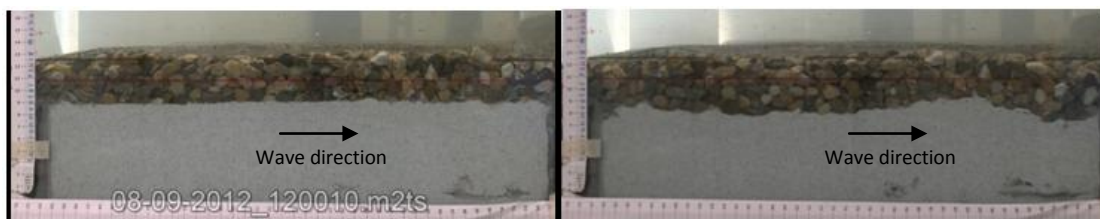


Figure 4-65 Test5c after 0 minutes (left) and after 125 minutes (right)

However, both the scour holes have reached equilibrium state in 100min after the start of the test. Afterwards, no further increase of depth or scour length was observed.

Final profile (magenta line) and average cross section (black line) not consistent to each other in any terms. Based on observations, scour depth in front of the breakwater is significant. On the contrary, according to the averaged cross section, scour depth next to the structure is zero.

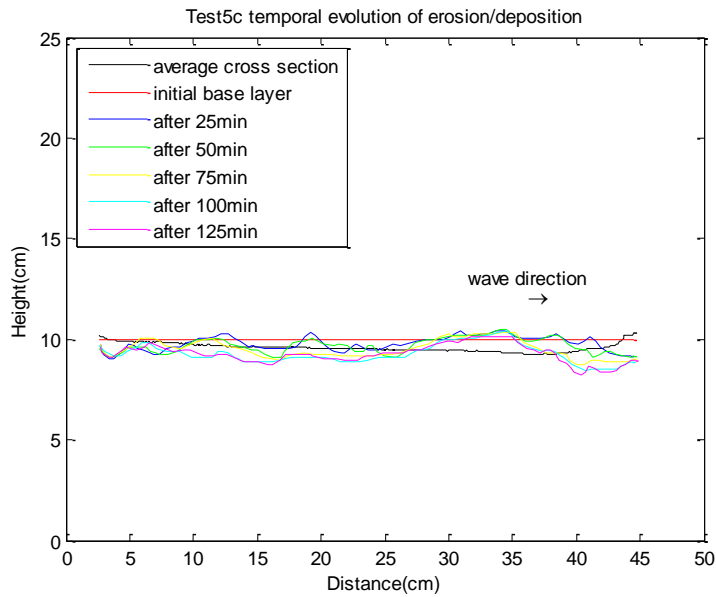


Figure 4-66 Temporal evolution of erosion of Test5c

When the entire box is considered, one major hole is formed in the center of the flume with a maximum depth that is not exceeding 1.6cm. Base material in the rest of the box remained unaffected by wave action.

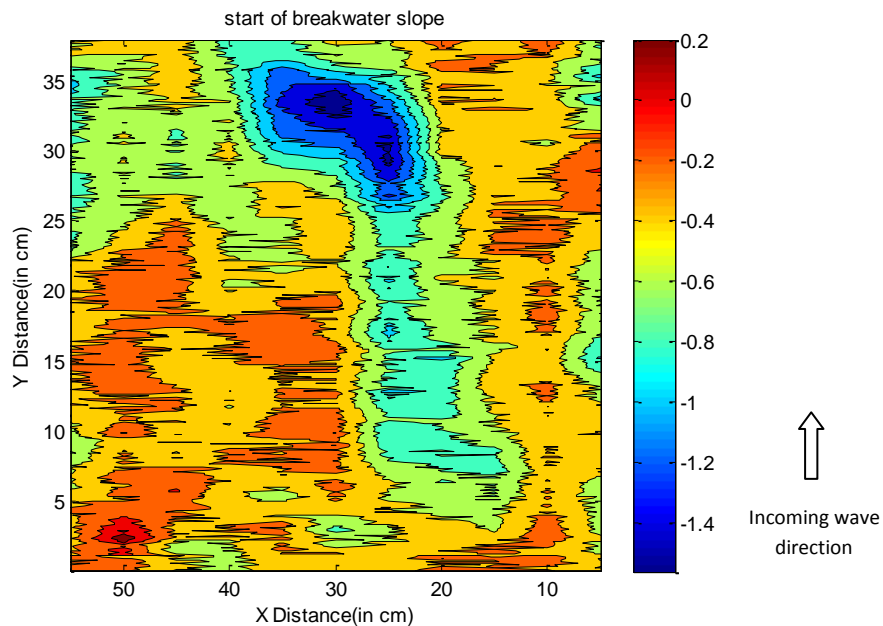


Figure 4-67 Contour map of erosion of Test5c

4.5.4. Test5d

Tes5d is a repetition of Test5a but with longer duration (7495 waves & 250min). Table 4–27 summarizes the test parameters of Test5d. After the execution of the test a substantial amount of eroded base material was picked up from the foreshore.

Test	N_m	D_{f50} cm	D_{b50} μm	D_{f50}/D_{b50}	d_f/D_{f50}	d_f m	D_{f85}/D_{f15}	Target WC	T_p s	H_s m
Test5d	7495	0.96	210	45.71	3.40	0.033	1.31	WC1	2.498	0.120

Table 4-27 Test parameters of Test5d

From Figure 4-68 it can be seen that a whole layer of base material was eroded, and in between the two major holes a spiked bar rises (Figure 4-68).



Figure 4-68 Test5d after 0 minutes (left) and after 250 minutes (right)

Until the first 125min of the test erosion process was developing very slowly. After that point, erosion rate was proceeding accelerated and therefore equilibrium state was not reached (Figure 4-69).

The shape of erosion patterns from the final profile (magenta line) and from the average cross section (black line) displays several differences. Furthermore, the averaged maximum scour depth is smaller than the maximum scour depth observed through the side glass; nevertheless the difference is trivial. In addition, scour depth in front of the breakwater is not zero; thus it is threatening breakwater stability.

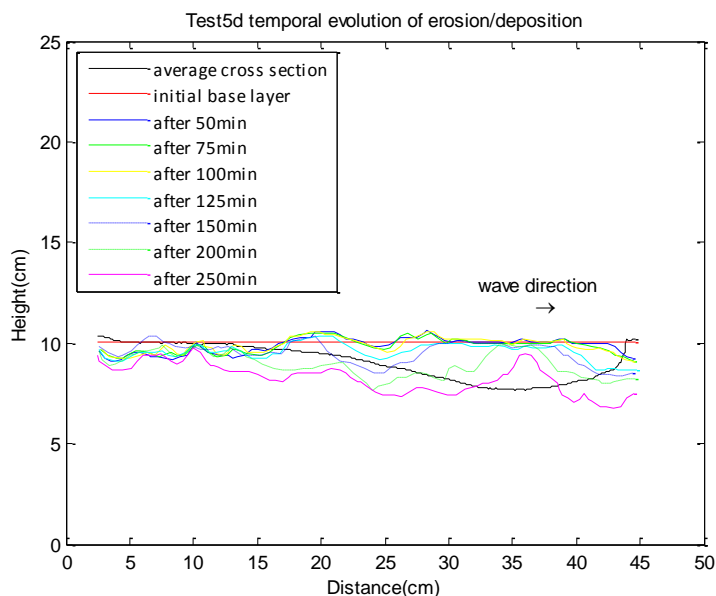


Figure 4-69 Temporal evolution of erosion of Test5d

In Figure 4-70 two major scour areas can be distinguished. The deeper scour hole was located in the middle of the flume and extended towards the left side glass. It had a maximum depth of 4.1cm; in general scour depth was in the order of 2.5-3cm. The scour hole at the right side glass has a uniform scour depth in the same order (2.5-3cm).

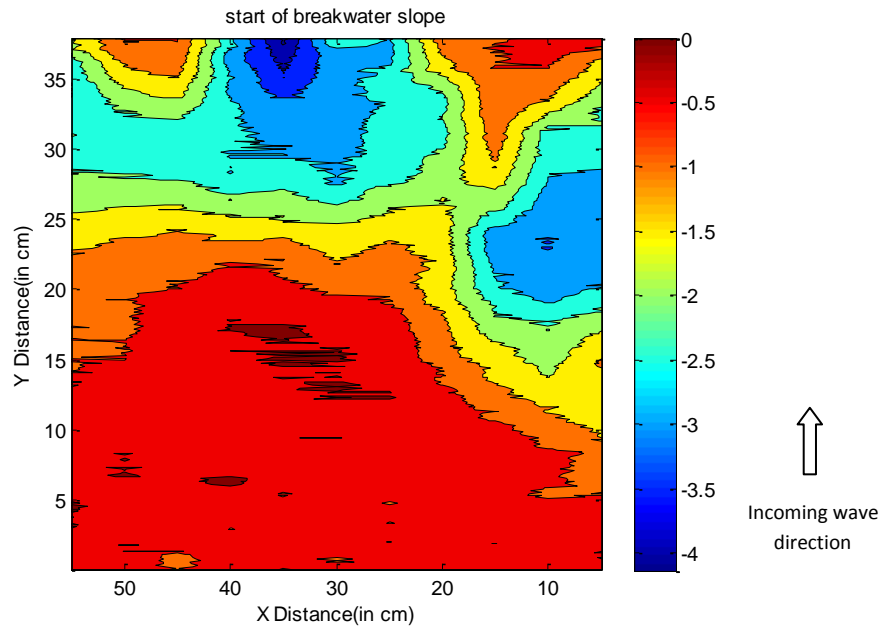


Figure 4-70 Contour map of erosion of Test5d

4.6. Summary

Chapter 4 has presented in an analytic way test results per each of the conducted tests. Mainly, three aspects were treated: erosion/deposition pattern of scour formation, temporal evolution of scour pattern and location of scour holes with focus on maximum scour depth. Therefore, Chapter 4 is an inventory that links test properties with the extracted results. These results are further analyzed in the next chapters to identify the general trends and extract important conclusions that will answer the research questions.

5. Qualitative analysis & observations

Previously, in Chapter 4, each test was treated separately to recognize the properties of scour formation and development. However, tests with mutual boundary conditions have revealed similarities in the observed damage; thus it is possible to derive some qualitative expressions that link scour properties with boundary conditions. Thereby, Section 5.1 discusses the effect of each of the related boundary conditions on scour pattern and magnitude.

Thereupon, Section 5.2 summarizes the important test observations. The subjects of stability of filter layer, mode of transport, scour pattern and equilibrium state are treated with detail. Section ends by discussing the utilization of video capturing through the flume's bottom and the exploitation of filter layer laser measurements and weight of removed material.

Finally, Section 5.3 elaborates upon the validity of the tests. Firstly, tests are compared with their repetitions with respect to scour pattern & scour hole location and the averaged maximum scour depths, to identify similarities and differences. Section ends by discussing the introduced laboratory effects and the implemented measurement errors due to the measuring equipment.

5.1. Qualitative relations

Major target of the present research is to draw the link between scour formation through a geometrically open filter with the characteristics of wave loading and filter configuration. In particular, filter configuration properties can be described with the relative grain diameter D_{f50}/D_{b50} , the relative thickness d_f/D_{f50} and filter layer grading¹⁴. Furthermore, the properties of wave loading can be represented with a characteristic value of the wave height H , wave period T and duration (storm/test) in terms of number of waves N . Thereby, this section elaborates upon the recognition of general trends between scour formation and boundary conditions.

5.1.1. Relative grain diameter D_{f50}/D_{b50}

Generally, the use of a higher D_{f50}/D_{b50} leads to a more open filter and thus for the same wave loading to larger amount of erosion. This was also observed in the tests; thereby base layer in tests from Test series 2 was eroded more with respect to the corresponding tests from Test series 3. The same holds also between Test series 4 and Test series 5.

On the other hand, the filter configuration from Test series 5 had the largest $D_{f50}/D_{b50}=45.71$ and the same filter material as Test series 3. In the latter the relative grain diameter was significantly smaller ($D_{f50}/D_{b50}=45.71$); nevertheless, the amount of erosion for corresponding tests was much smaller. Therefore, despite that the relative grain diameter

¹⁴ Base layer grading can also be used here; however in the present study the two base materials were narrow graded. Therefore, this parameter will not be discussed.

describes the openness of the filter configuration, for a stable filter, the properties of base material are also decisive in determining erosion level.

In general, for the same relative grain diameter, the amount of erosion was smaller for the finer base material ($D_{b50}=210\mu\text{m}$) and larger for the coarser base material ($D_{b50}=360\mu\text{m}$).

5.1.2. Relative thickness d_f/D_{f50}

A thicker and stable filter is able to provide larger damping of the wave loading and therefore can mitigate the amount of erosion of the underlying base material. Consequently, relative thickness increase should lead to a smaller amount of erosion.

In the present study three tests were executed in order to investigate relative thickness increase; Test 1d, 2d & 3d. Thereby, apart from the different filter thickness Test1d is similar to Test1a & Test1e, Test2d is similar to Test2a, Test2e and finally, Test3d is similar to Test3a. However, in all cases the amount of erosion was larger for the tests with larger relative thickness. Consequently, the results differ from expectations.

A major model effect is responsible for this unrealistic outcome. In particular, the density of the base material is much smaller than the density of the filter ($\rho_{\text{filter}}/\rho_{\text{base}}=1.76$) leading to different buoyancy. Consequently, when the flume was filled with water, filter material was already sinking in the base material causing initial damage that is irrelevant to wave loading. Furthermore, because of the different buoyancy, base material was staying in suspension longer than normal and thus filter layer settlement was enhanced. All tests are subject to this model effect and thus scour depth in this research is overestimated; however this error is more visible in tests with similar boundary conditions but different filter thicknesses. Thereby, tests with thicker and thus heavier filter suffered larger initial damage than similar tests with a thinner filter layer.

5.1.3. Filter grading

A wider graded filter material leads to a more densely packed filter layer with smaller permeability and smaller voids. Thereby, if the filter layer remains intact under the most severe loading, it can provide a more efficient shelter to the underlying base layer. In the present study Test series 1 and Test series 2 have the same base material ($D_{b50}=360\mu\text{m}$), similar relative grain diameter (Test series 1: $D_{f50}/D_{b50}=39.83$, Test series 2: $D_{f50}/D_{b50}=36.81$) but different filter grading (Test series 1: $D_{f85}/D_{f15}=2.11$, Test series 2: $D_{f85}/D_{f15}=1.48$). Thereby, despite that Test series 1 had larger D_{f50}/D_{b50} , they showed smaller amount of erosion than similar tests from Test series 2. Consequently, a stable, wider graded filter can lead to less base material erosion.

5.1.4. Wave height H

In principle, a higher wave height leads to more severe loading since it increases the wave orbital velocity and the shear stress applied on the grains of base layer. To investigate the effect of wave height increase, wave conditions were formulated such that WC1 and WC3 have the same wave period but the former had higher wave height.

Thereby, for tests with identical boundary conditions, tests with WC1 showed larger erosion than tests with WC3.

5.1.5. Wave period T

In principle, a higher wave period means longer waves and therefore for a given water depth, leads to shallower relative water depth (h/L), to the formation of longer water particle excursions and to higher amount of sediment transport. To investigate the effect of wave period increase wave conditions were formulated such that WC1 and WC2 have the same wave height but the former had longer wave period.

Thereby, for tests with identical boundary conditions, tests with WC1 showed larger erosion than tests with WC2. Furthermore, it seems that wave period has a more decisive influence in the amount of erosion than wave height. However, a direct comparison between these two cannot be accomplished.

5.1.6. Number of waves N

In principle, longer storm (test) duration will lead to larger amount of erosion. However, it is expected that the amount of erosion will not increase to infinity, but will approach asymptotically to a specific value (equilibrium state). To investigate the effect of storm duration, three tests were executed with a larger amount of waves.

In specific, filter configuration of Test2f was loaded by $N_m=7500$ waves, in Test3e with $N_m=9000$ waves and in Test5d with $N_m=7500$ waves. In the former and the latter case the observed damage was significantly larger (around 33-100%), therefore longer duration led to larger amount of erosion. On the other hand, the amount of damage in Test3e was smaller (30%) than Test3a although the latter was loaded with the 1/3 of the waves. Surprisingly, the damage evolved mainly at the second half of the test (after 125min) in contrast to other test observations where damage was evolving rapidly at the initial stages and then was slowing down.

Consequently, two conclusions can be drawn. Firstly, in case that equilibrium state is not reached, longer storm duration will lead to higher amount of erosion. Secondly, for unknown reasons, it is possible that a filter configuration is so efficient, that leads to significantly less damage than expected, despite the longer loading duration.

5.2. Observations

This section provides information with respect to visual observations that were extracted during the execution of the tests. Firstly, is treated the subject of filter layer stability and then are discussed the observed modes of transport. Section proceeds by apposing the subject of erosion/deposition patterns and the existence of an equilibrium state. Finally, argumentation is offered about acquired data that could not be used further in the analysis.

5.2.1. Stability of filter layer

In Paragraph 3.1.4 the Van der Meer formula (Meer *et al.* [1998]), for toe stone sizing with limited damage acceptance ($N=1$), was applied to pre-estimate the dimensions of toe filter

stones. However, in order to satisfy the demands for specific relative grain diameters, the used filter diameters were smaller than the computed ones.

Table 5–1 compares the computed maximum toe stone diameter for each of the Test series with the finally used filter stone.

Test series	Meer, van der [1998]	Model
	D_{n50} (m)	D_{f50} (m)
1	0.022	0.014
2	0.020	0.013
3	0.016	0.096
4	0.016	0.068
5	0.018	0.096

Table 5–1 Maximum computed toe stone diameter for each Test series in comparison to the used filter grain diameter.

In general, despite that in all the cases a smaller filter stone was used, no considerable instability or filter damage was observed. During the initial stages of some of the tests, some stone movement took place. However, as the test was proceeding, stones were moved to more stable positions and after that no movement was observed. Filter thickness remained intact in all test cases.

Especially for Test series 1, where a wide graded filter was tested, the smaller aggregates of the filter were wiggling during the test. Nevertheless, significant damage of the filter did not take place. In addition, the most extensive movement was observed in Test series 3 and particularly in Tests3a & Tests3b. Likewise to Test series 1 filter was not washed out. The same also holds for Test series 4 where the smaller filter diameter was used.

5.2.2. Hydraulically stable or unstable geometrically open filter?

Based on the theory for geometrically open, hydraulically stable geometrical filters, optimum economical design is obtained when filter and base layer start to move simultaneously. In the present study, a Jonswap wave spectrum was used, implying the existence of a variety of wave height & wave period combinations; thus different wave orbital and shear velocities. Thereby, the behavior of the filter configuration (hydraulically stable or transport filter) is strongly related to its reaction on the loading.

For the present study, even for the most severe (loading) combination the filter layer proved to be stable. In contrast to that, base layer movement was observed during most of the test duration. Consequently, for most of the test duration, filter configuration was ranging on the hydraulically unstable regime (transport filter). Additionally, under the loading combinations which base layer was not moving, filter layer was stable and thus over-dimensioned geometrically open filter. Despite that, it is difficult to exactly specify the critical velocity (or wave height/period combination) for base layer's threshold of motion, it is considered that its magnitude is not sufficient in order to cause movement of filter material. The reason for that is mainly due to the use of a lightweight material as a base layer; for this filter base layer combination simultaneous movement is unattainable.

5.2.3. Transport mechanisms

Filter layer was geometrically open; thus base material was able to pass through the voids of filter and be transported out of the filter configuration. In general, the three known modes of transport were observed during the tests: bed load transport, suspended load transport and sheet flow transport.

In general, bed load transport was the dominant mode of transport and the one responsible for the formation of the S-curve erosion/deposition pattern observed for most of the tests. Thereby, the steady, wave-induced streaming was transporting base material back and forth. However, the net sediment transport was directed offshore.

Simultaneously, as the waves become longer and higher, suspended load transport was also taking place in the form of winnowing. In particular, turbulence intensity was being enhanced and velocity fluctuations in time were sufficiently strong to form a cloud of base material that was able to move through the voids of filter layer. Figure 5-1 illustrates this mixed-mechanism.

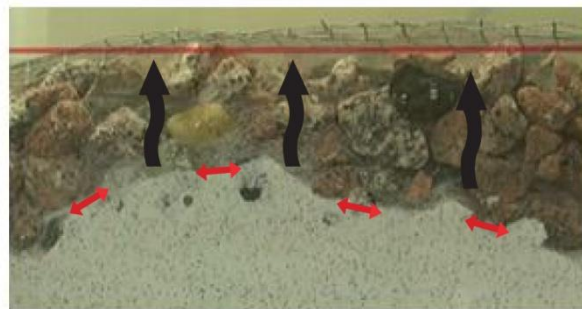


Figure 5-1 Cloud of suspended base material (winnowing) and bed load transport at the interface between filter and base layer.

Occasionally, for the largest waves, the whole transitional base layer (surface of base layer) was fluidized and transported by the water particles (Figure 5-2). During sheet flow transport the incumbent filter layer was able to settle easier into the base layer. Indeed,

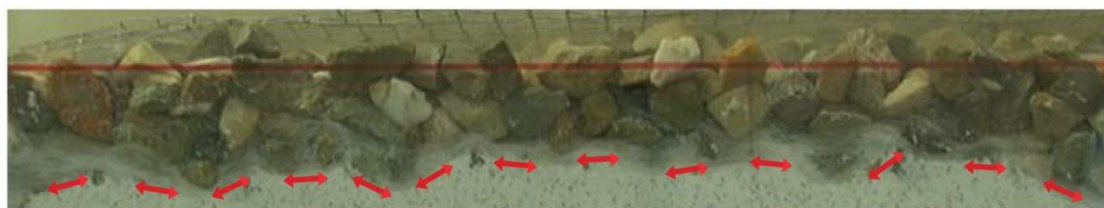


Figure 5-2 Sheet flow transport during severe wave loading. Filter material was able to settle more easily into the underlying base layer.

5.2.4. Erosion pattern & equilibrium state

Every test was captured with a video camera through the right side glass of the flume. Afterwards, snapshots were taken under specific time intervals and were digitized in order to get insight into the erosion/deposition pattern and to specify the existence of equilibrium state.

Generally, for Test series 1, 2 & 3 an S-curve erosion/deposition profile developed at the side glass. The curve's characteristics were enhanced when longer and higher waves were

attacking the structure. For tests with shorter waves the curve's characteristics were less discrete. On the contrary, Test series 4 & 5 did not reveal any specific pattern.

A mutual observation for almost all the tests (namely Tests: 1b, 1c, 1d, 1e, 2a, 2b, 2c, 2d, 2e, 2f, 3a, 3b, 3d, 4d, 5b, 5c, 5d) is that erosion started immediately at the downstream side of the box while further downstream a small bar (sill) was formed. This observation is in agreement with the scour patterns for irregular waves obtained by Sumer *et al.* [2000] and implies that breakwater stability is threatened by scour formation. For only few cases the scour hole was formed in the middle of the box (Tests 1a, 3c, 3e) or more than one scour holes appeared at the center of the box (Tests 4e, 5a). Finally, in Test 4a the base layer remained intact.

On the other hand, no clear conclusion can be drawn with respect to whether the equilibrium state has been reached or not. The problem is that for more than half of the data set the scour depth reaches a maximum value; however, scour hole continues to expand towards the horizontal direction. In general, Tests 1b, 1c, 1d, 1e, 2b, 2d, 2f, 3d, 3e, 4d, 5b have reached or are very close to reaching equilibrium maximum scour depth. Tests 3b & 3c were also close to reaching this point. In contrast to them, the maximum scour depth was still developing in Tests 1a, 2a, 2c, 2e, 3a, 4e, 5a, 5c, 5d. Finally, most of the tests with longer waves, arrived into equilibrium after around 100min, while for tests with shorter waves equilibrium was reached sooner (60-80min).

Overall, the deposition part (bar) was arriving into equilibrium even sooner (often after 50min) and without distinction with respect to the period of the attacking waves.

Laser profiling could not assist in this part of the analysis, since during the removal of the filter layer part of the deposition area (bar) was also being removed. To examine whether observations taken from the side glass are representative for the whole width of the flume, the final erosion/deposition profile taken from the side glass, was compared to the average cross section calculated from the laser profile measurements (analytical results offered in Chapter 4).

In Tests 2a, 2c, 2d, 3a, 3b & 3d the magnitude and shape of erosion profile were identical for both measurements. This was not the case for Tests 1a, 1d, 1e, 2b, 2f & 3e where the shape was similar but the magnitude was found to be exaggerated in measurements taken from the side glass. In Tests 3c, 4d, 4e, 5a, 5b & 5d the magnitude of scour hole was similar; however the shape was not consistent between the measurements. Finally, in Tests 1c, 4a & 5c there was no similarity in shape or magnitude of scour patterns. Consequently, a general conclusion cannot be drawn.

Furthermore, the presentation of base layer laser measurements had revealed the spatial character of scour hole formation. Thereby, different scour holes can form in various locations and can develop with different time scales. It seems that waves locate weak spots in the filter layer and focus their attack on these places.

In the end, it was found that in most of the cases, the properties of different scour holes converged into specific values; however it is safer to admit that conclusions extracted from

this analysis correspond only to the particular erosion/deposition profile that could be examined through the glass.

5.2.5. Video capturing from below (through flume's bottom)

The pursuit behind the placement of a video camera below the flume was to capture the temporal evolution of scour over the entire width of the flume. For that reason the downstream side of the box was made of transparent material (glass) in order to allow video capturing. However two major problems have arisen:

- The breakwater was placed upon a 1.8cm thick wooden plate. This implies that a scour hole deeper than 2cm is needed in order to be captured with the video camera.
- In the area below the foreshore particle velocities are lower; thus suspended sediments can settle on the flume bottom. Then, the trapped sediments hindered the visibility of the video camera; thus video quality was reduced.

In general, these videos cannot be utilized further in the analysis. Nevertheless, videos from the following tests were successfully captured to display the evolution of scour:

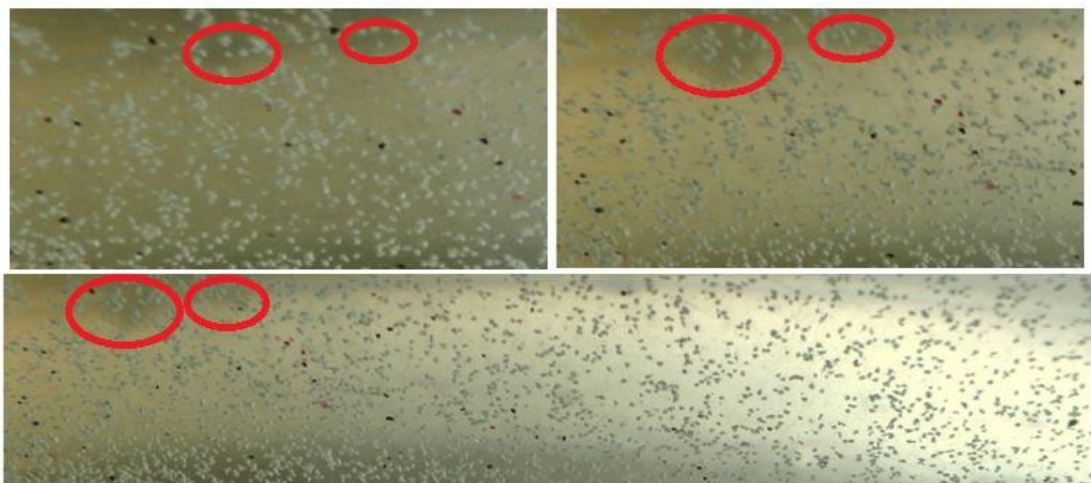


Figure 5-3 Scour development over the flume's width. View from below the flume. Upper left t=150min. Upper right t=250min. Down t=305min

5.2.6. Filter profile measurements

Prior and after the execution of each test the filter surface was profiles with the laser. However, the extracted data cannot be further utilized for the following reasons:

- The selected measuring step was 4-5 times larger than selected filter grain diameters. In general, the measuring step should be in the order of the grain diameter of the measured surface in order to capture the occurring individualities. However, due to time limitations it was not possible to measure with such precision.
- The captured signal contained a lot of spikes. To filter out the spikes a higher degree polynomial or an interpolation method could be used. However, this neglects the case were part of the base layer is exposed in between the filter stones. Therefore, large errors could have been introduced.

- The filter layer was found to fully follow the erosion deposition profile of the base layer. Therefore, analyzing the captured signal for the base layer is sufficient.

Figure 5-4 displays the raw measurement of the filter layer for the case of Test1a.

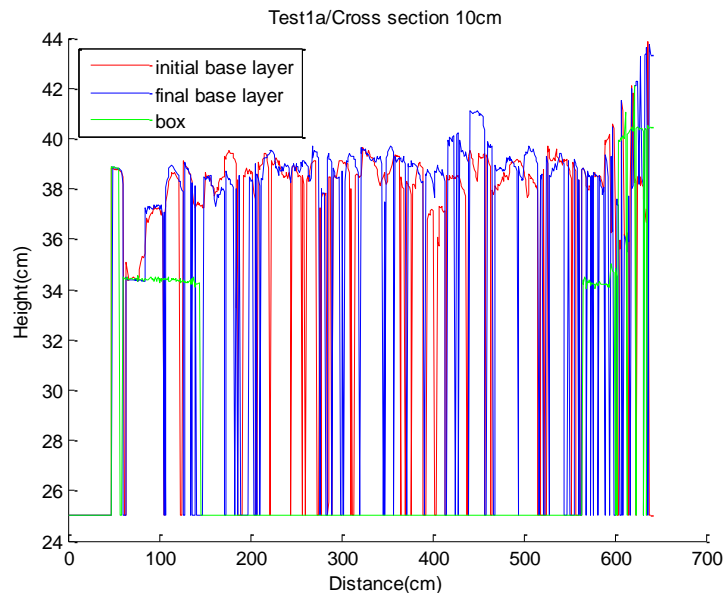


Figure 5-4 Raw filter profile measurements of Test1a at 10cm from the right side glass

5.2.7. Weight of removed base material

After the conduction of every test, the filter layer was being removed so that the laser could profile the base layer. However, during the removal of filter layer, base material was unintentionally removed (especially from the deposition area). To quantify the amount of removed base material, filter material was sieved and weighed. Finally, on this quantity was added the amount of base material that was eroded and found upstream of the box.

The volume of the removed base material is an indication of amount of damage and normally should be equal to the volume of erosion of the base layer. Further use of these data depends on the parameter that will be selected in order to specify the amount of damage. In general, it is suitable in case that a van der Meer type of Damage Number will be selected to quantify the level of damage.

5.3. Test validity

A major aspect behind the validity of physical model testing is the possibility to repeat a test under the same boundary conditions and acquire similar or proportional results. For that reason, before further analyzing the test results, tests with identical boundary conditions are being compared with respect to the averaged maximum scour depth and the location of scour patterns. Afterwards, measurement errors and laboratory effects are discussed briefly, in order to assist in setting up a valid and trustworthy analysis.

5.3.1. Test repeatability

Test repeatability is treated based on the convergence of not of two aspects; averaged maximum scour depth and location of scour holes. Identical tests are: Test1a with Test1e, Test2d with Test2e, Test4a with Test4d & Test4e. These pairs of tests have the same loading parameters and filter configuration set-up.

Averaged maximum scour depth

Figure 5-5 plots the averaged maximum scour depth for each of the aforementioned pairs. In particular, the maximum scour depths are taken from every cross section and then they are averaged over all the cross sections.

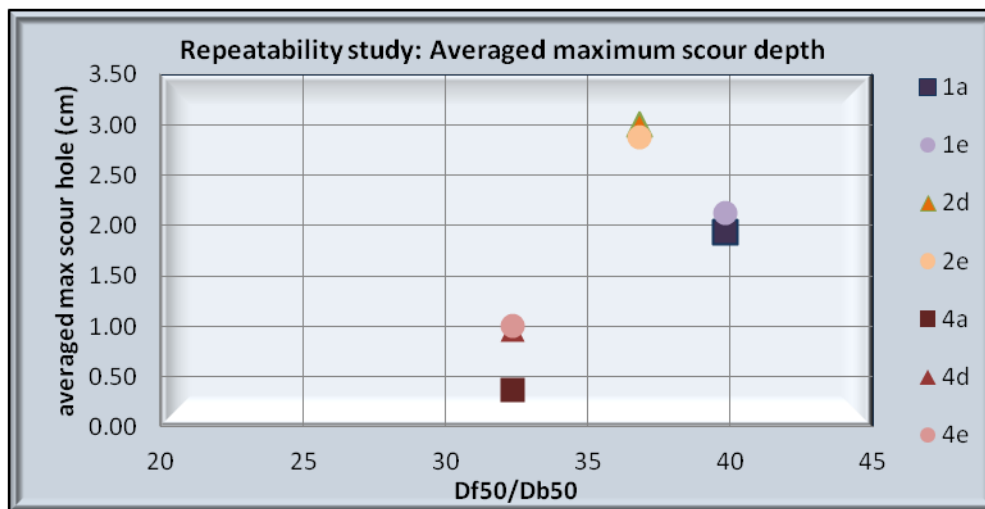


Figure 5-5 Comparison of maximum scour depth between identical tests

Consequently, the averaged maximum scour depth converges in the identical tests of Test series 1 and Test series 2. The same holds also for Test4d and Test4e; however Test4a diverges a lot with a 66% smaller averaged maximum scour depth. On the other hand; the amount of damage for this tests is very small and thus scour depth error is relatively increased (contribution of human factor).

Therefore, in general test repeatability for averaged maximum scour depth was successful except from Test4a.

Location of scour holes

Even in the case of identical tests, scour holes did not form in the same positions. The reason for that is mainly the character of this phenomenon which is highly spatial and depends on the weakness of the filter layer; a weak spot in the filter layer is traced by the waves and then erosion is generated and expanded from this location.

To identify the differences between similar tests, the base layer level change of the second test is deducted from the first. Positive values (marked with deep red color) address to larger scour depth for the second test. The reciprocal stands for the deep blue colors.

Figure 5-6 plots the difference in base layer level change between Test1a and Test1e. Differences occur in the upper half of the box. The reason for them is that for Test1a major scour hole was located in the center part of the box, while for Test1e it was located in the

upper right. However, when Figure 4-3 & Figure 4-15 are examined, it can be observed that the scour hole pattern has almost identical properties (depth, shape, length and width).

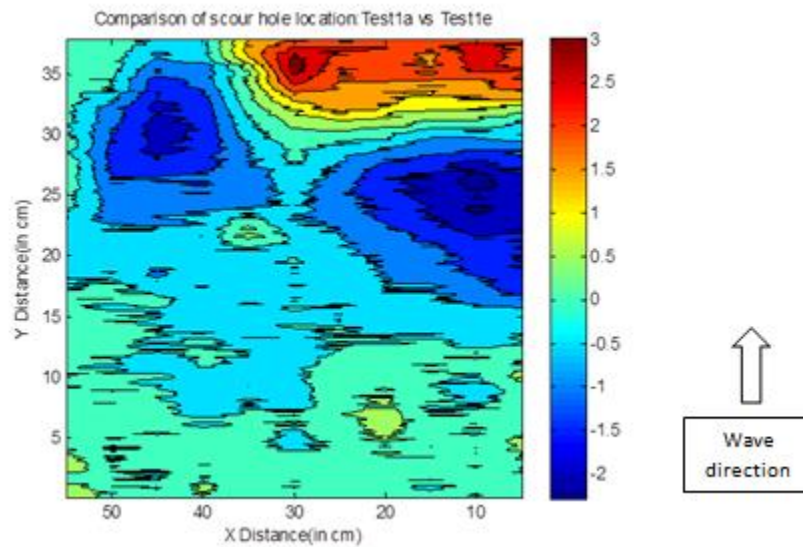


Figure 5-6 Comparison of scour hole location Test1a-Test1e

For the case of Test2a and Test2e the difference is negligible. Scour patterns are identical and only minor differences occur with respect to scour depth at specific locations (see also Figure 4-18 & Figure 4-31).

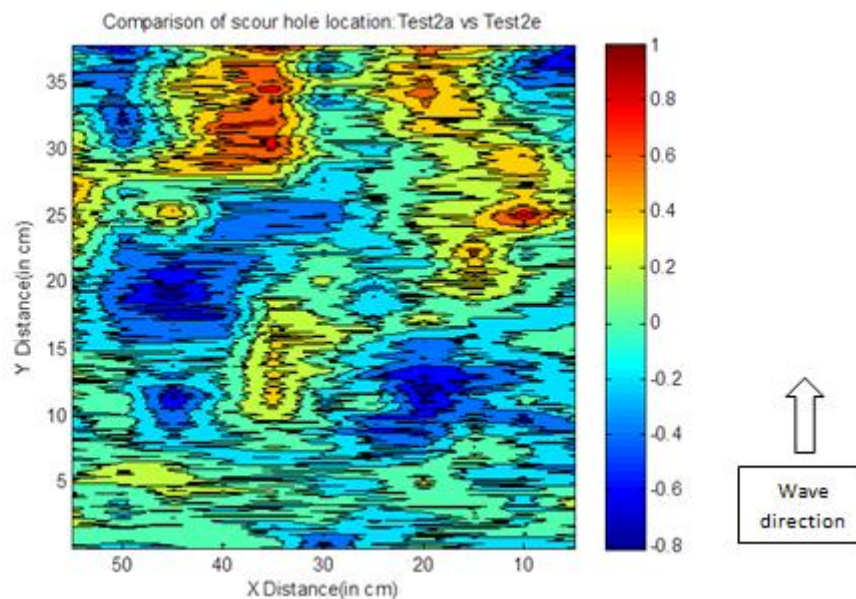


Figure 5-7 Comparison of scour hole location: Test2a-Test2e

Finally, for Test4d the major scour hole was formed at the upstream side of the box in front of the breakwater (Figure 4-55). On the other hand, base layer in Test4e was eroded in the mid-box area (Figure 4-58). Therefore, for the two tests scour pattern and location shows considerable differences (Figure 5-8).

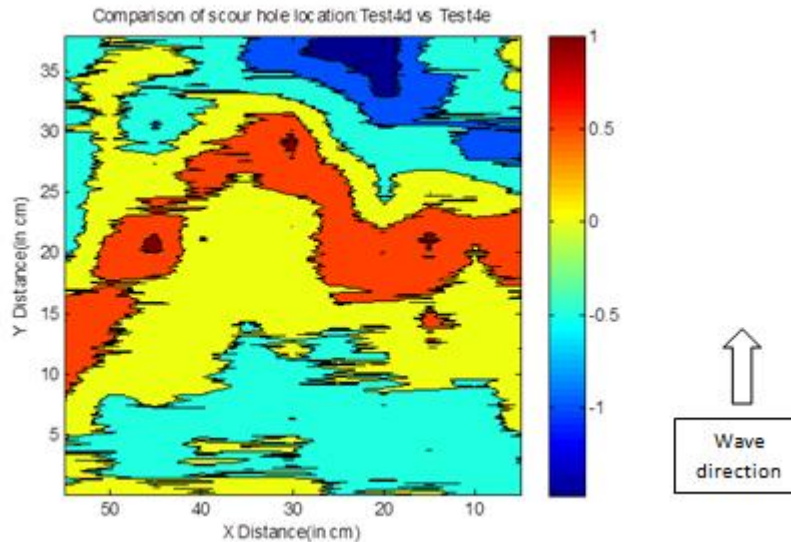


Figure 5-8 Comparison of scour hole location: Test4d-Test4a

5.3.2. Measurement errors

Apart from the human factor, all measuring devices have a certain accuracy and error. Wave gauges have a standard error of 0.5%. The EMS has also a standard error of 0.6% for the longitudinal velocity and 0.5% for the transversal. Additionally, digitization of the extracted snapshots is expected to have introduced an error in the order of 1-2mm plus a 1mm error due to the use of the measuring tapes during the photo scaling process.

5.3.3. Laboratory & model effects

Three effects can be recognized as major laboratory effects that need to be treated with care, so that analysis is not infected by the introduced errors. In particular, the major laboratory effects are: clear water scour, side wall effect and spatial asymmetry error.

Exaggeration of maximum scour depth

In the present study, the seabed was consisted of a granular lightweight material (plastic abrasive). Due to its lower density, there was difference between the buoyancy of base and filter layer. As it was mentioned in Paragraph 5.1.2, this difference had two major consequences. Firstly, when the flume was filling with water, filter layer was already settling inside the base layer, causing initial damage. Secondly, when set into motion, base material was settling slower than normal; therefore, during the test the settling of filter layer inside the base material was enhanced. Consequently, in the present study maximum scour depth and amount of erosion are being overestimated.

Transition-induced scour

To reduce the amount of lightweight material used in the experiments, a tracer model was built. In particular, the movable base material was placed inside a box (L x W x D: 43cm x 60cm x 9cm) which was then placed at the toe of the breakwater. However this has created an inevitable model effect; scour at the transition zone. Figure 5-9 displays the formation of artificial scour due to the transition zone between the wooden foreshore and the box that contains the movable material.



Figure 5-9 Test4d; clear water scour at the upstream side of the box

Possible locations for the formation of artificial scour are the upstream and the downstream edges of the box. For the downstream edge (next to the breakwater) the problem is less since it is the area where the maximum (due to live bed scour) scour depth is expected (reported by Sumer *et al.* [2000]). In order to mitigate this problem, the first 4cm at the upstream edge of the box and the last 2cm from the downstream edge are deducted from the analysis.

Furthermore, some pilot tests were executed without filter protection in order to determine maximum scour depth for the case of no protective layer. However, these tests were unsuccessful due to model effects. In particular, in the formed scour pattern a single scour hole was formed at the middle of the box and no deposition area was shaped. This type of scour is completely irrelevant to the present study. It is generated in the transition zone between the wooden foreshore and the box that contains the seabed material due to the limited dimensions of the box. Therefore, equilibrium maximum scour depth for the unprotected seabed was not determined.

Side wall effect

The irregularity of the filter layer is interrupted in the area next to the wall; therefore larger voids are expected in the transition between filter and glass. Consequently, a spatial enhancement of the erosion would be inevitable. To counteract this, the first measured cross section that contributes into the analysis is located 5cm from the flume's glass.

Spatial asymmetry error

Scour formation is a strongly spatial phenomenon. If the investigation would be limited into the observations through the side glasses it will neglect significant information. For that reason, the analysis of maximum scour depth would be based only on the profiled cross sections that were measured with the laser. Indeed, it was found that in most of the cases the maximum scour depth was located at the nearest to the glass cross sections. To absorb any artificial exaggeration of the measured scour depth, the data from the cross sections would be averaged over the flume's width. The forthcoming Chapter would provide more information into the analysis.

6. Quantitative analysis

Chapter 6 contains the quantitative analysis of the conducted physical model tests. The objective of this chapter is to draw the link between the temporal evolution of maximum scour depth and the boundary conditions in the form of wave loading and filter geometrical properties. This subject is treated with respect to time (Section 6.2) and with the aim to arrive to a general prediction tool (Section 6.4) that best describes the conducted data set.

Afterwards, is tested the performance of eq. (6-7) by comparing its output with a modified expression of eq. (2-3) and part of the data set from Sumer et al. [2000]. This is accomplished via two examples. Finally, the range of applicability of eq. (6-7) is discussed with respect to the findings from the analysis.

6.1. Calculation of test parameters

This section presents the result of the performed calculations in order to determine all the necessary parameters that can be used to describe the test outcome. In specific, it provides the results of the analysis with respect to the wave loading parameters, velocity measurements and additional important parameters that will be used further into the analysis. Afterwards, Paragraph 6.1.4 elaborates on the specification of damage so that an objective link could be formed between scour formation and loading/geometrical conditions. Finally, the deduction from the analysis of tests with unrealistic results is discussed in Paragraph 6.1.5.

6.1.1. Wave loading properties

Earlier, in Chapter 5 and in the primary results for every test were presented between tables Table 4–1 to Table 4–27. Table 6–1 assembles the main wave loading parameters for all tests. In addition, it provides the calculated wave length $L_{t,p}$ at the toe of the breakwater and the corresponding Iribarren Number $\xi_{t,p}$ and relative water depth $h_t/L_{t,p}$.

Test Series	N ₀ (-)	N _p waves	Time (s)	T _m (s)	T _p (s)	H _{rms} (m)	H _s (m)	H ₁₀ (m)	L _{t,p} (m)	ξ _{t,p} (-)	h _i /L _{t,p} (-)
1	Test1a	2987	6017	2.01	2.485	0.08	0.120	0.13	4.12	5.97	0.073
	Test1b	2953	4922	1.67	2.032	0.08	0.120	0.13	3.31	4.89	0.091
	Test1c	3025	6186	2.05	2.485	0.07	0.101	0.11	4.12	6.51	0.073
	Test1d	3027	6089	2.01	2.485	0.08	0.115	0.12	4.12	6.10	0.073
	Test1e	3130	6228	1.99	2.485	0.08	0.119	0.13	4.12	6.00	0.073
2	Test2a	3042	6129	2.02	2.485	0.08	0.117	0.12	4.12	6.05	0.073
	Test2b	2976	4949	1.66	2.032	0.08	0.119	0.13	3.31	4.91	0.091
	Test2c	3012	6136	2.04	2.485	0.07	0.097	0.10	4.12	6.65	0.073
	Test2d	3012	6033	2.00	2.485	0.08	0.115	0.12	4.12	6.10	0.073
	Test2e	3026	6069	2.01	2.485	0.08	0.116	0.12	4.12	6.08	0.073
	Test2f	5994	11965	2.00	2.498	0.08	0.118	0.13	4.14	6.06	0.072
3	Test3a	2960	5941	2.01	2.485	0.08	0.114	0.12	4.12	6.13	0.073
	Test3b	2945	4924	1.67	2.032	0.08	0.120	0.13	3.31	4.89	0.091
	Test3c	3012	6142	2.04	2.485	0.07	0.098	0.10	4.12	6.61	0.073
	Test3d	2885	5885	2.04	2.485	0.08	0.109	0.12	4.12	6.27	0.073
	Test3e	7269	14589	2.01	2.485	0.08	0.113	0.12	4.12	6.16	0.073
4	Test4a	2896	5844	2.02	2.485	0.08	0.118	0.13	4.12	6.02	0.073
	Test4d	2806	5622	2.00	2.485	0.08	0.118	0.13	4.12	6.02	0.073
	Test4e	3013	6051	2.01	2.485	0.08	0.117	0.13	4.12	6.05	0.073
5	Test5a	3167	6379	2.01	2.485	0.08	0.119	0.13	4.12	6.00	0.073
	Test5b	2929	4879	1.67	2.032	0.09	0.121	0.13	3.31	4.87	0.091
	Test5c	3168	6457	2.04	2.485	0.07	0.102	0.11	4.12	6.48	0.073
	Test5d	5995	11978	2.00	2.498	0.08	0.120	0.13	4.14	6.01	0.072

Table 6–1 Comprehensive table for the properties of wave loading

The calculation of $L_{t,p}$ is carried out via the use of Fenton approximation (Holthuijsen [2007]) and peak period. In addition, the outcome of relative water depth $h_i/L_{t,p}$ calculation shows that the executed tests are placed into the intermediate waters regime. Here, the use of peak period & significant wave height is preferable than other forms (i.e. T_{m0-1} & $H_{2\%}$ for shallow waters). Therefore, for the present study all calculations and analysis are based on the use of T_p and H_s extracted from the signal obtained by the nearshore wave gauges. Finally, for this case the number of the waves N is calculated based on the mean spectrum period T_m (according to the software that controls the wave generator).

6.1.2. Velocity measurements

Section 3.3 mentioned the use of an Electromagnetic Flow Meter (EMS) to obtain the velocity measurements at the center of the breakwater's toe. The probe of the device was placed at 6cm above the toe surface and was capturing the instantaneous voltage with a frequency of 100Hz. Afterwards, the obtained signal (voltage=f(time)) was transformed to velocity time series via the device's calibration formula:

$$|U| = -0.5428 * 10^{-3}V^2 + 0.1045 * |V| + 0.0046 \quad (6-1)$$

$|V|$ expresses the measured voltage, while the maximum error band is 0.6%. Figure 6-1 displays a snapshot from the velocity time series captured for Test1a. In order to get the absolute magnitude of the water particle velocities, the signal was detrended.

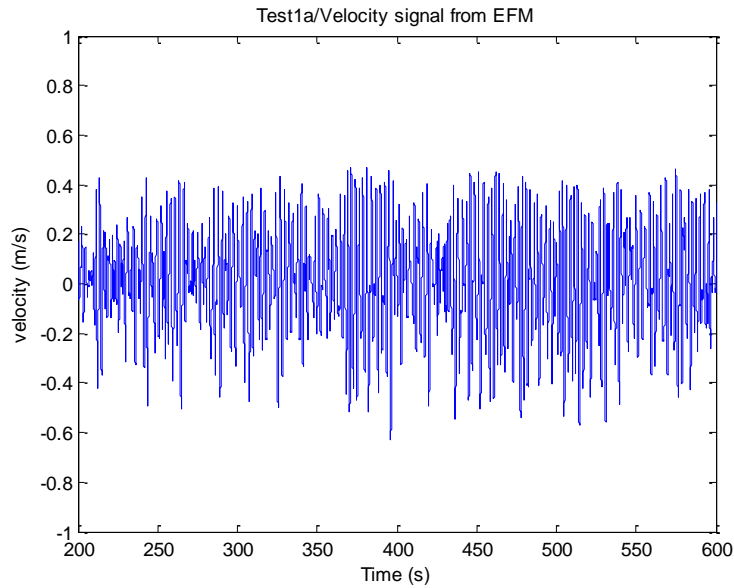


Figure 6-1 Detrended velocity signal for Test1a

The computation of a characteristic velocity magnitude that can be further used in the analysis, can be accomplished either by applying a velocity spectrum analysis, via the use of a Fast Fourier Transformation (FFT), or by just computing the statistical properties of the time series. Both the approaches gave almost the same result with trivial differences.

Using the former approach, the Amplitude Spectrum is firstly computed and then is transformed into Variance Density Spectrum. Figure 6-2 illustrates the VDS for Test1a. Most of the energy is concentrated around the frequency 0.4Hz, which is the frequency that corresponds in the spectrum's peak period (Test1a: $T_p=2.485s$). The area covered with blue corresponds to the spectrum's zero order moment m_0 . By knowing this, statistical properties, such as the significant velocity or the root mean square velocity, can be computed.

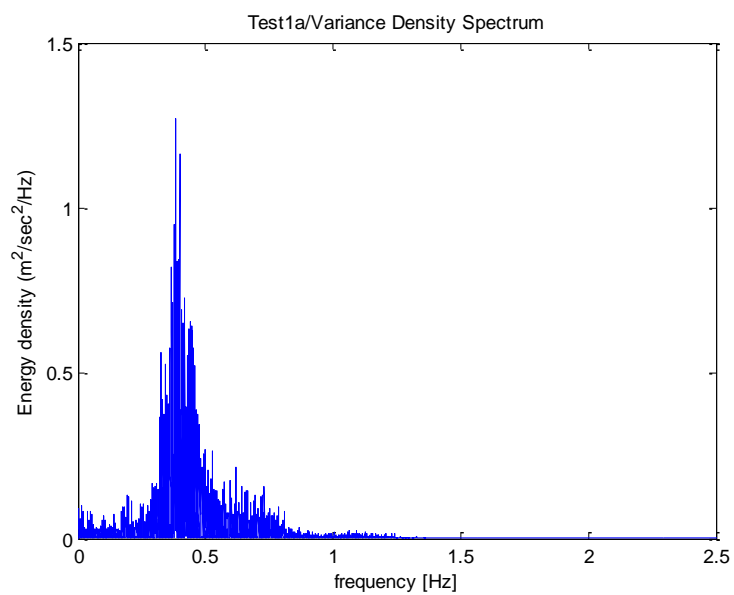


Figure 6-2 Variance density spectrum for Test1a

Additionally, LWT is used to calculate velocities based on the wave height and wave period measurements taken from the wave gauges. Table 6–2 shows characteristic values of the measured velocity (columns 3-5) and the calculated values using the LWT (using index I).

Test Series	N_0 (-)	u_{rms} m/sec	u_{10} m/sec	u_s m/sec	$u_{I,s,p}$ m/sec	$u_{I,m}$ m/sec
1	Test1a	0.198	0.393	0.299	0.334	0.211
	Test1b	0.193	0.381	0.291	0.329	0.210
	Test1c	0.173	0.352	0.261	0.281	0.179
	Test1d	0.213	0.423	0.321	0.317	0.203
	Test1e	0.202	0.400	0.305	0.331	0.211
2	Test2a	0.198	0.393	0.299	0.326	0.209
	Test2b	0.204	0.402	0.306	0.328	0.208
	Test2c	0.167	0.340	0.253	0.271	0.171
	Test2d	0.208	0.412	0.313	0.319	0.204
	Test2e	0.194	0.384	0.293	0.324	0.206
	Test2f	0.200	0.396	0.302	0.329	0.209
3	Test3a	0.187	0.370	0.282	0.320	0.205
	Test3b	0.191	0.377	0.287	0.333	0.214
	Test3c	0.161	0.328	0.243	0.275	0.172
	Test3d	0.197	0.391	0.297	0.305	0.199
	Test3e	0.188	0.373	0.284	0.317	0.205
4	Test4a	0.187	0.370	0.283	0.332	0.215
	Test4d	0.184	0.365	0.279	0.332	0.212
	Test4e	0.187	0.370	0.283	0.330	0.212
5	Test5a	0.190	0.377	0.287	0.334	0.214
	Test5b	0.201	0.395	0.302	0.336	0.216
	Test5c	0.168	0.341	0.253	0.286	0.181
	Test5d	0.193	0.381	0.291	0.337	0.214

Table 6–2 Comparison of velocity measurements with linear wave theory computations

A difference occurs between the measured u_s and the calculated velocity $u_{I,s,p}$ from LWT (using H_s & T_p). To quantify the difference RMSE and BIAS are used. The former expresses the standard deviation of the difference between the two categories and is RMSE=0.034. According to the latter, LWT gives on average higher values than the corresponding velocity measurements (BIAS=0.031).

There are two reasons that explain the aforementioned difference. Firstly, for constructional reasons the wave gauges set is placed in a distance of approximately 1.3m from the probe of the EMS. Thereby, and despite that the foreshore is horizontal, wave breaking was taking place decreasing the representative wave height that was attacking the structure and thus the orbital velocity. Secondly, just above the toe the applicability of LWT is dubious due to the small water depth (almost in the shallow water regime) and the breakwater induced reflection which is considered to enhance the magnitude of water particle velocity.

However, because the difference is generally small and the order of magnitude of the measured velocities is reasonable, it is considered safer to use them further in the analysis. Consequently, each of the values between the columns 3-5 can be used.

On the one hand, velocity u_{10} displays the magnitude of the higher velocities measured in the signal and is computed as the mean value of the highest 10% of the measured velocities. On the other hand, u_{rms} is a more general measure that is closer to the mean velocity of the water particles in the area above the toe. In general, research on the field of threshold of

motion or sediment transport uses maximum velocities. However, during all the tests, transport of base material was observed during most of the test duration; therefore a safer choice is a representative value that lies in between. In particular, the significant velocity u_s is used which is also in accordance with the significant wave height and peak velocity that are used to describe the wave spectrum.

Finally, Appendix D provides representative velocity VDS plots for the case of the three wave conditions & long duration test from Test series 2.

6.1.3. Calculation of important test parameters

On the basis of the parameters presented in tables Table 6–1 & Table 6–2 additional parameters were calculated. These parameters were used to link wave loading and test geometry with the test outcome and with respect to the dimensionless relations presented in Chapters 2 & Appendix A. Table 6–3 illustrates the calculated parameters for each test. Namely these parameters are: Dimensionless grain diameter for filter D_{f*} and base D_{b*} , wave Reynolds' Number $Re_{w,p}$, Shields' Number for filter $\Psi_{f,p}$, base $\Psi_{b,p}$ and critical Shields' Number for base Ψ_{cb} , base material settling velocity $w_{b,p}$, Dean Number for base material $Dean_{b,p}$ and Xie Number for base material $Xie_{b,p}$. Index p is used to annotate that the computation is based on T_p and H_s .

Test Series	N_0 (-)	D_{f*} (-)	D_{b*} (-)	$Re_{w,p}$ (-)	$\Psi_{f,p}$ (-)	$\Psi_{b,p}$ (-)	$\Psi_{cb,p}$ (-)	$w_{b,p}$ (m/s)	$Dean_{b,p}$ (-)	$Xie_{b,p}$ (-)
1	Test1a	359.99	6.10	35217	0.024	0.440	0.040	0.021	2.33	10.11
	Test1b	359.99	6.10	27277	0.028	0.456	0.040	0.021	2.85	9.91
	Test1c	359.99	6.10	26835	0.021	0.358	0.040	0.021	1.96	8.41
	Test1d	359.99	6.10	40590	0.029	0.515	0.040	0.021	2.23	11.20
	Test1e	359.99	6.10	36645	0.025	0.459	0.040	0.021	2.31	10.40
2	Test2a	335.50	6.10	35217	0.025	0.444	0.040	0.021	2.27	10.13
	Test2b	335.50	6.10	30162	0.031	0.506	0.040	0.021	2.83	10.64
	Test2c	335.50	6.10	25215	0.021	0.341	0.040	0.021	1.88	8.06
	Test2d	335.50	6.10	38592	0.028	0.490	0.040	0.021	2.23	10.82
	Test2e	335.50	6.10	33818	0.024	0.428	0.040	0.021	2.25	9.84
	Test2f	335.50	6.10	36115	0.025	0.451	0.040	0.021	2.28	10.26
3	Test3a	240.69	6.10	31326	0.025	0.399	0.040	0.021	2.21	9.33
	Test3b	240.69	6.10	26532	0.030	0.443	0.040	0.021	2.85	9.72
	Test3c	240.69	6.10	23261	0.021	0.314	0.040	0.021	1.90	7.56
	Test3d	240.69	6.10	34748	0.029	0.450	0.040	0.021	2.12	10.09
	Test3e	240.69	6.10	31772	0.026	0.406	0.040	0.021	2.19	9.43
4	Test4a	173.76	3.56	31549	0.026	0.562	0.054	0.011	4.15	17.02
	Test4d	173.76	3.56	30663	0.026	0.546	0.054	0.011	4.15	16.67
	Test4e	173.76	3.56	31549	0.027	0.564	0.054	0.011	4.11	17.03
5	Test5a	240.69	3.56	32447	0.025	0.576	0.054	0.011	4.18	17.36
	Test5b	240.69	3.56	29378	0.033	0.688	0.054	0.011	5.20	18.95
	Test5c	240.69	3.56	25215	0.022	0.472	0.054	0.011	3.58	14.59
	Test5d	240.69	3.56	33532	0.026	0.590	0.054	0.011	4.19	17.69

Table 6–3 Comprehensive table of calculated test parameters

The computation of dimensionless grain diameter D_{f*} & D_{b*} was done according to Sleath [1978] and van Rijn (Schierreck [2004]). Wave Reynolds' Number $Re_{w,p}$ was calculated based on Soulsby *et al.* [2005]. For the determination of critical Shields' Number Ψ_{cb} , Xie[1981] used Bagnold (1966), Sumer *et al.* [2000] used Sumer (1986); however the present study uses the modified diagram of Sleath found in Schierreck [2004]. The reason for that is that in

contrast to the other cases, this diagram provides in a straight forward way, the critical shear velocity for the case of wave action, as a function of dimensionless grain diameter. For the computation of Shields' Number for filter $\Psi_{f,p}$, base $\Psi_{b,p}$ was assumed roughness equal to $k_{r,f}=2D_{f50}$ & $k_{r,b}=2D_{b50}$

Afterwards, Xie Number $Xie_{b,p}$ was calculated based on critical Shields' Number and according to Xie [1991]. Based on that, Test series 1, 2 & 3 lay on the 'coarse' sand regime, while Test series 4 & 5 are in the transition area and towards the 'fine' sand regime. However, it should be noted that the computation refers to the case that no filter protection is applied. When the base layer is protected, loading is being damped and therefore, all tests should be laying in the 'coarse' sand regime. Finally, settling velocity $w_{b,p}$ is computed according to Hallermeier [1981].

6.1.4. Damage specification

The test outcome is the erosion of base layer and the formation of scour holes with different properties (position, depth, length, width). In order to compare the outcome of different tests a parameter is needed that quantifies damage in a representative and objective way.

For that reason, three parameters were deployed; the averaged maximum scour depth S_{aver} , the representative averaged maximum scour depth $S_{max,aver}$ and the damage number S_{dam} . Their computation is based on the comparison of the profile measurements taken with the laser prior and after the execution of a test. Figure 6-3 illustrates the base layer profile measurements prior and after the test for Test1a. The green line in the left picture represents the wooden box.

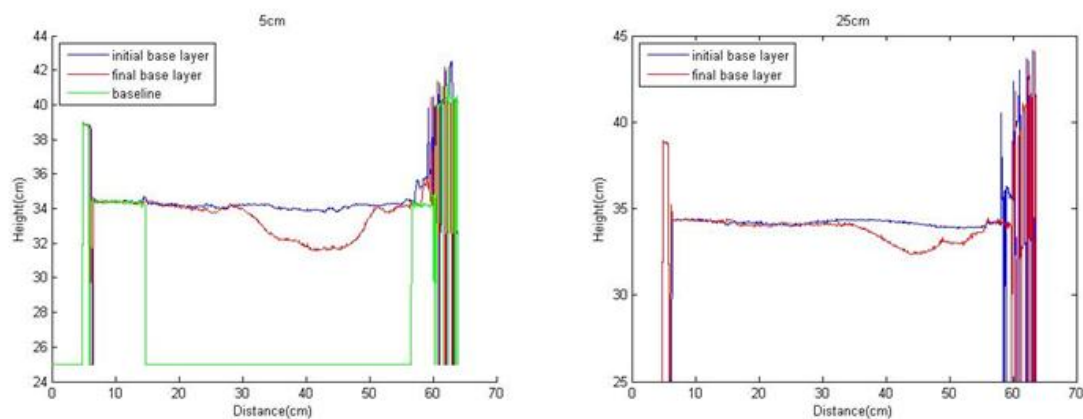


Figure 6-3 Test1a base layer profile measurements prior and after the test. Cross sections 5cm (left) and 25cm (right) with respect to right side glass.

Averaged maximum scour depth S_{aver} : The eleven measured cross sections are averaged over the width of the flume to acquire the base layer's representative average cross section. Then the maximum scour depth of the cross section is the averaged maximum scour depth S_{aver} .

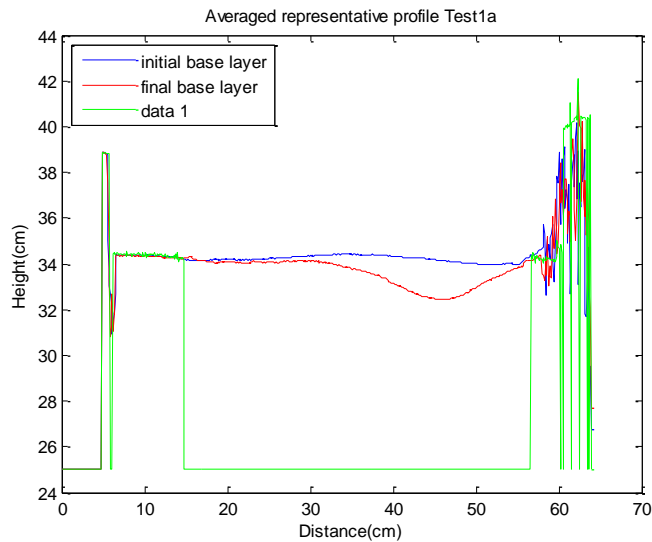


Figure 6-4 Averaged representative cross section for Test1a for the computation of S_{aver} .

Maximum averaged scour depth $S_{max,aver}$: Maximum scour depth is determined for each of the eleven measured cross sections. Then the average of these quantities is the maximum averaged scour depth $S_{max,aver}$.

Damage number S_{dam} : Similar to damage number S used in the van der Meer formulas (Meer, van der [1988]). The area measured after the test is deducted from the corresponding prior to the test and then is divided by D_{f50}^2 of the filter layer. It is a measure of the amount of filter stones that fit into the eroded area in each of the measured cross sections. Finally, the Damage Number for each test is the average of all cross sections.

Table 6–4 displays the values of the three parameters for all the tests.

Test Series	N_0 (-)	S_{aver} (m)	$S_{max,aver}$ (m)	S_{dam} (-)	Test Series	N_0 (-)	S_{aver} (m)	$S_{max,aver}$ (m)	S_{dam} (-)
1	Test1a	0.0175	0.0193	6.28	3	Test3a	0.0184	0.0196	12.51
	Test1b	0.0148	0.0163	4.50		Test3b	0.0063	0.0081	6.02
	Test1c	0.0101	0.0152	5.03		Test3c	0.0082	0.0108	7.34
	Test1d	0.0287	0.0305	9.84		Test3d	0.0221	0.0230	12.42
	Test1e	0.0193	0.0213	5.95		Test3e	0.0135	0.0155	12.94
2	Test2a	0.0253	0.0266	8.64	4	Test4a	0.0019	0.0037	3.93
	Test2b	0.0121	0.0134	3.86		Test4d	0.0062	0.0097	12.52
	Test2c	0.0212	0.0233	6.14		Test4e	0.0068	0.0100	16.13
	Test2d	0.0291	0.0301	9.87	5	Test5a	0.0113	0.0148	9.90
	Test2e	0.0274	0.0288	9.30		Test5b	0.0081	0.0107	7.72
	Test2f	0.0354	0.0367	12.37		Test5c	0.0068	0.0094	8.24
					Test5d	0.0220	0.0276	22.13	

Table 6–4 Representative values for damage specification

Comparison of the outcomes for the Damage Number had displayed inconsistencies in representing the visually observed amount of damage. The Damage Number takes into account the whole cross section; therefore the error introduced by the damage factor (during removal of filter layer) is enhanced. Consequently, it overestimates damage in tests

were erosion is widely spreaded but is less deep. However, a deeper scour hole is more dangerous to cause breakwater failure than a shallower but wider one.

On the other hand, maximum scour depth is a more objective parameter to represent the magnitude of damage for each of the tests. In Chapter 4 and in Paragraph 5.3.1, the inspection of the base layer erosion profile revealed the spatial character of scour formation. For the same test, despite that a large part of the base layer could remain intact narrow but deep scour holes could form in specific locations where the filter was probably weak. In order to account this phenomenon the boundaries of no scour formation and maximum scour depth have to be smoothed out over the flume width to acquire a representative damage level in terms of maximum scour depth.

The difference between the maximum scour depth S_{aver} and the maximum averaged scour depth $S_{\text{max,aver}}$ is trivial. In general, the latter is on average 2.2mm (BIAS) higher than the former. Consequently, each of them can be used further in the analysis. For the present study the choice is made towards the former in order to avoid overestimation of error introduced by constructional imperfections.

6.1.5. Exclusion of Tests

Tests that showed inconsistent or contradictory results need to be neglected from the analysis so that the final outcome would not be infected by the entailed errors. For the present study four tests have given inexplicable outcomes. Based on the values displayed in Table 6–4 the following remarks can be made:

- Test4a showed a negligible amount of damage. The base layer remained almost intact. For that reason Test4d & Test4e were executed as repetitions of Test4a. For these tests the averaged maximum scour depth was doubled. Test4a was the first test executed after the replacement of base material $D_{b50}=360\mu\text{m}$ with $D_{b50}=210\mu\text{m}$. Despite that, a pretest was executed it seems that the configuration had been not adapted properly. For unknown reasons, it is possible that a filter configuration is able to protect the underlying base layer more efficiently than expected. However, this is not the subject of the present study. Therefore, Test4a is neglected from the later stages of the analysis.
- Tests 1d, 2d, 3d were executed in order to get insight into the effect of filter's relative thickness increase. Despite that the loading conditions were identically reproduced these tests displayed a significantly larger maximum averaged scour depth than the corresponding tests with thinner filter thickness. The reason for that was explained in Paragraph 5.1.2 and has to do with the initial damage caused by the different density of filter and base material (different buoyancy). Consequently, this part of the analysis cannot be accomplished and therefore, these tests are neglected from the later stages.

6.2. Temporal evolution of scour depth

In general, as time progresses, scour depth increases. This section aims on determining the properties of the temporal evolution of scour depth and the possibility that common characteristics occur between tests with similar parameters.

To accomplish that, are analyzed videos, captured from the video camera at the right side glass of the flume. Details upon the analysis process and results per each test are offered also in Chapter 4. In brief, snapshots are taken from the video based on predefined time intervals (25min, 20min) and the availability of the videos and then they are digitized to determine the maximum scour depth in every specific moment. Based on that, comparisons can be made among similar tests and conclusions can be drawn with respect to the temporal evolution of maximum scour depth. Additionally, the deposition pattern was captured; however, it has minor physical importance for this study.

Nevertheless, there are two aspects that should not be omitted. Firstly, results and observations from Chapter 4 revealed the highly spatial character of scour formation; therefore, a safer claim is that this analysis does not represent the temporal evolution for scour depth for a specific test but the temporal evolution of a specific scour hole formed at the right side glass after the execution of a specific test. Secondly, next to the glass the voids between filter layer stones and glass are bigger than the corresponding voids between stones of the filter layer while friction between base layer and glass is smaller with respect to base layer and filter layer. Therefore, it is possible that the observed erosion is exaggerated.

6.2.1. Analysis

Generally speaking, in hydraulic engineering studies, evolution of erosion and damage is expressed with respect to the number of waves N of the design storm event. The same approach is adopted here. Figure 6-5¹⁵ plots the relative maximum scour depth S_t/S_{final} as a function of the number of peak waves N_p (computed by dividing the total test duration with the spectrum's peak period T_p) for WC1. Additional plots for the remaining WCs can be found in Appendix E.

¹⁵ In Figure 6-5 there are cases (i.e. Test4d, Test2f) where as time progresses, maximum scour depth temporarily acquires a smaller value than it used to have. This is caused by a limitation of the analysis procedure. The maximum scour depth in every moment is extracted from snap-shots captured through the right side glass, by marking a curve that follows the transition area between filter and base layer. For some cases, base material is trapped between the filter stones and the glass; thus the exact position of the transition area cannot be specified, since the base of the filter stones is hidden behind the base material. Thereby, it is possible that the level of the transition area lays lower than it observed through the glass.

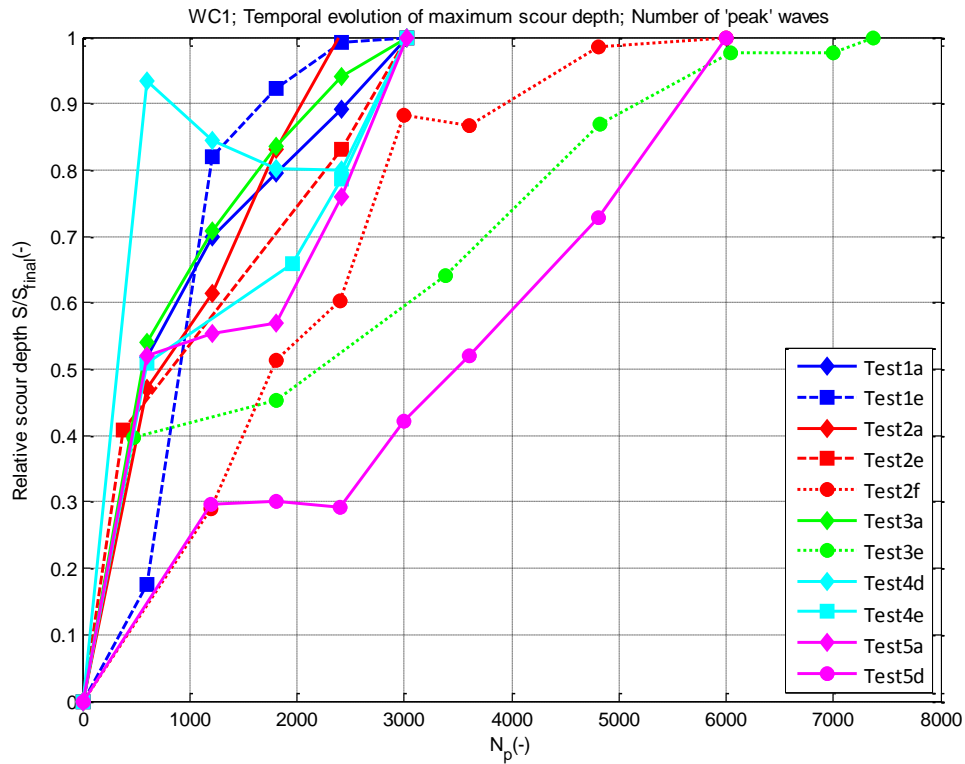


Figure 6-5 Temporal evolution of maximum scour depth as a function of N_p . Measurements taken through the right side glass. All tests with WC1.

Based on the figure above, maximum scour depth growth starts developing quickly at the first stages and after some time it slows down (i.e. Test1a, Test1e, Test2a, Test3a). However, no clear trend can be recognized, since there are cases where erosion starts quickly, then stops and starts accelerating again (i.e. Test5d). In other cases, just at the last stages of the test, scour depth development slows down so much that it seems to arrive in equilibrium state; however in some cases it starts again (i.e. Test5a, Test1b, Test3b).

According to Paragraph 5.2.4 only Tests 1b, 1c, 1e, 2b, 2f, 3e, 4d, 5b have reached or are very close to reaching equilibrium maximum scour depth. Consequently, in a very large part of the data set the maximum scour depth was still developing. In addition, even for tests where maximum scour depth was reached, the formed scour hole was still developing in the horizontal direction.

Thereby, in order to get a more objective measure of the pace of scour depth development, the square root of the number of 'peak' waves $N_p^{0.5}$ is used and plotted against the maximum scour depth. Then, for every test, the best fit line is computed in the form of $S_{final} = \alpha_t * N_p^{0.5}$ where α_t is the slope of the best fit line. A large α_t value corresponds to a fast development of maximum scour depth. In particular, α_t is not dimensionless and represents the mean erosion depth caused per wave for a specific test.

The analysis showed that every test has a unique α_t value. To illustrate the difference among similar tests, Figure 6-6 plots the temporal evolution of maximum scour depth for Tests 1a, 2a, 3a with respect to $N_p^{0.5}$, along with the best fit lines and the corresponding α_t values.

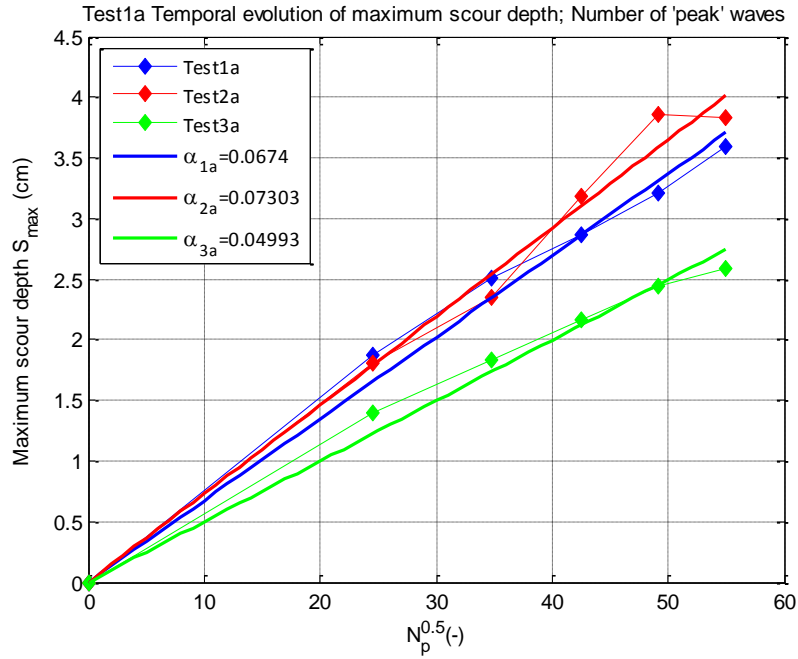


Figure 6-6 Representative plot for Tests 1a, 2a, 3a. Maximum scour depth $S_{max}=f(N_p^{0.5})$. Best fit lines and corresponding α values.

It can be easily observed that under the same wave loading erosion proceeds faster when the ratio D_{f50}/D_{b50} increases (Tests 2a, 3a). Additionally, when a wider graded filter is applied (Test1a), erosion is slowed down with respect to a filter with slightly smaller D_{f50}/D_{b50} (Test2a). Equivalent results were found for the rest of the data set. In general, the correlation of the best fit line was high for the majority of the tests. Results are presented in Table 6–5.

Test Series	N_0 (-)	α_t (cm)	R^2 (-)	Test Series	N_0 (-)	α_t (cm)	R^2 (-)
1	Test1a	0.0674	0.989	3	Test3a	0.0499	0.986
	Test1b	0.0471	0.897		Test3b	0.0301	0.885
	Test1c	0.0588	0.865		Test3c	0.0263	0.895
	Test1d	0.0874	0.970		Test3d	0.0413	0.985
	Test1e	0.0550	0.872		Test3e	0.0318	0.968
2	Test2a	0.0730	0.986	4	Test4a	0.0439	0.868
	Test2b	0.0510	0.992		Test4d	0.0264	0.607
	Test2c	0.0635	0.994		Test4e	0.0258	0.958
	Test2d	0.0655	0.930	5	Test5a	0.0285	0.922
	Test2e	0.0587	0.990		Test5b	0.0358	0.879
	Test2f	0.0698	0.926		Test5c	0.0303	0.952
				Test5d	0.0317	0.806	

Table 6–5 α_t values and R-squared values for every test.

Consequently, maximum scour depth development in time was found to be proportional to $N_p^{0.5}$ with a constant factor α_t . This factor is found to be well correlated with the corresponding data for almost the whole data set; therefore $N_p^{0.5}$ is a parameter that can contribute in the prediction of maximum scour depth given specific storm duration.

Finally, no direct link was found between the constant factor α_t and the wave climate or the characteristics of the filter. Nevertheless, some general trends were traced, namely:

- For tests with the same filter properties and $D_{b50}=360\mu\text{m}$, higher α_t values were found for tests with WC1 and lower for WC3. This does not hold for tests with $D_{b50}=210\mu\text{m}$.
- Among tests with the same wave loading and filter properties, tests with $D_{b50}=360\mu\text{m}$ displayed higher α_t values than tests with $D_{b50}=210\mu\text{m}$.

6.2.2. Discussion

Undoubtedly, the selection of a power function $S_{\text{final}}=\alpha_t * N_p^{0.5}$ is not the optimum way to represent the temporal evolution of scour. A power function implies that as time progresses, maximum scour depth will increase to infinity; however from a physical point of view this is not true. On the other hand, equilibrium maximum scour depth was not reached in a large part of the present data set, while for the tests where equilibrium was reached, this happened just before the end of the test. Furthermore, there were cases where equilibrium seemed to have been reached; however maximum scour depth started to develop again. Consequently, the phenomenon of scour for the largest part of the data set was still in progress. Thereby, a linear approach is a considerably good choice.

Secondly, in order to analyze the temporal development of scour, it is a common practice to express all related parameters in dimensionless way. The optimum selection in this case would be the equilibrium maximum scour depth. Nevertheless, this value is not known for a large part of the data set. Therefore, it was selected to use the absolute value of scour depth.

Nevertheless, in the long-term it is expected that maximum scour depth will reach a maximum value. Consequently, by using only the part of the data set where equilibrium maximum scour depth is reached, a different function can be fitted. Thereby, the temporal evolution of maximum scour depth for Tests 1b, 1c, 1e, 2b, 2f, 3e & 5b can be better described by the following expression:

$$\frac{S_t}{S_{\text{max}}} = 1 - \exp\left(-2.668 \frac{N_t}{N_{\text{max}}}\right) \quad (6-1)$$

Where S_t is the maximum scour depth after ' N_t ' waves ('peak') and S_{max} is the maximum/equilibrium scour depth. Correspondingly, N_{max} is the amount of waves in order to arrive to maximum/equilibrium scour depth. Result is illustrated in Figure 6-7. Additional information with respect to the derivation of eq. (6-1) can be found in Appendix E.

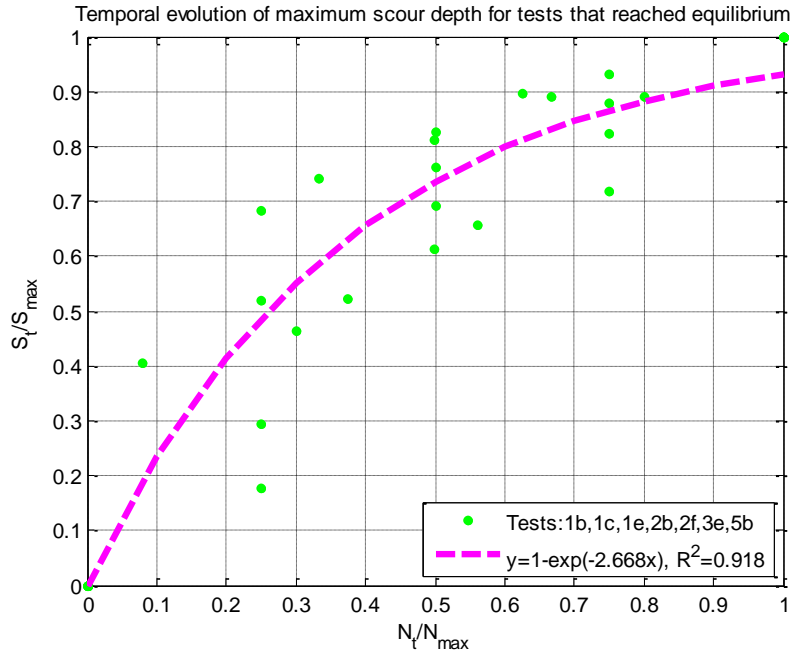


Figure 6-7 Temporal evolution of maximum scour depth for tests that reached equilibrium maximum depth. Tests 1b, 1c, 1e, 2b, 2f, 3e & 5b

6.3. Relations among dimensionless parameters

In Section 6.1 all important loading and erosion parameters were distinguished and presented in Table 6–1 to Table 6–4. The performed computations were based on the significant wave height and peak period from the Jonswap spectrum; however, other statistical spectrum properties could also have been used. Likewise, filter configuration properties can be expressed via a great variety of grain diameter expressions and dimensionless ratios. Additionally, damage specification could be expressed in various ways (Paragraph 6.1.4) resulting in an innumerable amount of loading/erosion combinations.

To deal with that, choices have already been made and argued in the previous sections. Thereby, as damage factor was used the relative scour depth S_{aver}/H_s on the basis of the averaged maximum scour depth and significant wave height. Finally, as loading and stability parameters were used the computed ones on the basis of T_p and H_s .

This section visualizes the most interesting combinations extracted during the analysis of the data. The selected combinations are merely taken from the dimensional analysis presented in Section A-3 at Appendix A and from the dimensionless relations from Sumer *et al.* [2000] discussed in Paragraphs 2.1.2 & 2.1.3. Additionally, plots with other important parameters are also mentioned here.

In this section of the analysis the long duration tests Test2f, Test3e, Test5e are excluded from the graphs while all remaining tests under consideration have a $d_f/D_{f50}=3.4-3.5$. Neglected tests Test4a, Test1d, Test2d, Test3d are visible on the plots; however they are not considered in the analysis.

6.3.1. Relative scour depth with relative grain diameter D_{f50}/D_{b50}

In Figure 6-8 the relative scour depth is plotted with the relative grain diameter in separate figures with respect to the wave loading (WCs). A common characteristic of all the plots is that the magnitude of relative scour depth of Test series 1, 2, 3 is larger than the corresponding values from Test series 4, 5. The difference between them is due to the use of base material with different D_{b50} .

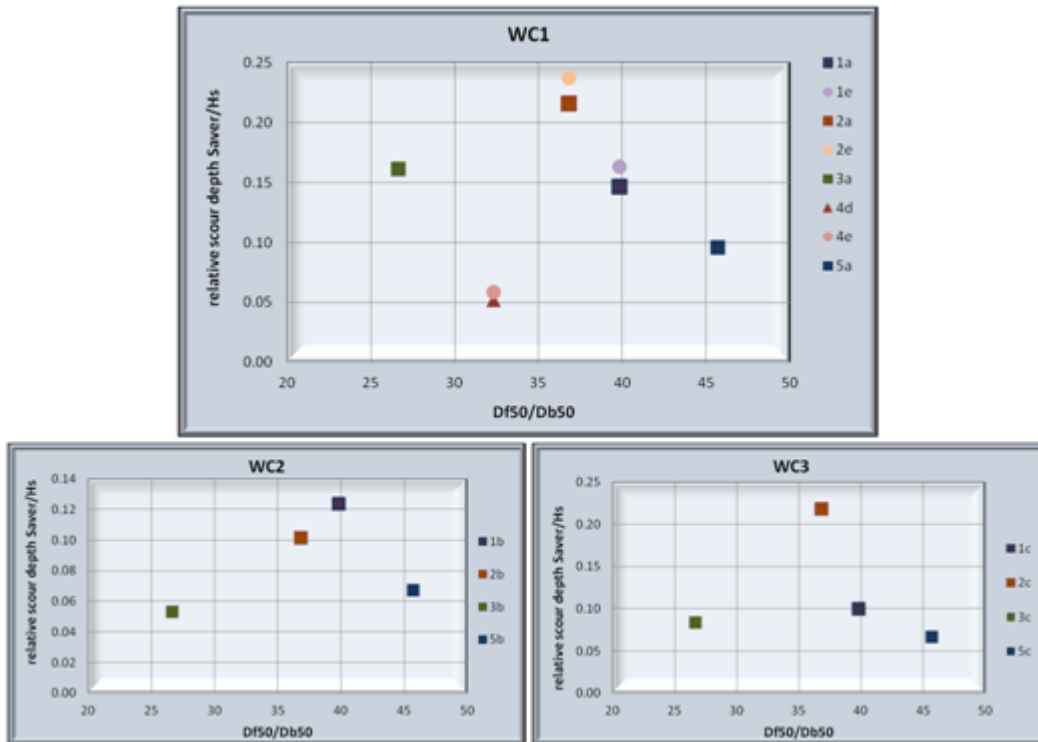


Figure 6-8 Relative scour depth with relative grain diameter in all wave conditions. Upper plot WC1, left plot WC2, right plot WC3

Additionally, if tests from Test series 1 are neglected, due to the fact that a different grading is applied, then a larger D_{f50}/D_{b50} leads in a larger relative scour depth. The linear increase is between Test series 2, 3 and Test series 4, 5 is almost double; however a prediction is not very trustworthy since the available data are very limited (they could even lay in parallel lines). To get more insight, the trend lines are plotted in Figure 6-9. Now y-axis contains the relative scour depth (S_{aver}/H_s).

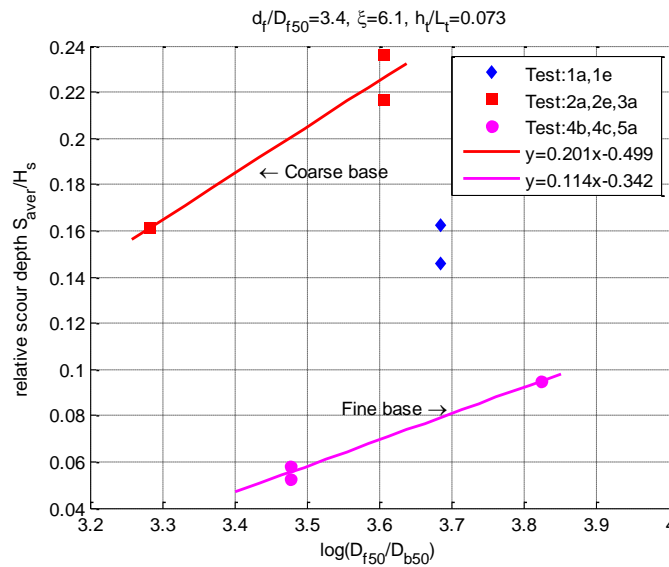


Figure 6-9 Relative scour depth with relative grain diameter. Trend lines for Tests 1a, 1e ($D_{b50}=360\mu\text{m}$, $D_{f50}=1.43\text{mm}$), Tests 2a, 2e ($D_{b50}=360\mu\text{m}$, $D_{f50}=1.33\text{mm}$), 3a ($D_{b50}=360\mu\text{m}$, $D_{f50}=0.96\text{mm}$) and Tests 4d, 4e ($D_{b50}=210\mu\text{m}$, $D_{f50}=0.68\text{mm}$), 5a ($D_{b50}=210\mu\text{m}$, $D_{f50}=0.96\text{mm}$).

Therefore, despite that the relative grain diameter is a dimensionless ratio cannot be linked in a straightforward way with the prediction of relative scour depth. On the contrary, it is found that different base layers (difference in diameter) result in different scour depth magnitudes and different rates of erosion increase (for the same relative grain diameter).

6.3.2. Relative scour depth with critical Shields' Number Ψ_{cb}

Generally, the Shields' formula is expressed via: $\Psi_c = \frac{\tau_c}{(\rho_s - \rho_w)gD} = \frac{u_*^2}{\Delta gD}$. Thereby, the computation of critical Shields' Number is accomplished on the basis of the modified diagram of Sleath (1978) ([Schierck [2004] see also Figure 6-10). In particular, firstly is computed the dimensionless grain diameter D_* , and then Ψ_{cb} is computed graphically.

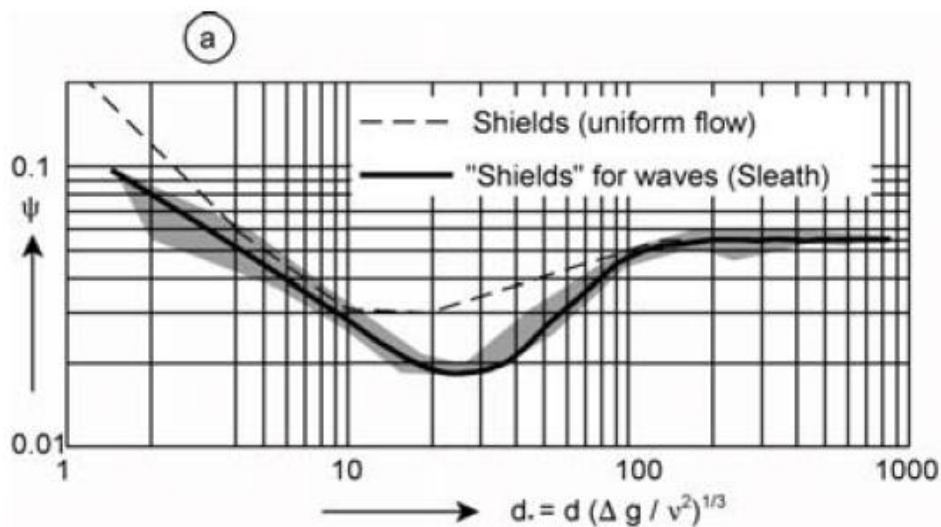


Figure 6-10 Modified Shields' diagram for waves used for the graphical computation of critical Shields' Number Ψ_{cb} (from Schierck [2004]).

In Paragraph 6.3.1 it was concluded that every base layer (D_b , ρ_b) displays a unique behavior in relating grain diameter to relative scour depth. Probably, the major reason for that is the

difference in the critical Shields' Number which is graphically computed from the curve originally designed by Sleath (Schierreck [2004]). From Figure 6-11 it can be seen that in Test series 4, 5 the base layer has a higher stability number although it has the same density with lower diameter. Therefore, for the same loading (wave spectrum) and filter properties the number of waves that cause erosion in Test series 4, 5 are less than the corresponding in Test series 1, 2, 3. Consequently, less sediment transport is expected and shallower scour formation. Finally, it should be noted that based on Sumer *et al.* [2000], Shields Number influences scour hole formation; however they assumed that in live bed scour, the increase of Shields' Number has trivial influence on maximum scour depth.

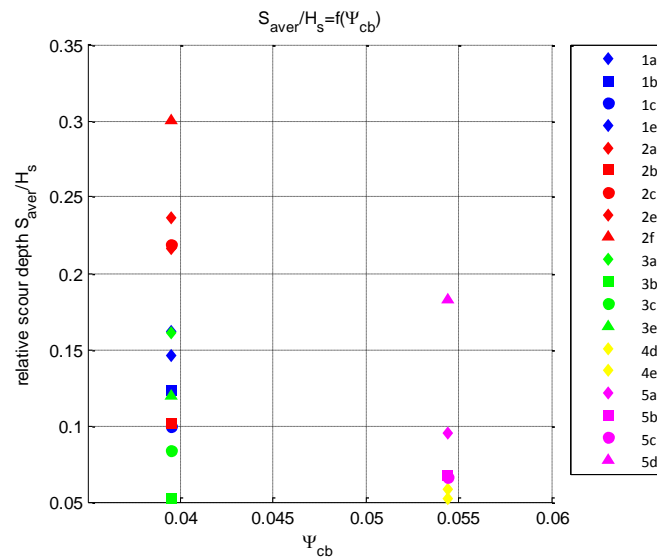


Figure 6-11 Relative scour depth critical Shields' Number for base layer

6.3.3. Relative scour depth with wave Reynolds' Number $Re_{w,p}$

In Figure 6-12 the relative scour depth is plotted with respect to the wave Reynolds' Number. According to Soulsby *et al.* [2005] wave Reynolds' Number is given by $Re_w = \frac{U_w A}{\nu}$ where A is the semi-orbital excursion of water particles given by $A = \frac{U_w T}{2\pi}$. Despite that the cloud is rather scattered, it seems that relative scour depth increases with increasing wave Reynolds' Number. They seem to be linked with a power relation; however specific characteristics cannot be distinguished.

Furthermore, based on Sumer *et al.* [2000] the wave Reynolds Number is among the dimensionless parameters that influence scour formation; nevertheless it was not incorporated in their formula¹⁶ for scour depth prediction. It can represent the magnitude of external loading therefore it is considered significant in the prediction of scour depth for the case where an open granular filter is applied.

¹⁶ Wave Reynolds' Number was not incorporated in the formula based on the assumption that seabed in most engineering problems acts as a rough wall.

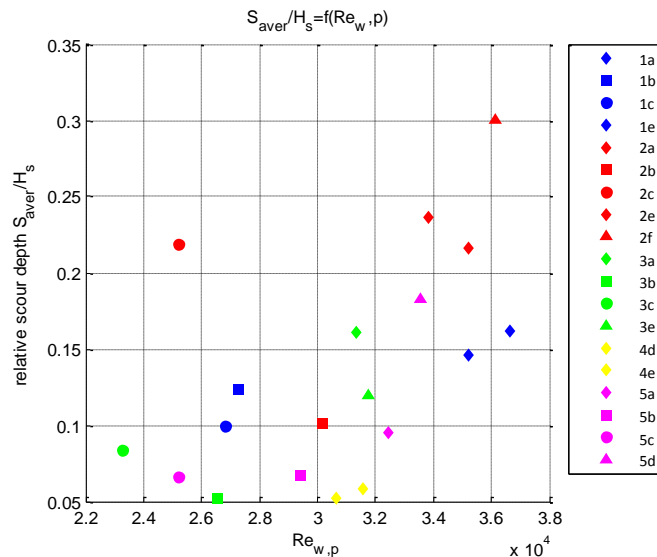


Figure 6-12 Relative scour depth with wave Reynolds' Number

6.3.4. Relative scour depth with relative water depth $h_t/L_{t,p}$

According to Sumer *et al.* [2000], for the same base material, scour depth increases with the decrease of relative water depth. This is also visible in Figure 6-13. Indeed, when tests with WC1 (diamonds) and the corresponding tests with WC2 (squares) are considered, maximum scour depth's magnitude decays.

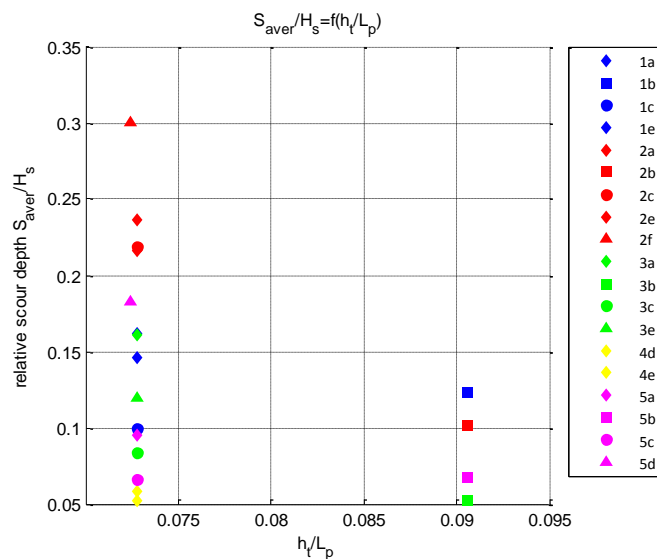


Figure 6-13 Relative scour depth with relative water depth

6.3.5. Relative scour depth with Dean Number $Dean_{b,p}$

Figure 6-14 plots relative scour depth with respect to Dean Number. According to Sumer *et al.* [2000] and Xie [1991], when suspended transport is the dominant type deeper scour holes are formed. Based on the figure, relative scour depth decreases with the increase of Dean Number (dominancy of suspended sediment transport); nevertheless this trend has no relation with the type of transport but has to do with the use of base material with different diameter.

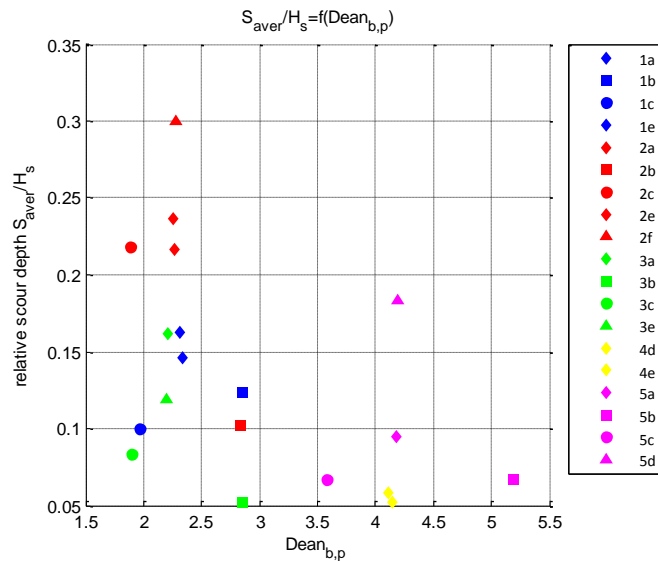


Figure 6-14 Relative scour depth with Dean Number

6.3.6. Relative scour depth with relative thickness d_f/D_{f50}

Figure 6-15 plots relative scour depth with relative thickness for tests with same conditions (geometry, loading) but with different thicknesses. Three test series were tested with respect to relative thickness increase. However, the results contradicted with the expectations. Apart from Test series 2 were the increase was small, the remaining test series showed significantly larger scour depths for larger relative thicknesses.

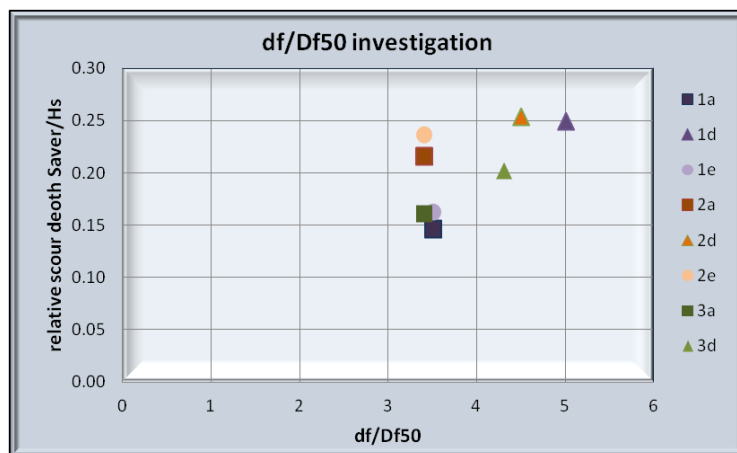


Figure 6-15 Relative scour depth with relative grain thickness

The existing results cannot be easily interpreted; however it is thought that probably the followed testing procedure is more sensitive to filter weight, therefore the larger weight of the thicker filter penetrates more on the smooth base layer and causes residual scour depth that is irrelevant to wave loading. However, in order to arrive in a safe conclusion, additional tests should have been executed.

Furthermore, according to Sumer *et al.* [2000] maximum scour depth decays as the number of protection layers increases. Their conclusion was based on the conduction of 4 tests with exactly the same conditions but with three different d_f/D_{f50} (3, 5, 7). However, when comparing Test31 with Test32, the reciprocal occurs. In particular, Test31 with $d_f/D_{f50}=7$

gave an $S/H=0.34$ and Test32 with $d_f/D_{f50}=5$ gave an $S/H=0.35$. In addition, their experimental procedure had many similarities with the present study.

Summarizing all the above, the amount of tests executed in order to investigate the effect of d_f/D_{f50} on maximum scour depth is not sufficient for a trustworthy conclusion. Consequently, in agreement with 6.1.5, these tests were excluded from the analysis and therefore, the effect of relative thickness increase could not be investigated in this research.

6.3.7. Relative scour depth with Iribarren Number $\xi_{b,p}$

In Figure 6-16 all tests are separated with respect to the Iribarren Number. Despite that it did not appear directly in the dimensional analysis it is a combination of the structural angle α from Sumer et al. [2000] and the term H/gT^2 extracted from dimensional analysis. Generally, it gives information on the type of breaking and contains also the structural slope of the breakwater. The latter, based on Sumer *et al.* [2000] affects also the amount of reflection the maximum run down. Therefore, it affects also the wave climate just above the toe for the breakwater.

Each of the applied WCs forms a cloud that corresponds to a specific range of Iribarren numbers. Therefore, ξ itself is not the dimensionless parameter that forms the connection between the tests. Additionally, it is considered that other parameters have more straightforward relationship with the test results.

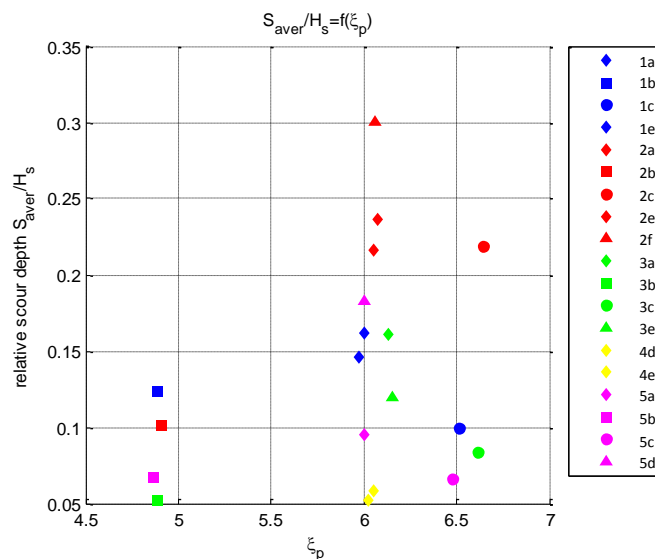


Figure 6-16 Relative scour depth with Iribarren Number

6.3.8. Summary

The analysis performed during this section has revealed the dimensionless quantities that significantly influence scour hole formation. These quantities (critical Shields' Number, relative water depth and possible wave Reynolds' Number) along with the filter configuration characteristics will be combined in the next section in order to arrive into a general formula that links wave loading and filter configuration properties with scour hole formation.

Finally, it should be underlined that there is no direct coupling between the relative grain diameter of the filter configuration and the magnitude of relative scour depth. The use of a different base material leads into a different behavior of scour evolution with respect to its position on the graph of Sleath [1978].

6.4. Scour depth=f(filter configuration geometry, wave loading)

Based on the dimensional analysis of Section A-3 (Appendix A), the findings of Sumer *et al.* [2000] discussed in Paragraph 2.1.2 and the analysis held in Section 6.3, it is considered that the relative scour depth of a sandy seabed is a function of the following dimensionless terms:

$$\frac{S}{H} = f\left(\frac{h}{L}, Re_w, \frac{D_{f50}}{D_{b50}}, \Psi_{cb}, \alpha, \frac{df}{D_{f50}}, N, V_{gr}\right) \quad (6-2)$$

By combining the aforementioned terms a prediction tool could be formulated that relates maximum scour depth to external loading and geometrically open filter properties.

The first four terms have already been discussed previously. The structural slope was not deviated during this research; therefore it drops out from the analysis. Tests with relative thickness increase, failed to give trustworthy results; therefore this effect cannot be investigated in the analysis. Finally, two remaining terms were introduced; the number of waves N is used in order to implement the duration of the design storm while the filter grading V_{gr} was used to interpret the lower relative scour depth that was found for Test series 1 (with respect to Test series 2, 3).

As it was mentioned in Paragraph 6.3.4, only two values of relative water depth h_t/L_t were examined in the data set of this study. On the other hand, Sumer *et al.* [2000] conducted tests with several values of h_t/L_t ranging between 0.05 and 0.2. Based on that, they concluded that the contribution of this parameter in the computation of maximum scour depth is expressed via $\sinh\left(2\pi \frac{h_t}{L_t}\right)^{1.35}$. In the present study the use of only two values of h_t/L_t cannot substantiate a different contribution of this term. Consequently, the term $\sinh\left(2\pi \frac{h_t}{L_t}\right)^{1.35}$ will form the basis of the analysis presented in the next stages.

6.4.1. $D_{b50}=360\mu\text{m}$

Firstly, the results of Test series 2 & 3 are used to investigate relative scour depth in the case of $D_{b50}=360\mu\text{m}$. Despite that Test series 1 have the same base material they are not used here, because their filter layer is wide-graded. For that reason, they will be incorporated in the analysis in a later stage.

Initially, the first four terms of eq. (6-1) are combined in order to deploy the best fit line for the collected data. Figure 6-17 displays the outcome. The values '0.001' and '100' are used to balance the difference between the order of magnitude in the nominator and the denominator (they have no mathematical importance). Based on the best fit line, the

relative scour depth is proportional to the relative grain diameter (to the power 0.85) and inversely proportional to relative water depth (to the power 1.35).

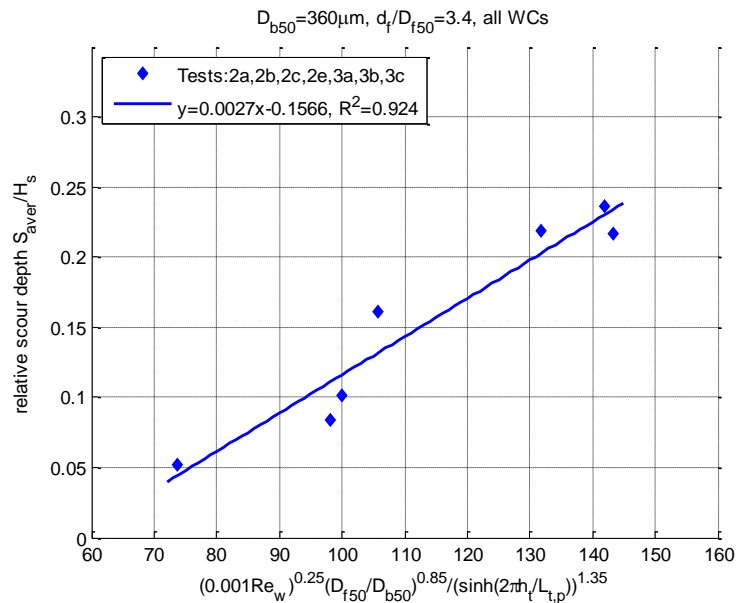


Figure 6-17 Best fit line for Tests 2a, 2b, 2c, 2e, 3a, 3b, 3c. $D_{b50}=360\mu\text{m}, d_f/D_{f50}=3.4$, narrow graded filter layer and all WCs

Wave Reynolds' Number appears also in the relationship; however its contribution is rather small (to the power 0.25). According to Table 6–3 and simple statistical computations the variation of wave Reynolds' Number in the whole data set is around 14%. However, it is possible that a data set with wider range of wave Reynolds' Numbers may reveal that this parameter is decisive for scour depth prediction. On the other hand, from a physical point of view, during storm conditions the bed acts mainly as rough bed (Sumer *et al.* [2000]); therefore the Reynolds' Number can be removed from the equation. However, additional tests need to be conducted to investigate whether this parameter should be included or not. Thereby, the same relation is plotted again in Figure 6-18 without the wave Reynolds' Number:

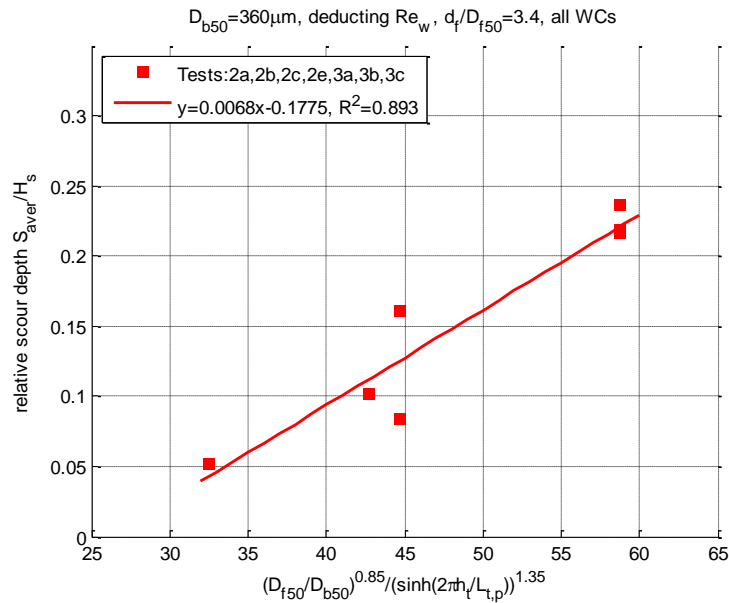


Figure 6-18 Neglecting wave Reynolds' Number. Best fit line for Tests 2a, 2b, 2c, 2e, 3a, 3b, 3c. $D_{b50}=360\mu\text{m}$, $d_f/D_{f50}=3.4$, narrow graded filter layer and all WCs

Despite deducting wave Reynolds' Number, the correlation remained high and close to the one found preciously ($R^2=0.893$ instead of $R^2=0.924$). In addition, the contribution of each of the rest terms remained the same.

Therefore, for this part of the data set, the relative scour depth is best represented as a function of $h_t/L_{t,p}$, D_{f50}/D_{b50} with the following expression:

$$\frac{S_{aver}}{H_s} = 0.0068 \left(\frac{\left(\frac{D_{f50}}{D_{b50}} \right)^{0.85}}{\left(\sinh \left(\frac{2\pi h_t}{L_{t,p}} \right) \right)^{1.35}} \right) - 0.1775 \quad (6-3)$$

6.4.2. $D_{b50}=210\mu\text{m}$

The combination of $h_t/L_{t,p}$ and D_{f50}/D_{b50} for the case of $D_{b50}=210\mu\text{m}$ gave a very low correlation. By introducing $Re_{wb,p}^{1.1}$ the correlation of data improved; however, in order to obtain the best fit line (by also keeping line $(\sinh(2\pi \frac{h_t}{L_t}))^{1.35}$) the interrelation between the powers of $h_t/L_{t,p}$ and D_{f50}/D_{b50} had to change. Figure 6-19 plots the best fit line for this part of the data set.

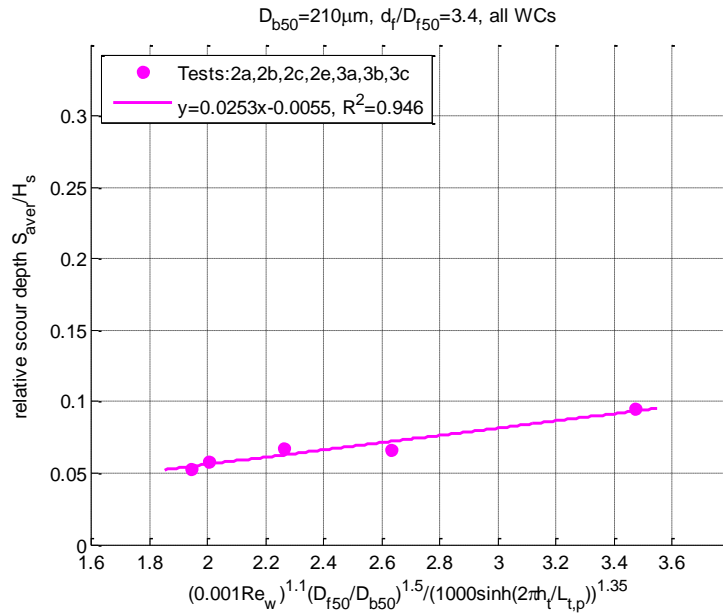


Figure 6-19 Best fit line for Tests 4d, 4e, 5a, 5b, 5c. $D_{b50}=210\mu\text{m}, d_f/D_{f50}=3.4$, narrow graded filter layer and all WCs

In particular, the equation of best fit line writes:

$$\frac{S_{aver}}{H_s} = 0.0253 \left(\frac{(0.001Re_{wb,p})^{1.1} \left(\frac{D_{f50}}{D_{b50}}\right)^{1.5}}{\left(1000\sinh\left(\frac{2\pi h_t}{L_{t,p}}\right)\right)^{1.35}} \right) - 0.0055 \quad (6-4)$$

Here, the contribution of $Re_{wb,p}$ is large with respect to D_{f50}/D_{b50} & $h_t/L_{t,p}$; therefore eq. (6-4) has limited physical importance.

6.4.3. General relation for $D_{b50}=360\mu\text{m}$ & $D_{b50}=210\mu\text{m}$

Until now two parts of the data set were investigated separately, leading to the formation of equations (6-3 & 6-4). This paragraph combines both parts in order to arrive in a general formula that incorporates the differences entailed by the use of different seabed grain diameters.

To accomplish that, another parameter has to be input in the existing three parameters; the critical Shields' Number Ψ_{cb} . Initially, all four parameters ($h_t/L_{t,p}$, D_{f50}/D_{b50} , Ψ_{cb} , $Re_{w,p}$) are used to obtain the best fit line for the considered part of the data set. Figure 6-20 plots the new best fit line.

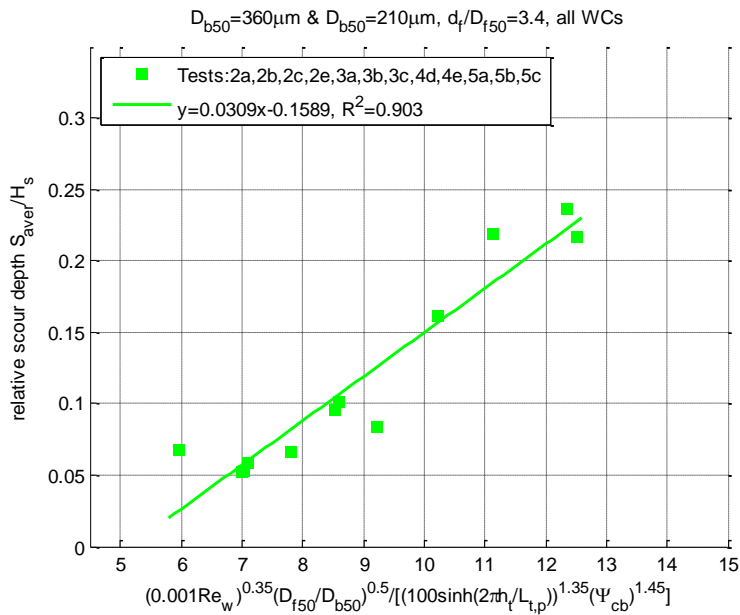


Figure 6-20 Best fit line for $D_{b50}=360\mu\text{m}$ & $D_{b50}=360\mu\text{m}$. $d_f/D_{f50}=3.4$, narrow graded filter layer and all WCs. Tests 2a, 2b, 2c, 2e, 3a, 3b, 3c, 4d, 4e, 5a, 5b, 5c.

Here, contribution of D_{f50}/D_{b50} has changed with respect to equations (6-3 & 6-4) and is now given to the power 0.5. Furthermore, the importance of critical Shields' Number is clearly underlined and is given to the power 1.45. On the other hand, eq. (6-4) uses the wave Reynolds' Number (to the power 0.35) which based on the assumptions (rough wall, small deviation in the data set) described in Section 6.4.1 can be dropped out. The result is plotted in Figure 6-21.

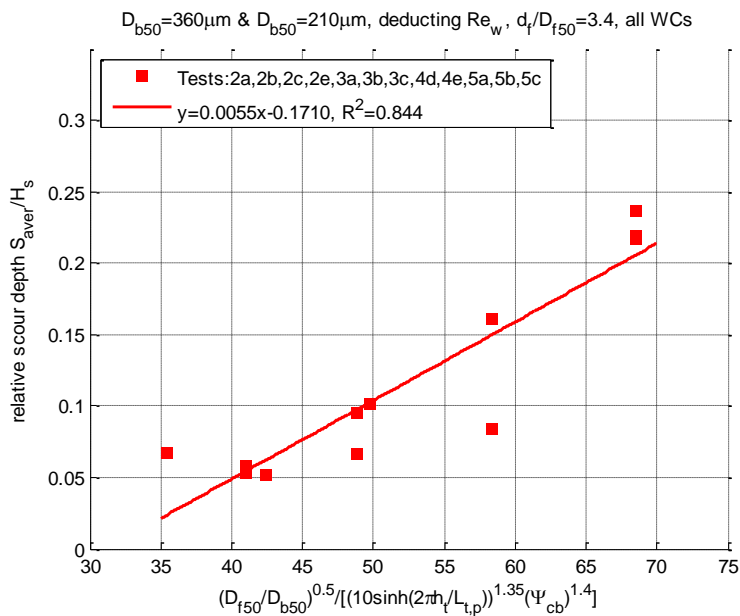


Figure 6-21 Neglecting wave Reynolds' Number. Best fit line for $D_{b50}=360\mu\text{m}$ & $D_{b50}=360\mu\text{m}$. $d_f/D_{f50}=3.4$, narrow graded filter layer and all WCs. Tests 2a, 2b, 2c, 2e, 3a, 3b, 3c, 4d, 4e, 5a, 5b, 5c.

Best fit line for Figure 6-21 is expressed by eq. (6-5)

$$\frac{S_{aver}}{H_s} = 0.0055 \left(\frac{\left(\frac{D_{f50}}{D_{b50}}\right)^{0.5}}{\left(10 \sinh\left(\frac{2\pi h_t}{L_{t,p}}\right)\right)^{1.35} (\Psi_{cb})^{1.4}} \right) - 0.1710 \quad (6-5)$$

Despite the removal of $Re_{w,p}$, the correlation between the best fit line and the data has not changed dramatically ($R^2=0.903$ instead of $R^2=0.844$). From the remaining parameters, only the contribution of Ψ_{cb} has changed imperceptibly (to the power 1.4 instead of 1.45) while the rest remained the same. Thereby, eq. (6-5) will be further analyzed to incorporate correction for storm duration and filter layer grading.

6.4.4. Waves/Time

Equation (6-5) can be extended to account for the duration of a storm event. For that reason, three very long tests were carried out; Test2f, Test3e & Test5d. In addition, the input of test duration is expected to improve the correlation of eq. (6-6) and the data set used in Paragraph 6.4.3, since the considered tests do not have exactly the same duration. In this paragraph the data set consists of the Tests: 2a, 2b, 2c, 2e, 2f, 3a, 3b, 3c, 3e, 4d, 4e, 5a, 5b, 5c & 5d. Figure 6-22 plots the result.

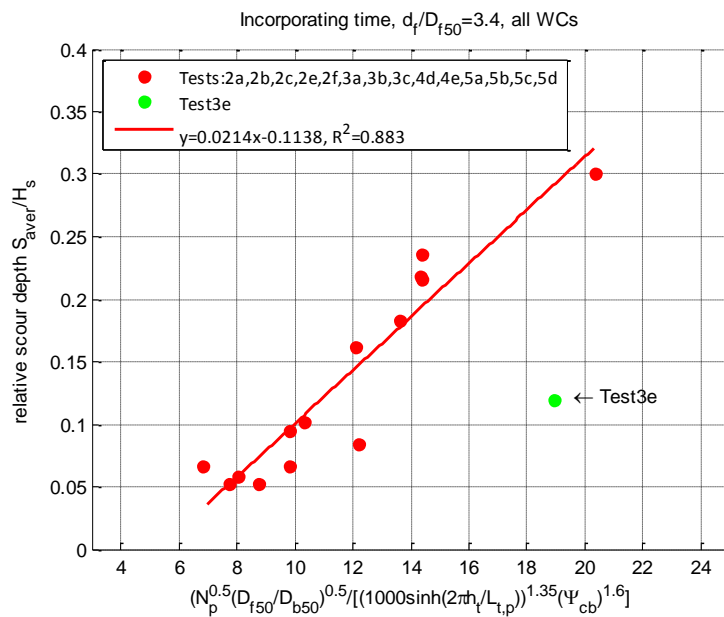


Figure 6-22 Incorporating duration of storm event. Best fit line for $D_{b50}=360\mu m$ & $D_{f50}=360\mu m$. $d_f/D_{f50}=3.4$, narrow graded filter layer, all WCs, all durations. Tests 2a, 2b, 2c, 2e, 2f, 3a, 3b, 3c, 4d, 4e, 5a, 5b, 5c, 5d. Test3e.

The best fit line was found by using the number of the waves N_p to the power of 0.5. Indeed, in Section 6.2 it was already concluded that $N_p^{0.5}$ is the parameter that best describes the temporal evolution of maximum scour depth; the same expression for this parameter was also found here. Generally, the square root of N is an important parameter in expressing temporal evolution of erosion processes in hydraulic engineering studies. Furthermore, the contribution of critical Shields' Number was slightly changed; now is given to the power 1.6 (to the power 1.4 in eq. (6-5)). The rest parameters remained the same. Finally,

The correlation with the data was found to be high ($R^2=0.883$) and thereby, the new equation that incorporates the time of the storm event writes:

$$\frac{S_{aver}}{H_s} = 0.0214 \left(\frac{N_p^{0.5} \left(\frac{D_{f50}}{D_{b50}} \right)^{0.5}}{\left(1000 \sinh \left(\frac{2\pi h_L}{L_{t,p}} \right) \right)^{1.35} (\Psi_{cb})^{1.6}} \right) - 0.1138 \quad (6-6)$$

Finally, in Figure 6-22 Test3e was depicted with a green circle. For this test was found a shallower averaged maximum scour depth compared to Test3a which had the same boundary conditions but significantly less duration. In particular, for Test3a $N_p=2960$ and $S_{aver}=1.84\text{cm}$ and for Test3e $N=7269$ and $S_{aver}=1.35\text{cm}$. Test3e was inexplicably strong and arrived into equilibrium sooner than expected. To avoid influencing the result it is deducted from the analysis.

6.4.5. Grading

In order to extend the range of applicability of the eq. (6-6), Test series 1 (except from Test1d) are inserted into the data set, so that the new equation could be able to account for the grading of the filter layer. Initially, the best fit line was computed for Tests 1a, 1b, 1c, 1e, 2a, 2b, 2c, 2e, 2f, 3a, 3b, 3c, 4d, 4e, 5a, 5b, 5c, 5d but without correction for filter grading. Figure 6-23 plots the result. Best fit line is marked with black color to show that is computed from all the data present in the plot.

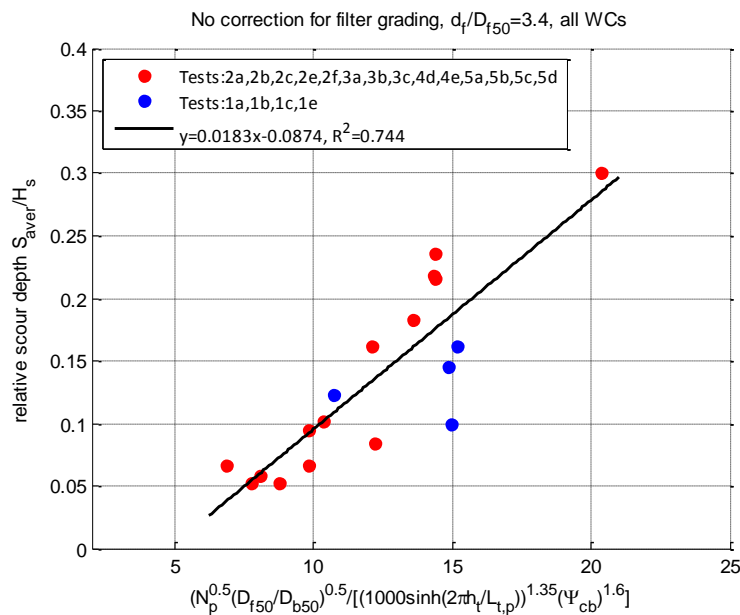


Figure 6-23 Best fit line for Tests 1a, 1b, 1c, 1e, 2a, 2b, 2c, 2e, 2f, 3a, 3b, 3c, 4d, 4e, 5a, 5b, 5c, 5d without grading correction. $D_{b50}=360\mu\text{m}$ & $D_{f50}=360\mu\text{m}$. $d_f/D_{f50}=3.4$, narrow graded filter layer, all WCs, all durations

Tests from Test series 1 are marked with blue circles to depict them from the rest of the data set. Indeed, they abstain the largest distance from the best fit line; therefore correction for filter grading needs to be incorporated into the equation.

In Test series 1, was tested the largest D_{f50}/D_{b50} . However, the S_{aver} found was lower than expected and in between the corresponding S_{aver} for Test series 2 & 3. This means that for the same loading and D_{f50}/D_{b50} , a wider graded filter gives less damage. Therefore, the parameter that best represents the effect of filter grading has to be placed in the denominator of the x-coordinate displayed in Figure 6-23.

To do so, grading is expressed via three characteristic diameter ratios namely D_{90}/D_{10} , D_{65}/D_{15} and D_{85}/D_{15} . The best correlation was found for D_{f90}/D_{f10} . The result is plotted in Figure 6-24.

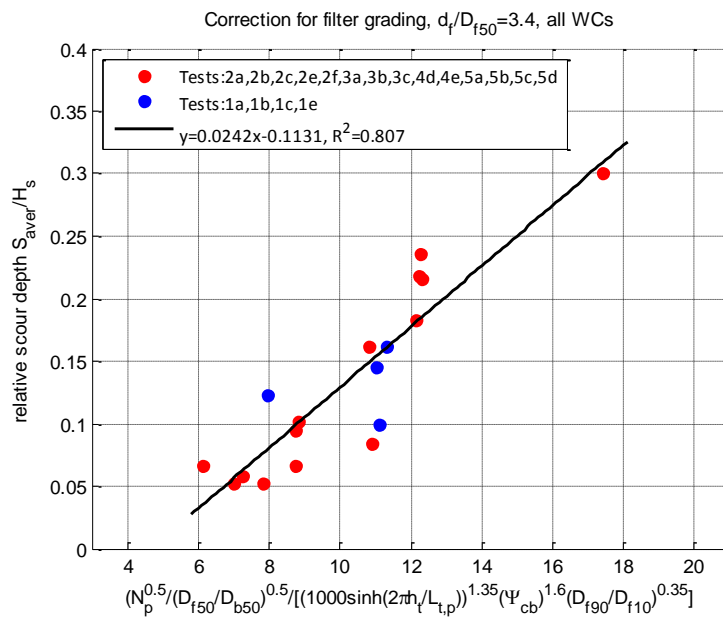


Figure 6-24 Incorporating grading variation. Best fit line for $D_{b50}=360\mu\text{m}$ & $D_{b50}=360\mu\text{m}$, $d_f/D_{f50}=3.4$, narrow graded filter layer, all WCs, all durations. Tests 1a, 1b, 1c, 1e, 2a, 2b, 2c, 2e, 2f, 3a, 3b, 3c, 4d, 4e, 5a, 5b, 5c, 5d.

The new expression that accounts also for filter grading writes:

$$\frac{S_{aver}}{H_s} = 0.0242 \left(\frac{N_p^{0.5} \left(\frac{D_{f50}}{D_{b50}} \right)^{0.5}}{\left(1000 \sinh \left(\frac{2\pi h_t}{L_{t,p}} \right) \right)^{1.35} (\psi_{cb})^{1.6} \left(\frac{D_{f90}}{D_{f10}} \right)^{0.35}} \right) - 0.1131 \quad (6-7)$$

6.4.6. Summary & Discussion

In order to arrive into a final expression that best describes all the total data set (except from the neglected tests), the latter was separated into parts with common characteristics. Initially, tests with $D_{b50}=360\mu\text{m}$ were treated and were successfully correlated with eq. (6-3). Then tests with $D_{b50}=210\mu\text{m}$ were found to be linked satisfyingly with eq. (6-4). Afterwards, the two tested groups were combined to get the expression of eq. (6-5).

To end up with a more general expression, the time via the number of waves N and the grading of filter layer were incorporated. Apart from the additional tests with significantly different duration and grading, the introduction of these parameters is thought to have increased the correlation of the existing data set, since minor differences in time and grading were already present in the first to test groups. Thereby, eq. (6-6) accounts also for design storm duration and eq. (6-7) incorporates the effect of filter grading on the maximum scour depth.

The latter, namely eq. (6-7) is thought to be the one that best describes the whole data set. Its physical validity and range of applicability will be discussed in the next section while the up-scaling to a possible prototype is treated in Appendix B.

On the other hand, there are parameters that influence maximum scour depth but are not present in eq. (6-7), either due to failure in the present tests or due to the fact that they were not deviated during the tests. In particular, due to serious model effects, the extracted results from the tests with thicker filter layers were unrealistic and could not be used further into the analysis. Therefore, the present prediction tool cannot account for the effect of relative thickness. Furthermore, the data set did not contain tests with wide graded base layer. The grading of base material is related to the permeability and the porosity of the base material; thereby a more porous base layer is expected to experience more damage than a less porous one. Additional tests need to be executed to arrive in a more general prediction tool that incorporates all the relevant parameters.

Eq. (6-7) has the form of $\gamma = \alpha x + \beta$ and assumes a linear relation (linear increase) between the relative maximum scour depth and the product of the independent dimensionless parameters. The assumed linear increase is only valid between the range (un-shaded area in Figure 6-25) of the independent parameters upon which eq. (6-7) was formulated. Using eq. (6-7) outside this area (shaded area in Figure 6-25), would mean that further increase of the independent product, leads to a relative maximum scour depth that goes to infinity. Apparently, this is not valid. This will be further discussed in Section 6.6.

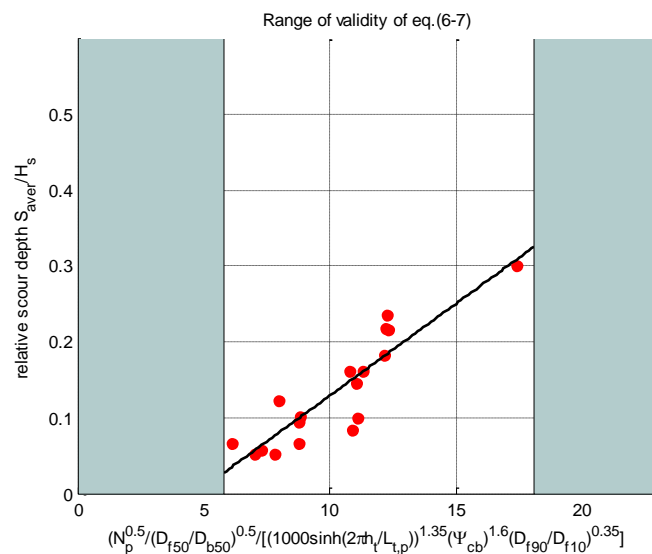


Figure 6-25 Range of validity for eq. (6-7)

In reality, it is expected that the maximum relative scour depth for a given design condition and combination of the independent dimensionless parameters will approach asymptotically to an equilibrium maximum scour depth which is less than the equilibrium scour depth of the corresponding unprotected case (seabed without filter). Consequently, replacing the linear function, with a different type that can simulate this behavior, could provide a more meaningful description of the link between the relative maximum scour depth and the independent, dimensionless product. With the present data set it was not possible to recognize this trend and to come up with such relation.

Finally, the equation needs to be evaluated and validated by using data sets from other studies. However, apart from the data set of Sumer *et al.* [2000] no such data are available.

Additionally, an objective comparison between these two is very difficult due to differences in the model set-up. Nevertheless, an attempt to accomplish that is provided in Section 6.5.

6.5. Comparison with the data set of Sumer *et al.* [2000]

In Appendix B, three up-scaling techniques were used to link the investigated physical model with a fictitious prototype. Apart from the entailed scale effects additional problems were found. In particular:

- Prototype seabed material was not sand
- The computed relative grain diameters are unrealistic
- Model underestimates amount of damage
- Finer base material in the prototype had higher stability number than coarser. The reciprocal occurred in the model

None from the presented up-scaling procedures was able to overcome all the aforementioned problems. Consequently, no prototype was found to successfully represent the investigated physical mode. Therefore, direct extrapolation of the results is doubtful. In addition, eq. (6-7) was formulated only based on the data set of the present study; therefore equation needs to be evaluated and validated by using data sets from other studies.

However, apart from the data set of Sumer *et al.* [2000] and the corresponding design tool of eq. (2-3) no other data are available. Additionally, an objective comparison between these two and eq. (6-7) cannot be done directly due to major differences in the corresponding model set-ups. In particular, Sumer *et al.* [2000] conducted physical model tests¹⁷ using two structural slopes $\alpha=30^\circ$ & $\alpha=40^\circ$, sand as base material while eq. (2-3) was formulated based on tests with regular waves. Thereby, eq. (2-3) predicts maximum scour depth for the case of unprotected seabed at the toe of a rubble mound breakwater.

To illustrate the differences, Figure 6-26 plots the dataset from the present study (filled, blue circles) along with the data set from Sumer *et al.* [2000]. In addition, eq. (2-3) is plotted for three different structural slopes $\alpha=30^\circ$ (magenta line), 33.6° (cyan, discontinuous line) & $\alpha=40^\circ$ (green line).

¹⁷ They also report non-breaking waves. However, also in the present study no wave breaking was taking place at the toe. Therefore, non-breaking conditions are assumed in both cases.

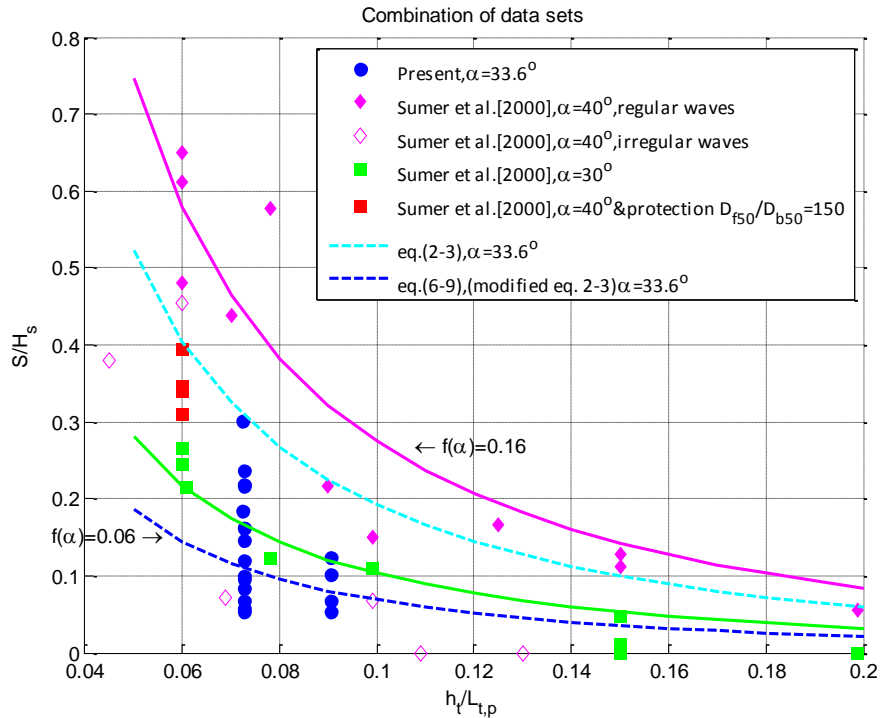


Figure 6-26 Combining the two data sets; present study (blue circles) with Sumer *et al.* [2000] for no protection & regular waves (filled, magenta diamonds & green squares), no protection & irregular waves (empty, magenta diamonds) and with protection (filled, red squares). In addition, eq. (2-3) is plotted for $\alpha=40^\circ$ (solid, magenta), $\alpha=30^\circ$ (solid, green), $\alpha=33.6^\circ$ (discontinuous, cyan) and eq. (6-9) (modified eq. 2-3, discontinuous, blue).

Tests with protective layer¹⁸ (filled, red squares) and eq. (2-3) for $\alpha=33.6^\circ$ can be used for the verification of eq. (6-7). However, comparison can only be accomplished by applying proper correction factors to account for the afore-mentioned differences.

Consequently, comparison with eq. (6-7) can be done in two ways:

1. Based on results extracted by modified eq. (2-3) (discontinuous blue line). This is described in Example 1.
2. Based on the results of Tests 30, 32 & 33 (depicted with red squares) from the data set of Sumer *et al.* [2000]. These tests were executed with a filter layer of $D_{f50}=3\text{cm}$. This is described in Example 2.

6.5.1. Example 1: Comparison with eq. (2-3) from Sumer *et al.* [2000]

As it was mentioned above, eq. (2-3) from Sumer *et al.* [2000] was formulated based on regular waves. In addition, Sumer *et al.* [2000] claimed that the relative maximum scour depth for tests with irregular waves was found to be reduced with a factor of 2. However, H_{rms} was used; therefore an additional correction should be applied to account for significant wave height H_s . Thereby, the modified eq. (2-3) writes:

$$\frac{S}{H_s} = \gamma * \delta * \frac{0.3 - 1.77e^{\left(-\frac{\alpha}{15}\right)}}{\left(\sinh\left(\frac{2\pi h}{L}\right)\right)^{1.35}} \quad (6-8)$$

¹⁸ These tests were not used by Sumer *et al.* [2000] in the formulation of eq. (2-3).

Where $\gamma=0.5$ (correction for irregular waves) and $\delta=1.4$ (correction for H_s). In addition, by applying structural slope $\alpha=33.6^\circ$ eq. (6-9) becomes:

$$\frac{S}{H_s} = 0.357 * \frac{0.1116}{\left(\sinh\left(\frac{2\pi h}{L}\right)\right)^{1.35}} \quad (6-9)$$

Eq. (6-9) is plotted in Figure 6-26 (discontinuous, blue line). Now, eq. (6-7) and eq. (6-9) can be compared directly by using the same input. Since eq. (6-7) is able to account for the initiation of motion of base material, for any given input, the result taken from eq. (6-7) should be lower than the corresponding result from eq. (6-9). However, because eq. (6-9) was formulated based on sand with $D_{b50}=200\mu\text{m}$, and does not count for different base materials, the same base material will be used in the example.

General input parameters: $\alpha=33.6^\circ$, $H_s=4\text{m}$, $h=9\text{m}$, $D_{b50}=200\mu\text{m}$, $\rho_{\text{base}}=2650\text{kg/m}^3$, $D_*=7.5$, $\Psi_{\text{cb}}=0.043$, $N=3000$ waves, $d_f/D_{f50}=3.4$, standard graded filter $D_{f90}/D_{f10}=1.5$.

Eq. (6-7) and eq. (6-9) will be compared for 5 relative grain diameter values ($D_{f50}/D_{b50}=25, 30, 35, 40$ & 45) in three different relative water depths ($h_t/L_{t,p}=0.092$ with $T_p=11\text{s}$, $h_t/L_{t,p}=0.076$ with $T_p=13\text{s}$ & $h_t/L_{t,p}=0.071$ with $T_p=14\text{s}$). Values were selected such that they agree with the range of the parameters upon which eq. (6-7) was formulated. Figure 6-27 plots the results.

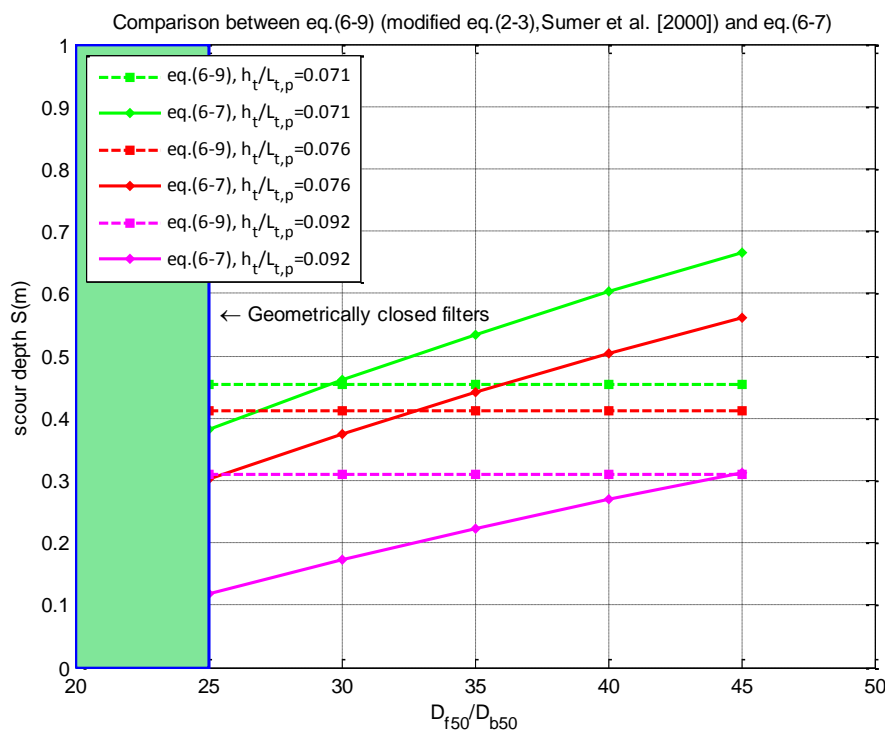


Figure 6-27 Comparison between eq. (6-9) (modified eq. (2-3) from Sumer *et al.* [2000]) and eq. (6-7)

For every $h_t/L_{t,p}$, the intersection point corresponds to the value of D_{f50}/D_{b50} which the application of the filter has no contribution on damping maximum scour depth. Based on the figure above, it can be easily observed, that for shallower relative water depths, the intersection point of the two equations moves to smaller values of relative grain diameter. Thereby, for $h_t/L_{t,p}=0.092$ the maximum scour depth for the case of no protection is equal to the maximum scour depth when a filter configuration with $D_{f50}/D_{b50}=45$ is applied. The

corresponding values for $h_t/L_{t,p}=0.076$ & $h_t/L_{t,p}=0.071$ are $D_{f50}/D_{b50}=32.5$ & $D_{f50}/D_{b50}=29$, respectively.

Furthermore, for the same decrease $h_t/L_{t,p}$ (i.e. from 0.092 to 0.076), eq. (6-7) assumes a larger increase of maximum scour depth than the corresponding increase given by eq. (6-9).

Finally, it should not be omitted that a possible increase of the averaged maximum scour depth is expected when a new storm arrives, since based on eq. (6-7), it is doubtful whether the system arrived into equilibrium.

6.5.2. Example 2: Sumer *et al.* [2000] with protection

Tests 30, 32 & 33, from the dataset of Sumer *et al.* [2000], were conducted with a protective layer, irregular waves and with a breakwater structural slope $\alpha=40^\circ$. The relative grain diameter was $D_{f50}/D_{b50}=150$ and the relative thickness of the protective layer was $d_f/D_{f50}=5, 5, 3$, respectively. The measured relative maximum scour depth was found to be 0.33 and 0.31 and 0.35 for the first two and 0.39 for the latter. The used significant wave height was $H_s=0.178\text{m}$ and the peak period was $T_p=3\text{s}$ with $h_t/L_{t,p}=0.061$.

However, eq. (6-7) was formulated for $d_f/D_{f50}=3.4$. Thereby, a correction has to be applied for the different relative thickness. Therefore it is assumed that the representative relative scour depth for these tests is $S/H=0.375$.

Likewise to previous paragraph the relative maximum scour depth needs to be corrected with respect to irregular waves, significant wave height H_s and structural slope $\alpha=33.6^\circ$. In agreement with the previous paragraph the correction factors are 0.5, 0.714 and 0.1116/0.16. Consequently:

$$\frac{S}{H_s} = 0.375 * 0.5 * 0.714 * \frac{0.1116}{0.16} = 0.094, \quad S = 0.094 * H_s = 1.7\text{cm}$$

Therefore, the corrected maximum scour depth from Sumer *et al.* [2000] is 1.7cm. This value can now be compared with the calculated value from eq. (6-7) when using as base material sand with $D_{b50}=200\mu\text{m}$, $\rho_{\text{base}}=2650\text{kg/m}^3$, $D_*=7.5$, $\Psi_{\text{cb}}=0.043$. In addition, it is assumed storm of $N=3000$ waves, standard graded filter $D_{f90}/D_{f10}=1.5$, $H_s=0.178\text{m}$, $T_p=3\text{s}$ and $D_{f50}/D_{b50}=150$. The calculated value is $S=9.3\text{cm}$; 5.5 times bigger than modified value from Sumer *et al.* [2000] experiments. Consequently, eq. (6-7) overestimates the magnitude of maximum scour depth.

6.5.3. Summary & discussion

Two examples were accomplished in order to compare eq. (6-7) with eq. (6-9) (modified eq. (2-3)) and with selected tests from the data set of Sumer *et al.* [2000]. The main difference between the two examples is that in Example 1, the input parameters lay between the range of the parameters used in the formulation of eq. (6-7). On the contrary, in Example 2, the input value of relative grain diameter is $D_{f50}/D_{b50}=150$; thus well outside the range of D_{f50}/D_{b50} (25 to 45) used to formulate eq. (6-7).

In both examples, it was found that eq. (6-7) overestimates the magnitude of maximum scour depth. Especially for input parameters outside the range upon it which was formulated

(Example 2), eq. (6-7) gives absolutely unrealistic results. When the input is in agreement with the range of formulation, the output of eq. (6-7) becomes more reasonable. However, when the filter configuration is placed in shallower waters (proceeding from $h_f/L_{t,p}=0.09$ to $h_f/L_{t,p}=0.07$) the magnitude of maximum scour depth predicted with eq. (6-7) is even larger than the prediction of eq. (6-9), which assumes no filter protection.

The major difference between the two studies is the use of different base materials. In the present study, the seabed consisted of a granular lightweight material (plastic abrasive). Due to its lower density, there was a difference between the buoyancy of the base and filter layer while the base layer was remaining in suspension for a longer time interval. Thereby, the surface of the base layer was fluidized and weakened; therefore the filter layer was able to settle more easily inside the base layer. This was causing damage enhancement in contrast to the study of Sumer et al. [2000] where the seabed consisted of sand and therefore the aforementioned model effect was not present.

On the other hand, it is also not sure whether output from eq. (6-9) is the most accurate prediction of what will happen in a real case. In specific, Eq. (6-9) is the modified expression of eq. (2-3). For the modification of eq. (2-3) very simplified rules were used that entail a lot of uncertainties. Therefore, conclusions from the comparison need to be treated with special care.

6.6. Range of applicability & design suggestions

Eq. (6-7) is an empirical expression, formulated upon the data set of the present study. It has limited physical background and is only valid between the range of the parameters used in the physical model tests. Outside this area, the extracted results are completely unrealistic.

Additionally, eq. (6-7) overestimates maximum scour depth due to a serious model effect; the different buoyancy between filter and base layer that was causing initial damage and damage exaggeration. Thereupon, eq. (6-7) gives a conservative, but not accurate prediction.

On the other hand, eq. (6-7) provides insight into the interrelation of the parameters that play a role in scour formation and development, by incorporating the contributions of wave loading characteristics and filter configuration properties. Indeed, the analysis of the present data set has also revealed the importance of stability Number (critical Shields' Number) in the determination of maximum scour depth. Thereby, by setting the characteristic grain diameters of the filter and base layer is not sufficient since the contribution of the base layer is extended via the use of critical Shields' Number. Therefore, despite the limited range of the tested parameters, eq. (6-7) delineates their relative contribution in scour depth formation.

Apparently, further research will be needed in order to provide a more accurate quantification of the interrelation between the parameters that play a role in scour formation and development. Furthermore, there are parameters (i.e. relative filter

thickness, base material grading) that play a role in scour formation and development and are not present in eq. (6-7). Their implementation is considered indispensable in order to acquire a more overall view on scour formation through a geometrically open filter placed at the toe of a rubble mound breakwater.

Consequently, at the time being, the use of eq. (6-7) as a scour prediction tool in real life is not recommended. Thereby, any design suggestion would not be valid.

6.7. Summary of Chapter 6

Chapter 6 contains the analysis of the conducted physical model tests. Based on the computations presented in Section 6.1 two major topics were treated; the temporal evolution of maximum scour depth and the determination of the relation between maximum scour depth with characteristic parameters that describe each experiment.

For the former, it was found that the development of maximum scour depth is related with the square root of the number of waves N_p that attack the structure. This relation is expressed via the parameter α_t and is constant along the test. No further dependence was found; however, some general trends were identified. Furthermore, especially for tests where equilibrium maximum scour depth was reached, a different approach was adopted that accounts for the tendency of maximum scour depth to approach asymptotically to an equilibrium value. This behavior was expressed via eq. (6-1).

Afterwards, the data set was investigated with the aim to find a relation between maximum averaged scour depth and characteristic parameters that represent wave loading and filter configuration. The result was the formation of equation (6-7) that is capable to account for:

- Filter configuration properties via: relative grain diameter, base layer critical Shields' Number, and filter grading.
- Wave properties via: relative water depth, wave height (directly)
- Storm duration via: number of waves.

Furthermore, in order to test the performance of eq. (6-7), the latter was compared with eq. (6-9) (modified eq. (2-3)) and with selected tests from the data set of Sumer *et al.* [2000]. In both examples, it was found that eq. (6-7) overestimates the magnitude of maximum scour depth. Outside the range of formulation, eq. (6-7) gives absolutely unrealistic results. Between the range of formulation, the output of eq. (6-7) becomes more reasonable. However, in shallower waters the magnitude of maximum scour depth predicted with eq. (6-7) becomes larger than the case of no filter protection.

On the other hand, eq. (6-7) gives a clue into the interrelation of the parameters that play a role in scour formation and development, by incorporating the contributions of wave loading characteristics and filter configuration properties. Further research will be needed in

order to provide a more accurate quantification of the interrelation between the parameters that play a role in scour formation and development and to implement parameters that are important but are missing. Consequently, at the time being, the use of eq. (6-7) as a scour prediction tool in real life is not recommended.

7. Conclusions & recommendations

This chapter provides an overview of the most important findings of this research along with the evaluation of the objective and recommendations for further research. No new information is presented; discussion takes place upon the conclusions drawn from previous sections. The recommendations for further research are established upon the lacking of knowledge after the analysis and limitations that were observed during the test execution.

7.1. Conclusions

Scour formation at the toe of a rubble mound breakwater can lead to abrupt failure. The counteraction of scour via geometrically closed filter rules is the common practice. Alternatively, in specific cases the use of geometrically open filters can save significant amount of time and decrease constructional costs. As a primary step towards this direction, the prediction of scour formation through a geometrically open filter can provide important information.

The results of this study show that scour formation and development can be predicted. Despite the limitations and drawbacks, the knowledge of scour formation and development has increased and interesting relations have been found.

7.1.1. Evaluation of the objective

The study's objective was to come up with a relation that express the effect of important parameters, on the formation and development of scour, under the toe of a rubble mound breakwater, laying upon sand and designed as a geometrically open filter. Objective's accomplishment was based on the conduction of physical model tests. This section discusses the evaluation of the objective by providing answers to the sequential questions posed in Chapter 1. In particular:

Which is the dependency between erosion of seabed material and wave properties? In total 23 tests were conducted and 5 different D_{f50}/D_{b50} were investigated. Consequently, the research focused more on the properties of filter configuration and less on the effects caused by wave loading. Nevertheless, three wave conditions were tested; namely WC1, WC2 and WC3. They were designed such way that WC1 and WC2 have the same H_s and different T_p , while WC1 and WC3 had the reciprocal.

Thereby, despite that only two H_s were tested it was found that higher wave height leads to deeper scour holes. Furthermore, longer waves cause deeper scour formation than shorter ones. Indeed, the effect of wave period is of substantial importance, since it determines the relative water depth. Consequently, for the same filter configuration WC1 was causing the highest amount of damage.

When does damage (erosion) start and how does it develop in time and loading? For the present study, an irregular wave field was used, generated by a Jonswap spectrum. As a result, the exact moment of incipient motion cannot be linked to a specific pair of wave

height and period. Nevertheless, for all three WCs, erosion took place for wave heights that were larger than H_m from wave spectrum.

Furthermore, scour formation expands rapidly during the initial stages of the test and then slows down. Indeed, maximum scour depth was found to be linked to the $N^{0.5}$ with a constant factor α_t which was unique for every test. In general, for $D_{b50}=360\mu\text{m}$, this factor was higher for WC1 and larger D_{f50}/D_{b50} . This does not hold for tests with $D_{b50}=360\mu\text{m}$. Nevertheless, no link was found that combines α_t with filter configuration properties and wave loading.

Does damage development arrive at an equilibrium state, and if so which parameters are decisive? For tests with similar wave heights, the tests with smaller wave periods were slowing down sooner than tests with longer waves; therefore equilibrium is strongly related to loading and probably to the maximum scour depth that the base layer attends when no filter is applied. Additionally, tests that seemed to have arrived into equilibrium, after some time, started again to show additional erosion.

Especially for tests where equilibrium maximum scour depth was reached, the following relation was derived that can give an indication on the time scale of scour development:

$$\frac{S_t}{S_{max}} = 1 - \exp\left(-2.668 \frac{N_t}{N_{max}}\right) \quad (6-1)$$

Eq. (2-3) gives the maximum scour depth (in equilibrium state) for the case of unprotected seabed. It is considered safe to use this equation to determine S_{max} since the equilibrium maximum scour depth for the case of protective layer(s) will be equal or smaller to the value predicted by eq. (2-3).

However, it should not be omitted that these conclusions are drawn from observations and analysis through the side glass. For a large part of the data set, the representative average cross section and the final erosion pattern through the side glass were not in agreement (in shape or magnitude). This means that conclusions address to the scour hole formed next to the glass and should not be generalized because scour formation is a highly spatial phenomenon.

How do filter configuration properties (grain size, filter thickness, grading) influence erosion pattern? Filter configuration properties are decisive for scour formation and development. However, the magnitude of their effect was found to be different between tests with different base materials.

In specific, higher relative grain diameters D_{f50}/D_{b50} lead to larger scour depth; however, for similar D_{f50}/D_{b50} , maximum scour depth is significantly larger for tests with $D_{b50}=360\mu\text{m}$ than tests with $D_{b50}=210\mu\text{m}$. To account for this difference the critical Shields' Number was introduced to incorporate the effect of higher stability number.

On the other hand, tests that were executed to investigate the effect of filter's relative thickness increase have given unrealistic results. Therefore, the effect of relative thickness was not investigated.

Finally, for equivalent D_{f50}/D_{b50} , a filter layer with wider grading led to smaller maximum scour depth. However, this effect needs additional investigation because it was formulated based on only three tests.

Which are the scale/model effects due to physical model testing? How can they be quantified and mitigated? In order to quantify the scale effects of a physical model, a target prototype is needed. However, for the present study no successful prototype was found.

In particular, there are two major problems with respect to this research. Firstly, wave kinematics, breakwater and filter configuration have to be up-scaled with the Froude law of similitude, while the base material can be up-scaled with the Dean Number or Shields' Number similitude. Apart from the entailed scale effects, the up-scaling procedure leads to either unrealistic D_{f50}/D_{b50} , or to base materials that are not sand anymore. Finally, another distortion is that in the up-scaled situation the D_{b50} that corresponds to $D_{b50}=210\mu\text{m}$ has lower stability than the corresponding one for $D_{b50}=360\mu\text{m}$. This contradicts with the test results.

Furthermore, the built physical model proved to be suffering from two model effects. Firstly, due to the fact that the seabed was consisted of a granular lightweight material (plastic abrasive), there was difference between the buoyancy of base and filter layer, causing two major consequences. Firstly, when the flume was filling up with water, filter layer was already settling inside the base layer, causing initial damage. Secondly, when set into motion, base material was settling slower than normal; therefore, during the test the settling of filter layer inside the base material was enhanced. Consequently, in the present study maximum scour depth and amount of erosion are being overestimated.

Secondly, scour was forming at the transition zone between the wooden foreshore and the box that contains the movable material. The observed scour pattern had the form of a single scour hole located at the middle of the box. No deposition area was shaped. This type of scour is completely irrelevant to the present study. Thereby, this prevented the determination of equilibrium maximum scour depth for the case of unprotected seabed.

7.1.2. Conclusions from observations

This section summarizes the most important observations from the conduction of the physical model tests.

Pattern of scour hole formation: The analysis and the observations of the conducted tests has revealed the highly spatial character of scour formation. Even for tests with identical boundary conditions the pattern of scour formation was different. Thereby, the horizontal dimensions (width, length) and the location of scour hole were varying from test to test. On the contrary, the measured maximum depths were converging upon specific values.

An explanation on the aforementioned is that wave loading locates a weak spot in the filter layer and then erosion starts to take place. Furthermore, erosion expands in the base layer causing additional damage. In general, the deeper scour holes were formed near the glasses. For that reason, analysis accounts for a lateral buffer area.

Furthermore, for the majority of the tests erosion started immediately at the downstream side of the box while further downstream a small bar (sill) was formed. This observation is in agreement with the scour patterns for irregular waves obtained by Sumer *et al.* [2000] and implies that breakwater stability is threatened by scour formation. Generally, for tests with $D_{b50}=360\mu\text{m}$ an S-curve erosion/deposition profile developed at the side glass. The curve's characteristics were enhanced when longer end higher waves were attacking the structure. For tests with shorter waves the curve's characteristics were less discrete. On the contrary, for tests with $D_{b50}=210\mu\text{m}$ these characteristics were less discrete or did not appear at all.

Filter layer stability: Despite that filter stones used in the present study were lower than the calculated values from the van der Meer formula for no damage, no considerable instability or filter damage was observed. During the initial stages of a test, few stones were rolling or wiggling until they reached a more stable position and after that no movement occurred. Under the stronger waves, filter remained stable and an imperceptible amount of stones was wiggling. In general, filter thickness remained intact for all test cases.

Hydraulically stable or unstable geometrically open filter?: For waves higher than the mean wave height of the spectrum, filter configuration was not able to prevent base layer erosion. Consequently, the filter configuration is characterized as geometrically open/hydraulically unstable for the corresponding maximum wave height of the spectrum. The failure in acquiring realistic results for tests with thicker filter layers has discouraged the design of geometrically open/hydraulically stable filter configurations.

7.1.3. Relations between loading and erosion

Dimensional analysis and literature review have revealed the most important parameters that have significant effect in scour formation. These parameters are combined in the form:

$\frac{S_{aver}}{H_s} = f\left(\frac{N \frac{D_{f50}}{D_{b50}}}{\sinh\left(\frac{2\pi h_t}{L_{t,p}}\right) \psi_{cb} \frac{D_{f90}}{D_{f10}}}\right)$ to describe scour formation properties based on the data set of the present study. The final outcome is expressed via eq. (6-7):

$$\frac{S_{aver}}{H_s} = 0.0242 \left(\frac{N_p^{0.5} \left(\frac{D_{f50}}{D_{b50}}\right)^{0.5}}{\left(1000 \sinh\left(\frac{2\pi h_t}{L_{t,p}}\right)\right)^{1.35} (\psi_{cb})^{1.6} \left(\frac{D_{f90}}{D_{f10}}\right)^{0.35}} \right) - 0.1131 \quad (6-7)$$

Eq. (6-7) is an empirical expression that assumes a linear relation (linear increase) between the relative maximum scour depth and the product of the independent dimensionless parameters. It has limited physical background and is only valid between the range of the parameters used in the physical model tests. Outside this area, the extracted results are completely unrealistic. Additionally, it overestimates maximum scour depth due to a serious model effect; the different buoyancy between filter and base layer that was causing initial damage and damage exaggeration. Thereupon, eq. (6-7) gives a conservative, but not accurate prediction.

On the other hand, the afore-mentioned expression is able to count for the deviation of relative grain diameter, relative water depth, storm duration, stability of the base layer

(expressed in critical Shields' Number) and for the grading of the filter layer. Therefore, eq. (6-7) is capable of delineating the relative contribution of each parameter in scour depth formation.

Apparently, for a more overall view of scour formation, further research will be needed in order to provide a more accurate quantification of the interrelation between the parameters that play a role in scour formation and development, and to implement the effect of missing parameters. Consequently, at the time being, the use of eq. (6-7) as a scour prediction tool in real life is not recommended.

7.1.4. Lacking of knowledge after the analysis

Interesting relations have been found between damage and boundary conditions; however satisfactory answers on some significant questions were not found. In specific:

Effect of relative filter thickness: Undoubtedly, filter thickness has an effect on the erosion pattern of the base layer. To investigate that, test conditions of Tests 1a, 2a & 3a, were repeated in Tests 1d, 2d, 3d but with a thicker filter. However, due to model effects the extracted results were unrealistic. Consequently, the effect of relative filter thickness was not incorporated in the dimensionless relation between averaged maximum scour depth and boundary conditions. It is expected that under the same boundary conditions a higher relative filter thickness d_f/D_{f50} will lead to a smaller maximum scour depth. Consequently, it is expected to appear in the denominator of eq. (6-7).

No successful prototype: No successful fictitious prototype was found, despite that alternative scaling techniques were applied to up-scale the present physical model. The major consequence is that it is not possible to quantify the difference between the tested D_{f50}/D_{b50} in the model and the corresponding D_{f50}/D_{b50} in the prototype. This term is considered substantial in describing filter properties. Therefore, with the present knowledge, the interpretation of model results in real life is hindered.

Representative time scale for temporal scour evolution: For every test, the temporal evolution of scour depth with respect to $N^{0.5}$ was found to be represented by a constant value α_t . Some general trends with respect to wave loading and filter properties were detected. However, no satisfying relationship was found to link all these aspects. Consequently, the establishment of a dimensionless parameter that objectively represents the temporal evolution of scour is still pending.

Errors caused by experimental procedure: In order to quantify damage, apart from the measurements, base layer was measured prior and after the test execution of each test. To accomplish that, filter layer was removed by hand by smoothly scratching the surface of the base layer to remove the settled filter stones. However, it is possible that human contribution was causing additional damage by removing base material that was still in place. Analysis of filter layer measurements was not successful, so it was not possible to give a reliable answer. Consequently, results were vulnerable to human interference while the introduction of human error was not quantified.

7.2. Recommendations for further research

This section elaborates on proposing possible solutions that will fill in the gaps described in Section 7.1.4 while extending the range of applicability of this research's findings. In particular, recommendations are treated in three main subjects:

Alternative experimental procedure: The present physical model is suffering from two major model effects. Firstly, different buoyancy (due to different density) between filter and base layer leads into the overestimation of maximum scour depth. Secondly, in the case of no filter protection the effect of transition-induced scour is so dominant that prohibits the determination of maximum scour depth (for the case of no protection) that can be used to assess the performance of filter configuration. Consequently, the following alternative experimental procedures can be suggested to overcome these problems.

Problem: Damage exaggeration due to different buoyancy between filter & base layer

Firstly, the pursuit behind the use of a lightweight material was to assure that the seabed is made of sand in both the model and the prototype. The same approach can be followed; but filter stones will have to be glued to prevent damage exaggeration due to different buoyancy. However, when erosion takes place then base layer would be free to form ripples below the filter layer and migrate upstream. This is not very realistic but is more conservative and has the advantage that always, exactly the same filter can be tested. Finally, another disadvantage is that with the present knowledge successful up-scaling of filter configuration to a fictitious prototype is almost impossible.

Secondly, an alternative possibility is to conduct physical model tests with sand instead of a lightweight material. This approach has the advantage that filter stones can be placed directly to base layer since differences in density would be imperceptible. Thereby, a more realistic approach would be developed since in real life filter layer will settle into the eroding base layer. Apparently, this is thought to decrease the magnitude of the formulated scour hole.

In addition, if the same boundary conditions would be used, a link can be drawn between similar tests but with different base layers and then it would be possible to quantify the difference. In particular it is suggested to use sand with $D_{b50}=210\mu\text{m}$ and $D_{b50}=360\mu\text{m}$. Additionally, the use of sand as base material would allow the investigation of a geometrically open/hydraulically stable filter configuration. Finally, it should not be omitted that the use of sand would raise problems with respect to wave kinematics scaling and the scaling of the breakwater. However, the related problems are considered to be less aversive than the corresponding case with the lightweight

Alternatively, profile measurements with two laser devices that point at the same spot can be a solution. The accuracy of the measurements would increase and filter layer would be free to follow the settlements of the base layer.

It is left to the researcher to decide which method is more convenient for his study.

Problem: Transition-induced scour

No matter which of the two afore-mentioned would be selected, it is extremely important to increase the length of the box that contains the base material. In the present study, the seabed material was placed into a box made of glass and wood, and incorporated into the artificial foreshore to reduce the amount of base material needed for experiments. However, this prohibited the possibility to assess filter performance by determining the maximum scour depth for the case when no filter protection is applied.

To assure that transition-induced scour effects are mitigated it is advised to extend the box dimensions towards the both the upstream and downstream side. Thereby, part of the breakwater would also lay upon sand. Therefore, the boundary between sandy seabed and foreshore should be placed as downstream as possible.

Extending the range of applicability of the present research: In order to obtain an overall description of scour formation and development under the toe of rubble mound breakwaters, additional research will be needed in order to provide a more accurate quantification of the interrelation between the parameters that play a role in scour formation and development, and to implement the effect of missing parameters.

Specifically, the present research has not treated the effect of the grading of base material and relative thickness increase. Therefore, additional tests are suggested to incorporate the effect of these parameters in a relationship similar to eq. (6-7). In addition, the relative water depth was found to be an important parameter that affects maximum scour depth. The tested filter configurations were placed in intermediate waters; for that reason, is suggested to implement the new expression in shallow and depth-limited waters. Afterwards, the next stage would be to test the configuration under oblique waves and to place it at the head of the breakwater.

Quantifying damping inside the filter: The most critical area for the process of scour formation through a filter is the transitional area between the base layer and the filter layer. The velocity magnitude and the turbulent intensity are expected to be damped there; however the amount of damping cannot be predicted. For that reason, measuring the pressure fluctuations at the surface of the filter, inside the filter and at the transitional area would provide insight that will aid in developing a more process-based design tool.

List of References

1. BRUUN, P. (1985) *Design and construction of mounds for breakwaters and coastal protection*, Elsevier Science Publishers B.V., Amsterdam
2. BARTELS, A., PHELP, D., KLOOS, M. (2003) *Repair of an Accropode breakwater: 5 years on*, COPEDEC VI, Colombo, Sri Lanka, paper 003
3. BEST, A. de, BIJKER, E.W., (1971) *Scouring of a sand bed in front of a vertical breakwater*, Communications on Hydraulics Report no. 71-1, Delft University of Technology
4. BOSMAN, D.E., RETIEF, G. de F., KAPP, J.F., KLOOS, M., RIDGE, A.B. (1990) *Design and construction of pleasure craft harbor Club Mykonos Langebaan*, Proceedings of the 22nd International Coastal Engineering Conference, Delft
5. BURCHARTH, H.F., ZHOU L., TROCH P., (1999). *Scaling of core material in rubble mound breakwater tests*, COPEDEC V, Cape Town, South Africa
6. CIRIA, CUR (1991) *Manual on the use of rock in coastal and shoreline engineering*, CIRIA, London
7. CIRIA, CUR, CETMEF (2007) *The Rock Manual. The use of rock in hydraulic engineering* (2nd edition), CIRIA, London
8. CUR, (1993) *Filters in de waterbouw*. Report 161, Gouda (in Dutch)
9. CUR, (2010) *CUR 233: Interface stability of granular filter structures*, Gouda
10. EBBENS, R.E. (2009) *Toe structures of rubble mound breakwaters. Stability in depth limited conditions*, MSc thesis, Delft University of Technology
11. GRASS, A.J., (1970) Initial instability of fine bed sand, Hydraulic Division, Proc. of the ASCE, 96, (HY3), 619-632.
12. HALLERMEIER, R.J., (1981) *Terminal settling velocity of commonly occurring sand grains*, Sedimentology, Vol 28, No 6, pp 859-865
13. HENRIQUEZ, M., RENIERS, A.J.H.M., RUESSINK, B.G., STIVE, M.J.F., STANTON, T.P., FOSTER, D.L., (2008) *On the scaling of sediment transport in the nearshore*, International Conference on the Application of Physical Modelling to Port and Coastal Protection - Coastlab '08, 2-5 July 2008, Bari, Italy ; pre-print version.
14. HOFFMANS, G.J.C.M. (1993) *A study concerning the influence of the relative turbulence intensity on local-scour holes*, Rep. W-DWW-93-251, Ministry of Transport, Public Works and Water Management, Rijkswaterstaat, Delft.
15. HOLTHUIJSEN, L.H. (2007) *Waves in oceanic and coastal waters*, Cambridge University Press, Cambridge, reproduced as lecture notes of Delft University of Technology (2007)
16. HUGHES, S.A. (1992) *Estimating wave-induced bottom velocities at vertical wall*, J. of Waterway, Port, Coastal and Ocean Engineering, ASCE, vol. 118, no. 2, p. 175-192
17. HUGHES, S.A. (1993) *Physical models and laboratory techniques in coastal engineering*. World Scientific
18. KLAR, M., (2005) *Design of an endoscopic 3-D particle tracking velocimetric system and its application in flow measurements within a gravel layer*. PhD thesis, University of Heidelberg, Germany.

19. MEER, J.W. van der, D'ANGREMOND, K., GERDING, E., (1995) *Toe structure stability of rubble mound breakwaters*, proceedings of ICE 1995, London, p. 308-321
20. MEER, J.W. van der, (1998) *Geometrical design of coastal structures*, Infram (www.infram.nl), Marknesse, also published as Chapter 9 in *Dikes and revetments: Design, maintenance and safety assessment*, Pilarczyk, K.W. (ed.), Balkema, Rotterdam
21. OCKELOEN, W.J. (2007) *Open filters in breakwaters with a sand core. Study into the stability of granular geometrically open, hydraulically sand-open filters in breakwaters with a sand core*. MSc thesis, Delft University of Technology
22. RANCE, P.J., WARREN, N.F. (1968) *Threshold of movement of coarse material in oscillatory flow*, proceedings of 11th ICCE, London, p. 487-491
23. SANDE, S.A.H. van de, (2012) *Stability of open filter structures*, MSc thesis, Delft University of Technology
24. SCHIERECK, G.J. (2004) *Introduction to bed, bank and shoreline protection*, Delft University Press, Delft
25. SLEATH, J. F. A., (1978) *Measurements of bed load in oscillatory flow*. ASCE Journal of the Waterway Port Coastal and Ocean Division, Volume 104, NoWW4
26. SOULSBY, R. L., and CLARK, S., (2005) *Bed shear –stress under combined waves and currents on smooth and rough beds*, Report TR 137 Rev 1.0, HR Wallingford
27. SUMER, B. M., FREDSOE, J., (2000) *Experimental study of 2D scour and its protection at a rubble-mound breakwater*, Coastal Engineering 40, pp59–87
28. UELMAN, E.F., (2006) *Geometrically open filters in breakwaters*, Delft University of Technology, MSc thesis, Delft
29. VERHAGEN, H.J., ANGREMOND, K. d', ROODE, F.C. van, (2000) *Breakwaters and closure dams*. VSSD, Delft
30. VERHAGEN, H.J., REEDIJK, J.S., MUTTRAY, M.O. (2006) *The effect of foreshore slope on breakwater stability*, Proc. 30th International Conference of Coastal Engineering, San Diego, ASCE, Vol. 5, 4828-4840
31. VERHEIJ, H.J., ADEL, H. den, PETIT, H., (2000) *Design formulas for granular filters*, Delft Hydraulics, Report Q2629, Delft.
32. WORMAN, A., (1989) *Riprap protection without filters*, J. of Hydraulic Engineering, 115 (12), p. 1615-1630.
33. XIE, S. (1981). *Scouring patterns in front of vertical breakwaters and their influences on the stability of the foundations of the breakwaters*, Delft University of Technology.
34. Xie, S.L. (1985) *Scouring patterns in front of vertical breakwaters*. Acta Oceanol. Sin. 4(1), pp153–164.

Appendixes

APPENDIX A PHYSICAL MODELING	A-1
A-1. MODELING TECHNIQUES	A-1
A-2. SCALING SPECIFICITIES.....	A-3
A-2-1. <i>Modeling difficulties</i>	A-3
A-2-2. <i>Interpretation approach</i>	A-4
A-3. DIMENSIONAL ANALYSIS	A-4
A-3-1. <i>Π-theorem</i>	A-4
A-3-2. <i>Application of Π-theorem</i>	A-5
A-3-3. <i>Summary for the application of Π-theorem</i>	A-10
A-4. SCALING APPROACH	A-11
A-5. MITIGATION OF SCALE EFFECTS	A-12
A-5-1. <i>Hydrodynamics</i>	A-13
A-5-2. <i>Rubble mound breakwater</i>	A-13
A-5-3. <i>Wave-structure interaction</i>	A-14
A-5-4. <i>Movable bed scale effects</i>	A-14
A-6. SUMMARY	A-14
A-7. LITERATURE APPENDIX A.....	A-15
APPENDIX B UP-SCALING TO A FICTITIOUS PROTOTYPE	B-1
B-1. UP-SCALING OF KINEMATICS, BREAKWATER & FILTER LAYER.....	B-1
B-2. UP-SCALING OF BASE MATERIAL	B-2
B-2-1. <i>Up-scaling with the Dean Number similitude</i>	B-2
B-2-2. <i>Up-scaling with the Shields' Number similitude</i>	B-3
B-3. SUMMARY	B-4
B-4. LITERATURE APPENDIX B	B-5
APPENDIX C SCALING OF CORE MATERIAL; BURCHARTH ET AL. (1999)	C-6
C-1. <i>PROBLEM AND CONCEPT</i>	C-6
C-2. <i>DESCRIPTION OF SCALING PROCESS</i>	C-7
C-3. <i>LITERATURE 0</i>	C-10
APPENDIX D VARIANCE DENSITY SPECTRUM PLOTS FOR ALL WCS	D-1
APPENDIX E ADDITIONAL ANALYSIS FOR TEMPORAL EVOLUTION OF SCOUR	E-1
E-1. <i>ADDITIONAL PLOTS FOR $S/S_{FINAL}=F(N_p)$</i>	E-1
E-2. <i>ANALYSIS FOR TESTS THAT REACHED EQUILIBRIUM MAXIMUM SCOUR DEPTH</i>	E-2
APPENDIX F ADDITIONAL TABLES WITH TEST PARAMETERS	F-1

Appendix A *Physical modeling*

Physical modeling and hydraulic engineering research are very closely related. Hydraulic engineering studies and numerical modeling are nearly always accompanied by physical model testing; the latter contributes in calibrating a model and validating its results. However, physical modeling results should not be taken unquestionably for granted; they may be infected by hidden model, scale and measurement effects. Consequently, their recognition is crucial for the proper interpretation of the extracted results.

For the present study, physical modeling forms the basis upon which will be based the validity of the research. Therefore, before a modeling strategy is developed, available physical modeling techniques are thoroughly investigated. Afterwards, a strategy is developed and a reasoned in detail. Expected model and scale effects are reported and when it is possible, mitigation measurements are taken to decrease their impact.

At first, the general modeling techniques are described in Section A-1. Then, in Section A-2 takes place a general introduction of the specificities and the resulted problems of this research along with the general outlines of the scaling approach. Afterwards, Section A-3 continues with the application of the Π -theorem into the various examined processes that play a role in the proper scaling of the physical model. Section A-4 describes the modelling strategy that is followed during this study. Finally, Section A-5 presents the mitigation measurements adopted in the modelling approach to counteract the identified scale effects. Argumentation takes place; scale effects are identified and underlined.

A-1. Modeling techniques

Complete similarity between a physical model and its corresponding real-world prototype implies absence of scale effects. In order to accomplish that, *mechanical similarity* (Hughes [1993]) has to be obtained; this is done via the satisfaction of the following criteria:

- *Geometric similarity*: Shape similarity where length dimensions of the physical scale model are n times smaller than the corresponding prototype.
- *Kinematic similarity*: Similarity of motion so that streamline patterns, velocity, acceleration etc. will be related with a constant ratio.
- *Dynamic similarity*: Similarity of forces between prototype and model with respect to a constant ratio. Inertial, gravitational, surface tension, pressure and elastic compression forces are the governing forces related to fluid mechanics (Hughes [1993]). Among them, the most important (Heller [2011]) is considered the inertial force; thus is present in all dimensionless numbers, expressing force ratios combinations that n to be kept constant. In particular these numbers are:
 - Froude Number $F_r = (\text{inertial force}/\text{gravity force})^{1/2} = V/\sqrt{gL}$
 - Reynolds' Number $R_e = \text{inertial force}/\text{viscous force} = LV/\nu$
 - Weber number $W_e = \text{inertial force}/\text{surface tension force} = \rho LV^2/\sigma$
 - Cauchy number $C_a = \text{inertial force}/\text{elastic force} = \rho V^2/E$
 - Euler number $E_u = \text{pressure force}/\text{inertial force} = p/\rho V^2$

However, keeping all ratios constant to obtain exact similitude is not possible. For example a simultaneous attempt to model properly Froude and Reynolds' Number would imply $F_r^P/F_r^M=R_e^P/R_e^M$ and $R_e^M/F_r^M=R_e^P/F_r^P$. This equal to:

$$\frac{g_M^{1/2}}{v_M} = n^{3/2} \frac{g_P^{1/2}}{v_P} \quad (A-1)$$

The value for the right hand of equation (4-2) for regular conditions with a scale factor of $n=40$ will approximate 10^6 . Therefore, for the physical model a fluid with a very small kinematic viscosity v_M will have to be used and/or the model will have to be installed in place with a very large gravitational acceleration g_M , such as a centrifuge (Kobus [1980], Heller [2011]).

However, with only very few exceptions the same fluid is used and the physical model is exposed to the same attraction force; thus simultaneous similarity for both ratios is impossible. For the same fluid in prototype and model, only one force ratio can be kept constant and therefore the most relevant has to be selected (Hughes [1993]). On the other hand, the inevitable choice will generate scale effects that will have to be mitigated.

Froude scaling

The criterion $F_r^M=F_r^P$ is the most common selection for the case of open channel flow. It is especially suited for flows with wave action as dominant force, negligible friction effects (deep water wave propagation) and highly turbulent phenomena (hydraulic jump) (Heller [2011]). Scale effects, such as differences in average velocity distribution occur (Hughes [1993]); however they are considered to have trivial importance. By maintaining Froude Number between prototype and model the following expressions for time (t), velocity (V) and pressure (p) can be derived with respect to geometric scale ratio n_L (Hughes [1993]):

$$n_t=n_v=n_L^{1/2} \text{ and } n_p=n_L$$

Reynolds' scaling

For the cases where viscous forces are dominant (laminar boundary layer, intake structures) the most proper selection is the criterion $R_p=R_M$ (Heller [2011]). Maintaining Reynolds' Number, the following expressions are derived:

$$n_t=n_L^2, n_v=n_L^{-1} \text{ and } n_p=n_L^{-2}$$

From the derived expressions the implied inconveniency of Reynolds' scaling, is rather obvious. For example, using a scale factor of $n=40$ will mean that, for a velocity of $V_p=1\text{m/s}$ in prototype, a new velocity 40 times larger will be needed in the model for similitude.

Weber, Cauchy & Euler similarity

Weber number similarity is relevant for cases where surface tension reproduction in the model is important. Examples are air entrainment in breaking waves, capillary waves, small water depths etc. (Heller [2011]).

Cauchy number similitude is an attempt to account for the different compressibility behavior of water/structure in reality and in the model. If Cauchy number is not preserved and because Young's modulus E cannot be scaled down, water impact will be more abrupt in the model. On the other hand, if air is trapped in the water then the fluid in the model will be

compressed more than it does in real world. Improper scaling of Young's modulus (structure stiffness in the model) is considered to be one of the reasons for Sines breakwater failure (Oumeraci [1984]). Therefore, Cauchy scaling is important when investigating fluid-structure interactions (Le Méhauté [1976]).

Euler number similarity is relevant for cases where high pressure and cavitation are dominant, such as in pipes and turbines; thus is not considered important for this study.

A-2. Scaling specificities

This section discusses the modeling difficulties of the present study and how can they be interpreted and counteracted.

A-2-1. Modeling difficulties

Subject of this study is to gain insight on scour development through a filter designed according to open filter criteria and placed at the toe of a rubble mound breakwater. For such a physical model it is rather obvious that several processes play role; hydrodynamic conditions, geometrical characteristics, wave-structure interactions and movable bed properties need to be similar in reality and in model. As a result, mutual and contradictory demands are risen hindering the selections of a proper scaling technique and eliminating the possibility to apply inspectional analysis.

For example when scaling down the breakwater also the seabed material has to be scaled down and therefore the geometrical similarity rules will lead to sand grain size far smaller than $80\mu\text{m}$, which is unacceptable since cohesion properties start to dominate the material's behavior (for $d < 80\mu\text{m}$).

Moreover, and because it is not possible to maintain both dynamic and kinematic similarity¹⁹, the decision to use the Froude scaling law (appropriate decision in case of wave induced load) will lead to a very small Reynolds' Number. Consequently, the viscous forces on the seabed will be overestimated, up-rush and down-rush velocities will be amplified and the amount of turbulence at the toe area will be overestimated. As a result, excessive transport will take place since the bed material will be relatively large and heavy while the turbulent induced pressure fluctuations that are responsible for lifting up the grains will be stronger. Therefore, the unreliability of the Froude scaling law encourages the decision for a process based model test.

Finally, there is no clear indication about the expected transport mode in the toe-seabed interface. Driving force for bed load transport is the bed shear stress that causes particles to move via rolling or short jumps, while for suspended load this role is played by turbulence that keeps particle into suspension. Both of them are considered to be responsible for scour development around hydraulic structures.

¹⁹ Unless a Lightweight model is applied according to Kamphuis [1975]. In this case, Froude and Reynolds similarity is obtained by using a slightly coarser material that has lower density.

In fact, the present problem is also a problem of scour; however, the presence of toe stones is expected to damp turbulence and interfere in the occurring mode of transport altering its characteristics. Consequently, none of the two transport modes is expected to dominate ultimately, hindering the selection of a scaling approach.

A-2-2. Interpretation approach

Due to the explained complexity, proper dimensioning of the physical model, or correct extrapolation of the investigated physical model in real-world dimensions, is very difficult, and cannot be based on inspectional analysis. Furthermore, interpretation of the extracted results is vulnerable to hidden scale effects that are raised by the contradictory demands of similarity techniques. In order to recognize the inevitable inconsistencies of scaling procedure apart from inspectional analysis, other three techniques are available; dimensional analysis, calibration and scale series tests.

Calibration is based into the occurrence of real-world configurations of a prototype that then can be used to scale it down. By that way, scale effects can also be quantified; however a prerequisite is the existence of reliable prototype data (Heller [2011]) which is not the case here.

Scale series tests (at least three) can take place with different values of scale factor n . The model with the smaller n acts as reference point and is quasi replacing the prototype in calibration procedure (Heller [2011]). Despite that is gained insight into scale effects, it is ambiguous whether the largest model simulates properly the real-world conditions. Furthermore, it is considered time and power consuming procedure that cannot take place during this research.

Dimensional analysis is a commonly applied technique in hydraulic engineering problems. Especially in problems where theoretical understanding of relating processes is limited, dimensional analysis can be used to specify which factors govern the correct reproduction of the related processes, how to dimension the scale model and how to interpret the results extracted from physical model tests. Therefore, is considered the most relevant option for this study.

A-3. Dimensional analysis

A-3-1. Π -theorem

By applying dimensional analysis on a particular process, a set of dimensionless parameters are formed, and used to describe the influence of different factors on the process itself. The scope is not to derive an equation that describes the process, but to identify which parameters are decisive and need to be preserved in a scale model to avoid or reduce scale effects. The most common way to perform dimensional analysis is via the Π -theorem which is based on the theorem (Hughes [1993]) that *“in a dimensionally homogeneous linear*

equation, the dimension of the left-hand side variable equals the dimension of any of the terms on the right-hand side that stands by itself’.

According to Π -theorem of Buckingham (Hughes [1993]), a physical problem with n independent variables (q_1, \dots, q_n) can be reduced to a product of $n-m$ independent, dimensionless parameters (Π_1, \dots, Π_{n-m}), where m is the number of reference, fundamental dimensions (such as mass (M), length (L) and time (T)) required to express the dimensions of the n variables.

Each of the formed Π groups is a function of the m governing or repeating variables and one of the rest $n-m$ independent variables. Therefore, the number of physical parameters that describe a phenomenon is reduced from n to $n-m$. However, the relative importance of dimensionless parameters remains undetermined (Heller [2011]) and, in case of $n > 6$ arbitrariness hinders the specification of similitude criteria.

However by keeping constant values, between model and real life, for each of the formulated dimensionless Π terms, similarity can be obtained. With respect to Ettema [2000] and Hughes [1993], Π -theorem can be applied based on the steps below:

- Identification all n independent parameters relevant to the physical process and transformation in terms of the fundamental dimensions.
- Specification of the dependent variable.
- Determination of the number of fundamental dimensions, m .
- Selection of m physical independent parameters as repeating variables in a way that:
 - None is dimensionless
 - No two have the same dimensions
 - Combined they do not form a Π -parameter
 - They include all fundamental dimensions involved.
- Expression of terms as product of the selected repeating terms.
- Specification of the unknown exponents.

A-3-2. Application of Π -theorem

The accent of this research is paid on the toe and the seabed-toe interface of a rubble mound breakwater; therefore scaling methodology has to assure the correct reproduction of this area and the related processes that occur in real-life. However, this would not be sufficient since loading conditions applied on the toe-bed interface, are directly related to hydrodynamic conditions that occur higher in the water column, and are strongly influenced by the presence of the breakwater. Consequently, proper scaling implies proper simulation of each of the following components:

- Wave properties
- Rubble mound breakwater and seabed material
- Wave-structure interactions
- Movable bed (bed/suspended load transport)

The related parameters for the first two are obvious, thus no further implementation is needed apart from the application of the basic scaling laws and the geometrical similarity (reference is made to the work of Ockeloen [2007]). On the other hand, this is not the case for the remaining two components, where the involving processes are more complex and their interrelations cannot be easily understood. The application of dimensional analysis would provide insight on the parameters that need to be preserved. Nevertheless, it is also expected that both coupling and contradictory conditions will be revealed and therefore compromise would be inevitable.

Below are presented the combinations of important parameters, extracted from the application of Π -theorem. The analysis is based upon computations and literature study findings from other researchers.

Waves-structure interactions

Waves-structure interaction category has to be divided into two sub-categories; interactions at the upper and interactions at the lower part of the structure. The former has to do with direct or first-order wave induced effects in contrast to the latter which are indirect and merely influenced by the character of the former. Both of them express the direct and indirect loading that threatens the stability of the open granular filter.

In particular, waves hitting on the breakwater no matter if they break or not, will cause the development of hydraulic gradient and porous flow inside the structure. The evolution and the way in which the structure is going to absorb the incoming wave energy affects processes and formations such as wave run up/down, reflection, transmission and orbital velocity potential in the area just above the toe. In particular, the latter will result in shear stress development in toe boundary layer. Additionally, the fluctuations in water level differences outside the structure (run up/down) and (in another time scale) inside the structure will affect seabed's, toe's and breakwater's porous flow regime.

Ockeloen [2007] applied dimensional analysis to investigate the dimensional dependences of hydraulic gradient I and filter velocity u_f in a rubble mound breakwater with a sand core. Using his computations as a basis, the parameter of material permeability k can be added in order to account for the ease with which water is flowing into the voids of granular material. Here, index *rep* refers to a fictitious breakwater with representative properties of porosity, permeability etc. that are equivalent to any specific breakwater formation with armor layer, core material and/or filter layer. As a result, the following dimensionless products are derived:

Hydraulic gradient as a function of loading and material properties

$$I = f \left\{ n_{rep}, \frac{H}{D_{rep}}, \frac{H}{T k_{rep}}, \frac{H}{g T^2}, \frac{H^2}{v T} \right\}$$

The term $\frac{H}{g T^2}$ suggests that in order to obtain an equivalent hydraulic gradient formation inside the model breakwater it is important to preserve the wave steepness. In addition, wave height has to be scaled with the square root of the scaling ration used for wave period, which can also be found in Froude scaling law. The ratio $\frac{H}{D_{rep}}$ implies that geometrical

distortions would cause scale effects. Finally, the terms $\frac{H}{Tk_{rep}}$ and $\frac{H^2}{vT}$ express that the fluid's rate of flow inside the structure has to be the same in reality and in model. However, the former term demands a wave height and wave period scaling with the same factor, thus not the use of Froude similarity.

Hydraulic gradient as a function of filter velocity and material properties

$$I = f\left\{\Pi_{rep}, \frac{u_{rep}D_{rep}}{v}, \frac{u_{rep}^2}{gD_{rep}}\right\}$$

For this case, Π -theorem revealed two important dimensionless products; the Reynolds' Number $\frac{u_{rep}D_{rep}}{v}$ for porous flow, and the square of Froude Number $\frac{u_{rep}^2}{gD_{rep}}$. Both of them have to be kept constant. However, their prerequisites are contradictory and therefore the introduction of scale effects in hydraulic gradient and filter velocity is inevitable.

Run up/down as a function of loading and breakwater properties

$$\frac{R_{u/d}}{H} = f\left\{\frac{\tan\alpha}{\sqrt{H/gT^2}}, \frac{k_r}{H}, P\right\}$$

Run up and run down contribute in the formation of the orbital velocity potential at the area just above the toe. Furthermore, their time scale affects the water level difference inside and outside the structure causing pressure gradient and oscillatory porous flow through the toe. Therefore, the controlled representation of these processes is considered substantial. Proper scaling is found to depend on the term $\frac{\tan\alpha}{\sqrt{H/gT^2}}$, which is the Iribarren number ξ . In fact, this criterion is in agreement with Froude similarity. In addition, the roughness k_r of material used in the structural slope has to be scaled with the same factor as length scale and finally, the notional permeability P in reality and in model has to be the same. The latter implies that one of the four reported breakwater configurations (Meer, van der 1988) has to be used.

Toe (filter) relative thickness as a function of filter velocity and material properties

$$\frac{d_f}{D_f} = f\left\{\frac{H}{D_f}, \frac{h}{D_f}, \frac{\rho_s}{\rho_w}, \frac{Tu_f}{D_f}, \frac{D_f u_f}{v}, \frac{u_f^2}{gD_f}\right\}$$

Fluctuation of water level differences, inside and outside the breakwater, will drive a flow of water and sand particles through the voids of the granular toe. Porous flow velocity will change direction and magnitude in order to follow these fluctuations. To simulate it properly in the physical model, apart from keeping the model geometrically undistorted, two terms have to be kept constant; $\frac{D_f u_f}{v}$ and $\frac{u_f^2}{gD_f}$. The former is an expression of Reynolds' Number inside the toe, while the second represents the square of Froude Number with filter grain diameter D_f as the length scale.

Movable bed/ fixed bed tracer model

Scaling of a movable bed is very complex, since apart from modeling the hydrodynamic processes, also sediment properties have to be properly scaled. In sediment transport

computations different approaches occur and can be followed with respect to the type of transport that takes place; bed load or suspended load transport. The same holds here for the scaling procedure; two approaches occur and are based on whether bed load or suspended load transport is the dominant type of transport.

Uelman [2006] and Ockeloen [2007] investigated the behavior of a breakwater with a sand core. Observations from their experiments didn't reveal the dominance of a specific type of transport since they noticed signs of both of them. Furthermore, in this research is not expected to take place a specific mode of sediment transport. At first, will take place fluidization of the upper layers of seabed material, that are closer to the transitional area, and then, water-sediment flux will travel through the porous media of the toe, to cause seabed erosion. Consequently, suspended sediment transport will be damped by the upper lying toe material although erosion will take place but with a regime that is different from bed load transport. However, what is important in this stage is to assure that flow conditions inside the pores of the toe and through the sand is located in the same regime as it happens in real life.

This part of dimensional analysis is merely based on the dimensionless products derived by Kamphuis [1991]²⁰, Dalrymple (1989)²¹ and Ockeloen [2007]. Additional computations have been done but they revealed processes' dependencies on the same dimensionless ratios.

Scour depth as a function of hydraulic loading

$$\frac{d_s}{H} = f\left\{\frac{D_f}{H}, \frac{D_b}{H}, \frac{d_f}{H}, \frac{h}{H}, \frac{\rho_s}{\rho_w}, \frac{H}{gT^2}, \frac{\sqrt{gHH}}{v}\right\}$$

In order to obtain at the model an erosion depth equivalent to the one in real, the model has to be geometrically undistorted. Additionally, according to $\frac{H}{gT^2}$ (function of wave steepness H/L) wave steepness has to be kept same. Furthermore, relative density s of grain material and water has to be the same in model and reality. Finally, the term $\frac{\sqrt{gHH}}{v}$ is an expression of Reynolds' Number. Ockeloen [2007] transforms it to the term $\frac{\sqrt{gHD_f}}{v}$ which is a measure of Reynolds' Number inside the pores of the filter.

Time scale of scour depth development

$$\frac{T_s}{T} = f\left\{\frac{H}{h}, \frac{D_b}{H}, \frac{gsD_bT^2}{H^2}, \tan\alpha, \frac{\sqrt{gHH}}{v}\right\}$$

Likewise to erosion depth, the time scale of erosion evolution depends merely on a measure of Reynolds' Number expressed by the term $\frac{\sqrt{gHH}}{v}$. Besides, the term $\frac{gsD_bT^2}{H^2}$ appeared on the results of the dimensional analysis. A transformation of this term was used by Fredsoe & Sumer [2000] to formulate a dimensionless time scale for scour development in the trunk of a breakwater.

²⁰ Hughes (1993)

²¹ Tirindelli *et al.* [2000]

Sediment transport as a function of shear velocity and material properties by Kamphuis (1991)²²

$$S_* = f \left\{ \frac{u_* D}{\nu}, \frac{\rho u_*^2}{\gamma_i D}, \frac{\rho_s}{\rho_w}, \frac{w_s}{u_*}, \frac{\lambda}{D} \right\}$$

Dimensionless sediment transport is a function of grain Reynolds' Number $\frac{u_* D}{\nu}$ and densimetric Froude Number $\frac{\rho u_*^2}{\gamma_i D}$, with $\gamma_i = (\rho_s - \rho_w)g$ the buoyant specific weight of the grains. Combined, they form the coordinates of Shields' diagram. The contradiction of these two has already been described. In addition, apart from the relative density $\frac{\rho_s}{\rho_w}$ the relative fall speed $\frac{w_s}{u_*}$ between shear velocity u_* and fall velocity w_s needs to be kept constant. Finally, no geometrical distortion is allowed with λ expressing the average wave amplitude (α_m) in case of short wave models. Therefore, grain size and model's geometrical characteristics are scaled with the same factor.

Sediment transport as a function of shear velocity and material properties by Dalrymple (1989)²⁰

$$S_* = f \left\{ \frac{u_* D}{\nu}, \frac{\rho u_*^2}{\gamma_i D}, \frac{\rho_s}{\rho_w}, \frac{H}{w_s T} \right\}$$

Two years before Kamphuis, Dalrymple revealed the same dependences between dimensionless sediment transport and shear velocity/material properties. Furthermore, he included the term $\Omega = \frac{H}{w_s T}$, known as Dean Number or relative fall speed parameter; the ratio between the time needed for a sediment to arrive at the bottom $\frac{H}{w_s}$, to the wave period T. It is also considered as the criterion that determines whether bed load or suspended load is the dominant type of sediment transport. Especially when suspended load is the dominant mode of transport, scaling is accomplished using Dean Number similarity. Unfortunately, scaling with respect to Dean Number is not in agreement with Froude scaling.

Sediment transport as a function of shear velocity and material properties by Kamphuis (1991)²³ under breaking conditions

$$S_{b*} = f \left\{ \frac{\sqrt{g H_b} D}{\nu}, \frac{\rho g H_b}{\gamma_i D}, \frac{\rho_s}{\rho_w}, \frac{w_s}{\sqrt{g H_b}}, \frac{H_b}{D} \right\}$$

Kamphuis (1991)²⁰ transformed the dimensionless ratios for the case of breaking waves. Therefore, the term $\frac{w_s}{\sqrt{g H_b}}$ expresses the ratio of propagation velocity of breaking wave $\sqrt{g H_b}$ and fall velocity w_s . Moreover, the term $\frac{\rho g H_b}{\gamma_i D}$ represents the mobility number criterion.

Bed load transport as a function of shear velocity and material properties

$$\frac{S_b}{D_b u_*} = f \left\{ \frac{k_r}{D_b}, \frac{h}{D_b}, \frac{\rho_s}{\rho_w}, \frac{u_*^2}{g D_b} \right\}$$

²² Tirindelli et al. [2000]

²³ Tirindelli et al. [2000]

Bed load transport can be made dimensionless by dividing it with the shear velocity u_* and a length scale which for this case sand particle diameter D_b is more appropriate. Ockeloen [2007] used a different pair of parameters by combining the friction coefficient k_r (length scale) and flow velocity u . Besides, the term $\frac{u_*^2}{gD_b}$ is the square of densimetric Froude Number, thus Froude similarity is the appropriate choice to avoid scale effects in bed load transport characteristics.

A-3-3. Summary for the application of Π -theorem

The most important conclusions drawn from the dimensional analysis are can be found below:

- The implementation of all the processes under consideration showed that the physical model should not be geometrically distorted. All length dimensions have to be scaled with the same factor. Therefore, the use of sand material that cannot be scaled down is expected to cause scale effects.
- Relative density s appears in almost all the series of dimensionless products; thus, the density ratio of materials used in the model has to be the same as in real life. For that reason, using a seabed material with lower density, to account for the scale effects due to geometrical distortion, will also disorder the similarity in relative density. However, minor scale effects will anyway rise due to the fact that fresh water will be used instead of salty sea water.
- As it was expected, Froude Number appeared as one of the dimensionless terms, in all the flow prevailing processes. It is considered substantial in the proper representation of hydraulic gradient and porous flow formation, inside the breakwater and the toe. Additionally, it influences sediment transport processes, and especially bed load transport. The use of Froude similarity as a scaling approach satisfies also the proper reproduction of wave steepness and Iribarren number that was found to be important for run up/down and scour development. Furthermore, densimetric Froude Number $\frac{\rho u_*^2}{\gamma_i D}$ or Shields parameter similarity can be used when bed load transport is dominant.
- Simultaneously, Reynolds' Number and consequently viscous forces equivalently impact the reproduction of porous flow, hydraulic gradient, sediment transport and scour development in time and space. Especially for filter processes reserving Reynolds' Number is considered crucial; thus at least when Froude similarity is used, a certain flow regime has to be preserved inside the granular material. To reduce viscous forces-induced scale effects, Reynolds' Number inside the porous media has to be kept as high as possible. Nevertheless, it should be underlined that during flow reversals flow will inevitable fall into the viscous regime.
- The Dean Number $\Omega = \frac{H}{w_s T}$ appeared as one of the dimensionless terms that influence sediment transport. In general, it is considered to be important for suspended load dominated transport. Besides, Dean Number and densimetric Froude Number cannot be preserved simultaneously, thus choice has to be made

that will generate scale effects, especially since there is no clear picture of the type of transport that is dominant.

A-4. Scaling approach

For the present study no real prototype occurs; therefore in reality, the described approach refers to the link between the model and a fictitious prototype. Furthermore, the establishment of scaling approach refers to the selection of the scaling techniques that will be used to simulate the following four aspects: wave properties, breakwater configuration, breakwater porous flow and seabed material. Later on, Section Appendix B will present quantitative details of the attempts to link .

Generally speaking, it is not possible to satisfy all requirements extracted by dimensional analysis; therefore perfect similitude cannot be achieved. The risen scale effects can be counteracted or mitigated by using different scaling approaches in parts of the physical model (seabed material) in combination with the application of certain boundary conditions (turbulent porous flow inside armor and filter layer).

Waves and wave properties

Wave characteristics were scaled using the Froude law. For breaking waves this will cause scale effects due to difference in air entrainment and the use of fresh water.

Breakwater configuration

One of the breakwater configurations with a reported notional permeability value, according to van der Meer (Meer, van der [1988]), was used. Geometrical characteristics (toe stone grain size, breakwater layer's grain size, water depth etc.) were scaled according to geometrical similarity of Froude scaling law without geometrical distortions. In combination with wave properties and porous flow scaling, flow conditions, at least inside the armor layer of the breakwater, have to be located into the turbulent regime.

Seabed material

Selection: Scaling of seabed material is the most significant and complex part of modeling approach. One of the most important prerequisites of this study is that the breakwater lies upon sand in both the model and prototype. In order to comply with that, a lightweight material will be used to simulate sand in the model's seabed. Previously, it was mentioned that it is not possible to preserve both the Dean and the densimetric Froude Number. Therefore, selection for the similarity approach implies also an assumption about which mode of transport is considered dominant.

Despite that it is considered a handy tool to simulate fine materials; the use of lower density material imposes scale effects, since it disorders other important scale factors. Firstly, relative density is not preserved leading into inaccurate particle accelerations. Paul *et al.*

(1972)²⁴ observed faster acceleration and increased extend of horizontal trajectory for light weight material particles. Furthermore, the use of a lightweight material disturbs relative length scale between the characteristic length λ (mainly the wave amplitude) and the seabed grain size.

Based on the properties of the selected lightweight material the model will be up-scaled with respect to:

- Dean Number similarity rule
- Shields' parameter similarity rule

Theoretical explanation of these methods will be offered in Chapter Appendix B along with the quantitative implementation of the up-scaling process.

Porous flow/hydraulic gradient

Geometrical scaling of rip rap strengthens viscous effects in the model and turns model structure to behave as it is less porous than the prototype. As a result, absorption, reflection, and transmission of wave energy do not correspond to reality. For that reason, Burcharth *et al.* [1999] developed a scaling approach that preserves a characteristic value of hydraulic gradient inside the breakwater configuration. Pressure and porous velocity inside the breakwater vary in time and space causing fluctuation of scaling conditions. To cope with that, the diameter of core material is computed in a way that Froude law holds for a characteristic pore velocity. This velocity is the average representative velocity of the most critical area in breakwater core. This approach is followed here and is treated in 0.

A disadvantage of this approach is that it seeks for pressure amplitude measurements of the prototype. This investigation is not addressed to a specific prototype and the results have to be extrapolated in order to be interpreted and applied in real life scale. Therefore, uncertainty is introduced concerning the validity of scaling computations for the porous flow and hydraulic gradient.

A-5. Mitigation of scale effects

In the previous paragraph, the scaling approach of the present study was explained and arguments were provided to reason the accomplished selections. This part of the report provides some general boundary conditions that need to be satisfied in order to reduce the magnitude of the inevitably occurring scale effects.

Quantification of scale effects is considered very ambiguous. Despite that, rough approximations of the expected scale effects in the upper part of the physical model do exist; their impact on seabed erosion is rather opaque. In particular, Hughes [1993] relates stability of outer layers with Reynolds' Number of the specific layer in order to determine the difference between stability numbers in model and prototype. Afterwards, this difference is expressed as a percentage and can be linked (via assumption) with a degree of overestimation or underestimation of porous flow and hydraulic gradient formation in the

²⁴ According to Hughes [1993]

structure. However, the degree on which these deviations affect loading and erosion of the seabed cannot be estimated.

A-5-1. Hydrodynamics

For proper reproduction of wave properties, it is of significant importance to preserve Froude Number (Tirindelli *et al.* [2000]). In general, Froude scaling is considered important for all processes that are flow dominated. Despite that Froude scaling will lead to a very low Reynolds' Number (overestimation of viscous forces), their effect on non-breaking laboratory waves is considered trivial if water depths $h > 2\sim 3\text{cm}$ and the distance of wave propagation is limited. Therefore, the structure should not be placed at a large distance from the location of wave generation.

Surface tension σ scale effects are also negligible for non-breaking waves when wave height $H > 2\text{cm}$ and wave period $T > 0.3\text{s}$; therefore for not very small and steep waves (Tirindelli *et al.* [2000]). On the other hand, this is not the case for breaking waves. Here, surface tension σ and viscosity affect scale-dependent breaker shape and type for waves with length $L < 0.5\text{m}$ and wave period $T < 0.5\text{s}$ (Tirindelli *et al.* [2000]).

In addition, in order to obtain short wave similarity between model and real-world, apart from Froude and Reynolds' Number, also Euler and Strouhal number have to be preserved (Hughes [1993]). Strouhal number expresses the ratio between oscillatory velocity and mean speed, is given by $S_t = \omega L / V$ and therefore is substantial for this study which focuses on the toe area.

A-5-2. Rubble mound breakwater

In general it is considered that the use of higher scale factor n increases the magnitude of the introduced scale effects. For that reason a variety of rule of thumbs exist that aims to compromise the demands of model size (availability of facilities and economics) and magnitude of scale effects (moderate degree). According to Heller [2011] the following rules apply with respect to the scale factor:

- Breakwater stability under short waves: 1:30 to 1:50 Hughes [1993].
- Rubble mound breakwater stability 1:20 to 1:80 Oumeraci [1984].
- Short wave reflection at porous breakwater 1:10 to 1:20 Oumeraci [1984].

For this study the selection of a specific scale factor is trivial since the developed physical model is not addressed to a real scale breakwater. However, real structures would be used as starting points for the selection of dimensions and hydraulic loading conditions; thus a scale factor has to be selected.

Based on dimensional analysis conducted by Hughes [1993], in order to avoid effects due to scaling of a rubble mound structure, the structure model should not be distorted. In addition, Froude scaling has to be applied but in combination with high values of Reynolds' Number to preserve turbulent flow conditions at least throughout the armor layer. Various

recommendations can be found in literature concerning the minimum value of Reynolds' Number. The following criteria were found in Tirindelli *et al.* [2000] for $Re = \frac{\sqrt{gH_s}D_f}{\nu}$:

- Van der Meer (1988) suggested that no significant scale effects occur for $Re=10^4$ to 4×10^4 and irregular waves.
- Jensen & Klinting (1983) suggested 0.7×10^4 as minimum Reynolds' Number value to avoid scale effects.
- Sharp & Khader (1984) proposed 4×10^5 for regular waves.
- Kajima & Sakakiyama (1994) proposed 3×10^4 for regular waves.

A-5-3. Wave-structure interaction

Van der Meer & Veldman (1991)²⁵ did not find substantial differences; thus scale effects in wave run up and reflection for physical models with scale factor of 1:7 and 1:35. Only wave transmission was 10-50% higher in the larger model. In addition, Bullock *et al.* (2001)²³ computed 10% higher impact pressures in a model scaled with Froude similarity, with a scale factor of 25 and a $H_s=0.25$ m.

A-5-4. Movable bed scale effects

Firstly, it should be mentioned that the current physical model is not a fully movable bed model but more a fixed bed tracer model, since seabed will be movable only in the area under the toe of the breakwater.

Secondly, since sand cannot be scaled down based on geometrical similarity, scale effects from movable bed are raised. These effects can be merely counteracted by the use of a material that is as fine as sand but has lower density. This was explained in detail in Paragraph 4.4 "Seabed material". Consequently, in order to mitigate movable bed-induced scale effects sediment has to be scaled in a different way than geometry and hydrodynamics.

A-6. Summary

Unquestionably, perfect similitude between real life and hydraulic physical models cannot be accomplished. Scale effects are inevitable; their identification and manipulation is decisive for the validity of the study. Especially when the existing theoretical knowledge upon the involved processes is limited the situation becomes very complex. Dimensional analysis is a tool that can provide insight on the parameters that play significant role on the involved processes, and thus draw the lines upon which scaling approach has to be based. Moreover, it reveals the contradictory demands of the involved processes that are responsible for scale effects.

Application of the Π -theorem showed three major implications of the scaling procedure:

²⁵ Tirindelli *et al.* [2000]

- both Froude and Reynolds' Number are important for proper scaling of all processes
- geometrical distortion is prohibited
- scaling of seabed material (sand) can be done by combining the prerequisites of Dean Number similarity, Densimetric Froude Number similarity and the use of a lightweight material.

Therefore, selecting Froude similarity creates viscous-induced scale effects and strengthens cohesive properties of seabed material. To cope with those problems an alternative scaling approach is developed that is a combination of similarity techniques and resembles the Dean approach. In particular:

- Froude scaling is applied in hydrodynamic (wave form) scaling and scaling of geometrical characteristics,
- To counteract overestimated viscous forces in sensitive areas (armor/filter layer) Reynolds' Number is kept as high as possible
- Seabed material is simulated in the model with the use of a lightweight material

Chapter 4 contains the numerical computations for the model set up according to the developed scaling approach described in Chapter 3.

A-7. Literature Appendix A

1. BUCKINGHAM, E. (1914). *On physically similar systems - Illustrations of the use of dimensional equations*. Physical Review 4, 345–376.
2. ETTEMA, R., ARNDT, R., ROBERTS, P., WAHL, T., 'Hydraulic Modeling – Concepts and Practice'. American Society of Civil Engineers, 2000
3. HELLER, V., (2011) *Scale effects in physical hydraulic engineering models*, Journal of Hydraulic Research, 49:3, 293-306
4. HENRIQUEZ, M., RENIERS, A.J.H.M., RUESSINK, B.G., STIVE, M.J.F., STANTON, T.P., FOSTER, D.L., (2008) *On the scaling of sediment transport in the nearshore*, International Conference on the Application of Physical Modelling to Port and Coastal Protection - Coastlab '08, 2-5 July 2008, Bari, Italy ; pre-print version.
5. HUGHES, S.A. (1993) *Physical models and laboratory techniques in coastal engineering*. World Scientific
6. KAMPHUIS, J. W. (1975) *Friction Factor under Oscillatory Waves*. Journal of Waterways, Harbours, Coastal Div., A.S.C.E., 101 (WW2) , 135-144.
7. KAMPHUIS, J. W. (1991) *Alongshore sediment transport rate*, Journal of Waterways, Port, Coastal and Ocean Engineering ASCE, 117(6), 624-641.
8. KOBUS, H., ed. (1980) *Hydraulic modeling*. German association for water resources and land improvement, Bulletin 7. Parey, Hamburg.
9. Le MEHAUTE, B. (1976) *An introduction to hydrodynamics and water waves*. Springer, New York.

10. OUMERACI, H., (1984) Scale effects in coastal hydraulic models. Symp. Scale effects in modeling hydraulic structures 7(10), 1–7. H. Kobus ed. Technische Akademie, Esslingen.
11. MEER, J.W. van der, VELDMAN J.J., (1991) *Singular points at berm breakwaters: scale effects, rear, round head and alongshore transport*, Coastal Engineer 17 (1992), Elsevier Amsterdam
12. OCKELOEN, W.J. (2007) *Open filters in breakwaters with a sand core. Study into the stability of granular geometrically open, hydraulically sand-open filters in breakwaters with a sand core*. MSc thesis, Delft University of Technology
13. OUMERACI, H., (2003) *Role of Large-Scale Model Testing in Coastal Engineering – Selected Examples Studies performed in GWK Hannover. Towards a Balanced Methodology in European Hydraulic research*, Budapest, May 2003
14. SAYAO, O.J. (2007) *Toe protection design for rubble mound breakwaters*, Proceedings Coastal Structures, Venice
15. SUMER, B. M., FREDSOE, J., (2000) *Experimental study of 2D scour and its protection at a rubble-mound breakwater*, Coastal Engineering 40, pp59–87
16. TIRINDELLI, M., LAMBERTI, A., *Wave Action on Rubble Mound Breakwaters: the Problem of Scale Effects*. DELOS EVK3-CT-2000-00041
17. UELMAN, E.F., (2006) *Geometrically open filters in breakwaters*, Delft University of Technology, MSc thesis, Delft

Appendix B *Up-scaling to a fictitious prototype*

Appendix B treats the model up-scaling technique with particular focus on the up-scaling of the seabed material along with the determination of the range of applicability of eq. (6-7) found in Section 6.4. In reality, this procedure does not represent a scaling process, but a technique to link the model characteristics with a fictitious prototype while identifying entailed scale effects.

In particular, this chapter starts by up-scaling the kinematics and the breakwater configuration used in this model, with respect to the Froude law. Afterwards, the seabed material is up-scaled with respect to the two major similitude rules; The Dean Number similitude and the Shields Number similitude.

Finally, the chapter ends by concluding the important findings. Finally, it should be mentioned that information with respect to the available scaling tools and how can they used in this particular research can be found in Section A-2. In addition, the overall scaling strategy of the present study is described in Section A-4; however the approach is only qualitative.

B-1. Up-scaling of kinematics, breakwater & filter layer

Up-scaling of wave kinematics, breakwater and filter layer is carried out based on the Froude law of similitude. Scaling of wave kinematics refers to wave properties (wave height, wave period etc.), behavior (breaking, shoaling etc.) and water depth which according to theory are properly reproduced in model and prototype. The term breakwater configuration refers to breakwater dimensions, armor layer and core material; however the former does not have particular importance for this research. Finally, ups-scaling of filter layer corresponds to the up-scaling of filter characteristic diameter D_{f50} and filter thickness d_f .

To quantify the process, a general scaling factor is assumed to be 1:35. The selection of this number is based on the general practice that is being followed during physical model studies in hydraulic engineering research. The results can be found in Table 0–1.

element	Dimension	Model (m)	Prototype (m)	element	Dimension	Model (m)	Prototype (m)
filter 1	D_{50}	0.0143	0.5005	WC1 _t	H_s	0.120	4.20
	d_f	0.0500	1.7500		T_p	2.485	14.70
filter 2	D_{50}	0.0133	0.4655	WC2 _t	H_s	0.120	4.20
	d_f	0.0450	1.5750		T_p	2.032	12.02
filter 3	D_{50}	0.0096	0.3360	WC3 _t	H_s	0.100	3.50
	d_f^*	0.0330	1.1550		T_p	2.485	14.70
	d_f^{**}	0.0330	1.1550	water depth	h_t	0.300	10.50
filter 4	D_{50}	0.0068	0.2380	armor layer	D_{n50}	0.041	1.44
	d_f	0.0230	0.8050	core material	D_{n50}	0.015	0.53
*:with $D_{b50}=360\mu\text{m}$				**:with $D_{b50}=210\mu\text{m}$			

Table 0–1 Up-scaling results for wave kinematics, breakwater configuration and filter layer properties

B-2. Up-scaling of base material

Two techniques are used to up-scale the model's seabed material; namely the Dean Number similitude and the Shields' Number similitude. The procedure is described below.

B-2-1. Up-scaling with the Dean Number similitude

During the experiment, at the start of the horizontal part of the foreshore and at the breakwater slope, wave breaking was taking place, leading in an abrupt increase of the turbulent kinetic energy relative to the bottom-friction induced turbulent energy. For that reason, preserving the Dean Number is of substantial importance (Henriquez [2008]).

In particular, if fresh water is used to simulate sea water then $n_\rho = n_u = 1$. In addition, from Froude similarity in wave kinematics (Section A-1) $n_H = n_T^2 = n_H = n$.

The Dean Number similitude is given by: $n_{DN} = n_H n_T^{-1} n_{ws}^{-1}$. Using the formula of Hailermeier [1981] for the settling velocity w_s it is found: $n_{ws} = n_v^{0.7} n_D^{1.1} n_\rho^{-0.7} n_u^{-0.4} = n_v^{0.7} n_D^{1.1}$. Afterwards, these two expressions are combined, the scaling factor is set to be $n_{DN} = 1$ and then the effect of Froude similarity is incorporated to arrive into the final expression:

$$n_D^{1.1} = n^{0.5} n_v^{-0.7} \quad (7-1)$$

Similarly to Section B-1 $n = 35$ is assumed. Therefore, for a given n_{ps} the grain diameter of the up-scaled seabed material can be computed. In the present study two grain diameters were used $D_{b50} = 210 \mu\text{m}$ and $D_{b50} = 360 \mu\text{m}$ with $\rho_s = 1500 \text{kg/m}^3$. Consequently, $n_{ps} = 1.77$, $n_v = 3.3$ and with the use of eq. (7-1) $n_D = 2.35$. Therefore, the corresponding values for the prototype are $D_{b50} = 494 \mu\text{m}$ and $D_{b50} = 848 \mu\text{m}$; therefore medium sand.

Furthermore, the relative grain diameter values that were tested in the model can now be extrapolated in real life scale. However, the calculated values address to unrealistic relative grain diameters. Results are shown in Table 0–2.

Application	Db50=360μm			Db50=210μm	
	Test series 1	Test series 2	Test series 3	Test series 4	Test series 5
Model	39.83	36.81	26.67	32.33	45.71
Prototype	590.49	549.2	396.42	481.36	679.57

Table 0–2 Up-scaling of relative grain diameter based on Dean Number similitude.

Evaluation: Dean Number similarity is used to simulate suspended load transport characteristics; however is responsible for bed load transport scale effects, since between model and real life, bed shear stress is not preserved. In addition, Reynolds' number in the model falls in the laminar/smooth turbulent regime while in prototype it is mostly located in the rough turbulent regime.

On the other hand, Dean Number similitude assures that the fall trajectory of suspended particles in the model is equivalent to the equivalent prototype and the model's particle fall time is proportional to the real life fall time. According Hughes [1993], Dean Number similarity is appropriate scaling approach for use in studying short term scour around coastal structures, under storm events.

Additionally, the analysis of model results have shown that for decreasing D_{b50} , erosion of base material was less intensive even though a larger D_{f50}/D_{b50} was applied. This was explained based on the diagram of Sleath (Schierck [2004]). Thereby, left from $D^*=20$, a lower D^* leads to a higher stability Number. When the up-scaled base materials are expressed as dimensionless grain diameter it is found $D^*=12.5$ and $D^*=21.45$. Therefore, $D_{b50}=494\mu\text{m}/D^*=12.5$ addresses to a higher stability Number than $D_{b50}=848\mu\text{m}/D^*=21.45$. Consequently, this up-scaling process arrives into a result that is qualitatively in accordance with the test results.

However, the critical Shields' Number is not preserved between the model and prototype. In particular, for the prototype $D^*=12.5$ corresponds to $\Psi_{cb}=0.0257$ and $D^*=21.45$ corresponds to $\Psi_{cb}=0.0188$. This means that model underestimates the erosion and therefore the scour hole of the prototype situation. Unfortunately, the difference cannot be quantified.

Thereupon, for Dean Number similitude the following conclusions can be drawn:

- Prototype seabed material is medium sand
- The computed relative grain diameters are unrealistic
- Model underestimates amount of damage
- Both in model and prototype, the finer base material has higher stability number.
- Up-scaling is not successful.

B-2-2. Up-scaling with the Shields' Number similitude

The Shields' Number similitude is given by $n_\psi = n_u^2 n_v^{-1} n_D^{-1}$. A relation for the shear velocity similitude can be extracted by combining the expression of Jonsson (Schierck [2004]) for shear velocity along with the expression for the friction factor given by Swart (Schierck [2004]) and the application of Froude similarity. In particular the scale factor for shear velocity is given by: $n_u = n^{0.7} n_D^{0.3}$. Combining these expressions and setting $n_\psi = 1$ gives the following expression:

$$n_D^{0.7} = n^{0.7} n_v^{-1} \quad (7-2)$$

Similarly to Section B-1 $n=35$ is assumed. Therefore, for a given n_{ps} the grain diameter of the up-scaled seabed material can be computed. In the present study, two grain diameters were used $D_{b50}=210\mu\text{m}$ and $D_{b50}=360\mu\text{m}$ with $\rho_s=1500\text{kg}/\text{m}^3$. Consequently, $n_{ps}=1.77$, $n_v=3.3$ and with the use of eq. (7-2) $n_D=6.36$. Therefore, the corresponding values for the prototype are $D_{b50}=1.3\text{mm}$ and $D_{b50}=2.3\text{mm}$. Therefore, coarse sand and fine gravel, respectively.

Table 0–2 presents the up-scaled values of relative grain diameter. Calculated values are closer to reality; however their validity is still quite doubtful.

Application	Db50=360µm			Db50=210µm	
	Test series 1	Test series 2	Test series 3	Test series 4	Test series 5
Model	39.83	36.81	26.67	32.33	45.71
Prototype	217.61	202.39	146.09	183.08	258.46

Table 0–3 Up-scaling of relative grain diameter based on Shields' Number similitude.

Evaluation: Densimetric Froude Number or Shields parameter similarity preserves bed load transport characteristics but raises suspended load transport scale effects. It is very important for the accurate reproduction of the different modes of transport. However, scale effects rise by the fact that the Dean Number is not preserved.

In addition, the up-scaled base materials are expressed as dimensionless grain diameter it is found $D_* = 32.88$ and $D_* = 58.18$. Therefore, $D_{b50} = 1.3\text{mm}/D_* = 32.8$ addresses to a lower stability number than $D_{b50} = 2.3\text{mm}/D_* = 58.18$. This is in contrast to what was observed during the tests.

Furthermore, the critical Shields' Number is not preserved between the model and prototype. In particular, for the prototype $D_* = 12.5$ corresponds to $\Psi_{cb} = 0.0189$ and $D_* = 58.18$ corresponds to $\Psi_{cb} = 0.0303$. This means that model underestimates the erosion and therefore the scour hole of the prototype situation. The difference between the two cannot be quantified.

Thereupon, for Shields' Number similitude the following conclusions can be drawn:

- Prototype seabed material is not in all cases sand
- The computed relative grain diameters are unrealistic
- Model underestimates amount of damage
- In contrast to the model, in prototype the finer base material has lower stability number.
- Up-scaling is not successful.

B-3. Summary

Three up-scaling techniques were used to link the investigated physical model with a fictitious prototype. Apart from the entailed scale effects additional problems were found. In particular:

- Prototype seabed material was not sand
- The computed relative grain diameters are unrealistic
- Model underestimates amount of damage
- Finer base material in the prototype had higher stability number than coarser. The reciprocal occurred in the model

None from the presented up-scaling procedures was able to overcome all the aforementioned problems. Consequently, no prototype was found to successfully represent the investigated physical mode.

B-4. Literature Appendix B

1. HALLERMEIER, R.J., (1981) *Terminal settling velocity of commonly occurring sand grains*, Sedimentology, Vol 28, No 6, pp 859-865
2. HENRIQUEZ, M., RENIERS, A.J.H.M., RUESSINK, B.G., STIVE, M.J.F., STANTON, T.P., FOSTER, D.L., (2008) *On the scaling of sediment transport in the nearshore*, International Conference on the Application of Physical Modelling to Port and Coastal Protection - Coastlab '08, 2-5 July 2008, Bari, Italy ; pre-print version.
3. HUGHES, S.A. (1993) *Physical models and laboratory techniques in coastal engineering*. World Scientific
4. SCHIERECK, G.J. (2004) *Introduction to bed, bank and shoreline protection*, Delft University Press, Delft

Appendix C *Scaling of core material; Burcharth et al. (1999)*

Section A-2 described the scaling specificities of this study; among them one of the most important is the mitigation of viscous scale effects of the porous flow inside the breakwater, induced by the selection of Froude scaling law to model hydrodynamics. In Section A-4 is selected a technique (Burcharth *et al.* [1999]) to solve this problem; however solution is treated only qualitatively. At this section, is offered detailed explanation of the computational steps needed for the conduction of scaling of core material in rubble mound breakwaters.

Finally, it should be noted that for the present study a factual prototype does not exist. However, a fictitious prototype is considered and is assumed to have the properties of the model when extrapolated using the Froude law similarity. Therefore, the goal at this section is to preserve turbulent flow conditions in the armor and core of the breakwater.

C-1. Problem and concept

Simultaneous preservation of Froude and Reynolds' Number between model and prototype is not possible; thus for a model breakwater where hydrodynamics are scaled according to Froude law will lead to a very low Reynolds' Number and to inevitable viscous induced scale effects. These scale effects influence among others, parameters and processes such as porous flow inside the breakwater, permeability (thus energy absorption) and wave run up/down. On their turn, the distorted parameters alter the loading conditions in front of and on the breakwater; leading to a situation which is not representative to real life conditions.

Mitigation of the viscous induced scale effects can be succeeded by proper reproduction (in the model) of prototype's hydraulic gradient and porous velocity. However, both of them vary in space and time hindering the selection of representative scaling factor.

In order to solve this problem, Burcharth *et al.* [1999] proposed that breakwater's core material should be scaled with a different factor than the (Froude extracted) geometrical factor used to scale the rest of the structure. This factor can be determined by means of sequential, computational steps which include the calculation of wave induced pressure distribution and the corresponding wave induced pore velocities inside the rubble mound breakwater. The basis for the development of the method was a series of model tests (Bürger *et al.* [1988]) and the measurements on the breakwater of Zeebrugge. Thereby, porous flow inside the breakwater is kept at the turbulent flow regime (like the breakwater of Zeebrugge).

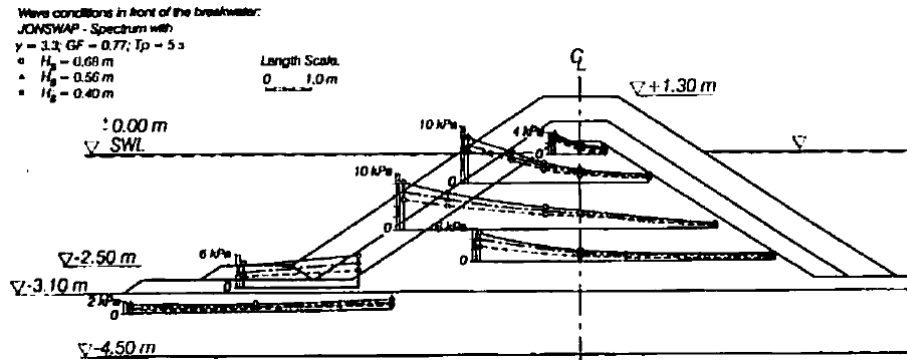


Figure C-1 Horizontal distribution of the wave induced pore pressure amplitudes from Bürger *et al.* (1988)

Porous flow regimes (from Dybbs and Edwards [1984])

Based on particle Reynolds number Re_p , Dybbs & Edwards [1984] identified four porous flow regimes:

- $Re_p < 5$: Darcy flow regime - viscous dominated flow.
- $5 < Re_p < 200^+$: steady inertial flow regime or laminar Forchheimer flow – initiation of inertial forces dominance.
- $200^+ < Re_p < 350^+$: unsteady laminar flow regime. Theoretically, oscillatory flows should occur in this regime. Transitional regime to the fully turbulent flow regime.
- $200^+ < Re_p < 350^+$: fully developed turbulent flow regime.

Particle Reynolds number is defined as:

$$Re_p = \frac{2 \langle u \rangle d_p}{3 \nu} \frac{n}{1-n} \quad (B-1)$$

In which:

- $\langle u \rangle$: intrinsic averaged pore water velocity
- d_p : particle diameter

If, according to Froude scaling of core material, the porous flow inside the model's core is found into one of the first two regimes, then viscous induced scale effects will be expected. To cope with the entailing scale effects, a smaller scale factor will be used to scale core material in way that will assure that porous flow will be placed at least in the transitional zone.

C-2. Description of scaling process

From the analysis of data from Bürger *et al.* [1988] and the in-situ measurements at the breakwater of Zeebrugge the following empirical expression was derived that relates pressure distribution and horizontal distance x :

$$p_{max}(x) = p_{0,max} e^{-\delta \frac{2\pi}{L} x} \quad (B-2)$$

In which:

- x : horizontal coordinate with $x=0$ in the interface between armor layer and under-layer or core
- $p_{0,max}$: maximum reference pressure
- δ : damping coefficient

L' : wave length in the core ($L' = L/D^{0.5}$)
 L : wave length
 D : coefficient to account for seepage length, empirical value of 1.4 at Le Mehaute, Biesel [1950] gave a theoretical value of 1.5

A reasonable estimate of the maximum reference pressure can be reasonably estimated with:

$$p_{0,max} = \rho_w g \frac{H_s}{2} \quad (B-3)$$

The empirical expression for the damping coefficient derived by Burcharth:

$$\delta = 0.0141 \frac{n^{0.5} L^2}{H_s b} \quad (B-4)$$

In which:

n : core porosity

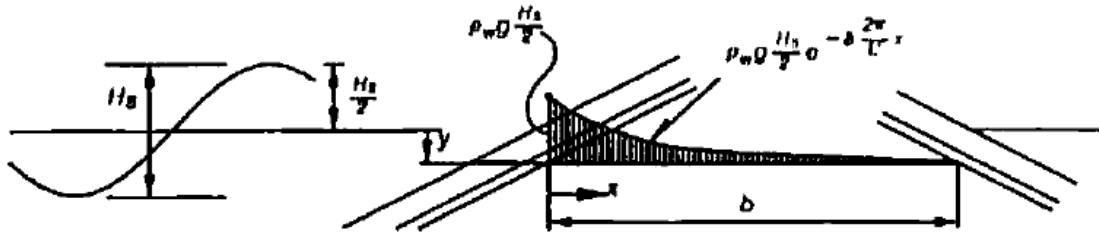


Figure C-2 Core pressure distribution by Burcharth *et al.* (1999)

By assuming a harmonic oscillating water motion the final expression for the pressure inside the structure is derived.

$$p(x, t) = \rho_w g \frac{H_s}{2} e^{-\delta \frac{2\pi}{L'} x} \cos \left(\frac{2\pi}{L'} x + \frac{2\pi}{T_p} t \right) \quad (B-5)$$

Likewise the horizontal pressure gradient is given by:

$$I_x = \frac{1}{\rho g} \frac{dp(x,t)}{dx} = -\frac{\pi H_s}{L'} e^{-\delta \frac{2\pi}{L'} x} \left[\delta \cos \left(\frac{2\pi}{L'} x + \frac{2\pi}{T_p} t \right) + \sin \left(\frac{2\pi}{L'} x + \frac{2\pi}{T_p} t \right) \right] \quad (B-6)$$

Horizontal pressure gradient is also given by the extended Forchheimer equation (Burcharth *et al.* [1995]) for porous flow:

$$I_x = \alpha \left(\frac{1-n}{n} \right)^2 \frac{v}{g d_{50}^2} \left(\frac{u}{n} \right) + \beta \frac{1-n}{n} \frac{1}{g d_{50}} \left(\frac{u}{n} \right)^2 \quad (B-7)$$

In which:

- v : pore velocity (m/sec)
- ν : kinematic viscosity (m²/sec)
- α, β : coefficients dependent $Re = u \cdot d_{50} / \nu$, grain size and grading (Burcharth *et al.* [1995])

Combining equations (B-6) and (B-7), pore velocities can be calculated for any given boundary condition. In total, computation is repeated for six points; in distances $x=0, x=b/4$ and $x=b/2$ and for two water levels; $y=0$ and $y=-H_s$. In case that the computed pore velocities

are not located in the turbulent flow regime, a new scale factor can be derived such that turbulent flow conditions inside the breakwater are assured.

Core pressure at two (vertical) distances from the waterline is calculated, with the three wave conditions (WC1, WC2, WC3). The outcome is displayed in Figure C-3 where pressure is plotted as a function of distance inside the breakwater.

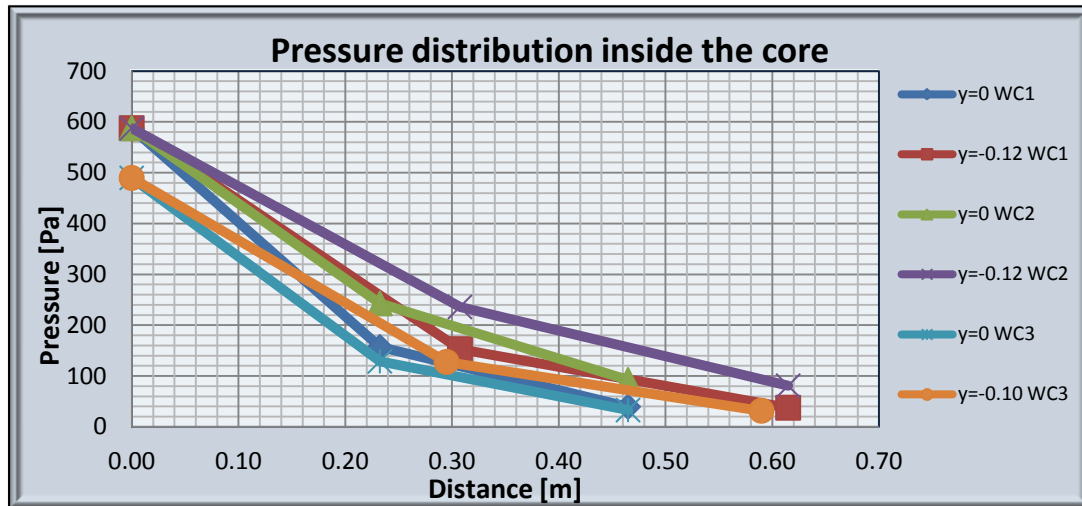


Figure C-3 Core pressure distribution inside the breakwater. All wave conditions.

By knowing the pressure distribution, the gradient can be calculated and based on that pore velocity distribution can be specified. Afterwards, the velocity at three distances along the x-axis is used to determine the average velocity at this y-level. By knowing the average velocity at two y-levels; $y=0$ and $y=-H_s$, the representative core velocity is computed. Finally, the corresponding particle Reynolds Number Re_p specifies whether flow conditions are located in the laminar or turbulent regime.

Figure C-4 provides the porous velocity distribution inside the breakwater. For the core, the corresponding particle Reynolds Number using $D_{n50}=0.015m$ was $Re_p=280$, $Re_p=200$, $Re_p=220$ for WC1, WC2, WC3 respectively. Therefore, porous flow inside the breakwater is located into the transitional turbulent regime. No further action will take place since the entailed slightly enhanced amount of reflected energy increases the amount of energy that is gathered in front of the breakwater, thus contributes on the safe side of this research.

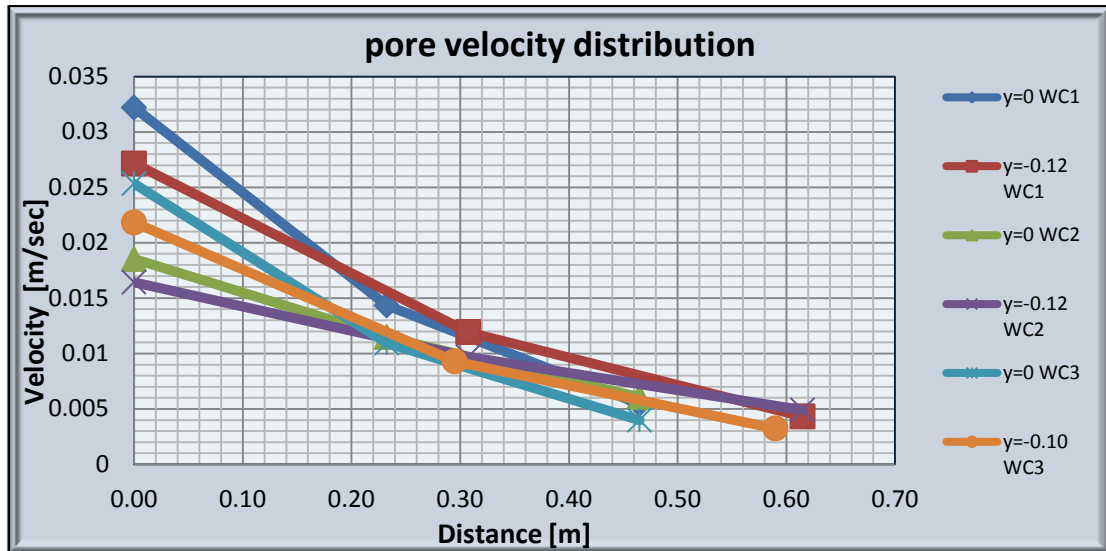


Figure C-4 Core pressure distribution inside the breakwater. All wave conditions.

C-3. Literature 0

1. BURCHARTH, H.F., CHRISTENSEN, C., (1991) *On stationary and non-stationary porous flow in coarse granular materials*. MAST G6-S, Project I, Aalborg University, Department of Civil Engineering, Report
2. BURCHARTH, H.F., ZHOU L., TROCH P., (1999). *Scaling of core material in rubble mound breakwater tests*, COPEDEC V, Cape Town, South Africa
3. BURGER, W., OUMERACI, H., PARTENSKY H.W., (1988). *Geohydraulic investigations of rubble mound breakwaters*, Proc. Int. Conf. on Coastal Engineering, ASCE 1988
4. DYBBS, A., EDWARDS, R., (1984). A new look at porous media mechanics Darcy to turbulent, in *Fundamentals of Transport Phenomena in Porous Media*, edited by J. Bear and Y. Corapcioglu, pp. 199–254, Martinus Nijhoff, Zoetermeer, Netherlands

Appendix D Variance density spectrum plots for all WCs

Figure D-1 illustrates the VDS for the case of WC1 and Test2a. The differences between the tests with WC1 are trivial, and the resulting plots are identical. This holds also for the other wave conditions. The highest peaks and thus the larger amount of energy is located around the frequency 0.4Hz since the peak period of WC1's spectrum is $T_p=2.485s$.

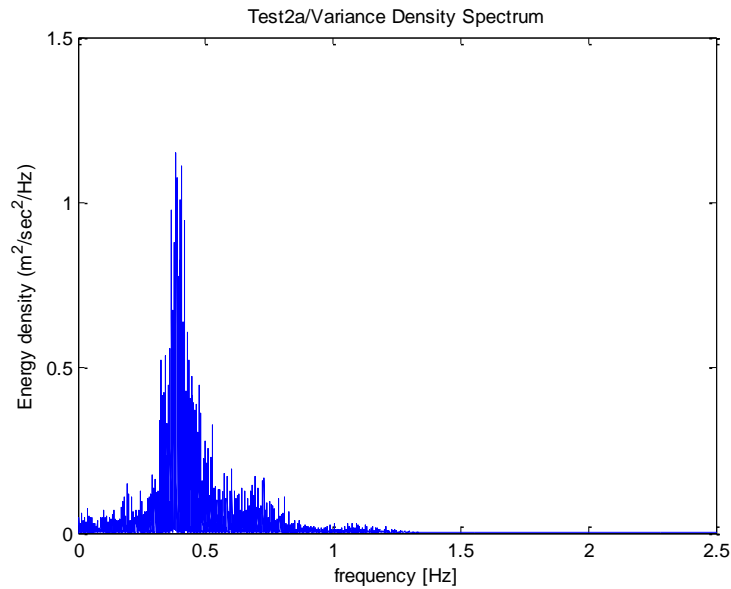


Figure D-1 Test2a: Variance density spectrum

Figure D-2 illustrates the VDS for the case of WC2 and Test2b. Here, the highest peaks and thus the larger amount of energy is displaced towards the frequency 0.5Hz because peak period of WC2's spectrum is $T_p=2.485s$. Finally, the signal is more symmetrical around this frequency with respect to VSD of WC1.

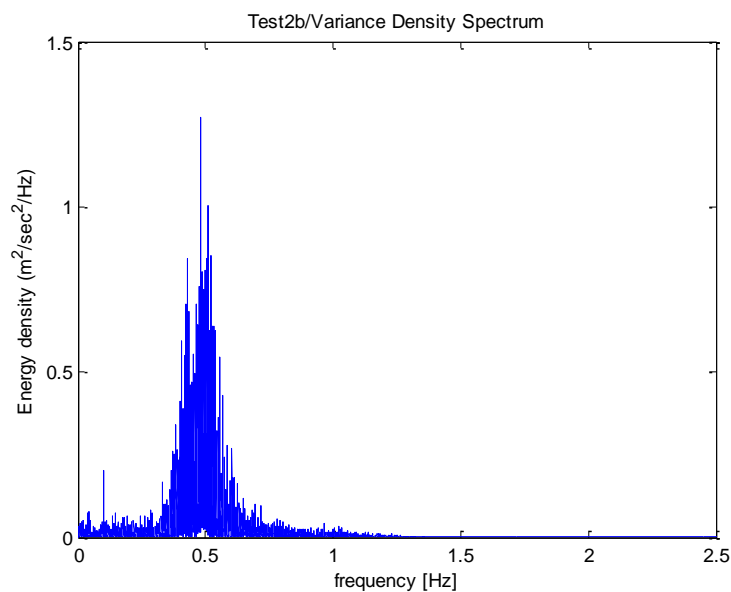


Figure D-2 Test2b: Variance density spectrum

From Figure D-3 it is clearly visible that the amount of energy for WC3 is less than the WC1; thus a lower representative velocity is expected. The shape of the signal resembles the case of WC1, while the largest amount of energy is concentrated around 0.4 Hz (WC3 $T_p=2.485s$).

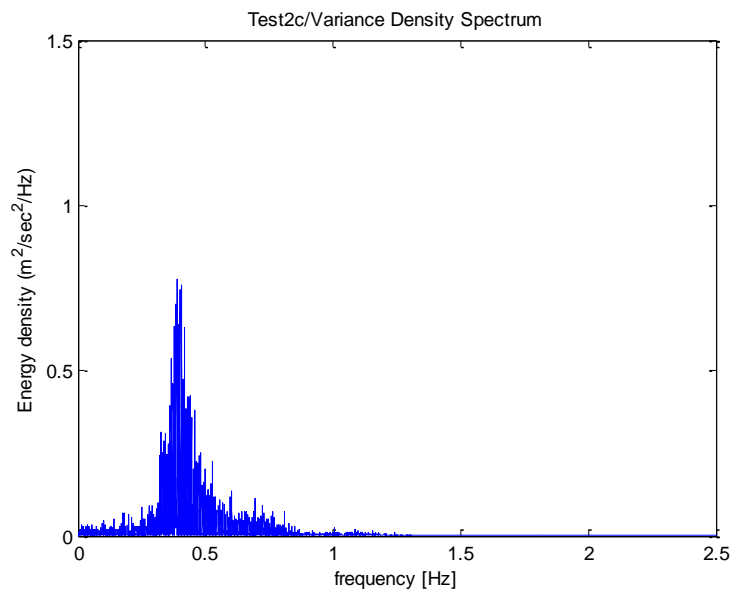


Figure D-3 Test2b: Variance density spectrum

Finally, Figure D-4 presents the VSD for WC1 and the long duration Test2f. The shape of the signal is similar to Test2a; however, the area enclosed under the curve is larger due to the larger durations. Likewise to Test2a highest peaks are located around the frequency 0.4 Hz.

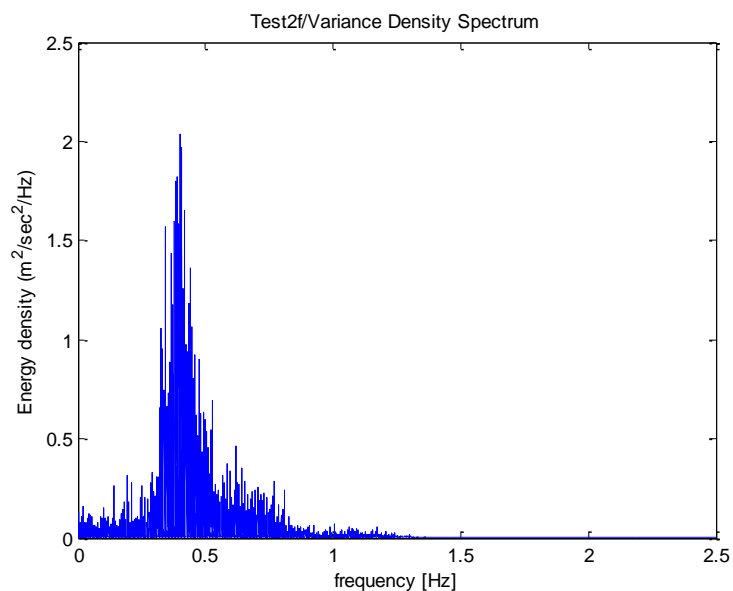


Figure D-4 Test2b: Variance density spectrum

Appendix E Additional analysis for temporal evolution of scour

Appendix E consists of two sections. Section E-1 provides contains additional plots (for all WCs that link relative maximum scour depth S/S_{final} with the number of peak waves N_p and are used to supplement the analysis presented in Section 6.2. Section E-2 treats the analysis of temporal evolution of maximum scour depth for the part of the dataset where equilibrium maximum scour depth was reached.

E-1. Additional plots for $S/S_{final}=f(N_p)$

The following plots are offered to supplement analysis presented in Section 6.2.

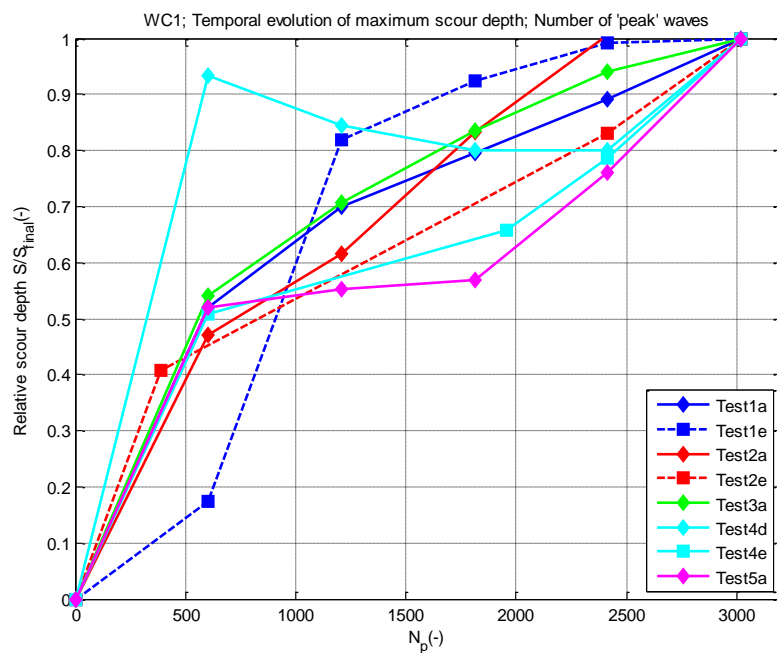


Figure E-1 Temporal evolution of maximum scour depth. Measurements taken through the right side glass. Tests WC1 and regular duration (3000 'peak' waves)

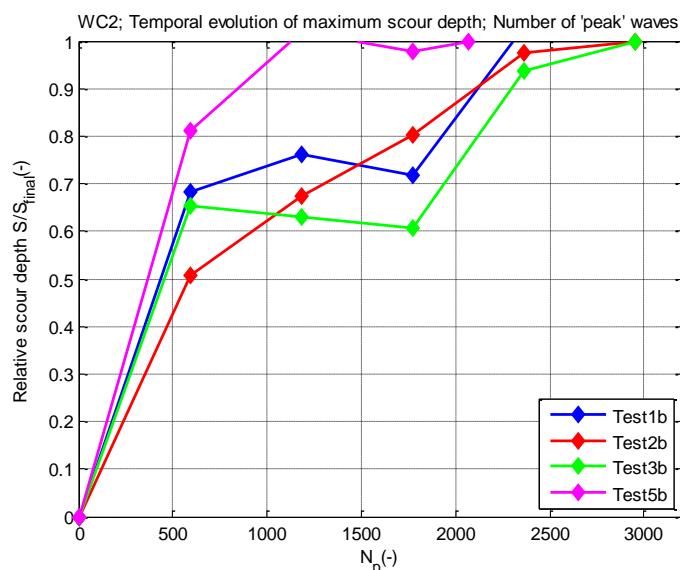


Figure E-2 Temporal evolution of maximum scour depth. Measurements taken through the right side glass. All tests WC2

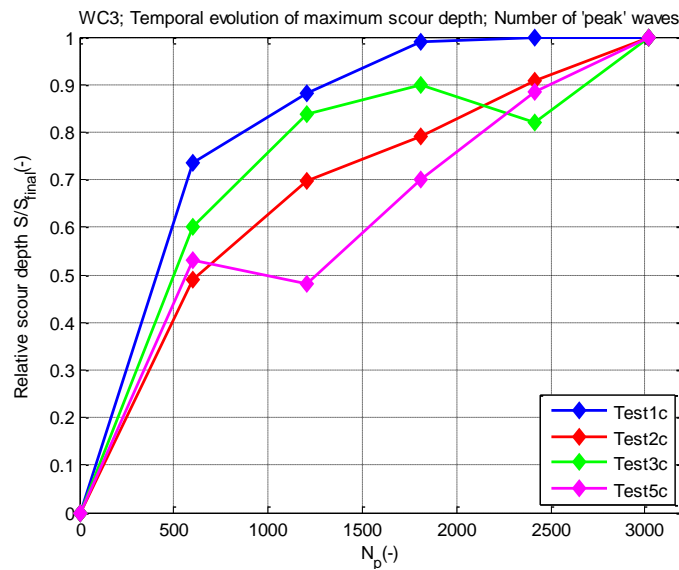


Figure E-3 Temporal evolution of maximum scour depth. Measurements taken through the right side glass. All tests WC3

E-2. Analysis for tests that reached equilibrium maximum scour depth

According to Paragraph 5.2.4, equilibrium maximum scour depth was reached for Tests²⁶ 1b, 1c, 1e, 2b, 2f, 3e & 5b. For these tests, a different approach can be followed in order to analyze the temporal evolution of maximum scour depth.

In particular, for these tests, maximum scour depth was increasing until a specific point in time after which no further increase was observed. This point corresponds to equilibrium maximum scour depth S_{\max} and is expressed via the number of 'peak' waves N_{\max} . Thereby, every moment "t" during a test corresponds to a specific amount of waves N_t and to a specific maximum scour depth S_t . Table E-1 for every test the values of equilibrium maximum scour depth and the corresponding time expressed with the number of peak waves N_{\max} .

N_0	S_{\max}	N_{\max}	N_0	S_{\max}	N_{\max}
-	cm	-	-	cm	-
Test1b	2.43	2362	Test2b	2.58	2362
Test1c	2.71	1810	Test2f	5.11	4803
Test1e	2.81	2414	Test3e	2.61	6036
			Test5b	1.45	1181

Table E-1 Equilibrium maximum scour depth S_{\max} and equilibrium time expressed via N_{\max} per each test

²⁶ Test4d had also reached equilibrium maximum scour depth. However, the results from the analysis through the side glass cannot give a clear picture about when equilibrium was reached (see Figure 6-5). Therefore, it was not included into this part of the analysis.

As long as maximum scour depth is developing with time, every moment “t” corresponds to a specific pair of S_t/S_{max} & N_t/N_{max} . Consequently, every pair is plotted in x-y coordinates to distinguish the link between the two variables. Figure E-4 plots the result.

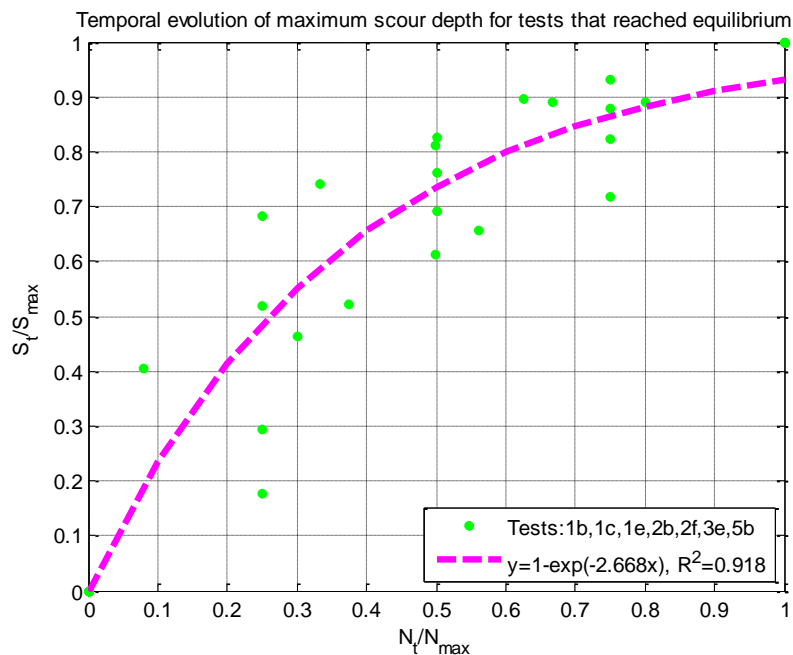


Figure E-4 Temporal evolution of maximum scour depth for tests that reached equilibrium maximum depth. Tests 1b, 1c, 1e, 2b, 2f, 3e & 5b

The plotted data set can be best described with the following equation:

$$\frac{S_t}{S_{max}} = 1 - \exp\left(-2.668 \frac{N_t}{N_{max}}\right) \quad (6-1)$$

The type of the afore-mentioned equation is the proper form to simulate the behavior of a system that approaches asymptotically to a specific value which in this case is the equilibrium maximum scour depth. Additionally, the correlation between the data set and eq. (6-1) is more than satisfying ($R^2=0.918$).

Apparently, the data set used in this case consists of tests with different wave loading (WC) different filter configuration properties and different base materials. However, the population of each of the categories is very limited in order to distinguish alternative trends and extract safe conclusions. For this reason, no further analysis can take place.

Appendix F Additional tables with test parameters

Below can be found, two tables that contain information, with respect additional test parameters, that could not be presented in the main body of the report.

Test Series	N ₀ (-)	N _p (-)	Time (sec)	D _{f90} cm	D _{f85} cm	D _{f65} cm	D _{f15} cm	D _{f10} cm	W _{rem} kg	C _r -
1	Test1a	2987	7424	2.10	2.00	1.60	0.95	0.90	0.686	0.494
	Test1b	2953	6000	2.10	2.00	1.60	0.95	0.90	0.665	0.494
	Test1c	3025	7517	2.10	2.00	1.60	0.95	0.90	0.660	0.505
	Test1d	3027	7521	2.10	2.00	1.60	0.95	0.90	1.094	0.491
	Test1e	3130	7777	2.10	2.00	1.60	0.95	0.90	0.850	0.481
2	Test2a	3042	7558	1.57	1.55	1.40	1.03	1.00	0.827	0.500
	Test2b	2976	6047	1.57	1.55	1.40	1.03	1.00	0.528	0.495
	Test2c	3012	7486	1.57	1.55	1.40	1.03	1.00	0.501	0.501
	Test2d	3012	7485	1.57	1.55	1.40	1.03	1.00	1.024	0.494
	Test2e	3026	7518	1.57	1.55	1.40	1.03	1.00	1.019	0.497
	Test2f	5994	14974	1.57	1.55	1.40	1.03	1.00	2.194	0.493
3	Test3a	2960	7356	1.10	1.10	1.00	0.84	0.80	0.874	0.506
	Test3b	2945	5984	1.10	1.10	1.00	0.84	0.80	0.343	0.503
	Test3c	3012	7485	1.10	1.10	1.00	0.84	0.80	0.558	0.517
	Test3d	2885	7169	1.10	1.10	1.00	0.84	0.80	0.921	0.514
	Test3e	7269	18063	1.10	1.10	1.00	0.84	0.80	0.782	0.506
4	Test4a	2896	7196	0.79	0.75	0.72	0.60	0.59	0.525	0.498
	Test4d	2806	6972	0.79	0.75	0.70	0.60	0.59	0.579	0.497
	Test4e	3013	7488	0.79	0.75	0.70	0.60	0.59	0.675	0.502
	Test5a	3167	7871	1.10	1.10	0.10	0.84	0.80	0.565	0.497
5	Test5b	2929	5951	1.10	1.10	0.10	0.84	0.80	0.572	0.497
	Test5c	3168	7873	1.10	1.10	0.10	0.84	0.80	0.599	0.506
	Test5d	5995	14975	1.10	1.10	0.10	0.84	0.80	0.870	0.497

Table F-1 Additional test parameters per test. Filter layer grading properties, test duration, reflection coefficient and weight of the removed base material

Test Series	N ₀ (-)	Cross section										
		5cm	10cm	15cm	20cm	25cm	30cm	35cm	40cm	45cm	50cm	55cm
1	Test1a	2.44	2.39	2.04	1.99	1.83	2.01	2.09	1.96	2.27	1.76	0.46
	Test1b	1.93	1.93	1.55	1.53	1.50	1.14	0.82	1.35	1.59	1.93	2.61
	Test1c	1.49	1.24	0.77	1.09	1.27	1.28	1.90	2.06	1.70	2.08	1.84
	Test1d	3.92	3.61	2.89	3.01	2.39	2.97	2.51	2.95	2.96	3.15	3.17
	Test1e	2.82	2.96	2.87	2.72	3.05	3.42	2.12	0.92	0.70	0.71	1.17
2	Test2a	3.45	3.03	2.55	2.27	2.39	2.51	2.04	2.19	2.59	3.15	3.13
	Test2b	1.78	1.55	1.47	0.93	0.92	0.86	0.97	1.04	1.53	1.60	2.08
	Test2c	2.90	2.66	2.59	2.08	2.42	2.26	2.14	1.79	2.08	2.39	2.37
	Test2d	3.45	3.89	3.42	3.05	2.49	2.75	2.47	2.72	2.92	2.80	3.17
	Test2e	3.32	2.91	2.85	2.90	2.63	2.24	2.83	2.72	2.96	2.81	3.46
	Test2f	4.41	4.33	4.24	3.85	3.85	3.80	3.20	2.96	3.25	3.36	3.08
3	Test3a	2.96	2.66	2.16	1.90	1.62	1.28	1.75	1.68	1.59	1.97	2.01
	Test3b	1.29	0.84	0.86	1.06	1.20	0.65	0.50	0.47	0.53	0.82	0.70
	Test3c	1.15	1.00	1.02	1.28	1.32	1.04	1.28	1.17	0.86	1.06	0.70
	Test3d	2.22	2.28	2.38	2.43	2.18	2.35	2.32	2.22	2.57	2.37	1.95
	Test3e	2.27	1.78	1.22	1.30	0.89	1.02	1.07	1.36	1.82	1.77	2.59
4	Test4a	0.44	0.43	0.39	0.32	0.46	0.27	0.39	0.41	0.30	0.33	0.36
	Test4d	0.87	1.07	0.88	1.64	1.52	1.06	0.79	0.40	0.94	0.67	0.78
	Test4e	1.01	1.05	1.19	0.88	1.01	1.31	0.81	0.76	1.17	0.87	1.00
	Test5a	2.09	1.56	2.04	1.08	1.38	1.04	1.38	1.83	1.22	1.23	1.41
5	Test5b	2.31	1.76	1.25	1.39	0.63	0.75	0.50	0.76	0.78	0.71	0.96
	Test5c	0.88	0.45	0.73	0.98	1.52	1.56	1.32	0.73	0.73	0.61	0.87
	Test5d	2.72	3.07	2.86	2.20	2.67	2.87	4.14	2.76	2.29	2.27	2.53

Table F-2 Maximum scour depth S_{max} per test and per cross section. Distance is measured from right side glass.